

ABSTRACT

FAELI, ZAHRA. Reactive Flow and Transport Analysis in Unsaturated and Saturated Profiles with Focus on MICP Soil Improvement and Ingress of Contaminants into Subsurface Concrete Pipeline (Under the direction of Dr. Mo Gabr and Dr. Brina M. Montoya).

Microbial induced calcium carbonate precipitation (MICP) offers a sustainable biological technique to improve geologic properties of onshore and offshore subsurface areas of engineering structures. MICP employs micro-organisms and reaction kinetics to hydrolyze urea, which in the presence of calcium, may favor the calcium carbonate (CaCO_3) precipitation. Due to the high cost of large-scale field trials and the limited number of variables that can feasibly be investigated, the use of numerical modeling has drawn the attention of researchers in the recent years. Although several mathematical models have been recently developed to predict MICP processes in porous media, but many of them suffer from a lack of comprehensive coverage of all MICP parameters and are intended to match results from a series of experiments conducted under specific conditions.

A comprehensive reactive transport model was developed to determine the effects of controlling factors in terms of treatment protocols and experimental methods using finite element method and COMSOL Multiphysics 5.5. The developed model framework aims to properly capture MICP reactive transport process in small- and large-scale tests and contributes to the effort of upscaling and design of field deployment protocols. The bacterial transport/attachment/decay, ureolysis rate, microbial distribution, porosity/permeability modification, and cyclic injections are included in the transport model.

The model parameters have been calibrated using six column tests in literature and a range for the key parameters has been determined. There were differences between soil type, column dimensions, initial properties of porosity and hydraulic conductivity, treatment protocol, flow rates, and injection direction. The capability of the model to predict CaCO_3 precipitation within a reliable range of accuracy utilizing data reported in literature has been shown. Fifteen key parameters were assessed through sensitivity/parametrization analyses. The results emphasized the effects of two principal factors of specific ureolysis rate, and attachment model on the precipitation content and distribution.

After calibration, numerical analyses were conducted to explore the influence of various layouts and configurations of injection wells in delivering effective deployment of the MICP process. To scrutinize the extent of predicting the attached biomass distribution in both small- and

field-scale tests five proposed attachment models have been assessed; (a) constant rate, (b) nonlinear power-law distribution, (c) exponential distribution, (d) gamma distribution, and (e) the c_{str} based on the colloid attachment theory. The colloid attachment theory with velocity and straining terms was shown to be the most efficient approach in yielding the most fitted calcium carbonate distribution with experimental measurements. A new parameter c_{str} , was incorporated into the model to constraint straining at distances farther from injection source.

The key parameters of MICP process in unsaturated soils have been assessed through comparing mass percentage of calcium carbonate at various degrees of saturation, 20%, 40%, 80%, and fully saturated condition in sandy soil media. The bacteria attachment coefficient (K_{at}) has been calibrated at various degrees of saturation.

Contaminant transport in the unsaturated domain has been recognized as a complex multiphase multicomponent process. A series of three-dimensional numerical reactive flow and transport analyses were conducted using T2VOC code to explore transport aspects related to benzene breakthrough into gasketed subsurface concrete pipe embedded in unsaturated soil profile. The rate and magnitude of mass transport through the unsaturated media, into the pipe trench and breakthrough into the different material classes of concrete pipes have been assessed in both gaseous and aqueous phases.

A new pipe material monitoring capsule (PMMC) has been simulated to evaluate volatile organic compounds (VOCs) and chlorinated solvents (CS) breakthrough three types of pipe gasket materials; Neoprene, Buna-N, and Viton. Three contaminated sites were selected to deploy PMMCs. A 3D field-domain model including PMMC has been developed for each site using finite difference method incorporated in GMS to calibrate hydraulic parameters of pipe materials. Protocols were recommended for installing/retrieval of PMMCs to monitor breakthrough rate.

© Copyright 2021 by Zahra Faeli

All Rights Reserved

Reactive Flow and Transport Analysis in Unsaturated and Saturated Subsurface Profiles with
Focus on MICP Soil Improvement and Ingress of Contaminants into Subsurface
Concrete Pipeline

by
Zahra Faeli

A dissertation submitted to the Graduate Faculty of
North Carolina State University
in partial fulfillment of the
requirements for the degree of
Doctor of Philosophy

Civil Engineering

Raleigh, North Carolina

2021

APPROVED BY:

Dr. Mo Gabr
Committee Co-Chair

Dr. Brina M. Montoya
Committee Co-Chair

Dr. Mohammad Pour-Ghaz

Dr. Ashley Cabas

DEDICATION

To my beloved parents and my exceptional sister, and brothers. I could not have done this without your unwavering support.

BIOGRAPHY

Zahra Faeli is a doctoral candidate in the Department of Civil, Construction, and Environmental Engineering at North Carolina State University. She earned her Bachelor of Science in civil engineering from K.N. TOOSI University (KNTU), and then Master of Science in geotechnical engineering from University of Tehran. Her work during master program was related to the allowable differential settlement of oil pipelines in conditions of heterogeneous soil beds or adjacent to tanks. She worked for geotechnical consulting companies after getting her master's. She started her PhD at North Carolina State University in August 2017 under direction of Dr. Mo. Gabr and Dr. Brina M. Montoya.

ACKNOWLEDGMENTS

This Dissertation would not have been possible without the immense help and support from my advisor Dr. Mo Gabr. He provided me with the opportunity to pursue my Ph.D. studies at NC State and I'm really happy from working with an advisor with exceptional knowledge and attitude. I could not have asked for a better advisor. It has been a great learning experience working with him during my research.

My special appreciation goes to my co-advisor Dr. Brina Montoya for her invaluable guidance and help with my project. She has been a role model to me and has provided me with her advice whenever I needed one.

Furthermore, I want to extend my gratitude to Dr. Pour-Ghaz for his support, constructive feedbacks and suggestions during our project. Last but not least, I would like to thank Dr. Cabas, and Dr. Kay for being in my committee, their availability, and willingness to help. The North Carolina Department of Transportation (NCDOT) financially supported the research presented in this dissertation.

I'm also honored and grateful to have incredible teachers at North Carolina State University, Dr. Rahman, Dr. Gabr, Dr. Montoya, Dr. Mahinthakumar, and Dr. Autry who helped me to grow and flourish throughout my PhD.

I want to thank my great advisors during my master's, Dr. Fakher, Dr. Behnia, and also my great colleague Mr. Kiani at Pandam Company who supported me and always shared their valuable knowledge without any expectation.

I would like to wholeheartedly thank my parents, Mr. Mohammad Faeli, Mrs. Akhtar Pad, for their unconditional love, sacrifice, and patience. I cannot thank them enough for the selfless sacrifices they have made to give me a comfortable life and quality education. I am thankful to my lovely brothers and sister, Reza, Farzaneh, Mehdi, their nice families and my adorable niece Helia for their encouragement and inspiring me to strive for greater heights.

I want to thank my best friends in Raleigh who made everything easier for me, Zeynab Jouzi, and Hanieh Moghadam.

I am thankful to my fellow geotechnical graduate students at NCSU, Ashkan Nafisi, Jinung Do, Sultan Alhomeir, Atefeh Zamani, Pegah Ghassemi, Mona Doostmohammadi, Amin Rafie, Jennifer Vaughn, Rowshan Jadid, Ishika Chowdhury, Qianwen Liu, Thomas Na, Maria Ramos, Long Vo, Ahsan Uz Zaman, Chunyang Ji, Nancy Ingabire Abayo, Azmayeen Shahriar, Faria

Ahmed, Conor O'Toole, Marlee Strong, Neda Jamaledin and also my friends outside of the geotechnical department; Parisa Javani, Zahra Aghazadeh, Mojtaba Noghabaei, Payam Hosseini, Narges Matini, Ali Tajik, Zarinaz Sadri, Ammirreza Sahebi, Mohammad Ali Khaksar, Kasra Darabi, Mojtaba Sardar Mehri, Mojdeh Pajouh, Mona Arabshahi, Golbarg Hadi, and Arezu Mohammadpour. I am grateful to them for always being there for me and sharing the most beautiful moments of my life.

TABLE OF CONTENTS

LIST OF TABLES	x
LIST OF FIGURES	xii
CHAPTER 1. Overview of Dissertation	1
1.1 Introduction	1
1.2 Scope of Research	3
1.3 Dissertation Organization.....	4
CHAPTER 2. Elucidating Factors Governing MICP Biogeochemical Processes at Macro-Scale: A Reactive Transport Model Development	7
Abstract	7
2.1 Introduction.....	7
2.2 Model Development.....	9
2.2.1 COMSOL-Multiphysics framework.....	9
2.2.2 Biogeochemical Processes and Mathematical Model Development.....	9
2.2.3. Simulations of 1-D Column Testing.....	12
2.3. Model Calibration	14
2.4. Parametrization and Sensitivity Analyses.....	16
2.5. Results and Discussion.....	17
2.6. Conclusion.....	22
CHAPTER 3. Reactive Transport Modeling of Microbial Induced Calcium Carbonate Precipitation Utilizing Various Configurations of Injection Wells	39
Abstract	39
3.1. Introduction	39
3.2. Model Development.....	40
3.3. Model Calibration	42
3.4. Field-Scale Model Configuration.....	43
3.5. Results and Discussion.....	44
3.6. Conclusion.....	46
CHAPTER 4. Various Bacterial Attachment Functions and Modeling of Distribution of Biomass and Calcium Carbonate Precipitation in MICP Implementations	53
Abstract	53
4.1. Introduction	53
4.2. Model Development.....	56

4.2.1. The COMSOL-Multiphysics Framework.....	56
4.2.2. Bio-geochemical Process and Mathematical Model Development.....	57
4.2.3. Bacteria Transport, Attachment, Decay, and Encapsulation.....	58
4.3. Application to small-scale experiments.....	64
4.4. Application to Large-scale Experiments.....	64
4.4.1. Large-scale Test - Montoya et al. (2021).....	64
4.4.2. Meter-scale Biocementation Test-San Pablo et al. (2020).....	65
4.5. Results and Discussion.....	66
4.5.1. 1-D Column Testing.....	66
4.5.2. Large-scale MICP Experiment.....	68
4.5.3. Meter-Scale Biocementation Test.....	74
4.6. Conclusion.....	75
CHAPTER 5. Development of a Reactive Transport Model for Microbial Induced Calcium Carbonate Precipitation in Unsaturated Conditions.....	93
Abstract.....	93
5.1. Introduction.....	93
5.2. Model Development.....	94
5.2.1. Constitutive Model.....	94
5.2.2. Material Properties.....	96
5.2.3. Model Configuration.....	96
5.3. Results and Discussion.....	97
5.4. Conclusion.....	100
CHAPTER 6. Benzene Migration in Unsaturated Profile with Subsurface Drainage Concrete Pipe.....	111
Abstract.....	111
6.1. Introduction.....	111
6.2. Governing Equations.....	112
6.3. Site Description.....	114
6.4. Model Development.....	114
6.4.1. Domain Configuration.....	114
6.4.2. Model Parameters.....	115
6.4.3. Boundary Conditions.....	115
6.4.5. Simulation Process.....	116

6.5. Results and Discussion.....	117
6.6. Summary and Conclusion	118
CHAPTER 7. Factors Affecting Multiphase Benzene Breakthrough into Drainage Concrete Pipe in the Unsaturated Subsurface Profile	125
Abstract	125
7.1. Introduction	125
7.2. Multiphase Transport of VOC in Subsurface.....	128
7.3. Case Study.....	131
7.3.1. Site Description	131
7.3.2. Model Development	132
7.3.3. Model Parameters	133
7.3.4. Simulation Approach.....	135
7.3.5. Sensitivity Analyses of Domain and Mesh Size.....	135
7.3.6. Model Verification	136
7.4. Results and discussion.....	136
7.4.1. Pipe Material Quality.....	137
7.4.2. Gasket Material Quality.....	139
7.4.3. The NAPL Phase Thickness at the Source	140
7.4.4. Native Soil Material.....	141
7.4.5. Emission to the Atmosphere Layer and Adsorption.....	141
7.5. Conclusions	142
CHAPTER 8. A New Monitoring Approach for Sustainability Assessment of Subsurface Utilities Gasket Materials Against Gasoline and Chlorinated Solvents: Field Evaluation and Model Development.....	158
Abstract	158
8.1. Introduction	158
8.2. Methods.....	161
8.2.1. PMMC Design.....	161
8.2.2. Deployment/Retrieval Strategies.....	161
8.2.3. Field sites.....	162
8.2.4. Measurements of retrieved PMMC	164
8.3. Model Development.....	164
8.4. Model Calibration	167

8.5. Results and Discussion.....	167
8.5.1. Benzene Contaminated Sites	167
8.5.2. PCE Contaminated Site	169
8.6. Conclusion.....	171
CHAPTER 9. Contributions and Future works	189
9.1. Contribution	189
9.2. Future Work	191
REFERENCES.....	192
APPENDICES.....	201
Appendix A.....	202
Appendix B	205

LIST OF TABLES

Table 2.1 Specific rate of ureolysis (K_u), Maximum microbial activity (V_{max}), half-saturation rate (K_m), and initial biomass concentration from past studies.....	24
Table 2.2 Microbial attachment rate coefficient (K_{at}).....	25
Table 2.3 Microbial decay rate coefficient (K_{decay}).....	25
Table 2.4 Simulated column tests properties.....	26
Table 2.5 Bio-injection treatments in simulated tests.....	26
Table 2.6 Cementation treatments in simulated tests.....	27
Table 2.7 Column tests calibrated parameters.....	28
Table 2.8 Model parameters used in sensitivity analyses in four categories.....	29
Table 2.9 Results of sensitivity analyses. Trend of $CaCO_3$ and COV indicates how these variables change when a parameter increases within the defined range based on past studies.....	30
Table 3.1 MICP model parameters.....	48
Table 3.2 Simultaneous and Phased injection results.....	48
Table 4.1 Comparison between the different biomass distribution approaches from literature and modified relationship used in this study.....	77
Table 4.2 Comparison between use of various bacteria attachment approaches using 1-D column test (experimental measurements per Do et al. 2019): calibrated and statistical parameters; mean $CaCO_3$, normalized hydraulic conductivity with initial one, and normalized attached biomass with initial injected bacteria.....	78
Table 4.3 Simulated large-scale test; comparison between calibrated parameters for different bacteria attachment approaches.....	79
Table 4.4 Simulated large-scale test; comparison between different bacteria attachment approaches, mean $CaCO_3$ (%), and statistical parameters for each approach.....	81
Table 4.5 Calibrated parameters for small- and large-scale tests modeled with the c_{str} based on the colloid attachment theory compared to the calibrated parameters by Bradford et al. (2003) for different soil grain sizes ($d_{50}=0.15, 0.24, 0.36, 0.74$ mm) and colloids' size ($d_p=2, 3.2$ μm). Average size for <i>S. pasteurii</i> used in MICP (d_p) is 2.8 μm	82
Table 5.1 Summary of numerical equations implemented in model development.....	101
Table 5.2 SWCC and Retention model.....	102
Table 5.3 MICP model parameters.....	103
Table 5.4 Bio-injection and cementation treatments in simulated tests.....	104
Table 6.1 Main properties of soil and concrete domain.....	119
Table 6.2 Capillary pressure and relative permeability of soil and concrete.....	119
Table 6.3 Diffusion and adsorption parameters used in simulations.....	120
Table 7.1 Allowable benzene concentration.....	144
Table 7.2 Main petro-physical properties of soil and concrete materials.....	144
Table 7.3 Capillary pressure and relative permeability of different soils and concrete.....	145

Table 7.4 Diffusion and adsorption parameters of benzene.	145
Table 7.5 Benzene Concentrations in groundwater samples (Antea 2016).	146
Table 7.6 Total benzene mass in different phases in the domain including volatilized and normalized adsorbed mass (as % of remained mass).....	146
Table 8.1 Deployment/retrieval schedule of PMMCs.	172
Table 8.2 Monitoring well characteristics and detected VOC concentration history before and during PMMC deployment.	172
Table 8.3 Results of PMMC measurements.	173
Table 8.4 Model flow and transport parameters.	174
Table 8.5 Site material flow and transport parameters.	174
Table 8.6 Calibrated hydraulic parameters of gasket samples (D and k_e) for each site and after each deployment/retrieval.....	175
Table 8.7 Calibrated hydraulic parameters of gasket samples (D and k_e) for benzene and PCE used in prediction studies.	175
Table 8.8 Error estimation of calibrated model.	175
Table 8.9 Recommended protocol for installing/retrieval of gasket-capsules to monitor breakthrough rate.	176
Table 8.10 Recommended protocol for installing/retrieval of gasket-capsules to monitor PCE breakthrough rate.	176
Table 8.11 Calculated Peclet number for benzene and PCE breakthrough the gasket materials installed in PMMC.	176

LIST OF FIGURES

Figure 2.1 (a) Schematic sketch for column test experiment, (b) initial and boundary conditions. (note: injection and outflow can be applied in opposite locations: upward or downward direction, C _{urea} , q(t) and urea(t) represent injected concentration, flow schedule with time, urea treatment schedule with time, respectively, and the same are defined for other components).	31
Figure 2.2 Measured and simulated mass of CaCO ₃ for (a) Whiffin et al. (2007), (b) Martinez et al. (2012), (c) Martinez et al. (2014), (d) Do et al. (2019), and (e) Nafisi et al. (2020) (2 triaxial tests, moderately and heavily cemented sand).	32
Figure 2.3 (a) CaCO ₃ content (%) after treatment, (b) reagent concentrations during treatment period; calcium (Ca) , carbonate (C), urea, ammonium (amm), suspended bacteria (Ssu), attached bacteria (Sat), (c) CaCO ₃ content with time in the middle of specimen for benchmark model in sensitivity analyses.	33
Figure 2.4 CaCO ₃ distribution with variations of : (a) K _u (mol/l.s.OD), (b) injection direction (c) k ₀ (m/s), and (d) L (m) as an example of each category. The same data were obtained for all 15 parameters presented in appendices.....	34
Figure 2.5 Coefficient of variation vs mean CaCO ₃ for the parameters categorized as (a) microbial activity and attachment; (b) specimen preparation; (c) treatment protocol; (d) specimen dimension. The benchmark result was specified with star symbol.	35
Figure 2.6 The results of sensitivity analyses and column test measurements: normalized mean post-treatment hydraulic conductivity (k _f /k ₀) (%), normalized mean post-treatment porosity (θ _f /θ ₀) (%), normalized attached biomass (%), mean CaCO ₃ mass (%),with variation of MICP parameters (a) K _u (b) K _{at} (c) K _{decay} (d) K _m (e) initial hydraulic conductivity, k ₀ (f) initial porosity, θ ₀ (g) flow rate, q (h) number of treatment (i) retention time (j) number of injected PVs (k) column height, L (l) column diameter, D.....	36
Figure 3.1 Model development and calibration flowchart.	49
Figure 3.2 Field-scale model and discretized mesh domain.....	49
Figure 3.3 Differing well configuration assumed to represent potential field situations. In all figures, an extraction well is located at the center of layout surrounded by injection wells. The red numbers indicated phased-injection process studied for layouts (a), (d), and (g) described in the next section; 1 and 2 represent first and second phase treatments, respectively. (a) 2 wells-D=1 m, (b) 3 wells-D=1 m (Extraction well at the center of the injection wells), (c) 3 wells-D=1 m-Ext. (Extraction well at the center of the domain), (d) 4 wells-D=1 m, (e) 4 wells-D=0.5 m, (f) 4 wells-D=0.5 m-P (Parallelogram), (g) 8 wells-D= 0.5 m, (h) 8 wells-D=0.5/1 m.	49
Figure 3.4 Initial pressure head, and CaCO ₃ content; 4-well, Q _i =10 cm ³ /s, Q _o =-5 cm ³ /s, K _u =1x10 ⁻⁶ mol/l.s.OD600.....	50

Figure 3.5 The effect of injection flow rates on various well configuration variables; $Q_o=-5$ cm^3/s , $K_u=2 \times 10^{-6}$ $\text{mol}/\text{l.s.OD600}$. Hollow symbols represent injection flow rate (Q_i)= 5 cm^3/s , filled/colored symbols indicating $Q_i=10$ cm^3/s , and hatched ones showing $Q_i=15$ cm^3/s	50
Figure 3.6 The effect of extraction flow rates on various well configuration variables; $Q_i=10$ cm^3/s , $K_u=2 \times 10^{-6}$ $\text{mol}/\text{l.s.OD600}$. Hollow symbols represent extraction flow rate (Q_o)= -10 cm^3/s , and filled/colored symbols show $Q_o=-5$ cm^3/s	51
Figure 3.7 The effect of specific ureolysis rates (calibrated upper and lower bounds) on various well configuration variables; $Q_i=10$ cm^3/s , $Q_o=-5$ cm^3/s . Hollow symbols represent ureolysis rate (K_u)= 1×10^{-6} $\text{mol}/\text{l.s.OD}$, and filled/colored symbols show $K_u=2 \times 10^{-6}$ $\text{mol}/\text{l.s.OD}$	52
Figure 3.8 Phased injection with middle flow rate ($Q_i=10$ cm^3/s , $Q_o=-5$ cm^3/s , $K_u=2 \times 10^{-6}$ $\text{mol}/\text{l.s.OD}$) from left (a) Phased: first injection at corners, (b) Phased: first injection in the middle of sides, (c) Simultaneous injection.	52
Figure 4.1 Flowchart of model development and analyses in this study.	83
Figure 4.2 Initial and boundary conditions in simulated small-scale column test.....	83
Figure 4.3 (a) Large-scale soil box experiment (Montoya et al. 2021), (b) Schematic sketch of experiment, initial and boundary conditions in model.....	84
Figure 4.4 Model development of large-scale soil box, (a) initial and boundary conditions (b) discretized model domain, and the location of injection source during experiments.	85
Figure 4.5 (a) Horizontal long trough (San Pablo et al. 2020) (b) discretized Model domain, initial and boundary conditions.	86
Figure 4.6 Mass of CaCO_3 with the cstr based on the colloid attachment theory in simulated column test.	86
Figure 4.7 Simulated 1-D column test (experimental measured CaCO_3 per Do et al. 2019); CaCO_3 content and attached biomass within depth resulted from different bacteria attachment functions compared to constant rate (a) Nonlinear power-law distribution function, (b) Exponential distribution function, (c) Gamma distribution function, (d) the cstr based on the colloid attachment theory (the graph labeled with $\text{cstr}=1$ shows the results when this coefficient is not applied). ...	87
Figure 4.8 Simulated Large-scale test (a) mass of CaCO_3 (%) using the cstr based on the colloid attachment theory, (b) mass of CaCO_3 (%) using constant rate.....	88
Figure 4.9 Simulated large-scale test (experimental measurements per Montoya et al. 2021); comparison between measured and calculated CaCO_3 content using the cstr based on the colloid attachment theory and constant rate, (a) mass of CaCO_3 (%) at nodal locations, (b) averaged mass of CaCO_3 (%) at subareas.	89
Figure 4.10 A plot of fitted attachment and straining coefficients as a function of size of bacteria (d_p), mean soil particle size (d_{50}), sample diameter/width (D), sample	

height (L), injected bacteria (PVbact.), and soil pore volume (PVsoil), a) Katt Uz, b) Kstr.....	90
Figure 4.11 Simulated Large-scale test (experimental measurements per Montoya et al. 2021) using the cstr based on the colloid attachment theory (a) normalized hydraulic conductivity (%) with respect to initial hydraulic conductivity, (b) normalized porosity (%) with respect to initial porosity.....	91
Figure 4.12 Simulated large-scale test; Da number with distance from injection source.....	91
Figure 4.13 Simulated horizontal trough test using colloid attachment theory, mass of CaCO ₃ (%), Ku= 1x10 ⁻⁶ mol/l.s.OD, Katt=1x10 ⁻⁶ 1/s, β=0.75, Kstr=2x10 ⁻³ 1/s.....	92
Figure 4.14 Simulated horizontal trough test, CaCO ₃ content along horizontal trough resulted from the cstr based on the colloid attachment theory compared to constant rate. In all colloid theory models Katt=1x10 ⁻⁶ 1/s and β=0.75. In constant rate model Kat=3x10 ⁻⁶ 1/s. The cstr coefficient was defined in horizontal direction for the graph labeled with cstr as Eq. (16).	92
Figure 5.1 Grain size distribution for coarse sand (Cheng et al. 2013).	104
Figure 5.2 Soil-Water characteristic curves of materials.....	105
Figure 5.3 Column model and discretized mesh domain.....	105
Figure 5.4 CaCO ₃ content- S:40%-No. of treatment: 8	106
Figure 5.5 Comparison between 3D horizontal and axisymmetric columns after 3 treatments for 20, 40, 80% and 4 treatments at saturated condition.	106
Figure 5.6 Inlet and outlet velocity during treatment.	107
Figure 5.7 CaCO ₃ content at different degree of saturations, drying and wetting branches of SWCC for coarse sand compared with laboratory measurements (a) CaCO ₃ content with normalized injected volumes (b) CaCO ₃ content with injected volumes.	108
Figure 5.8 CaCO ₃ content at different degree of saturations, various normalized injected volumes, drying and wetting branches of SWCC for coarse sand-type II compared with laboratory measurements.....	109
Figure 5.9 Hydraulic conductivity variations with CaCO ₃ precipitation at different degrees of saturation, k ₀ =4.47x10 ⁻⁴ m/s for sand, k ₀ =2.20x10 ⁻⁷ m/s for clay.	109
Figure 5.10 Porosity variations with CaCO ₃ precipitation at different degrees of saturation, ε ₀ =0.39 for sand, ε ₀ =0.43 for clay.....	110
Figure 5.11 Comparison between coarse and fine sands indicating changes in unsaturated properties of coarse sand during treatment. Fine sand has the permeability and porosity equal to the ones for the treated coarse sand after 8 treatment cycles.....	110
Figure 6.1 Jacksonville site map with monitoring wells locations and area utilized as model domain (site map from Antea, 2016).....	120
Figure 6.2 Schematic sketch of Model.	121
Figure 6.3 The Model and created Mesh (pipe and trench are located above water table level in unsaturated zone).....	121

Figure 6.4 The discretized mesh with pipe and gaskets (Distances of gaskets are 2.5 m).	122
Figure 6.5 Water Retention Curves and SWCCs used in simulations.	122
Figure 6.6 Benzene concentration inside the pipe for two water table levels a) Aqueous phase b) Gas phase.	123
Figure 6.7 Cumulative mass breaking through the pipe for two water table levels a) Aqueous, phase and b) Gas phase.	124
Figure 7.1 Site map with the gas station location, model domain, the monitoring well locations, and the groundwater flow direction (Antea 2016).	147
Figure 7.2 Schematic sketch of model.	147
Figure 7.3 The Discretized model domain and pipe located in the unsaturated soil.	148
Figure 7.4 Water Retention Curves (WRCs) and Soil Water Characteristic Curves (SWCCs) used in analyses.	149
Figure 7.5 Simulation flowchart.	149
Figure 7.6 Size and mesh sensitivity analyses, a) Simulations for 15 m and 33 m horizontal distances. b) Concentrations in the aqueous phase inside the pipe for different model dimensions.	150
Figure 7.7 Estimation of benzene concentration in the aqueous phase in MW-4 location.	150
Figure 7.8 Water saturation within the depth and flux directions in the domain, a) Gas fluxes, b) Aqueous fluxes.	151
Figure 7.9 Benzene quantity inside the pipe for different pipe material qualities, a) Peak concentration in the aqueous phase, b) Peak concentration in the gas phase.	152
Figure 7.10 Benzene mass breaking through the pipe for different pipe material qualities, a) Cumulative mass breaking through the pipe in the aqueous phase, b) Cumulative mass breaking through the pipe in the gas phase.	153
Figure 7.11 Benzene quantity inside the pipe in the case of damaged and undamaged gaskets, a) Peak concentration in the aqueous phase, b) Peak concentration in the gas phase.	154
Figure 7.12 Benzene permeation into the pipe in the case of damaged and undamaged gaskets, a) Cumulative mass breaking through the pipe in the aqueous phase, b) Cumulative mass breaking through the pipe in the gas phase.	155
Figure 7.13 Benzene quantity inside the pipe for different NAPL phase thicknesses at the source, a) Peak concentration in the aqueous phase, b) Peak concentration in the gas phase.	156
Figure 7.14 Benzene mass breaking through the pipe for different NAPL phase thicknesses at source, a) Cumulative mass breaking through the pipe in the aqueous phase, b) Cumulative mass breaking through the pipe in the gas phase.	157
Figure 8.1 The pipe material monitoring capsule (PMMC) designed at the lab and deployed on the contaminated sites. The components include stainless cup open at one end, ultrapure water as liquid receiving phase, pipe material sheet fixed at open end, and sealing hollow grooved cap.	177

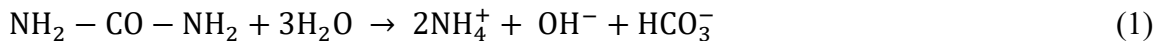
Figure 8.2 Nashville site map and model domain (after Wood, 2019).....	177
Figure 8.3 Newton site map and model domain (after Hart & Hickman 2018, Pace analytical services report 2020).	178
Figure 8.4 Durham site map and model domain (After URS 2015).....	178
Figure 8.5 Model development of Nashville site, (a) 3D domain, (b) Plan view, (c) Cross section view of the simulated model and (d) the PMMC being simulated in MW3.....	179
Figure 8.6 (a) The hydrograph of monitoring well (MW-3) where the PMMCs have been deployed in Nashville site, (b) the hydrograph of monitoring well PW-3 located near MW-3 indicating groundwater level and benzene fluctuation (after Wood Inc., 2021).....	180
Figure 8.7 Model development of Newton site, (a) 3D domain, (b) Plan view, (c) Cross section view of the simulated model.	181
Figure 8.8 The hydrograph of monitoring well (MW-3) where the PMMCs have been deployed in Newton site, indicating benzene fluctuation during deployment.	182
Figure 8.9 Model development of Newton site, (a) 3D domain, (b) Plan view, (c) Cross section view of the simulated model and the capsule being simulated in MW3.....	183
Figure 8.10 The hydrograph of monitoring well (Rw-2) where the PMMCs have been deployed in Newton site, indicating benzene fluctuation during deployment.	184
Figure 8.11 Calibration flowchart (Cc: PMMC measurement).	184
Figure 8.12 Benzene breakthrough the sample (Neoprene) installed at the top of the PMMC after one, two, three, and four months at Nashville site. The direction and relative magnitude of velocity vectors are shown here.	185
Figure 8.13 Normalized benzene breakthrough concentration in Nashville site using calibrated parameters of both gasoline contaminated sites.	186
Figure 8.14 Normalized benzene breakthrough concentration in Newton site using calibrated parameters of both gasoline contaminated sites.	186
Figure 8.15 Benzene breakthrough rate for Neoprene comparing two sites and two deployment/retrieval (Cwi: concentration measured in monitoring well at each time slot).....	187
Figure 8.16 Benzene breakthrough rate for Buna-N comparing two sites and two deployment/retrieval (Cwi: concentration measured in monitoring well at each time slot).....	187
Figure 8.17 Normalized PCE breakthrough concentration in Durham site using calibrated parameters of PCE contaminated site.....	188
Figure 8.18 PCE breakthrough rate for Neoprene and Buna-N comparing two deployment/retrieval normalized with concentration at each time slot (Cwi: concentration measured in monitoring well at each time slot).....	188

CHAPTER 1. Overview of Dissertation

1.1 Introduction

Flow and transport in the subsurface ground have been the center of attention from two important aspects; firstly chemical transport can notoriously affect groundwater, porous media, and infrastructure properties, and secondly, the transport mechanisms through porous media are very complicated for unknown parameters especially when it comes to the unsaturated condition and reactive transport phenomena. Among applied flow and transport studies, some applications have been extensively investigated during the last decades; i) microbial induced calcium carbonate precipitation (MICP) as a reactive chemical transport method with bioremediation and soil reinforcement applications, and ii) contaminant transport in subsurface profile and effects on subsurface utilities.

MICP method employs reactive transport idea to deliver a privileged approach to soil improvement. This method offers an engineering option using bacterial strain *Sporosarcina pasteurii* to mediate calcite precipitation by microbial ureolysis to alter the geologic properties of an aquifer, specifically shear stress improvement and the permeability and porosity reduction (Barkouki et al. 2011). This technology was originally developed for enhancing oil recovery and controlling the transport of groundwater contaminants such as Strontium-90 (Ferris et al. 1996, Hammes et al. 2003). MICP has been proposed for permeability control (Chu et al., 2013), mitigating well leakage (Mitchell et al., 2013), sealing fractured rock (Cuthbert et al., 2013), hydraulic barriers for enhanced oil recovery or increasing storage security of CO₂ (Cunningham et al., 2009, Wu et al., 2017), trapping contaminants (Fujita et al., 2004), liquefaction reduction (DeJong et al., 2006), soil strengthening (Whiffin et al., 2007, Montoya et al. 2015), and scour mitigation (Montoya, Do and Gabr, 2019). The chemical reactions related to the MICP are shown as follows (Eqs. 1 and 2) (Stocks-Fischer et al. 1999).



Several approaches have been suggested to control the transport of contaminations (e.g. Gabr et al. 1996). In situ bioremediation techniques have been proven to be among the most

promising techniques for remediating toxic chemicals (e.g. Iwamoto and Nasu 2001). The biomineralization processes were introduced as alternative and appropriate methods to constrain contaminants away from the surrounding environment. The focus was on bio-remediating of the heavy metals with ionic radius approximate Ca^{2+} . Pb^{2+} and Hg^{2+} can be incorporated in CaCO_3 lattice and substitute Ca^{2+} ions. In such a way, MICP traps heavy metals, preventing them from release in ambient environment (Eltarahony et al. 2020). MICP method can be able to trap PCE and VOCs by locally permeability reduction around the distributed sources of pollution. However, MICP is not just of interest for controlling contaminant transport, as it can address the extensive applications of soil improvements as mentioned before.

Past studies have helped shape our understanding of the fundamental processes that occur during MICP, yet there remains a gap between our laboratory-scale understanding of these processes and field implementation of MICP in a managed and optimized manner in order to achieve intended targets. Given the expense of large-scale field trials and the limited number of variables that can feasibly be investigated, it would appear prudent to use numerical modeling to narrow down the large number of effective variables on transport mechanism into a handful of the most promising that can then be experimentally verified. Current models of MICP have mostly been developed to reproduce individual experimental results and are each well-suited for their intended use. However, none include all of the comprehensive features essential for field-scale modeling (Minto et al. 2019).

Leakage from permanently closed, or in service, underground storage tanks (UST) and pipelines as well as from disposal area practices dry cleaning facilities leads to contamination of the vadose zone and groundwater aquifers. Volatile Organic Compounds (VOCs) of hydrocarbon fuels such as Benzene, Toluene, Ethylbenzene, and Xylene (BTEX) or chlorinated solvents such as Tetrachloroethene (PCE) are significant environmental contaminants that can lead to high levels of toxicity upon exposure even at low concentrations. Reports of drinking water contamination in the United States revealed that petroleum products (diesel and gasoline) were involved in 89% of the incidents of permeation to the subsurface mains (US Environmental Protection Agency (EPA) 2002). Benzene has significant partial vapor pressure and an aqueous phase solubility that can exceed the standard limits of drinking water by more than five orders of magnitude (Sleep and Skyes 1989).

A large number of subsurface utilities and drainage pipes are installed within miles-long right of ways by US Department of Transportation (DOT) every year. In some instances, when the presence of contaminations is not known prior to the excavation and installation, these subsurface structures are installed in subsurface profiles that are contaminated by compounds derived from fuel hydrocarbons or dry-cleaning solvent. Petroleum hydrocarbons (gasoline, diesel, BTEX) or chlorinated aliphatic hydrocarbons (CAHs) can migrate through the unsaturated subsurface profile and breakthrough installed utilities such as culverts and water/drainage pipes; provide potential pathways for the accelerated migration of contaminants and potentially the transfer of contaminants to other locations resulting in contamination of surface and groundwater. However, the contaminant migration in the vadose and saturated zone with the presence of subsurface utilities has received little attention in the literature; specifically, data related to the potential of contaminant breakthrough gasketed concrete pipes in unsaturated profiles are scarce.

1.2 Scope of Research

The main focus of this research is to employ reactive flow and transport analysis to assess factors governing two important applications; a) MICP process, b) contaminant transport in unsaturated and saturated subsurface profiles. Both applications contribute to geo-environmental engineering. The overall goal is to develop reactive transport modeling frameworks which enable researchers to predict the rate and concentrations of transported and reacted chemicals in various conditions of porous media. To achieve this, axisymmetric, 2D, and 3D numerical models have been developed within various simulation environments and data from field or laboratory investigations were used to calibrate those aforementioned models.

To assess MICP process, reactive transport models were developed using COMSOL Multiphysics and the most dominant parameters for reliable prediction of CaCO_3 content and distribution have been calibrated using laboratory experimental measurements in literature. The most efficient model which can properly simulate spatial distribution of CaCO_3 content within the depth has been introduced and modified by incorporating new parameters. In addition, the analyses were conducted to explore the influence of various layouts and configurations of injection wells in delivering effective deployment of the MICP process. The model was calibrated in variably saturated condition and bacteria attachment coefficients were determined at different degrees of saturation. In addition, post-treatment hydraulic conductivity, porosity and attached biomass were assessed.

In contaminant transport application, numerical analyses were conducted using 3D models developed in T2VOC and GMS to investigate the extent of benzene and PCE transport in porous media. The specific focus was on quantifying the breakthrough rate and magnitude of mass transported into concrete subsurface utility with polymeric gaskets embedded in unsaturated and saturated subsurface profiles. A new pipe material monitoring capsule has been designed and deployed in the fields. The breakthrough parameters of various pipe materials have been calibrated through simulation of field-domain models including these monitoring tools.

1.3 Dissertation Organization

This dissertation is composed of nine chapters. The seven chapters are research papers that have been published or under submission process to conferences or journals and the last chapter summarize all findings. A brief description of the next chapters are described as follows.

Chapter 2 describes a comprehensive reactive transport model that was developed using finite element method and COMSOL Multiphysics 5.5 to capture key processes of MICP. The model was shown to be efficient in predicting CaCO_3 precipitation within a reliable range of accuracy utilizing data reported in literature. The study explored the influence of key factors in terms of treatment protocols through sensitivity/parametrization analyses and recommended the most relevant variables for reliable prediction of CaCO_3 content and distribution. This chapter entitled “Elucidating factors governing MICP biogeochemical processes at macro-Scale: A reactive transport model development” and authored by Zahra Faeli, Brina M Montoya, and Mo Gabr and will be submitted to *Computers and Geotechnics Journal*.

In Chapter 3, the efficacy of differing injection/extraction well layouts on the MICP process have been explored. The average induced CaCO_3 mass, CaCO_3 distribution within the domain, and total post-treatment by-product ammonium (NH_4) have been calculated for various layouts and configurations of injection wells and the most efficient field design has been introduced. The study considered the effect of specific ureolysis rates, injection flow rates, extraction flow rates, and phased injection practices on the MICP process. This chapter, entitled “Reactive transport modeling of microbial induced calcium carbonate precipitation utilizing various configurations of injection wells” authored by Zahra Faeli, Brina M Montoya, and Mo Gabr, has been accepted in ASCE publications in *Geo-Congress 2022*.

Chapter 4 focuses on spatial distribution of calcium carbonate content within subsurface profile. Various bacteria attachment models presented in literature were calibrated in both small-

and large-scale tests. The most efficient approach in yielding the most fitted calcium carbonate distribution was introduced and then modified by incorporating a new parameter in the model. The attachment bacteria model parameters of large-scale tests have been compared with small-scale column tests. This chapter, entitled “Various bacterial attachment functions and modeling of distribution of biomass and calcium carbonate precipitation in MICP implementations” authored by Zahra Faeli, Brina M Montoya, and Mo Gabr, will be submitted to *Journal of Geotechnical and Geoenvironmental Engineering*.

Chapter 5 presents MICP model development in unsaturated conditions. The model was calibrated using variation of CaCO_3 content at 20, 40, 80, 100 % saturations for sand column tests done by Cheng et al. (2013). The results describe the effects of saturation degrees and unsaturated parameters on attachment coefficient (K_{at}) and CaCO_3 precipitation of coarse sand materials. This chapter, entitled “Development of a reactive transport model for microbial induced calcium carbonate precipitation in unsaturated conditions” authored by Zahra Faeli, Brina M Montoya, and Mo Gabr.

In Chapter 6, another application of reactive transport model; contaminant transport in subsurface profile; has been assessed. A series of three-dimensional numerical analyses were conducted using T2VOC code with the Petrasim2018 graphical user interface to investigate multiphase multicomponent transport of VOCs (benzene) into the gasketed drainage concrete pipes embedded in unsaturated profiles. The main mechanisms of contaminant transport in vadose zone and the effect of depth to groundwater table has been described in this work. This chapter, entitled “Benzene migration in unsaturated profile with subsurface drainage concrete pipe” authored by Zahra Faeli, Sultan Alhomair, Mo Gabr, Mohammad Pour-Ghaz, Cyrus Parker, and has been published in ASCE publications in *Geo-Congress 2020*.

Chapter 7 is the following of the previous chapter on mass transfer into the subsurface concrete pipe located in unsaturated subsurface profile. Benzene phase partitioning was described in this chapter. The breakthrough rate and magnitude of mass transported in both gaseous and aqueous phases have been calculated considering the effects of pipe material quality levels, gaskets condition, volume and depth of NAPL in the domain, the presence of fine or coarse soil types, and the magnitude of volatilization to the atmosphere. This chapter, entitled “Factors affecting multiphase benzene breakthrough into drainage concrete pipe in the unsaturated subsurface

profile” authored by Zahra Faeli, Sultan Alhomair, Payam Hosseini, Mo Gabr, and Mohammad Pour-Ghaz, has been published in *Journal of Pipeline Systems Engineering and Practice*.

Chapter 8 presents the results of a new pipe material monitoring capsule (PMMC) which has been designed to evaluate volatile organic compounds and chlorinated solvents breakthrough three types of pipe gasket materials; Neoprene, Buna-N, and Viton. The PMMCs were deployed in gasoline and PCE contaminated sites in North Carolina. The field data has been used to calibrate hydraulic parameters of pipe materials through a series of field-domain simulations using GMS. Afterwards, the calibrated parameters were used to evaluate the rate of breakthrough. A protocol was recommended for installing/retrieval of PMMCs to monitor PCE and benzene breakthrough rate of pipe materials. This chapter, entitled “A new monitoring approach for sustainability assessment of subsurface utilities gasket materials against gasoline and chlorinated solvents: Field evaluation and model development”, authored by Zahra Faeli, Payam Hosseini, Mo Gabr, and Mohammad Pour-Ghaz.

Finally the main contributions achieved in this study are reviewed in chapter 9.

CHAPTER 2. Elucidating Factors Governing MICP Biogeochemical Processes at Macro-Scale: A Reactive Transport Model Development

This chapter is proposed to be submitted for publication in *Computers and Geotechnics Journal*.

Abstract

MICP influenced by biofilm metabolism in the subsurface can be exploited for a variety of engineered applications encompassing geotechnical ground improvement, environmental bioremediation, and hydraulic barriers. A reactive transport model was developed to determine the effects of controlling factors in terms of treatment protocols and experimental methods. Six column tests from literature were calibrated and a range for the key parameters has been determined. Fifteen key parameters of MICP reactive transport model were assessed. The results emphasized the effects of two principal factors of specific ureolysis rate, and attachment model on the precipitation content and distribution. The traditional constant attachment rate model is useful to yield average mass of precipitation but more accurate models are needed to capture exact distribution. Post-treatment hydraulic conductivity, porosity, and attached biomass were assessed.

2.1 Introduction

Microbial Induced Calcium Carbonate Precipitation (MICP) is a novel subsurface engineering method that uses micro-organisms and reaction kinetics to improve engineering soil properties. *Sporosarcina pasteurii* is commonly used for such application and is capable of hydrolyzing urea, which in the presence of calcium, may favor the calcium carbonate (CaCO_3) precipitation (Ferris et al., 2003). Calcite is the most dominant and permanent CaCO_3 crystal. The method requires careful design of injection chemicals and control of hydraulic flow to target even inaccessible subsurface locations in many applications. These include trapping contaminants (Fujita et al., 2000, 2004, Mitchell et al. 2006, Eltarahony 2020), hydraulic behavior control (Chu et al. 2013, Zamani and Montoya 2017), cut off highly permeable pathways for enhanced oil recovery (MacLeod et al. 1988, Phillips et al. 2013), repairing cracked concrete structures (van Tittelboom et al. 2010), liquefaction reduction (DeJong et al. 2006, Zamani and Montoya 2018), soil strengthening (DeJong et al. 2013, Montoya et al. 2015, Gomez et al. 2017, Nafisi et al. 2020), and scour mitigation (Do et al. 2019, 2020, Montoya et al. 2021).

Controlling precipitation/mineralization during the MICP process can be assessed by balancing the reaction with transport through manipulating treatment procedures. The injection strategies, injection rates, reactant concentrations, the number of treatment applications, and controlling the distribution of active microbes can affect CaCO_3 precipitation and the efficacy of the process (Whiffin et al. 2007, Ebigbo et al. 2012, Hommel et al. 2015).

MICP reactive transport modeling has been investigated in the last decade to predict precipitation patterns and optimize treatments (e.g. van Wijngaarden et al. 2011, 2016, Barkouki et al. 2011, Ebigbo et al. 2012, Martinez et al. 2012, 2014, Hommel et al. 2015, 2016). van Wijngaarden et al. (2011) developed 1D/2D MICP advection-dispersion-reaction transport model using partial differential equations (PDEs) which were solved by standard Galerkin finite-element method. Cuthbert et al. (2013) explored fractured rock transmissivity reduction with the introduction of MICP using a 2D model and the results from an experimental setup with injection/abstraction between four boreholes. Nassar et al. (2018) employed PHT3D to develop 2D MICP modeling for a meter-scale tank biostimulation experiment with transient nonuniform transport controlled by three wells. Minto et al. (2019) used OpenFOAM framework to implement MICP reactive-transport equations in conjunction with Navier-Stokes equations of fluid flow, and Darcy-Brinkman momentum equations to account for velocity impact on bacteria attachment-detachment. There have also been several MICP modeling works that explored biogeochemical kinetics and reaction rates at pore-scale (e.g. Zhang et al. 2010, Kim et al. 2020). Using a pore-scale model, Qin et al. (2016) concluded more biomass attachment in a pore throat compared to the surrounding pore bodies due to the larger specific area of pore throat.

Previous models generally have focused on addressing complexities of interacting processes and often were developed to match results from a series of experiments conducted under specific conditions. Most of these models do not include essential features of a comprehensive model such as porosity/permeability change with precipitation (not applied in Barkouki et al. 2011, Martinez et al. 2014, Nassar et al. 2018), bacteria attachment/decay model (not applied in Nassar et al. 2018), and cyclic injections (not applied in van Wijngaarden et al. 2016, Qin et al. 2016).

The objective of work herein is to develop and calibrate a comprehensive reactive transport model that includes the following: i. capture key processes of MICP, ii. predict CaCO_3 precipitation within a reliable range of accuracy utilizing data reported in literature, and iii. determine the influence of key factors in terms of treatment protocols through

sensitivity/parametrization analyses and recommend the most relevant variables for reliable prediction of CaCO₃ distribution.

2.2 Model Development

2.2.1 COMSOL-Multiphysics framework

COMSOL-multiphysics V5.5 (2020) was employed to develop coupled biogeochemical model to simulate the implementation of the MICP process. The model utilizes a nonlinear time-dependent solver to compile the governing Partial Differential Equations (PDEs). The solution approach is based on backward differentiation formulas (BDF) and Finite Element Method (FEM). The COMSOL modules' interfaces for the analysis of mass transport and chemical reaction kinetics, as well as the ability to incorporate user-defined auxiliary PDEs for immobile species and porous medium modifications, provide a robust modeling environment to simulate various processes of the MICP approach.

2.2.2 Biogeochemical Processes and Mathematical Model Development

Flow model (Richards' 1931)

While generally past studies on modeling MICP process used Darcy's law to model fluid flow (Ebigbo et al. 2012, Nassar et al. 2018), the model presented herein employs Richards' equation as a general flow model for saturated and unsaturated zones. The approach utilized herein is expressed in Eq. 1. Minto et al. (2019) used Navier-Stokes equations for no-density-driven high flow rates neglecting gravity in depth. Since the simulations of this study explore fluid flow with depth, Richards' model is versatile for simulating saturated and unsaturated flow applications and is deemed appropriate to use herein. The relationship determines fluid velocity (u), pressure and flow net.

$$\frac{\partial(\theta\rho)}{\partial t} + \nabla \cdot (\rho u) = Q_m, \quad \frac{\partial(\theta\rho)}{\partial t} = \rho \left(\frac{C_m}{\rho g} + S_e S \right) \frac{\partial p}{\partial t} \quad (1)$$

$$u = -\frac{k}{\mu} (\nabla p + \rho g \nabla z), \quad k = k_s k_r(S_e)$$

where θ denotes the volume fraction of fluid (porosity in saturated), S is storage coefficient (m^{-1}) is defined with compressibility of fluid (1/Pa) and effective compressibility of matrix (1/Pa), p is pressure (Pa), t is time (s), ρ is the fluid density (kg/m^3), k is the hydraulic conductivity (m/s), k_s and k_r are saturated hydraulic conductivity and relative hydraulic conductivity, respectively, μ is the fluid dynamic viscosity (Pa.s), z is the direction that represents vertical elevation (m), and Q_m is the fluid source or sink. The unsaturated parameters, S_e (residual

saturation), C_m (specific moisture capacity), and k_r (relative permeability), are 1, 0, and 1 respectively, for saturated conditions of the present study.

Chemical transport model (Zhang and Klapper 2010, van Wijngaarden et al. 2011)

The general form of mass balance for chemical species transport is shown in Eq. (2) with advection-dispersion-reaction relationship:

$$\frac{\partial(\theta C_i)}{\partial t} + \frac{\partial(\rho_b C_{p,i})}{\partial t} - \nabla \cdot (\theta D_i \nabla C_i) + \nabla \cdot (u C_i) = R_i \quad (2)$$

$$D_i = \alpha_{L,T} |u| + D_e, R_i = m\theta r_{uh}$$

where C_i denotes solute concentration (urea, ammonium (NH_4), and calcium (Ca^{2+}), carbonate (CO_3^{2-}) (mol/m^3)), D_i is the dispersion tensor, and R_i is reaction term.

The bacteria transport can be defined using Eq. (2) with different units (OD_{600}) and reaction terms as will be illustrated in the following sections. The Dispersion tensor D_i is denoted by longitudinal and transverse dispersivities (α_L and α_T), and D_e is effective diffusion coefficient ($1 \times 10^{-9} \text{ m}^2/\text{s}$, van Wijngaarden et al. 2016). R_i is a product of fluid volume fraction (θ), urea hydrolysis rate (r_{uh}), and stoichiometry constants (m : -1 for urea and Ca^{2+} , 1 for CO_3^{2-} , and 2 for NH_4). $C_{p,i}$ is the mass of absorbed species to solid particles (such as Langmuir or Freundlich models), and ρ_b is the bulk density (kg/m^3). Absorbed concentration is sometimes defined by a retardation factor as $= 1 + \frac{\rho_b}{\theta} \frac{\partial C_{p,i}}{\partial C}$. However, absorbed mass of diluted species is not considered herein as the study is focused on sand-type soil, and solid-phase attached biomass and precipitated calcium carbonate are modeled using separate PDEs coupled with flow and transport equations.

Urea hydrolysis reaction kinetics (Barkouki et al. 2011, Minto et al. 2019)

Each mole of urea is hydrolyzed with two moles NH_4 and one mole CO_3^{2-} produced. The ureolysis rate in Eq. (2) is expressed as Michaelis-Menten kinetics in Eq. (3), as presented by Minto et al. (2019).

$$r_{uh} = K_u (S_{su} + S_{at}) \frac{C_{urea}}{K_m + C_{urea}} \cdot \frac{K_{NH_4}}{K_{NH_4} + C_{NH_4}} \quad (3)$$

where S_{su} is suspended bacteria concentration (OD_{600}), S_{at} is the bacteria attached to the surface known as biofilm (OD_{600}), K_u is the specific rate of ureolysis ($\text{mol}/\text{l.s.OD}$) parallel to V_{max} in Michaelis-Menten kinetics ($V_{max} = K_u S_{at}$), K_m is half-saturation rate constant (M), C_{urea} the concentration of urea (M), C_{NH_4} the ammonium concentration (M), and K_{NH_4} denotes the optional ammonium inhibition (M) that is put off here (Nassar et al. 2018, Minto et al. 2019). According to Nassar et al. (2018), previously, an inhibition term considering ammonia has been incorporated

for jack bean urease enzyme (Fidaleo and Lavecchia 2003), however for the *Sporosarcina pasteurii* bacteria cells, ammonium does not have significant effects on ureolysis rates.

Note that half-saturation parameter is the concentration of urea in which rate of urea hydrolysis is half of the maximum. Table 1 compares the different values of V_{max} and K_u adopted from past studies. K_u represents maximum microbial activity used in literature with different units.

Calcium carbonate precipitation kinetics (van Wijngaarden et al. 2011)

CaCO_3 is precipitated as immobile mass when each mole of Ca^{2+} and CO_3^{2-} is reacted at a rate equal to ureolysis rate (van Paassen et al. 2009, Qin et al. 2016, Burdalski and Gomez 2020). According to van Paassen et al. (2009), after nucleation has occurred and in vicinity of sufficient calcium present in the media, the hydrolysis rate and bulk precipitation rate are approximately equal during the major part of the reaction. At low hydrolysis rates, precipitation occurs at relatively low supersaturation. The precipitation is incorporated into the model by coupling a PDE as Eq. (4).

$$\frac{\partial \text{CaCO}_3}{\partial t} - m_{\text{CaCO}_3} \theta r_p = 0 \quad (4)$$

where CaCO_3 is the kilograms of calcite ions per total volume (kg/m^3) converted to percentage of mass soil, r_p is precipitation rate (mol/l.s) that is considered to be equal to ureolysis rate (r_{uh}) and m_{CaCO_3} is the molar mass of CaCO_3 (kg/mol).

Porosity and hydraulic conductivity modification (van Wijngaarden et al. 2011)

Two more partial differential equations have been coupled with the model to account for porosity and permeability reductions. The porosity is modified using Eq. (5) per each time increment following CaCO_3 precipitation filling pore volumes (van Wijngaarden et al. 2011).

$$\frac{\partial \theta}{\partial t} = - \frac{1}{\rho_{\text{CaCO}_3}} \frac{\partial \text{CaCO}_3}{\partial t} \quad (5)$$

In which ρ_{CaCO_3} is the bulk density of precipitated CaCO_3 (kg/m^3).

Using a Kozeny-Carman relationship, hydraulic conductivity (k_s) is updated based on new porosity per Eq. (6). k_0 represents initial hydraulic conductivity as function of mean particle size (d_m). n is a dimensionless scaling factor often assigned as 3 (vanWijngaarden 2011, Minto et al. 2019).

$$k_s = k_0(d_m) \frac{\theta^n}{(1-\theta)^2} \quad (6)$$

Bacteria transport/attachment/decay model (van Wijngaarden et al. 2012, Minto et al. 2019)

The concentration of intra- and extracellular urease is difficult to determine as these are associated with the attached bacteria in porous medium (Ebigbo et al. 2012). While the rate of bacteria attachment determines the amount and distribution of reaction rate, quantifying the attachment rate by direct experiments is difficult due to the many conditions that influence the rate such as ionic strength of fluid (Torkzaban et al. 2008), pore size distribution, cell size, surface charge, roughness of the porous medium, flow velocity (Hommel et al. 2016), random (tumbling) motion of bacteria (Yavuz Corapcioglu et al. 1984), and activity of metabolically active attached microbes (Cunningham et al. 2007). A typical first-order-rate model is shown per Eq. 7 to give bacteria attachment rate ($R_{S_{su}}$). The attached bacteria cells may decay over time due to cell death or be inactivated due to encapsulation within CaCO_3 matrix, per Eq. (8).

$$R_{S_{su}} = -K_{at}\theta S_{su}, K_{at} \text{ is a constant attachment rate coefficient (1/s).} \quad (7)$$

The attached biomass S_{at} is driven by:

$$\frac{\partial S_{at}}{\partial t} = K_{at}\theta S_{su} - K_{decay}\theta S_{at} + \frac{CaCO_3}{K_{encapsulation}} S_{at} \quad (8)$$

In which, K_{decay} is decay rate coefficient (1/s), and $K_{encapsulation}$ is the encapsulation rate constant ($\text{kg}\cdot\text{m}^3\cdot\text{s}$). Please note that both encapsulation and decay were modeled using decay term herein. Tables 2 and 3 compare attachment and decay parameters from the studies reported in literature.

The standard deviation (SD) and coefficient of variation (COV) of model results are calculated as follows.

$$SD = \frac{\sqrt{(CaCO_{3i} - CaCO_{3m})^2}}{n} \quad (9)$$

$$COV = \frac{SD}{CaCO_{3m}} \quad (10)$$

where CaCO_{3i} is defined as the spatially distributed CaCO_3 at various depths per given location i , and CaCO_{3m} is the average CaCO_3 content within depth. SD and COV are representative of CaCO_3 distribution.

2.2.3. Simulations of 1-D Column Testing

Six column tests from Whiffin et al. (2007), Martinez et al. (2012) and (2014), Do et al. (2019), and Nafisi et al. (2020) were adopted to investigate the key parameters for modeling MICP process. The objective is to calibrate key unknown parameters including ureolysis rate (K_u),

bacterial attachment (K_{at}), half-saturation (K_m), and decay rate coefficient (K_{decay}). Figure 1(a) and 1(b) show schematic sketch of column test experiment, as well as the numerical model boundary and initial conditions, respectively. An axisymmetric domain was employed to simulate the column test sample. The flow boundary conditions include an inlet velocity at one column end (bottom, top, or alternatively changed between top and bottom depending on the experiment), applied pressure at the top and no flow boundary at peripheral areas. Initial conditions include confining pressure, zero concentration for reactive chemicals, and zero attached biomass and CaCO_3 content. To simulate chemical transport, if fluid flows in upward direction, an injection mass source was located at the center of bottom boundary whereas an outlet boundary condition was applied at the top and no flow boundaries at sidewalls. Downward and alternative flow directions were examined by reversing boundary conditions. A total of 5 transient piecewise functions have been defined to simulate injection of bacteria, urea, NH_4 , Ca^{2+} , and flow intervals, respectively. The materials and methods of the experiments are summarized in Tables 4, 5, and 6 and briefly demonstrated here for simulation purposes.

To simulate the experiment by Whiffin et al. (2007), a five-meter column high was configured with 5 m hydraulic head at the top boundary, outlet boundary at the bottom at atmospheric pressure, and transient piecewise functions simulating downward flow of chemicals. The soil type is itterbeck sand with $d_{50} = 0.165$ mm. The treatment consists of, i.1 pore volume (PV) bacteria (1.583 OD₆₀₀) at 18.1 h injection duration, followed by 0.05 M CaCl_2 at 17.1 h duration, ii. 1.1 M urea and 1 M CaCl_2 at 24.9 h duration time followed by 102 h retention time, followed by 23.7 h water flush. The flow rate was 9.7×10^{-8} m³/s (5.8 ml/min) during the experiment.

Two column experiments, 2A and 3A, were adopted from Martinez et al. (2012), and (2014); these two experiments differed in flow directions, flow rates, treatment duration, and recipes. The soil type for these two experiments was Ottawa 50-70 with $d_{50}=0.21$ mm. To simulate stopped flow test 2A, one biological and 20 cementation treatment cycles were applied as time-dependent boundary conditions at the bottom boundary, prompting upward flow direction. The upward flow rate temporally changed to 1.67×10^{-7} m³/s (10 ml/min) during bio-injection, and $2 \times 1.67 \times 10^{-7}$ m³/s (20 ml/min) during cementation treatment, and zero at retention times. Test 3A was simulated as stopped-flow with bacteria injection from the top in downward flow direction. After bio-injection, the boundary conditions were altered to simulate upward flow direction for

cementation treatments. Similar to test 2A one biological and 20 cementation treatments were employed.

The column test (test 4) conducted by Do et al. (2019) utilized poorly graded silica sand with $d_{50}=0.49$ mm, a minimum and maximum void ratio (e_{min} and e_{max}) of 0.61 and 0.91, respectively, and a relative density of approximately 30%. One bacteria inoculation injection followed by 42 cementation treatment steps was applied with 5–5–11 h retention times between those injection intervals. The injection volume was two times the pore volume of each specimen. The mass source was located at the bottom boundary to prompt upward flow direction. A confining pressure of 10 kPa was applied as initial and boundary conditions at the top of column.

Nafisi et al. (2020) conducted triaxial tests on Ottawa 50-70 sand with $d_{50}=0.22$ mm, and relative density of 40%. Two tests were simulated with applied confinement pressure of 10 kPa, and total cementation treatments of 15 for test 5 and 35 for test 6, corresponding to moderately and heavily cemented sands, respectively, repeated at 5.0-5.0-11.0 h intervals (retention times). Two PVs of solutions were injected with the direction alternated from top to bottom and bottom to top to improve the uniformity of calcium carbonate distribution. Accordingly, the boundary conditions of the simulations have been alternated between top and bottom after each cementation step to simulate subsequent downward and upward flow directions followed during the experimental process.

2.3. Model Calibration

The calibrated parameters for aforementioned column testings are presented in Table 7. The K_u values were fitted for each experiment to induce the average CaCO_3 within the column equal to the average measurements. K_m has been adopted from measurements or assumed based on results from sensitivity analyses. Using an optimization tool in COMSOL Multiphysics, an upper, a fitted, and a lower limit of K_u were adjusted for each experiment to induce $mean+SD$, $mean$, and $mean-SD$ of CaCO_3 , respectively. SD shows the deviation of calcium carbonate measurements from mean across the depth. K_u varies within a range of 1.06×10^{-6} -to- 1.8×10^{-5} mol/l.s.OD with biomass optical density of 0.80 to 1.58 OD. Considering different procedures used in the experiments, the results from the numerical model showed general agreement in trend and average induced CaCO_3 (Figure 2) with the measured values. In Figure 2., the measured and simulated mass of CaCO_3 are shown using data per (a) Whiffin et al. (2007), (b) Martinez et al. (2012), (c) Martinez et al. (2014), (d) Do et al. (2019), and Nafisi et al. (2020). Safavizadeh et al.

(2019) reported K_u as of 3.5×10^{-6} -to- 5.60×10^{-6} mol/l.s.OD for urea concentration of 200 mM using the same method of bacteria incubation as Do et al. 2019 (test 4) and Nafisi et al. (2020) (tests 5 and 6, Table 4) which is close to the values obtained herein. Martinez et al. (2012, test 2A), (2014, test 3A) measured the average bulk ureolysis rate as of 1.65×10^{-5} and 2.83×10^{-6} mol/l.s for test 2A and 3A, respectively. The K_u was calibrated herein as $(1.0 \text{ -to- } 1.50) \times 10^{-5}$ (1.10×10^{-5} as fitted) and $(1.50 \text{ -to- } 8.0) \times 10^{-6}$ (3.2×10^{-6} as fitted) mol/l.s.OD for tests 2A and 3A, respectively, per 1 OD injected bacteria. These calibrated values are the initial and maximum ureolysis rates which are comparable with average ureolysis rates measured over the course of treatment by Martinez et al. (2012, 2014).

K_{at} and K_{decay} values were calibrated to yield the attached biomass and CaCO_3 according to the measurements provided in Table 7. K_{at} values were calculated within the range of 1.15×10^{-5} -to- 1.0×10^{-4} 1/s with such a range comparable to values from the past studies, as presented in Table 2. Only Martinez et al. (2012, 2014) reported retained biomass as 51% and 74% for tests 2A and 3A, respectively. Since there was no retained biomass measurement for the other column testing utilized herein, a minimum attached bacteria of 50% was assumed for calibration of the other tests. Considering the attached biomass per Do et al. (2019, test 4) same as the value from test 2A per Martinez et al. (2012), higher K_{at} was achieved for test 4 (10^{-4} 1/s) compared to test 2A (2.55×10^{-5} 1/s). This result would be due to less retention time of 5.17 h implemented by Do et al. (2019, test 4) compared to retention time of 12 h used by Martinez et al. (2012, test 2A), prompting an increase in K_{at} to keep the same attached biomass considering initial 1.0 OD injection. Thus, an increase in retention time by 2 times leads to approximately one order of magnitude decrease in K_{at} for the similar attached biomass. This result shows the retention time is a key parameter can significantly increase attachment if adjusted properly. Accordingly, the long bio-injection time (18 h) in experiment per Whiffin et al. (2007) and high retention time before cementation treatment (17 h) results in a lower value of K_{at} and higher attachment (75%). While the retention times after bio-injection allow more bacteria attachment, Martinez et al. (2012) showed such a high retention time as 62 h (compared to 5-12 h) decreases attached bacteria from 70% to 30% due to nutrient limitation followed by detachment, thereby emphasizing the importance of retention time adjustment.

Comparing results from moderately (test5) and heavily (test 6) cemented sand experiments per Nafisi et al. (2020), the higher attached biomass of 63% was obtained for moderately cemented

sample compared to 50% for heavily cemented sample, using the same attachment/decay coefficients. Since the total treatment duration is more for heavily cemented sample (11.75 d) compared to the moderately cemented sample (5.25 d), higher biomass was decayed/detached during heavily cementation test and less bacteria retained at the end of experiment. Similar trend was observed for test 4 by Do et al. (2019) and test 6 by Nafisi et al. (2020) with 14 d vs 11.75 d duration of treatment, respectively. Accordingly, a longer treatment duration leads to higher decay and less attached biomass, given the same attachment/decay coefficients.

Standard Deviation (*SD*) and coefficient of variation (*COV*) yield distribution of CaCO_3 with depth (Table 7 and Figure 2). Results show the differences between CaCO_3 distribution from the numerical model and from experimental results (Figure 2) are less than 1% assuming linear bacteria attachment rate and constant K_{at} with depth as introduced per Eqs. (7) and (8).

An important conclusion was derived through the comparison of CaCO_3 distribution between simulations and experiments. The most crucial factor determining calcium carbonate distribution in the developed model is the distribution of attached bacteria. Other studies confirmed this inference experimentally through monitoring urea consumption and spatial ureolytic potential. According to Martinez et al. (2012), the distribution of microbes is the key factor to achieve uniform CaCO_3 precipitation and the spatial distribution of attached microbes varies depending on the injection procedure variables such as amendment recipe, inclusion of nutrient broth, injected microbe concentration, and biological amendment retention period.

2.4. Parametrization and Sensitivity Analyses

Fifteen model parameters were assessed in four categories, as presented in Table 8. These categories are: i. microbial activity and attachment parameters, ii. sample preparation, iii. treatment protocol, and iv. column dimensions. One parameter was varied whereas the other parameters were maintained constant as highlighted by the “bolded” values (benchmark) in Table 8. A benchmark case is defined by one bio-injection, 15 cementation treatments, and total of 16 retention time intervals implemented in 126 h (5.25 d). The flow was regulated in upward direction. Two PVs of cementation solution were percolated on each specimen in 5.0, 5.0 and 11 h intervals. Note that some parameters are dependently related and a variation in one parameter results in change in the others. For instance, when initial porosity varies, subsequently hydraulic conductivity must be updated in accordance with Eq. (6). Additionally, following any variations in porosity, hydraulic conductivity, or flow rate, the time of each injection was updated so that the volume of cementation

solution can be maintained as two PVs of the specimen. The inlet velocities varied according to the changes in column diameter.

2.5. Results and Discussion

Figure 3 presents the reagent and CaCO₃ concentrations from the numerical model during the period of treatment using the benchmark model parameters. The CaCO₃ distribution with depth is shown in Figure 4 with variations of four parameters; (a) K_u (mol/l.s.OD), (b) injection direction (c) initial hydraulic conductivity, k_0 (m/s), and (d) dimension, L (m), as an example of each category. The same data were obtained for all 15 parameters, and are not shown here for brevity. The COV (distribution) vs average CaCO₃ content is shown in Figure 5. The variations of COV and CaCO₃ with alteration of each parameter are indicated in Table 9.

Microbial activity, microbial attachment/decay and column dimensions

Results of sensitivity analyses shown in Table 9 and Figure 5 indicate that the key factor of increasing CaCO₃ is ureolysis rate (K_u). An increase in K_u by two orders of magnitude can improve average CaCO₃ by up to 13% (the average increases from 1.3% to 14%).

The number of treatments and attachment coefficient (K_{at}) are the other important factors affecting the sensitivity of the model results. Using a minimum $K_{decay} = 1.15 \times 10^{-7}$ 1/s (0.01 1/day) and a retention time of 5.0 h, the K_{at} should not be less than 2.5×10^{-5} 1/s (2.16 1/day), as the attached bacteria in that case would be less than 20%. Such a low value was not reported in the previous studies. Similarly, applying $K_{at} = 1 \times 10^{-4}$ 1/s, a K_{decay} higher than 5×10^{-6} 1/s is not reasonable. These results suggest the K_{decay} and K_{at} should have at least two orders of magnitude difference in value to keep the attached bacteria within a reasonable range.

Simulation results shown in Table 9 indicate the trend of CaCO₃ and COV are also influenced by the decay coefficient (K_{decay}) and height of column (L). These two parameters are the main factors correlated to decreasing CaCO₃ once their values are increased in the experiments per data in Table 8. Furthermore, half-saturation parameter (K_m), flow rate (q), diameter (D), and dispersivity (α_L) also decrease the average CaCO₃ content in the column when the values of these parameters are increased. K_m and K_{decay} affect the urea hydrolysis rate (r_{uh}) and attached bacteria (S_{at}) whereas an increase in dimension (D or L) lengthens the distance of reagent transport from the injection source, and consequently reduces the average precipitated CaCO₃ in the expanded domain under the same flow rate and treatment protocol.

Treatment protocol-flow rate

As the flow rate increases from 8.3×10^{-8} to 3.3×10^{-7} m³/s (5 to 20 ml/min), the average CaCO₃ decreases from 6.1% to 4.8%. Even though the attachment and decay coefficients are assumed to be constant when the flow rates increase, higher velocities result in mobilizing more reagents and bacteria toward the outlet, lowering the reaction, and attachment processes. Al Qabany et al. (2012) showed the injection rate within the range herein maintained the reactant efficiency (precipitation compared to the injected chemicals) as high as more than 90%. Similarly, the results herein show a small reduction in CaCO₃ content with increasing the flow rate. At higher flow rates than this range, the efficiency decreases because the rate of bacterial urea hydrolysis is slower than the flow rate (Al Qabany et al. 2012). Additionally, the results indicate increasing the flow rates (5 to 20 ml/min) contributes to more uniform induced calcium carbonate as the *COV* was reduced from 13.5% to 5.5%. The results herein show higher flow rates inhibit immediate precipitation of calcium carbonate at the location near the injection source and more distribute the chemicals and CaCO₃ precipitation. Similarly, Al Qabany et al. (2012) indicated the importance of flow rates in prevention of clogging at injection point and accordingly demonstrated the advantage of pulse-flow method (flow and between retention times) over the continuous injection to produce more uniform distribution of chemicals and CaCO₃ due to higher flow rates used in the pulse-flow tests. In addition, Stocks-Fischer et al. (1999) indicated that injection of bacteria and chemicals at low flow rates results in clogging near the injection source. Whiffin et al. (2007) did not observe any clogging over 5 m specimen using the flow rates as low as 5.8 ml/min, however, made this point that the fast flow rates will move the cementation reactants further along the column providing less time for reaction immediately near the injection point and resulting in more homogeneous distribution (Whiffin et al. 2007).

Treatment protocol-injection direction

Data in Figures 4(b), 5(c), and Table 9 indicate that the direction of injection whether upward, downward or alternating between the two does not change the mean CaCO₃ significantly. However, the alternating flow direction (15 times change in percolation direction) leads to more uniformity in CaCO₃ precipitation which is consistent with experimental results (Nafisi et al. 2020, Figure 2(e)). Conducting a series of column tests, Martinez et al. (2012) found where microbial density gradients exist the bi-directional flow (where cementation injection is implemented from

the opposite direction of the bio-augmentation-injection) limits urea consumption close injection source, thereby enhances more uniform distribution.

Treatment protocol-recipe

To investigate the effects of recipe, the concentrations and molar ratios of chemical constituents, urea to NH_4Cl to CaCl_2 [concentration of urea in bracket], are varied per the data shown in Table 8. An increase in reagent molarity from 50 to 300 Mm (1:1:1) improved the mean CaCO_3 from 3.2% to 6.3% (3 %), while there was no significant change in CaCO_3 content between 1:1:1 (300 mM) and 3:3:1 (300 mM) (6.3% compared to 5.3% in mean CaCO_3 and no difference in *COV*). Data in Figure 5(c) and Table 9 indicate that more treatment concentrations (urea- NH_4Cl - CaCl_2) lead to more CaCO_3 precipitation under the same number of injections and less *COV*, thereby more homogeneity/uniformity. Using equimolar urea and calcium chloride solution, an increase from 50 mM to 300 mM reduced *COV* from 12% to 8% and improved homogeneity.

Al Qabany et al. (2012) reported that the amount of CaCO_3 precipitation was not affected by a reagent concentrations up to 1M, however, Al Qabany et al. did not keep the number of injections and retention times constant during their trials with various concentrations. According to Al Qabany et al. (2012), the use of concentrations of chemical reactants as 250 mM (urea and CaCl_2) over a larger number of injections (14 injections), as used in simulations herein, induces more homogeneous cementation over the sand grains at the microscale and higher concentrations of chemicals (1000 mM urea and CaCl_2) generates thicker calcite (CaCO_3) matrices and crystal size. Similarly, more homogeneous distribution was obtained herein for 300 mM solutions. Martinez et al. (2012) obtained similar results to our study regarding calcium carbonate content but made different conceptual conclusions regarding uniformity. This disagreement in different literature requires further investigation. According to their experiments, increasing molar ratio from 1:1:1 [50 mM] to 3:3:1 [333 mM] raises PH, results in more microbial activity and ureolysis rate, accordingly yields higher calcium carbonate precipitation, however a lower ureolysis rate in 1:1:1 [50 mM] can be advantageous to the distribution of nutrients and yields more uniform CaCO_3 precipitation, given a uniform distribution of microbes (Martinez et al. 2012). This is opposite to the higher *COV* obtained herein for 50 mM concentration of chemicals.

Treatment protocol-number of treatment-number of injected PVs

The increased number of treatments from 9 to 39 as implemented in lightly, moderately, and heavily cemented sands (Table 8) can increase the average CaCO_3 content from 3% to 11%

(8%) and decrease the non-uniformity from 8.8% to 7% (1.8%) as shown in Table 9 that is validated by results of Nafisi et al. (2020).

At the same time, the number of pore volume injections (1, 1.5, or 2) is a less dominant factor impacting the CaCO₃ content compared to the other parameters. Results of simulation and experiments indicated more of a homogeneous distribution using 2 PVs injection of cementation solution.

Post-treatment hydraulic conductivity and porosity

The sensitivity analyses indicated that any increase in initial hydraulic conductivity (k_0) and initial porosity (θ_0) increased the precipitation content and COV . The average hydraulic conductivity and porosity after treatment of specimens, modeled in sensitivity analyses of this study, were normalized with initial ones to give normalized mean post-treatment hydraulic conductivity (k_f/k_0) and normalized mean post-treatment porosity (θ_f/θ_0), respectively. The k_0 and θ_0 are initial hydraulic conductivity and porosity before treatment, and k_f and θ_f are final hydraulic conductivity and porosity after treatment, respectively. The k_f/k_0 and θ_f/θ_0 and a variation of each parameter were utilized in sensitivity analyses. The results of these analyses are shown in Figure 6. The final hydraulic conductivity (k_f) decreased to 43% of the initial one (k_0) as K_u increased by two orders of magnitude from 1×10^{-6} to 1×10^{-4} mol/l.s.OD (Figure 6(a)). Any variations in K_{at} and K_{decay} by two orders of magnitude can reduce k_f to 70% of k_0 ($k_f/k_0=70\%$) (Figures 6(b) and 6(c)). Additionally, as the number of treatments increased from 9 to 39, k_f/k_0 declined to 83% and 53%, respectively (Figure 6(h)). The aforementioned parameters were the crucial factors highlighted in sensitivity analyses.

The mean CaCO₃ within the sample from sensitivity analyses is delineated with a red dashed line in Figures 6. For each simulated column test, the experimental results are marked with blue star symbol as shown in Figures 6(a) and 6(b). with “W”, “M2A”, “M3A”, “D”, “NH”, and “NM” denoted the experiments by Whiffin et al. (2007), Martinez et al. (2012, test 2A), Martinez et al. (2014, test 3A), Do et al. (2019), and heavily cemented, and moderately cemented tests by Nafisi et al. (2020), as was explained in the previous section. According to Figure 6(b), the corresponding k_f/k_0 to mean CaCO₃ from “D” experiment is 71% that yields post-treatment hydraulic conductivity as $0.71 \times 3.5 \times 10^{-5}$ m/s = 2.48×10^{-5} m/s which agrees well with the values of $2.2-2.5 \times 10^{-5}$ m/s measured by Do et al. (2019).

According to the correlation between hydraulic conductivity and porosity (Eq. 6), the key factors affecting the porosity are the same as the factors of hydraulic conductivity. The increase of K_u by two orders of magnitude results in a reduction about 19% in normalized porosity (Figure 6(a)). The variation in K_{at} , K_{decay} , the number of treatments, and column height lead to change in normalized porosity by less than 10% whereas the effect of the other parameters would lead to lower than 3% change in normalized porosity (Figure 6).

While K_u , K_{at} and K_{decay} are needed to be measured or calculated for each experiment, most of assessed parameters are related to the treatment protocol, thus, such derived diagrams (Figure 6) enable post-treatment hydraulic conductivity, post-treatment porosity, and attached biomass prediction, given the CaCO_3 content and treatment protocol for each experiment. On the other hand, if post-treatment variables are measured at laboratory, the presented diagrams can help to derive reactive transport parameters.

Total attached biomass

The attached biomass at the end of treatment was normalized with respect to the injected bacteria as shown in Figure 6. The results of the present study show the main factors affecting the attached biomass are attachment/decay coefficient, flow rate, retention time, the number of injected PVs, and the specimen dimensions. The attached biomass increased up to 73% of initial injection once the K_{at} rises by two orders of magnitude from 5×10^{-6} to 3×10^{-4} 1/s (Figure 6(b)). The K_{decay} can reduce the normalized attached biomass within a column test sample from 50% to 3% (47%) when K_{decay} is increased from 1.15×10^{-7} to 1×10^{-5} during total treatment time of 126 h (Figure 6(c)). The flow rate variations from 5 to 20 ml/min decreased the normalized attached biomass from 56% to 48% (8%) (Figure 6(g)). Increased flow rates and corresponding higher velocities do not provide sufficient time for the suspended bacteria to attach to the porous media when injected biomass volume is kept the same for all flow rates. Varying retention time from 5 h (introduced as benchmark in Table 8) to 14 h led to an increased bacteria attachment from 50% to 65% (15%) (Figure 6(i)). Increased number of bio-injected PVs from 1 to 2 enhanced the attached biomass from 43% to 50% (7%) (Figure 6(j)). In addition, for the higher column height (2.5 m) the average attached biomass in the domain was reduced by approximately 44% compared to a column length of 0.14 m as long as the volume of injected bacteria and the injection protocol are maintained the same Figure 6(k).

2.6. Conclusion

There is a lack of literature to include a comprehensive study discussing all parameters of MICP simulation. Previous models were developed to imitate some specific experiments with limited implementations. None has been found to i. identify the key factors dominated biogeochemical processes yielding both precipitation content and distribution, and ii. determine a range for the key parameters of MICP through calibration with various studies and sensitivity analyses. The reactive transport model developed in this study involved the most important features of MICP method and showed to be efficient in prediction of variables in all MICP practices regardless of the employed treatment protocol such as the location of injection source with the depth or the number of treatment cycles.

A range for important model parameters has been determined. Six column tests from different studies with various procedures were used for calibration. Specific ureolysis rate (K_u) varied within a range of 1.06×10^{-6} - 1.8×10^{-5} mol/l.s.OD with biomass optical density of 0.8-1.58 OD. Attachment rate coefficients (K_{at}) were calibrated within 1.15×10^{-5} - 1×10^{-4} 1/s depending on the attached bacteria mass of 50%-75% and retention time within 5-17 h. The results also suggest the K_{decay} and K_{at} must always be at least two orders of magnitude different to keep the attached bacteria within a reasonable range.

The results emphasized the effects of principal factors of microbial activity, microbial attachment efficiency, and number of treatments (among all 15 assessed parameters) on the precipitation content and distribution; i. K_u , ii. K_{at}/K_{decay} , and iii. number of treatments.

Once K_u and K_{at} are raised by two orders of magnitude, the mass percentage of CaCO_3 can increase from 1.3% to 14% and from 0.6% to 6.5%, respectively, with an increased COV of 16%. These results are important since given the maximum microbial activity, the attachment model dictates the CaCO_3 content and distribution in the domain. The differences between model and experimental CaCO_3 distribution are due to assumed constant attachment rate across the depth. The traditional constant attachment rate model is useful to determine average mass of CaCO_3 within subarea but more accurate models are needed to capture exact distribution of CaCO_3 which is the focus of the next studies being done by the authors of the present work.

The number of treatment and flow rates (q) are the other key factors than microbial activity and attachment affecting the amount and distribution of minerals. Increasing the flow rates from 5 to 20 ml/min contributes to more uniform induced calcium carbonate as the COV was reduced

from 13.5% to 5.5%. Higher flow rates inhibit immediate precipitation of calcium carbonate at the location near the injection source. The increased number of treatments from 9 to 39 as implemented in lightly, moderately, and heavily cemented sands can increase the average CaCO_3 content from 3% to 11% (8%) and decrease the non-uniformity (COV) from 8.8% to 7% (1.8%).

Given the domain dimensions, the main physical factors governing attached biomass are attachment/decay coefficients, flow rate, retention time, and the number of injected PVs. Two orders of magnitude increase in K_{at} can increase normalized attached biomass up to 73%. Retention time is another key parameter for attached biomass and thereby precipitation in domain. An increase in retention time from 5 h to 14 h in column tests results in increased attachment percentage about 15%.

Table 2.1 Specific rate of ureolysis (K_u), Maximum microbial activity (V_{max}), half-saturation rate (K_m), and initial biomass concentration from past studies.

V_{max} (mol/l.s)	K_u	K_m (M)	Initial Bacteria (OD ₆₀₀)	Reference
-	6.4×10^{-9} mmol/cell. h	0.3	3×10^6 to 7×10^7 cells/ml	Burdalski and Gomez (2020)
-	5 mM urea/min/OD = 8.33×10^{-5} 1/s	0.301	0.125-0.25	Minto et al.(2019)
-	3.50×10^{-6} to 5.60×10^{-6} mol/l.s.OD	-	1	Safavizadeh et al. (2019)
4.007×10^{-5}	-	0.156	Unknown (Biostimulation)	Nassar et al. (2018)
4.26×10^{-5} (x Sat ratio=0.25)	-	0.01	Unknown	van Wijngaarden et al. (2016)
-	706.7×10^2 mol/kgbiomas/s = 6.4×10^{-9} mmol/cfu.h	0.355	Unknown	Hommel et al. (2016)
-	Not reported	0.0032	$1.4-7.2 \times 10^5$ cells/ml	Martinez et al. (2014)
1.67×10^{-4} (10 U/ml)	-	-	1.5-2	Cheng et al. (2013)
-	45000 1/m/d/OD	-	1	Cuthbert et al. (2013)
-	Complex $K_u = k / (1 + mH/KEU, 1 + KEU, 2/mH)$	0.0173	1.3×10^7 - 4×10^9 cfu/ml	Ebigbo et al. (2012)
1.39×10^{-6} - 5.55×10^{-6}	-	-	0.8-1.2 (10^7 cells/ml)	Al Qabany et al. (2012)
-	Not reported	0.0032	2×10^6 cells/ml	Barkouki et al. (2011)
9.1×10^{-5}	-	0.01	Unknown	vanWijngaarden et al. (2011)
-	0.23 mS/min 1mS/min=11 mM urea/min	0.0185	1.583	Whiffin et al. (2007)

Table 2.2 Microbial attachment rate coefficient (K_{at}).

K_{at} (s^{-1})	Reference	Equation	Coefficients
0.01,0.1,1,10	van Wijngaarden et al. (2012)	Parametric studies	
1.3×10^{-3}	Ebigbo et al. (2012)	$K_{at}=c_{a,1} \cdot \varphi_f + c_{a,2}$	$c_{a,1}=0.0443$, $c_{a,2}=9.19 \times 10^{-4}$ (φ_f : calibrated volume fraction of biofilm)
1.16×10^{-5}	Cuthbert et al. (2013)	calibrated	
4.12×10^{-15} - 1.5×10^{-4}	Hommel et al. (2016)	$K_{at}=c_{a,1} \cdot \varphi_f + c_{a,2}$	$c_{a,1}=1.55 \times 10^{-13}$ - 1.55×10^{-2} $c_{a,2}=2.57 \times 10^{-15}$ - 3.72×10^{-6}
$K_{attach}=5 \times 10^{-3}$ $K_{straining}=5 \times 10^{-4}$	Minto et al. (2019)	Assumed	-

Table 2.3 Microbial decay rate coefficient (K_{decay}).

K_{decay}	Reference	Note
1-10 1/d = 1.15×10^{-5} - 1.15×10^{-4} 1/s	Cuthbert et al. (2013)	10 1/d: during cement injection 1 1/d: overnight
12 $kg/m^3 \cdot s$	Minto et al. (2019)	Considered K_{decay} as zero and calibrated $K_{encapsulation}$ as specified

Table 2.4 Simulated column tests properties.

Simulated test	Whiffin et al. (2007) Test 1	Martinez et al. (2012) Test 2A	Martinez et al. (2014) Test 3A	Do et al. (2019) Test 4	Nafisi et al. (2020) Tests 5&6
Soil type	Itterbeck sand $d_{50}=0.165$ mm	Ottawa 50-70 $d_{50}=0.21$ mm	Ottawa 50-70 $d_{50}=0.21$ mm	Silica Sand $d_{50}=0.49$ mm	Ottawa 50- 70 $d_{50}=0.22$ mm
Column diameter (m)	ID=0.066	OD=0.0572 ID=0.0508	OD=0.0572 ID=0.0508	ID=0.072	ID=0.072
Column height (m)	5	0.424	0.523	0.144	0.144
Initial bulk porosity	0.378	0.34	0.36	0.45	0.45
Initial hydraulic conductivity (m/s)	2×10^{-5}	1.8×10^{-4}	2.2×10^{-4}	3.56×10^{-5}	3.56×10^{-5}
Soil dry density (kg/m ³)	1650	1750	1700	1463	1458
Pore volume (ml)	6340	292	374	256	256
Total treatment duration (h)	162 (6.75 d)	79.5 (3.3 d)	87.6 (3.65 d)	342 (14 d)	M: 126 (5.25 d) H:282 (11.75 d)

Table 2.5 Bio-injection treatments in simulated tests.

Simulated test	Whiffin et al. (2007) Test 1	Martinez et al. (2012) Test 2A	Martinez et al. (2014) Test 3A	Do et al. (2019) Test 4	Nafisi et al. (2020) Tests 5&6
No of injected pore volume	1	1.4	1.5	2	2
Flow rate in bio (m ³ /s) (ml/min)	9.7×10^{-8} (5.8)	1.67×10^{-7} (10)	1.67×10^{-7} (10)	1.67×10^{-7} (10)	1.67×10^{-7} (10)
Velocity in bio (m/s)	2.84×10^{-5}	8.24×10^{-5}	8.24×10^{-5}	4.1×10^{-5}	4.1×10^{-5}
Injection time in bio (h)	18.1	0.682	0.935	0.83	0.83
Retention time in bio (h)	17.1	12	8	5.17	5.17
Source location in bio	Top	Bottom	Top	Bottom	Bottom
Solution recipe for bio Urea : NH ₄ Cl: CaCl ₂ [urea]	Only bacteria	3:3:0 [333 mM]	1:1:0 [50 mM]	3:3:0 [333 mM]	3:3:0 [333 mM]
Injected bacteria	OD600: 1.583	1.9×10^5 cells/ml	4.3×10^5 cells/ml	OD600: 1 (15 ml /100 ml)	OD600: 0.8- 1.2

Table 2.6 Cementation treatments in simulated tests.

Simulated test	Whiffin et al. (2007) Test 1	Martinez et al. (2012) Test 2A	Martinez et al. (2014) Test 3A	Do et al. (2019) Test 4	Nafisi et al. (2020) Tests 5&6
No of treatment cycles	1	20	20	42	15 (M)-35 (H)
Flow rate in cementation (m ³ /s)	9.7x10 ⁻⁸ (5.8)	3.34x10 ⁻⁷ (20)	1.67x10 ⁻⁷ (10)	1.67x10 ⁻⁷ (10)	1.67x10 ⁻⁷ (10)
Velocity in cementation (m/s)	2.84x10 ⁻⁵	16.48x10 ⁻⁵	8.24x10 ⁻⁵	4.1x10 ⁻⁵	4.1x10 ⁻⁵
Injection time in cementation (h)	24.9	0.34	0.935	0.83	0.83
Retention time in cementation (h)	102	3	3	5.17-5.17-11.17 (repeated each 3 intervals)	5.17-5.17-11.17 (repeated every 3 intervals)
Source location in cementation	Top	Bottom	Bottom	Bottom	Varied Alternatively
Solution recipe for cementation Urea: NH ₄ Cl: CaCl ₂ [urea]	1:1 (urea: Ca) [1100 mM]	3:3:3 [333 mM]	1:1:1 [50 mM]	3:3:0.5 [333 mM]	3:3:1 [333 mM]

Table 2.7 Column tests calibrated parameters.

Simulated Test	Whiffin et al. (2007) Test 1	Martinez et al. (2012) Test 2A*	Martinez et al. (2014) Test 3A*	Do et al. (2019) Test 4	Nafisi et al. (2020) Moderately cem. Test 5	Nafisi et al. (2020) Heavily cem. Test 6
Upper limit K_u (mol/l.s.OD)	1.8×10^{-5}	1.50×10^{-5} **	8.00×10^{-6}	1.58×10^{-6}	1.90×10^{-6}	2.4×10^{-6}
Fitted K_u (mol/l.s.OD)	1.1×10^{-5}	1.10×10^{-5}	3.2×10^{-6} **	1.30×10^{-6}	1.65×10^{-6}	2.2×10^{-6}
Lower limit K_u (mol/l.s.OD)	2.5×10^{-6}	1.00×10^{-5}	1.50×10^{-6}	1.06×10^{-6}	1.45×10^{-6}	2.02×10^{-6}
K_{at} (1/s)	1.15×10^{-5}	2.55×10^{-5}	8.60×10^{-5}	1.0×10^{-4}	1.0×10^{-4}	1.0×10^{-4}
K_{decay} (1/s)	1.15×10^{-7}	1.15×10^{-7}	1.15×10^{-7}	1.15×10^{-7}	1.15×10^{-7}	1.15×10^{-7}
K_m (mol/l)	1.85×10^{-2}	3.2×10^{-3}	3.2×10^{-3}	1.0×10^{-2}	1.0×10^{-2}	1.0×10^{-2}
Attached Biomass (%)	75	51 ⁺	74 ⁺	50-51	63	51-54
Retention time after bio- injection (h)	17.1	12	8	5.17	5.17	5.17
Total duration (d)	6.75	3.3	3.65	14	5.25	11.75
Mean CaCO ₃ (%)	3.3	3.7	1.90	4.8	2.68	6.7
SD from mean (%)	1.45	0.55	0.98	0.9	0.36	0.6
COV (%)	44.5	14.96	51	18.6	13.5	9.18

*The notations test 2A and 3A are the exact notations used per Martinez et al. (2012), (2014).

** The average bulk ureolysis rate were measured as 1.65×10^{-5} and 2.83×10^{-6} mol/l.s for tests 2A and 3A, respectively.

+ The attached biomass was calibrated for test 2A and 3A according to the measurements, whereas at least 50% attached biomass were assumed for the other experiments.

Table 2.8 Model parameters used in sensitivity analyses in four categories.

										Range	
1		K_u (mol/l.s.OD)	1×10^{-6}	5×10^{-6}	1×10^{-5}	2×10^{-5}	5×10^{-5}	1×10^{-4}		10^{-6} - 10^{-4}	
2	Microbial Activity and attachment	K_{at} (1/s)	5×10^{-6}	1×10^{-5}	2.5×10^{-5}	5×10^{-5}	8×10^{-5}	1×10^{-4}	2.5×10^{-4}	3×10^{-4}	5.0×10^{-6} - 3.0×10^{-4}
3		K_{decay} (1/s)	1.15×10^{-7}	5×10^{-7}	1×10^{-6}	5×10^{-6}	1×10^{-5}				10^{-7} - 10^{-5}
4		K_m (mol/l)	0.005	0.01	0.05	0.1	0.15	0.2			0.005-0.2
5	Sample Preparation	Initial hydraulic conductivity (k_0) (m/s)	1×10^{-5}	2×10^{-5}	3.5×10^{-5}	1×10^{-4}	2×10^{-4}	2.5×10^{-4}			1.0×10^{-5} - 2.5×10^{-4}
6		Initial porosity (θ_0)	0.30	0.35	0.40	0.45	0.50	0.55	0.6		0.3-0.6
7		Flow rate (q) (m^3/s) (ml/min)	8.33×10^{-8} (5)	9.66×10^{-8} (5.8)	1.67×10^{-7} (10)	2.5×10^{-7} (15)	3.33×10^{-7} (20)				5.0-20
8	Treatment Protocol	Number of treatment (cementation)	9	15	21	27	30	39			9-39
9		Recipe (mM)	3:3:1 [300]	1:1:1 [300]	1:1:1 [100]	1:1:1 [50]					-
10		Direction	Upward	Downward	Alternative						-
11		Retention time (h)	5.17	8	11	14					5.17-14
12		Number of injected PVs	1.0	1.5	2.0						1-2
13	Dimensions	Dimension (L) (m)	0.144	0.3	0.5	1	2.5				0.14-2.5
14		Dimension (D) (m)	0.055	0.072	0.08	0.09	0.1				0.055-0.1
15		Dispersivity (α_L) (m)	0.01	0.05	0.1						0.01-0.1

Table 2.9 Results of sensitivity analyses. Trend of CaCO_3 and COV indicates how these variables change when a parameter increases within the defined range based on past studies.

	Parameter	Min. CaCO_3	Max. CaCO_3	Min COV	Max COV	CaCO_3 variation	COV variation	Trend of CaCO_3 variation	Trend of COV variation
Microbial Activity and attachment	Specific ureolysis rate (K_u)	1.31	14.00	8.32	24.3	12.7	16.00	Increase	Increase
	Half saturation (K_m)	4.03	5.33	8.32	9.17	1.3	0.8	Decrease	Increase
	Attachment (K_{at})	0.63	6.52	0.45	17.08	5.9	16.63	Increase	Increase
	Decay (K_{decay})	1.74	5.28	8.19	9.23	3.5	1.0	Decrease	Increase
Sample preparation	Hydraulic conductivity (k_0)	3.75	8.24	6.80	10.70	4.5	3.9	Increase	Increase
	Porosity (θ_0)	3.31	7.52	6.31	10.12	4.2	3.8	Increase	Increase
Treatment Protocol	Flow rate (q)	4.83	6.17	5.45	13.48	1.3	8.0	Decrease	Decrease
	Recipe	3.21	6.26	8.07	12.18	3.1	4.1	Increase	Decrease
	No. treatment	3.18	11.18	7.03	8.80	8.0	1.8	Increase	Decrease
	No. Pore volumes (PVs)	4.52	5.28	8.32	9.37	0.8	1.0	Increase	Decrease
	Retention time	5.28	7.28	8.32	10.91	2.0	2.6	Increase	Increase
	Direction	5.12	5.28	5.22	8.32	0.2	3.1	-	-
Dimensions	Height (L)	0.95	5.28	8.32	190.85	4.3	182.5	Decrease	Increase
	Diameter (D)	4.66	5.48	5.45	13.69	0.8	8.2	Decrease	Increase
	Dispersivity (α_L)	4.82	5.28	4.85	8.32	0.5	3.5	Decrease	Decrease

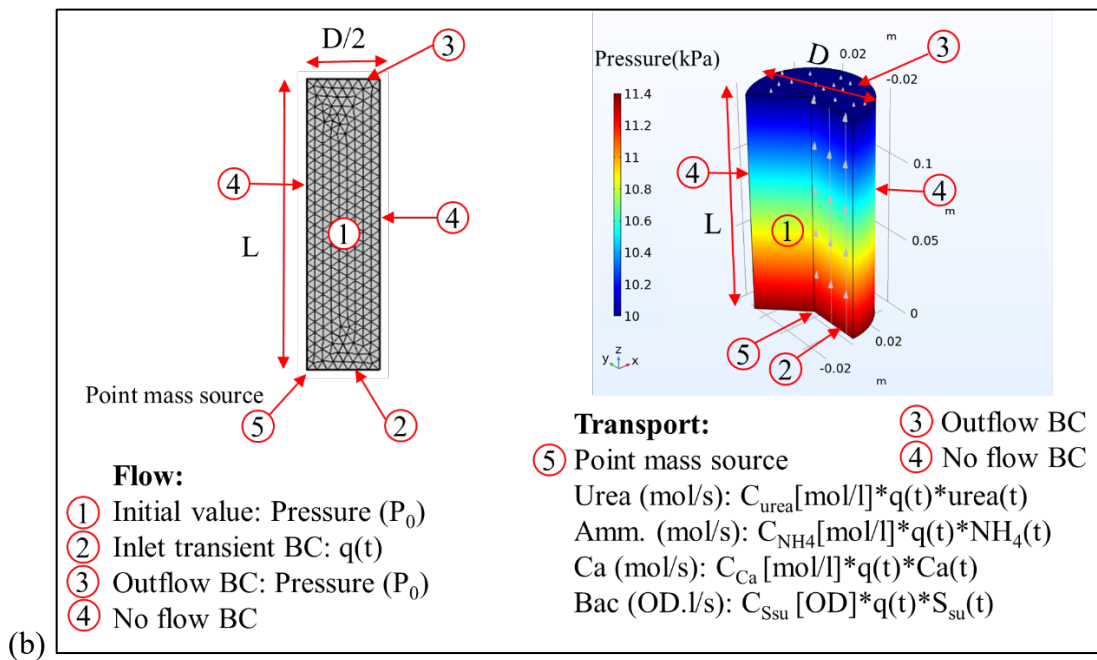
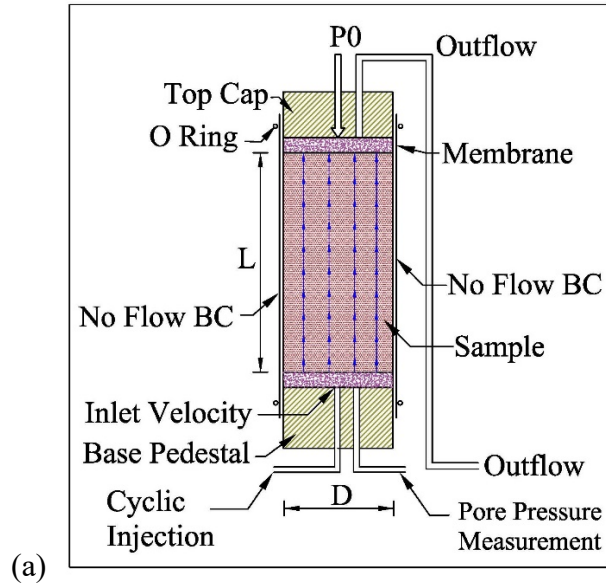


Figure 2.1 (a) Schematic sketch for column test experiment, (b) initial and boundary conditions. (note: injection and outflow can be applied in opposite locations: upward or downward direction, C_{urea} , $q(t)$ and $urea(t)$ represent injected concentration, flow schedule with time, urea treatment schedule with time, respectively, and the same are defined for other components).

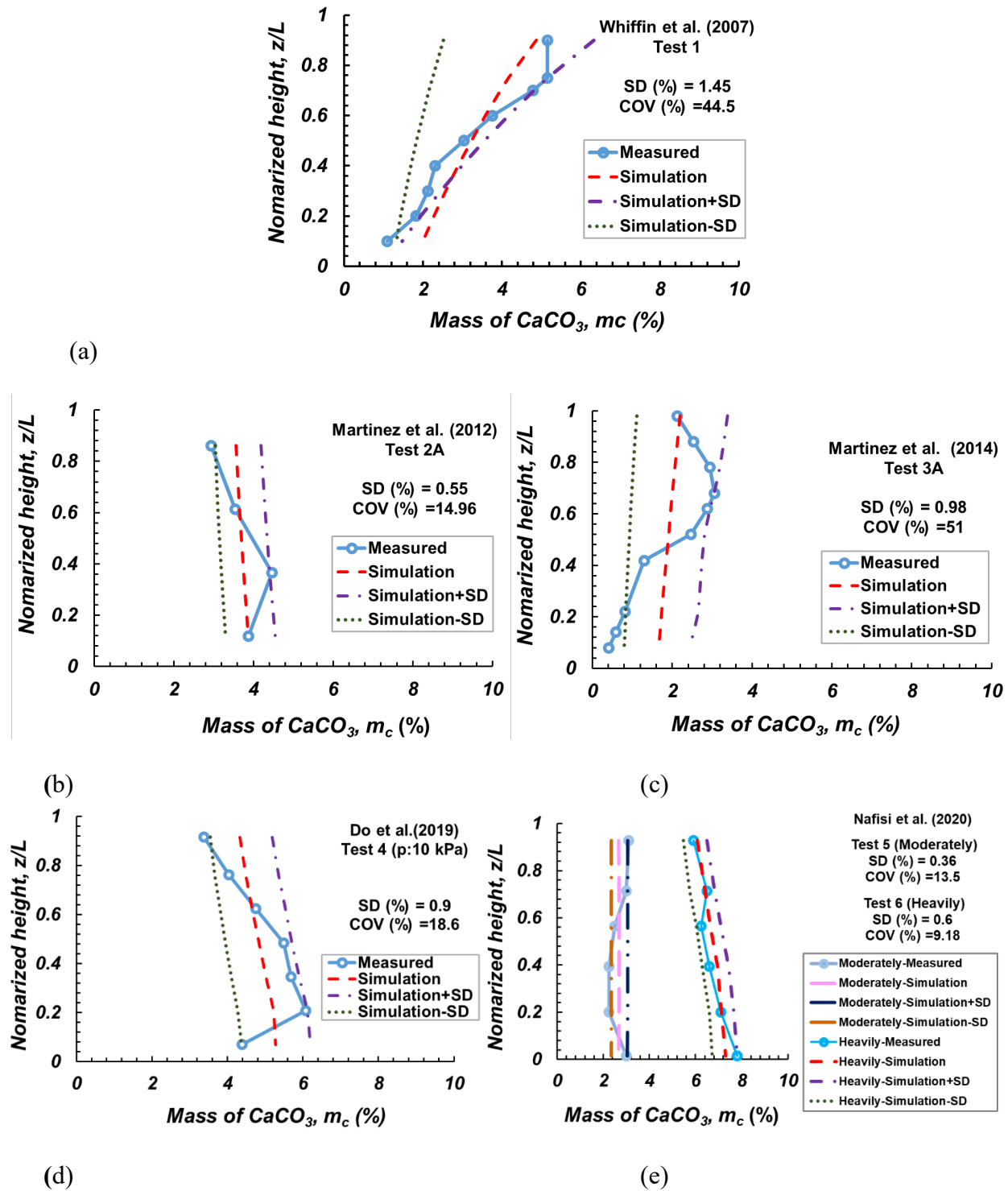
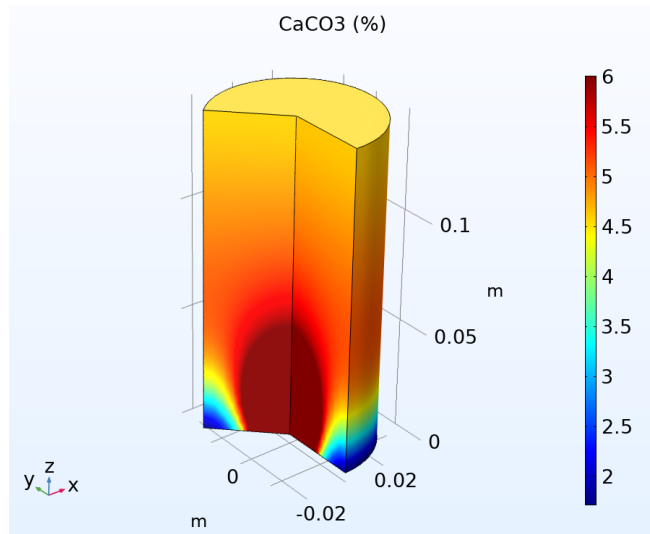
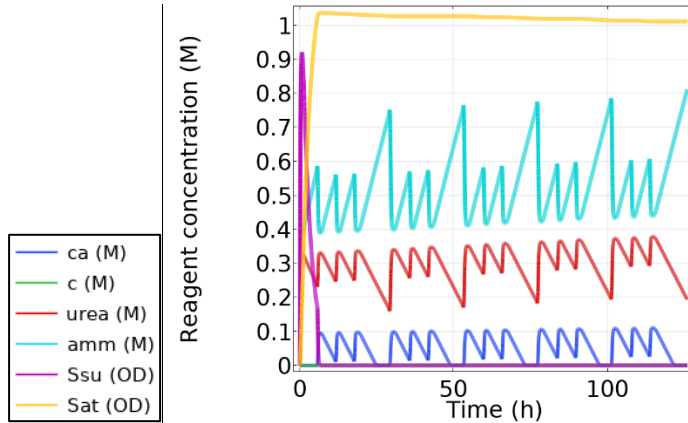


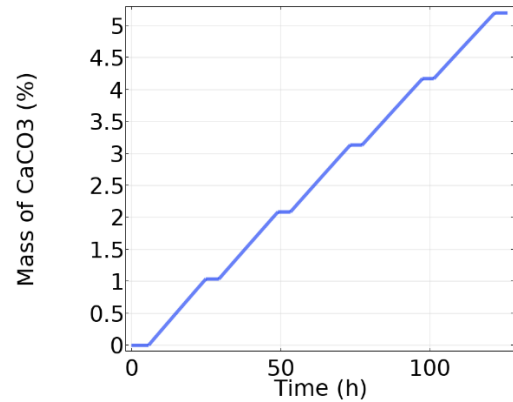
Figure 2.2 Measured and simulated mass of CaCO_3 for (a) Whiffin et al. (2007), (b) Martinez et al. (2012), (c) Martinez et al. (2014), (d) Do et al. (2019), and (e) Nafisi et al. (2020) (2 triaxial tests, moderately and heavily cemented sand).



(a)



(b)



(c)

Figure 2.3 (a) CaCO_3 content (%) after treatment, (b) reagent concentrations during treatment period; calcium (Ca), carbonate (C), urea, ammonium (amm), suspended bacteria (S_{su}), attached bacteria (S_{at}), (c) CaCO_3 content with time in the middle of specimen for benchmark model in sensitivity analyses.

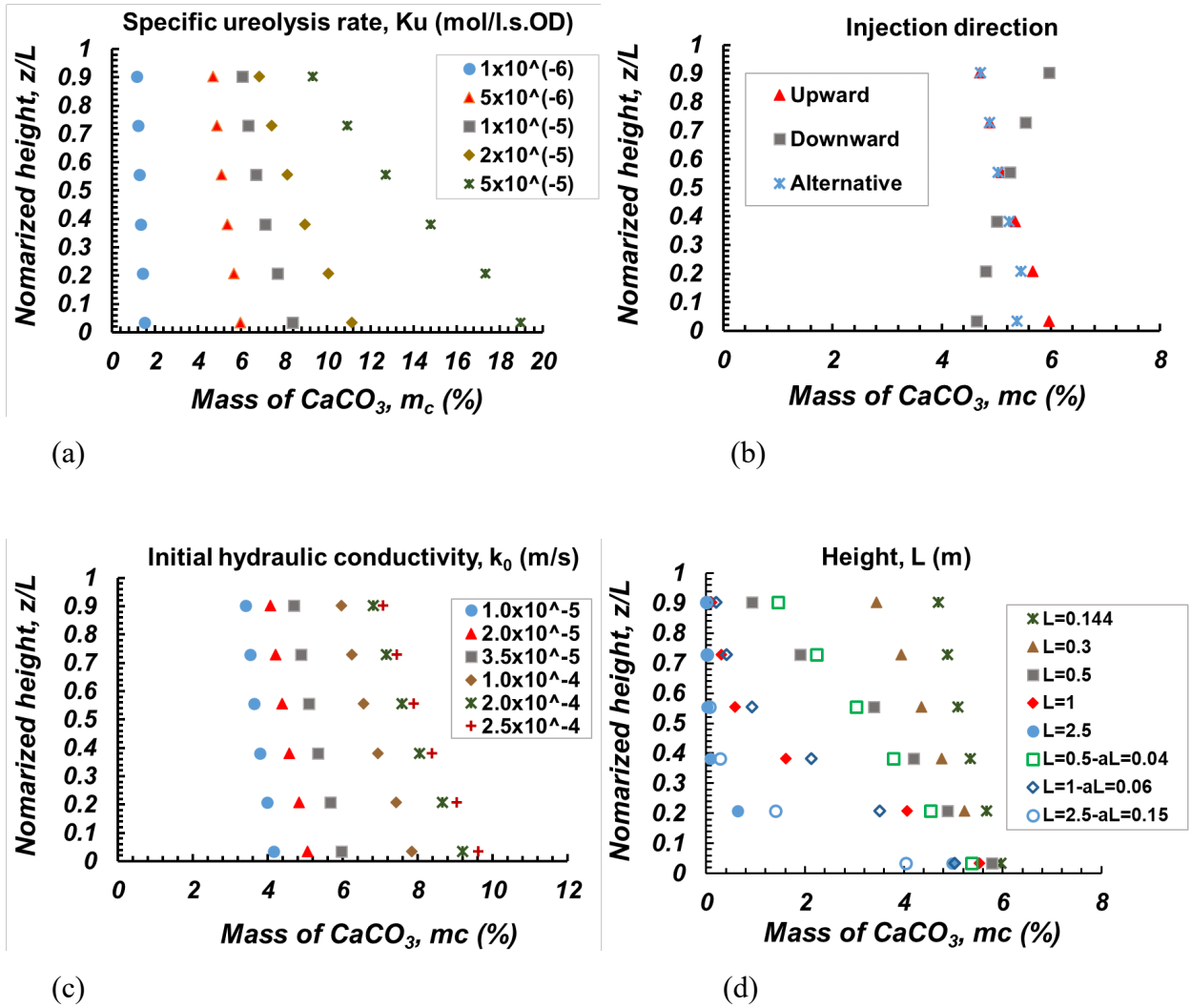


Figure 2.4 CaCO_3 distribution with variations of : (a) K_u (mol/l.s.OD), (b) injection direction (c) k_0 (m/s), and (d) L (m) as an example of each category. The same data were obtained for all 15 parameters presented in appendices.

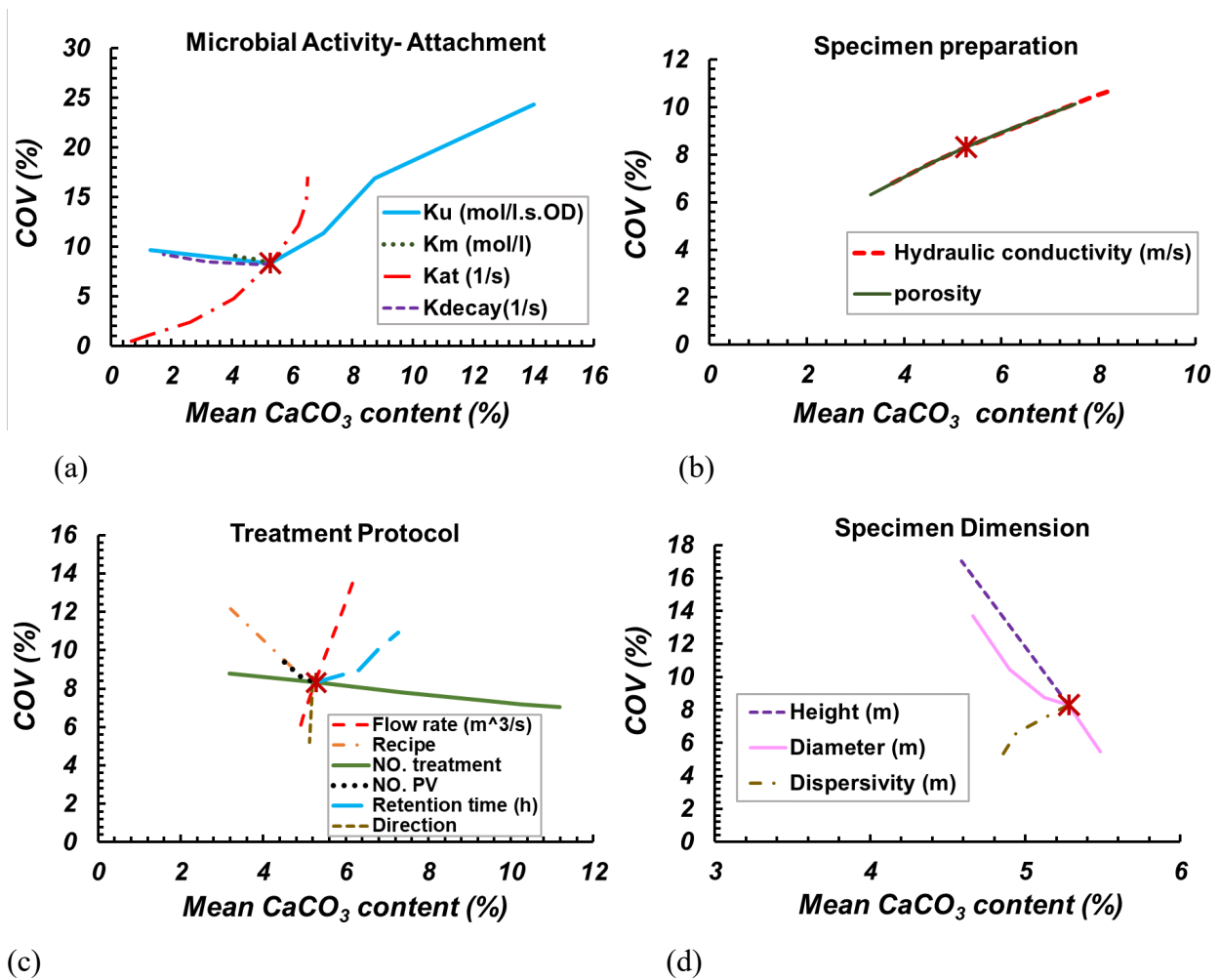
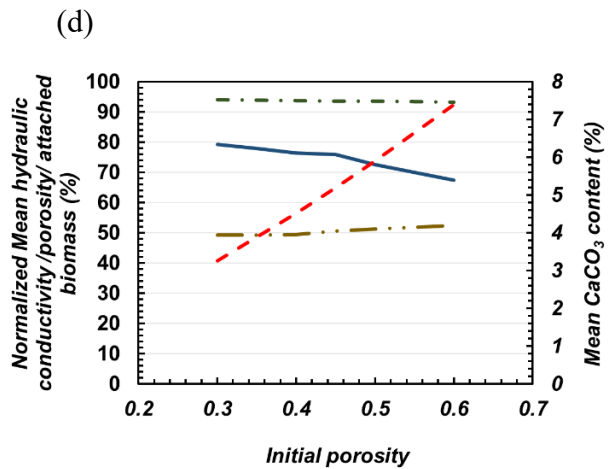
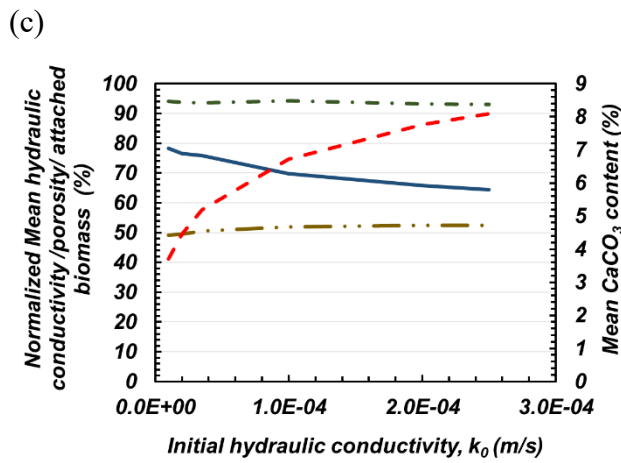
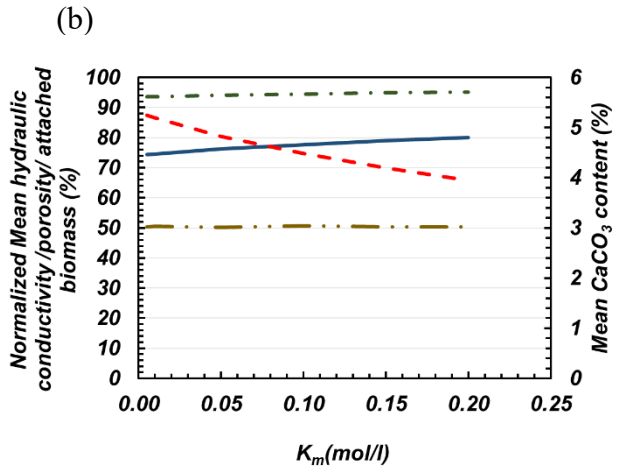
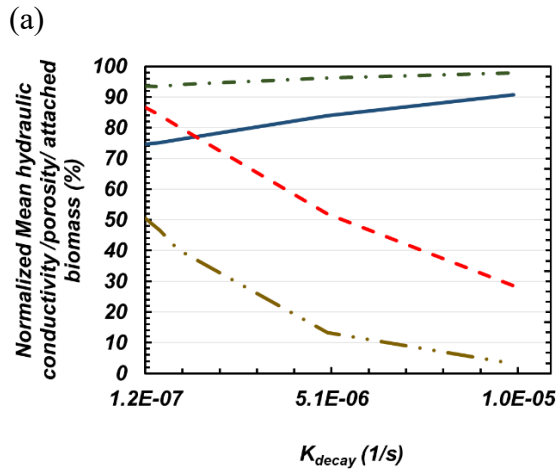
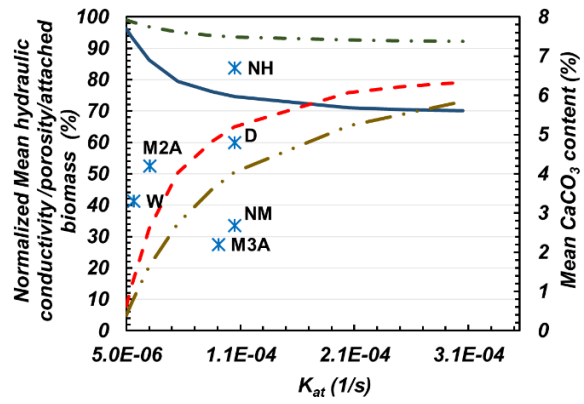
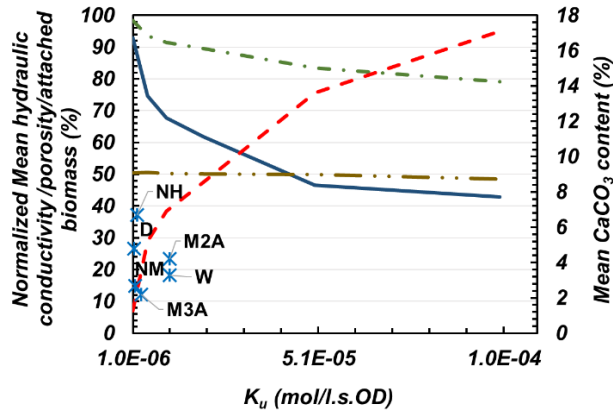


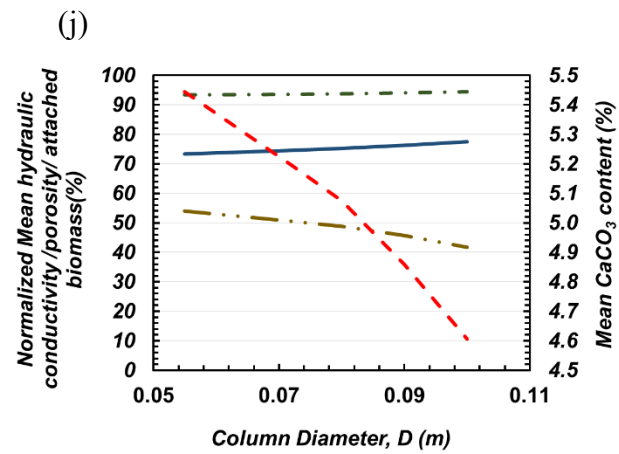
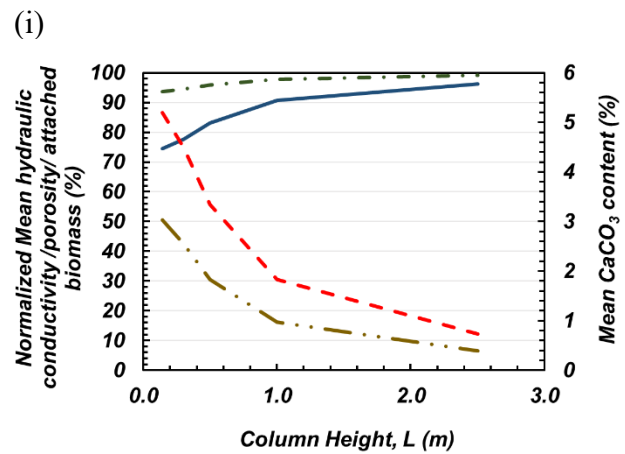
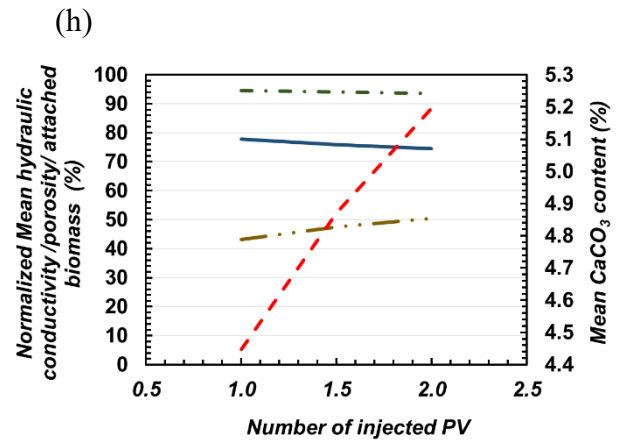
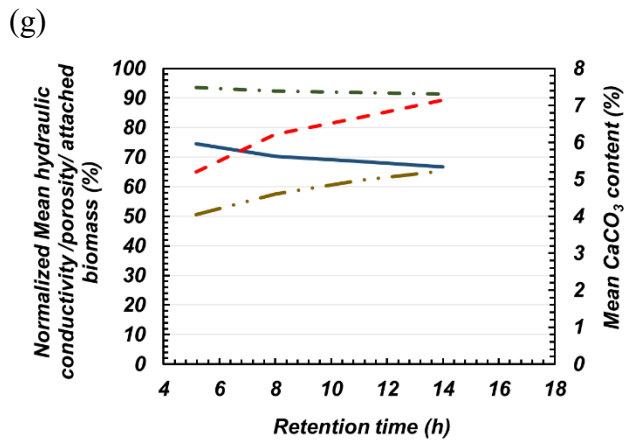
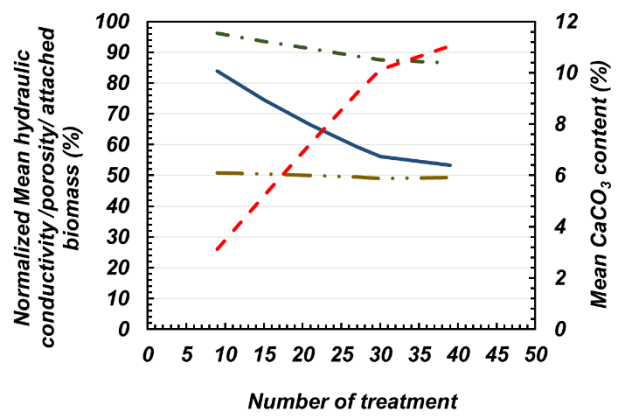
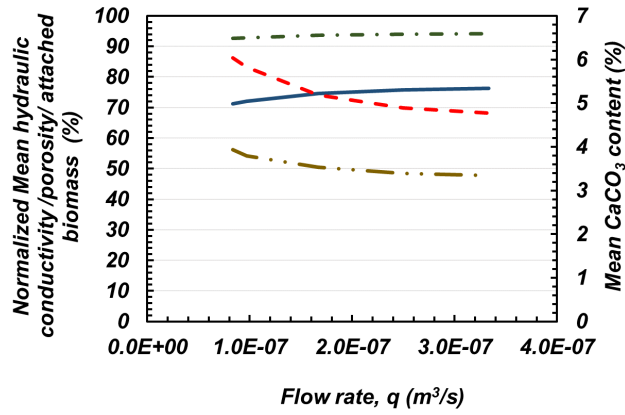
Figure 2.5 Coefficient of variation vs mean CaCO_3 for the parameters categorized as (a) microbial activity and attachment; (b) specimen preparation; (c) treatment protocol; (d) specimen dimension. The benchmark result was specified with star symbol.

Figure 2.6 The results of sensitivity analyses and column test measurements: normalized mean post-treatment hydraulic conductivity (k_f/k_0) (%), normalized mean post-treatment porosity (θ_f/θ_0) (%), normalized attached biomass (%), mean CaCO₃ mass (%), with variation of MICP parameters (a) K_u (b) K_{at} (c) K_{decay} (d) K_m (e) initial hydraulic conductivity, k_0 (f) initial porosity, θ_0 (g) flow rate, q (h) number of treatment (i) retention time (j) number of injected PVs (k) column height, L (l) column diameter, D .



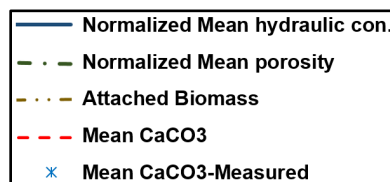
(e)

(f)



(k)

(l)



CHAPTER 3. Reactive Transport Modeling of Microbial Induced Calcium Carbonate Precipitation Utilizing Various Configurations of Injection Wells

This chapter has been accepted in ASCE publications in *Geo-Congress* 2022.

Abstract

While experimental studies on the use of microbial-induced calcium carbonate precipitation (MICP) for soil improvement have focused on assessment of cemented soil properties, there is a gap between small-scale laboratory experiments and modeling for the design of large-scale field implementation. Numerical analyses are conducted herein to explore the influence of various layouts and configurations of injection wells in delivering effective deployment of the MICP process. Metrics of evaluation include continuity and level of cementation as well as associated by-products. The bacterial transport/attachment/decay, and ureolysis rate parameters are included in the transport model. The model is calibrated using column-scale experimental data. Under the same flow rate and injected volumetric solutions, results indicated that 2-, 3-, and 4-well configurations with distance between wells equal to 1m produce the highest average CaCO_3 in the target area. Among the well configurations which induce the highest CaCO_3 content, 4-well configuration with 1 m distance between wells provided more uniform distribution of CaCO_3 (less standard deviation), with relatively lower by-product ammonium (NH_4).

Keywords: COMSOL Multiphysics, Microbial induced calcium carbonate precipitation (MICP), Numerical analyses, Reactive transport model, Field deployment.

3.1. Introduction

MICP approach encompasses reactive transport of urea, calcium chloride and bacteria to deliver an effective soil improvement technique. This technology was originally developed for oil recovery enhancement and controlling the transport of groundwater contaminants such as radionuclides and Strontium-90 (Ferris et al. 1996). The MICP approach has evolved for a wide range of applications from soil stabilization and liquefaction mitigation to hydraulic barriers for enhanced well recovery, crack sealing, and scour mitigation (e.g., van Paassen 2009, DeJong et al. 2010, Cuthbert et al. 2013, Ghasemi et al. 2020, Montoya, et al 2021).

Past studies have enhanced our understanding of the complex principal processes that occur during MICP through conducting a batch of experiments at small scale, yet there remains a

challenge to be able to extend those laboratory-scale experimental results to field implementation of MICP to achieve intended targets. A few studies have assessed the model of MICP at multiscale levels. Current models of MICP have mostly been developed to mimic some specific experimental setup with limited intended applications, and none incorporate the comprehensive features and parameters essential for field-scale simulation (Minto et al. 2019). Nassar et al. (2018) developed MICP modeling using PHT3D for a meter-scale tank experiment with transient non-uniform transport in a natural soil. The delivery of the experiment solutions was controlled by three wells, via a cycle of injection/withdrawals followed by no-flow intervals. However, Nassar et al. (2018) did not consider porosity/permeability reduction, and bacteria attachment/decay in their modeling.

The objective of work in this paper is to develop a reactive transport model to assess the efficacy of differing injection/extraction well layouts on the MICP process. The average induced calcium carbonate (CaCO_3) mass, CaCO_3 distribution within the domain, and total post-treatment by-product ammonium (NH_4) have been calculated for all well configurations. The study considers the effect of specific ureolysis rates (K_u), injection flow rates (Q_i), extraction flow rates (Q_o), and various injection practices on the MICP process. Modeling also included assessment of NH_4 within the system, as NH_4 must be recovered as a part of a successful MICP field deployment.

3.2. Model Development

A comprehensive reactive transport model representing the MICP process is numerically developed using finite element approach and COMSOL Multiphysics 5.5. The partial differential equations for the MICP process were defined as follows.

i. Flow Model:

Richards' equation is used as a general flow model for saturated and unsaturated zones which will be converted to Darcy's law in a saturated profile to give fluid velocity (u):

$$\frac{\partial(\theta\rho)}{\partial t} + \nabla \cdot (\rho u) = Q_m, \quad \frac{\partial(\theta\rho)}{\partial t} = \rho \left(\frac{C_m}{\rho g} + S_e S \right) \frac{\partial p}{\partial t} \quad (1)$$

where θ denotes the volume fraction of fluid (porosity in saturated conditions), u is fluid velocity, S is storage coefficient (m^{-1}), pressure p is the dependent variable (Pa), t is time (s), ρ is the fluid density (kg/m^3), and Q_m is the fluid source (positive) or sink (negative). Unsaturated parameters C_m and S_e were adjusted to establish saturated subsurface conditions for the study presented herein.

ii. Chemical Species Transport Model:

$$\frac{\partial(\theta C_i)}{\partial t} + \frac{\partial(\rho_b C_{p,i})}{\partial t} - \nabla \cdot (\theta D_i \nabla C_i) + \nabla \cdot (u C_i) = R_i + R_s \quad (2)$$

where C_i denotes dissolved concentration (mol/m³), ρ_b is the bulk density (kg/m³), D_i is the liquid-gas dispersion tensor, R_i is reaction term and R_s represents source term. R_i is a product of fluid volume fraction (θ), urea hydrolysis rate (r_{urea}), and stoichiometry constants (-1 for urea and calcium, 1 for carbonate, and 2 for ammonium).

Reaction rate (R_i) for suspended bacteria (S_{su}) is given by:

$$R_{S_{su}} = -K_{at}\theta S_{su}, K_{at} \text{ is the attachment rate coefficient (1/s).} \quad (3)$$

iii. Urea Transport, and Ureolysis:

The rate of urea hydrolysis is expressed as (Barkouki et al. 2011):

$$r_{urea} = K_u ZH \frac{C_u}{K_m + C_u} \cdot \frac{K_{NH4}}{K_{NH4} + C_{NH4}} \quad (4)$$

where ZH represents the concentration of total urease enzyme or total attached and suspended bacteria ($S_{at} + S_{su}$) (OD₆₀₀), K_u is the initial specific rate of ureolysis or maximum bacteria activity (mol/l.s.OD₆₀₀) in Michaelis-Menten kinetics, K_m half-saturation rate constant (M), C_u the concentration of urea (M), C_{NH4} the ammonium concentration (M), and K_{NH4} denotes the optional ammonium inhibition (M) which is not considered herein according to Nassar et al. (2018).

The urea hydrolysis rate depends on the concentration of the released urease that is defined as an immobile species (Ebigbo et al. 2012).

iv. Bacterial transport, Attachment, Decay, and Encapsulation:

The attached biofilm (S_{at}) is given by (Minto et al. 2019):

$$\frac{\partial S_{at}}{\partial t} = K_{at}\theta S_{su} - K_{decay}\theta S_{at} + \frac{CaCO_3}{K_{encapsulation}} S_{at} \quad (5)$$

In which, S_{at} is the concentration of biofilm (M), S_{su} is the concentration of suspended bacteria (M), t time, K_{at} attachment rate coefficient (1/s), K_{decay} decay rate coefficient (1/s), and $K_{encapsulation}$ is the encapsulation rate constant (kg.m³.s), not calibrated in this study.

v. CaCO₃ Precipitation (van Wijngaarden et al. 2011):

$$\frac{\partial CaCO_3}{\partial t} - m_{CaCO_3} r_p \theta = 0 \quad (6)$$

where r_p (mol/l.s) is precipitation rate and is considered equal to urea hydrolysis rate (r_{urea}) based on van Paassen et al. (2009) and m_{CaCO_3} is the molar mass of CaCO₃ (kg/mol). The

precipitation rate can be defined as Eq. (7) per Minto et al. (2019). Applying Eq. (7) instead of precipitation rate as Eq. (4) did not affect the model results.

$$r_p = K_p \min(C_{ca}, C_{co3}) \quad (7)$$

vi. Porosity and hydraulic conductivity modifications:

The porosity is updated to indicate the decrease in its magnitude due to the volume of CaCO₃ being precipitated within the pore volume. The porosity updating is given by Eq. (8) (van Wijngaarden et al. 2011):

$$\frac{\partial \theta}{\partial t} = - \frac{1}{\rho_{CaCO_3}} \frac{\partial CaCO_3}{\partial t} \quad (8)$$

In which ρ_{CaCO_3} is the bulk density of precipitated CaCO₃.

$$k_s = k_0 (d_m) \frac{\theta^n}{(1-\theta)^2} \quad (9)$$

Hydraulic conductivity (k_s) is modified using a Kozeny-Carmen style relationship. k_s is incorporated in fluid velocity given by Eq. (1). k_0 indicates permeability as function of mean particle size (d_m). The exponent “ n ” in Eq. (9) is a dimensionless scaling factor that is often assigned a value=3 per van Wijngaarden et al. (2011).

Figure 1 depicts model development flowchart employed herein.

3.3. Model Calibration

To calibrate the model parameters, six column tests from studies reported in literature have been simulated. There were differences between soil type, column dimensions, initial properties of porosity and hydraulic conductivity, treatment protocol, flow rates, and injection direction. To simulate treatment procedure, chemical concentrations, injection and retention times have been defined specifically for each reagent and for each experiment separately using functions programmed within COMSOL Multiphysics time domain. Various initial and boundary conditions were applied to simulate specific flow and transport conditions for each experiment.

A set of sensitivity analyses (not reported herein) was conducted to assess 15 model parameters. It was revealed that microbial activity and attachment rate were the most impactful MICP controlling factors that influence CaCO₃ content and distribution. Therefore, the parameters K_u and K_{at} representative of ureolysis rate and bacteria attachment, respectively, were assessed. The upper and lower limits for these parameters were calibrated to obtain the simulated results within a range of average experimental results \pm standard deviation (SD). To simulate a field-scale condition, a treatment procedure from Montoya et al. (2021), as well as calibrated parameters of

lower bound $K_u=1 \times 10^{-6}$ mol/l.s.OD₆₀₀, upper bound $K_u=2 \times 10^{-6}$ mol/l.s.OD₆₀₀, $K_{at}=1 \times 10^{-4}$ 1/s, $K_m=1 \times 10^{-2}$ M, and $K_{decay}=1.15 \times 10^{-7}$ 1/s have been employed. The retained bacteria, change in hydraulic conductivity and porosity were monitored during simulation and compared with experimental data.

3.4. Field-Scale Model Configuration

The developed model was employed in COMSOL Multiphysics to simulate large-scale MICP application. The domain dimension is 2m × 2m × 0.3m which was discretized with triangular fine mesh elements as shown in Figure 2. The analyses are conducted in 2-D mode, and per unit depth of the domain. Multiple injection wells along with an extraction well in the center of wells' array were simulated using "line mass source" boundary conditions. Treatment was completed through 12 injection cycle during 320 h (about 13 days). Each injection cycle consists of 2-3 h injection of solutions followed by 24 h retention time for chemical reactions (first 8 injections with 3 h and the last 4 injections with 2 h duration).

The biological solution comprised bacteria cells of *Sporosarcina pasteurii* (1.0 OD₆₀₀) suspended in media of 0.333 M urea, and 0.374 M ammonium chloride (NH₄Cl). The biological solutions were injected three times every 4.5 days followed by 3 cementation treatments. Subsequent cementation solutions consisted of 0.333 M urea, 0.374 M NH₄Cl, and 0.25 M calcium chloride (CaCl₂). The various injection flow rates of 5, 10, and 15 cm³/s (low, middle, high) were applied separately to investigate the effect of such flow rates on the cementation results. An extraction well was simulated using a line mass source with the two extraction flow rates of -5 and -10 cm³/s, respectively. The extraction flow rate was fixed as constant for varying injection flow rates. As an initial condition, hydrostatic pressure head of 0.3 m (equal to domain thickness) was assigned to the domain. The outer bounds of the modeled domain were established as pressure-controlled outflow boundaries allowing groundwater flow exchange through the sides. As no flow gradient was set for model domain, no flux boundaries also give the similar results.

Table 1 summarizes the model parameters. Figure 3 shows various well configurations which were assessed. For the sake of comparison, the total flow rates for all configurations were maintained constant. As an example, for total injection flow rate of 10 cm³/s, if a 2-well layout was considered, Q_i is 10/2=5 cm³/s; for a 3-well layout, Q_i would be 10/3=3.33 cm³/s for each well. The average and integration functions incorporated in COMSOL Multiphysics library were

employed to compute the total, average, and standard deviations of results for all triangular elements.

3.5. Results and Discussion

Various well layouts were assessed in terms of average induced CaCO_3 content, CaCO_3 distribution within the domain, and total NH_4 by-product remaining in the domain after the treatment was completed. Figure 4 shows an example of the initial head and calcium carbonate distribution for a configuration with 4 injection wells. Figures 5, 6, and 7 compare the results considering the effects of injection flow rates (Q_i), extraction flow rates (Q_o), and upper and lower bounds of specific ureolysis rate (K_u). Figure 8 evaluates phased injection practice versus simultaneous treatment. Please note in the following discussion that the number of injection wells will be used to describe the layouts; for example, the layout presented in Figure 4 will be referred to as a 4-well configuration. All layouts are associated with one extraction well.

Number of wells and configuration

Since the total flow rate is constant, in the case of a 2-well configuration, the reagents are injected with higher flow rates through each well inducing higher CaCO_3 content; thus increasing the number of wells does not necessarily increase the average CaCO_3 within the domain. However, with more injection wells, more uniform distribution and lower induced by-products can be guaranteed. As shown in Figure 5(a) among all configurations which induce high CaCO_3 content, the 4-well configuration with 1 m distance results in a more uniform distribution (Figure 5(b)), and lower by-product (Figure 5(c)). Considering the 4-well case, when distance between wells decreases from 1 m to 0.5 m, the average CaCO_3 content, decreases from 7.6% to 7.2%, and from 4.6% to 4.18%, in the case of highest, and middle flow rate, respectively (Figure 5(a)). Applying a parallelogram 4-well configuration does not improve the results (7% and 3.6% for the case of high and middle flow rates, respectively). Consequently, when distance increases from the extraction well, more CaCO_3 content with a more uniform distribution is induced. Two simulations, 3-well ($Q_i/4$) and 4-well ($Q_i/4$) were compared to assess the results when the flow rates are the same for each well, but the number of wells is different. Obviously, total flow rate is lower for the less number of wells in this case. The results show the CaCO_3 content significantly decreases from 7.6 to 5.6% when the number of wells decreases from 4 to 3, while the uniformity is not noticeable (SD as 4.8 and 5.1%). Total NH_4 decreases from 1388 kg (4-well) to 1111 kg (3-well) for the highest flow rate injection (Figure 5(c)).

Injection flow rates

The optimum flow rates depend on target shear strength and CaCO₃ content within the target area. Three injection flow rates, $Q_i = 5, 10, 15 \text{ cm}^3/\text{s}$ were compared while the extraction flow rate was kept as $Q_o = -5 \text{ cm}^3/\text{s}$. The bacteria attachment and reagents transport are significantly affected by injection flow rates, thus CaCO₃ precipitation is affected subsequently. The results show when injection flow rate increases from 5 to 15 cm³/s, the average normalized CaCO₃ increases from 1.5-2% to 6-9% (Figure 5(a)). However, higher flow rates result in more non-uniform distribution as indicated by comparison between standard deviations for all model configurations, in the case that injection time remains the same (Figure 5(b)). Total by-product mass which is remained in the domain increases with higher injection flow rates as well. The results indicate that 2-well configuration induces higher CaCO₃ content of 8.73% with higher SD of 8.26% represents the most non-uniformity, and more total NH₄ as 2060 kg than all MICP well layouts, when total Q_i and Q_o are 15 and 5 cm³/s, respectively. Compared to 2 wells, 8-well configuration induces the least CaCO₃ as 6.15%, more uniform distribution with SD 3.5%, and total NH₄ 1112 kg with the same Q_i and Q_o (Figures 5(a), (b), (c)). The similar results were obtained for the other flow rates. These results highlight the notable effect of injection flow rate.

Extraction flow rates

Two extraction flow rates $Q_o = -5, \text{ and } -10 \text{ cm}^3/\text{s}$ were analyzed having similar total injection rate Q_i equal to 10 cm³/s. Extraction flow rates are more effective for the induced by-product (Figure 6 (c)) while the effects on CaCO₃ content and uniform distribution are negligible as indicated by Figures 6(a), and 6(b). When injection flow rate decreases from 10 to 5 cm³/s the average CaCO₃ content decreases by approximately 3%, while if extraction flow rate decreases from 10 to 5 cm³/s, the CaCO₃ content varies by trivial amount, less than 0.5% for all well configurations. More by-products are recovered when extraction flow rates increase.

Specific Ureolysis rates

To study initial specific ureolysis rate (maximum microbial activity), $K_u = 1 \times 10^{-6}$ and $K_u = 2 \times 10^{-6} \text{ mol/l.s.OD}_{600}$ as calibrated by laboratory column-test data have been incorporated into the model. The specific ureolysis rate does not have major effects on uniformity as shown in Figure

7(b), however, the average CaCO_3 content, hydrolyzed urea, and NH_4 mass decrease when the rate is cut in half (Figures 7(a) and 7(c), respectively).

Phased versus simultaneous injection

For 2, 4, and 8-well configurations, phased-injection schedules were explored and compared with simultaneous injections. The results are presented in Table 2. Reagents are injected in two phases, as shown in Figures 3(a), (d), and (g). The wells which are numbered 1 were injected through first and then followed by injection of wells numbered 2. Phased injection did not change the average CaCO_3 content and uniformity, but significantly decreased remained by-product due to more extraction in each phase (Figure 8, Table 2). Treatment duration increased for the phased schedule. In addition, more CaCO_3 mass was obtained near the injection wells in phased-injection treatment. If an additional step including injection through the center well is implemented after injection of surrounding wells, better-distributed CaCO_3 can be attained (Minto et al. 2019). The distribution can be explained using Damkohler number (Da). Da number increased during the 2nd phase due to higher reaction rate vs transport just from a limited number of wells at each phase.

3.6. Conclusion

The developed model framework in this study aims to properly capture MICP reactive transport process in small- and large-scale tests and contributes to the effort of upscaling and design of field deployment protocols. As the injection flow rate is increased from 5 to 15 cm^3/s , the results highlight the influence of injection flow rates on average normalized CaCO_3 , non-uniform distribution CaCO_3 , and on total by-products. The readers are referred to Faeli (2021) for more details on the present study. Based on the results obtained herein, the following conclusions are advanced:

- Among all well configurations which induce the highest CaCO_3 content, 4-well configuration with 1 m distance between wells, produces more uniform distribution (less standard deviation), and lower by-product ammonium (NH_4).
- The 2-, 3-, and 4-well configurations with distance between wells as half of the domain (1m) produce the highest average CaCO_3 in the target area, when total flow rate and injected volumetric solutions are the same for all well configurations. When the number of wells increases, each well injects less flow volume per injection cycle compared to the wells set in a

reduced number of well layout. Thus increasing the number of wells beyond 4 does not necessarily improve treatment extent.

- Extraction flow rates are more effective on recovered by-product NH_4 , while the effects on CaCO_3 content and uniformity of distribution are negligible in all well configurations.
- The variation in specific ureolysis rate (maximum microbial activity) does not have major effects on uniformity of CaCO_3 distribution; however, induces lower hydrolyzed urea, lower average CaCO_3 content, and NH_4 mass within area, when decreased by a factor of 2.
- Exploring the effect of phased and simultaneous injection approaches for 2, 4, and 8 wells, indicated that phased injection did not change the average CaCO_3 content and uniformity, but significantly decreases by-product remaining in the subsurface due to higher extraction volume in each phase. More CaCO_3 mass was obtained near each injection well in phased-injection treatment.

Table 3.1 MICP model parameters.

Model Parameter	Symbol	Unit	Value	Note
Domain Area		m	2x2	
Domain thickness		m	0.3	
Porosity	θ		0.44	Lab data
Hydraulic conductivity	k_s	m/s	1.7×10^{-4}	Lab data
Specific ureolysis rate	K_u	mol/l.s.OD ₆₀₀	$1-2 \times 10^{-6}$	Calibrated*
Attachment rate coefficient	K_{at}	1/s	1×10^{-4}	Calibrated
Half-saturation rate Constant	K_m	mol/l (M)	1×10^{-2}	Calibrated
Decay rate coefficient	K_{decay}	1/s	1.15×10^{-7}	Calibrated
Dispersivity	$\alpha_L = \alpha_t$	m	0.3	Lab data
Diffusion coefficient	D_e	m ² /s	1×10^{-9}	
Soil Dry Density	γ_d	kg/m ³	1489	Lab data
fluid density	γ_f	kg/m ⁴	1000	
Compressibility of fluid	X_f	1/Pa	4.4×10^{-10}	Storage
Matrix Effective compressibility	X_p	1/Pa	1×10^{-8}	Storage
Dynamic Fluid viscosity	μ	Pa.s	8.9×10^{-4}	
Molar mass of CaCO ₃	m_{CaCO_3}	g/mol	100.087	
Molar mass of NH ₄	m_{NH_4}	g/mol	18.039	
CaCO ₃ bulk density	ρ_{CaCO_3}	kg/m ³	2710	
Injection flow rates	Q_i	cm ³ /s	5-10-15	Parametric
Extraction flow rates	Q_o	cm ³ /s	5-10	Parametric
Bacterial solution	<i>Bacteria-Urea-NH₄Cl</i>	OD-M-M	1-0.333-0.374	Lab data
Cementation solution	<i>Urea-NH₄Cl-CaCl₂</i>	M-M-M	0.333-0.374-0.25	Lab data
Injection time		h	2-3	Lab data
Retention time		h	24	Lab data

*The parameters have been calibrated using six simulated column tests, and further simulation of large-scale tests per Montoya et al. (2021). The lab data was obtained per Montoya et al. (2021).

Table 3.2 Simultaneous and Phased injection results.

Well configuration	Treatment procedure	Average CaCO ₃ (%)	Uniformity SD (%)	NH ₄ (kg)
2 wells	Simultaneous treatment	5.17	6.03	1148.04
	Phased treatment	4.89	5.61	804.68
4 wells	Simultaneous treatment	4.63	3.97	857.00
	Phased treatment	4.78	3.69	849.06
8 wells	Simultaneous treatment	3.80	3.00	658.37
	Phased treatment- (Figure 8 (a))	3.80	3.39	595.20
	Phased treatment- (Figure 8 (b))	3.63	3.29	516.35

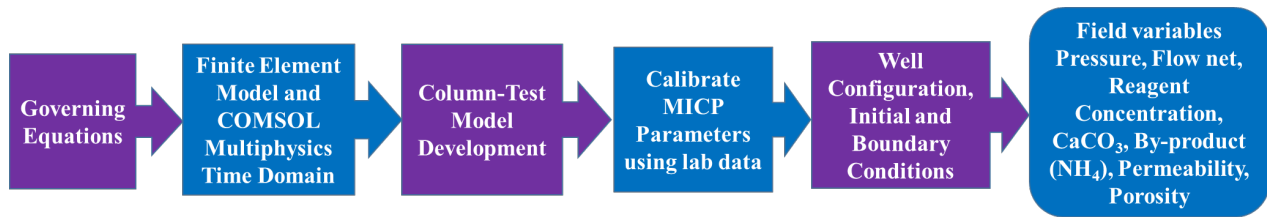


Figure 3.1 Model development and calibration flowchart.

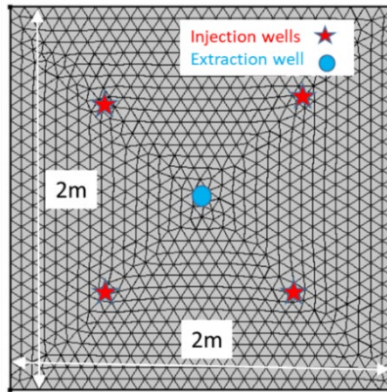


Figure 3.2 Field-scale model and discretized mesh domain.

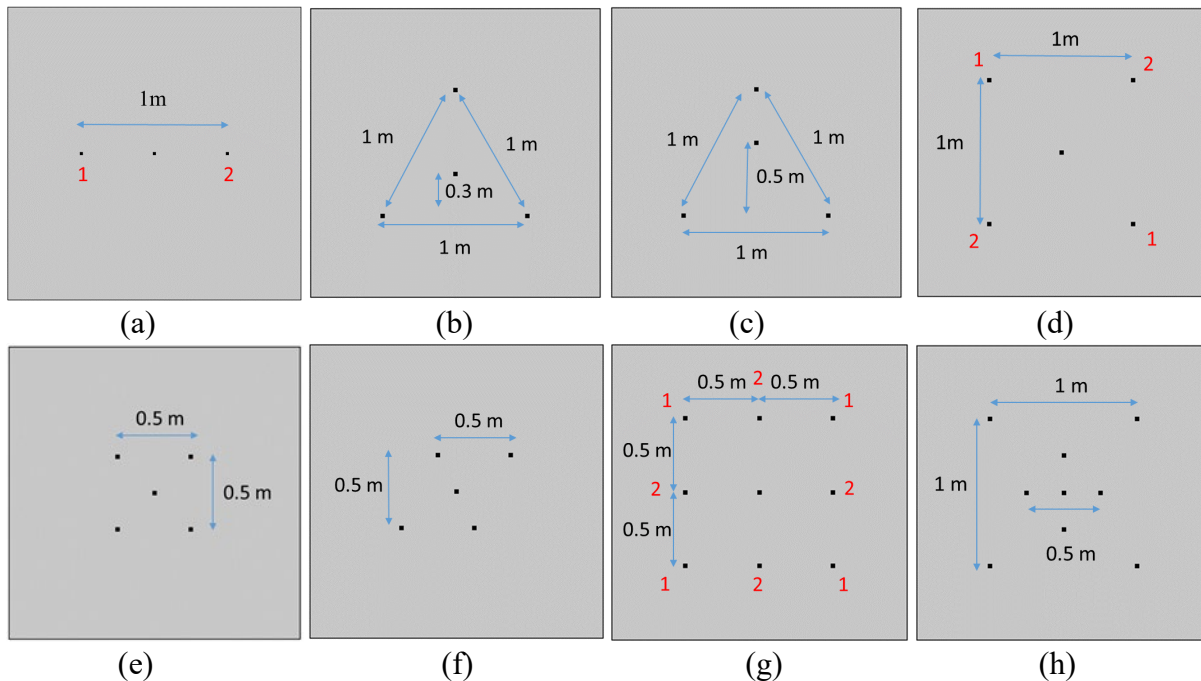


Figure 3.3 Differing well configuration assumed to represent potential field situations. In all figures, an extraction well is located at the center of layout surrounded by injection wells. The red numbers indicated phased-injection process studied for layouts (a), (d), and (g) described in the next section; 1 and 2 represent first and second phase treatments, respectively. (a) 2 wells-D=1 m, (b) 3 wells-D=1 m (Extraction well at the center of the injection wells), (c) 3 wells-D=1 m (Extraction well at the center of the domain), (d) 4 wells-D=1 m, (e) 4 wells-D=0.5 m, (f) 4 wells-D=0.5 m-P (Parallelogram), (g) 8 wells-D= 0.5 m, (h) 8 wells-D=0.5/1 m.

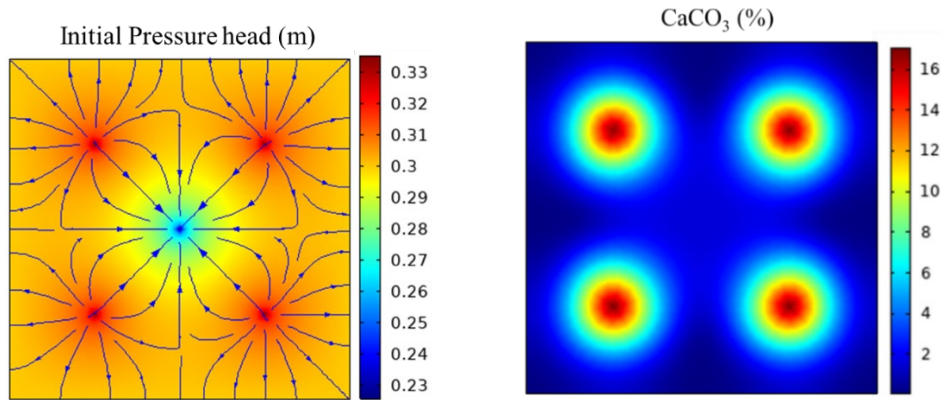


Figure 3.4 Initial pressure head, and CaCO₃ content; 4-well, $Q_i=10 \text{ cm}^3/\text{s}$, $Q_o=-5 \text{ cm}^3/\text{s}$, $K_u=1 \times 10^{-6} \text{ mol/l.s.OD}_{600}$.

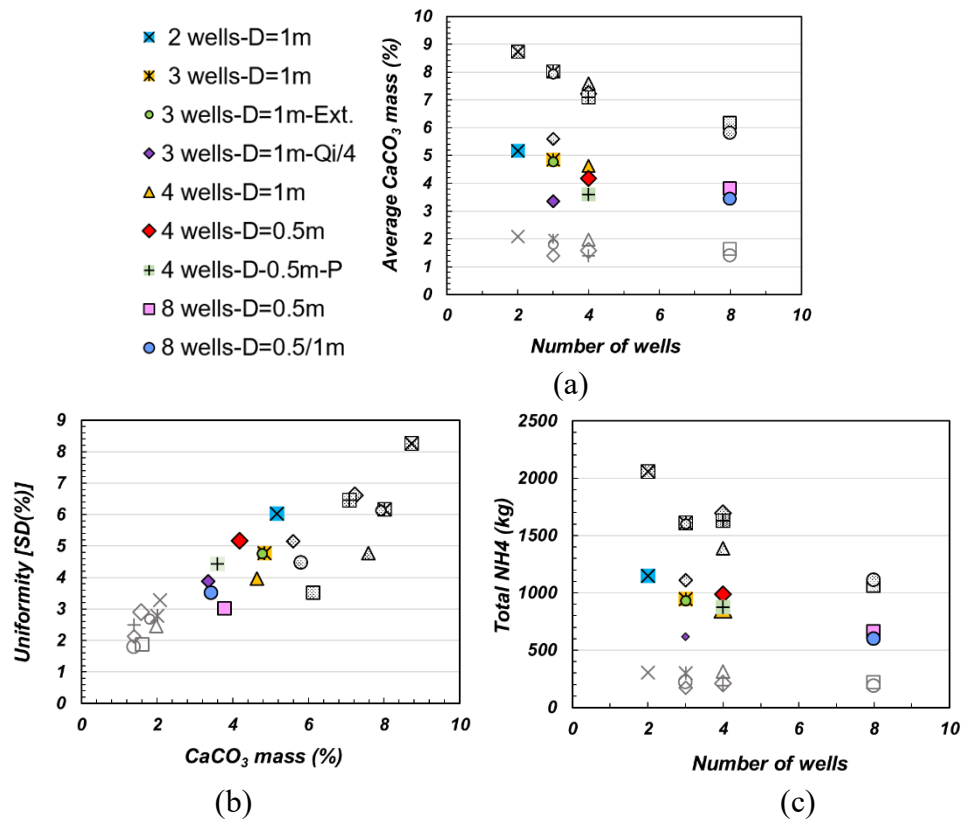


Figure 3.5 The effect of injection flow rates on various well configuration variables; $Q_o=-5 \text{ cm}^3/\text{s}$, $K_u=2 \times 10^{-6} \text{ mol/l.s.OD}_{600}$. Hollow symbols represent injection flow rate (Q_i)=5 cm^3/s , filled/colored symbols indicating $Q_i=10 \text{ cm}^3/\text{s}$, and hatched ones showing $Q_i=15 \text{ cm}^3/\text{s}$.

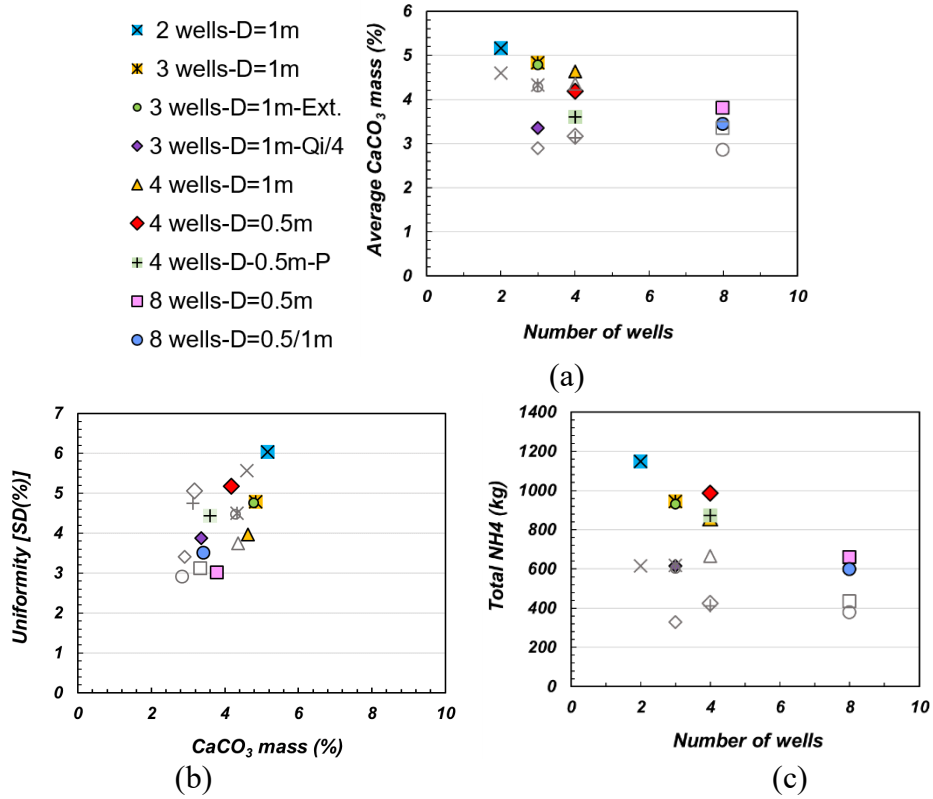


Figure 3.6 The effect of extraction flow rates on various well configuration variables; $Q_i=10 \text{ cm}^3/\text{s}$, $K_u=2 \times 10^{-6} \text{ mol/l.s.OD}_{600}$. Hollow symbols represent extraction flow rate (Q_o)= $10 \text{ cm}^3/\text{s}$, and filled/colored symbols show $Q_o=5 \text{ cm}^3/\text{s}$.

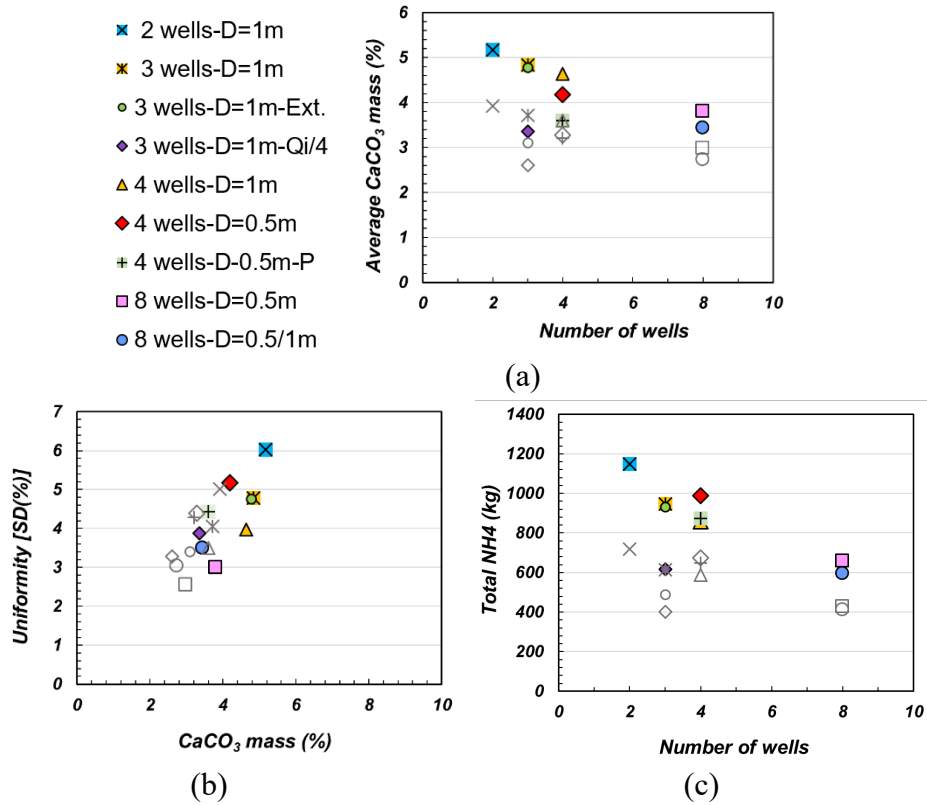


Figure 3.7 The effect of specific ureolysis rates (calibrated upper and lower bounds) on various well configuration variables; $Q_i=10 \text{ cm}^3/\text{s}$, $Q_o=-5 \text{ cm}^3/\text{s}$. Hollow symbols represent ureolysis rate (K_u)= $1 \times 10^{-6} \text{ mol/l.s.OD}$, and filled/colored symbols show $K_u=2 \times 10^{-6} \text{ mol/l.s.OD}$.

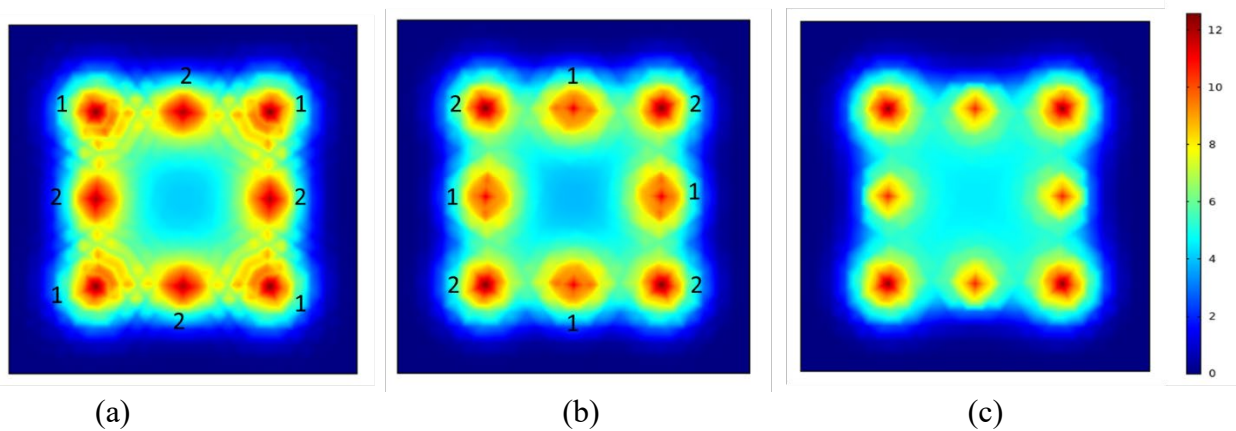


Figure 3.8 Phased injection with middle flow rate ($Q_i=10 \text{ cm}^3/\text{s}$, $Q_o=-5 \text{ cm}^3/\text{s}$, $K_u=2 \times 10^{-6} \text{ mol/l.s.OD}$) from left (a) Phased: first injection at corners, (b) Phased: first injection in the middle of sides, (c) Simultaneous injection.

CHAPTER 4. Various Bacterial Attachment Functions and Modeling of Distribution of Biomass and Calcium Carbonate Precipitation in MICP Implementations

This chapter will be submitted to *Journal of Geotechnical and Geoenvironmental Engineering*.

Abstract

Microbial induced calcium carbonate precipitation (MICP) offers a robust technique to improve geologic properties of subsurface areas supporting infrastructures. While experimental studies have been extensively explored the cemented soil properties, several unknown factors make field implementation unpredictable and have faced the upscaling with many challenges. One major challenge is to predict spatial distribution of calcium carbonate content within subsurface area since it affects the soil strength and hydraulic properties at different spots of soil profile. It was shown that calcium carbonate distribution is highly affected by biomass profiles in subdomain. Five bacteria attachment models (constant rate, power-law, exponential, gamma distributions, and the c_{str} based on the colloid attachment theory) were calibrated in both small- and large-scale tests. The colloid attachment theory with velocity and straining terms was shown to be the most efficient approach in yielding the most fitted calcium carbonate distribution with experimental measurements. A new parameter c_{str} , for the first time, was incorporated into the model to constraint straining at distances about or larger than $0.14 * L$ (targeted depth) and give biomass and calcium carbonate distribution with steeper slope in flow direction. The velocity dependence, straining shape factors, and decay coefficient in this model can be extended from laboratory column scale to large-scale experiments. However, the results show higher bacteria entrapped in pore throats on large-scale leading up to one order of magnitude higher straining coefficient rate (K_{str}) in field implementation compared to the small-scale practices.

4.1. Introduction

During the MICP process, the bacteria hydrolyze urea to raise the pH of the system and carbonate is produced, which leads to the precipitation of calcium carbonate (CaCO_3) in the presence of a calcium source (Al Qabany and Soga 2013). While the effectiveness of MICP to improve soils has been demonstrated extensively at the scale of column testing (DeJong et al. 2006, Whiffin et al. 2007, Harkes et al. 2010, Cheng et al. 2013, Do et al. 2019, Nafisi et al. 2019, 2020, and others), a few pilot large-scale experiments have been implemented at laboratory or field with

focus on characterizing strength and monitoring cementation level (van Paassen et al. 2009b, Gomez et al. 2017, San Pablo et al. 2020, Ghasemi and Montoya 2020, Montoya et al. 2021). Due to the high cost of large-scale field trials and the limited number of variables that can feasibly be investigated, the use of numerical modeling provides a viable option to enhance full understanding of MICP process as well as optimizing treatment in the field (Minto et al. 2019).

Mathematical Models for predicting MICP processes in soils have been developed by coupling reaction kinetics of chemical variants and fluid transport in one- or two-dimensional domains (van Wijngaarden et al. 2011, 2012, 2016, Barkouki et al. 2011, Ebigbo et al. 2012, Martinez et al. 2012, 2014, Hommel et al. 2015, 2016, Cuthbert et al. 2013, Nassar et al. 2018, Minto et al. 2019, Zeng et al. 2021). These models, as reported in literature, captured precipitation at small/pore scales or surficial applications. Recently, Zeng et al. 2021 developed a simplified 2D model using COMSOL to interpret the results of a field trial. The numerical model was used only to simulate one stage of treatment procedure (amendment/cementation injection phase) and exclude transient boundary conditions simulating the bacteria injection phase and retention time resulting in precipitation. The reaction rate was simply assumed to be constant during the treatment time calculated based on ammonium production which was independent of initial volume of injected bacteria and bacteria was assumed to be equally distributed throughout the domain ignoring gradually transportation, attachment, detachment, decay, and flushing out. Neither the variation in vertical direction nor soil properties alteration (hydraulic conductivity and porosity modification) was considered in the model (Zeng et al. 2021). These assumptions and simplifications expose field simulations to many approximations and unpredicted errors in ultimate design and performance evaluations.

The results from these models indicated the necessity of developing and calibrating a three-dimensional large-scale model that simultaneously captures macro-scale spatial variations within the surface and depth, temporally variations during cyclic injection/retention times, and the potential influence of the precipitation on porosity/permeability reduction.

In bio-augmentation, bacteria are injected into the porous medium, transported through the pores and attached to the soil particles. Once attached bacteria cells (known as biofilm or attached biomass) rupture, urease is released, adsorb to the biofilm, and catalyzes ureolysis process. The concentration of biofilm and released urease in the porous medium is difficult to determine and remained a challenge in MICP development techniques (Bouwer et al. 2000, Cunningham et al.

2007, Hommel et al. 2016). Several studies showed calcium carbonate distribution is highly affected by attached bacteria patterns in subdomain (Barkouki et al. 2011, Martinez et al. 2012, Faeli et al. 2021). Once MICP is used in a larger field scale, bacterial injection and attachment to the soil grains as well as bacterial distribution over the treatment volume need to be taken into account (Al Qabany et al. 2012). Given the unknown behavior of bacteria and released enzymes, the previous studies introduced various bacteria attachment models to better represent their experimental results while suffering from uncertainties in large-scale field predictions. Many studies employed traditional filtration theory (van Wijngaarden et al. 2011, Cuthbert et al. 2013) to describe a spatially constant rate of deposition. Traditional filtration theory uses a velocity-dependent or simply a constant attachment coefficient which leads to an exponential spatial distribution of retained bacteria in porous media (Ginn et al. 2002). The previous simulations showed inability of constant rate attachment to accurately predict spatial distribution of precipitation (Barkouki et al. 2011, Ebigbo et al. 2012, Martinez et al. 2012). Ebigbo et al. (2012) and Hommel et al. (2015) modeled the attached biomass using nonlinear power-law equation. Barkouki et al. (2011) simulated final urease as an immobile species with an exponential distribution function in terms of the distance from injection inlet. Martinez et al. (2012, 2014) used an improved spatially distributed expression, including gamma distribution function, that was adopted to represent total immobile urease in bacterial augmentation. Minto et al. (2019) modeled attachment as a function of velocity. In that model, bacteria retention due to straining was also incorporated with a constant straining coefficient regardless of geometric dependence per Bradford et al. (2003).

Traditional filtration theory was developed based on experimental data of colloid attachment to the solid-water interface of same size spherical grains. Accordingly, traditional filtration theory does not include the potential influence of pore structure, grain-grain junctions, and surface roughness on attachment, which may result in non-exponential deposition profiles (Tufenkji and Elimelech, 2005). In contrast to this theory, attachment rates have been mostly found to vary spatially with depth (Bolster et al. 1999, Bradford et al. 2003, 2004). Bradford et al. (2006), and (2007) are thus demonstrating the important role of straining in colloid deposition. Assessing 12 major soil textural groups, Bradford et al. (2006) concluded that depending on soil texture, straining was predicted in 10.5 to 70.8%, 10.5 to 86.2%, and 10.5 to 91.8% of the soil pore space for virus, bacteria, and protozoa transport, respectively. The geometric compatibility between

microbes and soil, and the size of pore throats are critical to the issue of treatment uniformity (Mitchell and Santamarina 2005, DeJong et al. 2010).

To simulate bacteria attachment, multitude of different approaches were employed. Many of these approaches incorporated a final profile of attached biomass that better fitted into their experimental measurements regardless of the time-scale-dependent attachment during treatment. Accordingly, if the experimental set-up, the scale, soil type, and solution mixture change, these models may not be applicable. Little attention has been paid to colloid attachment theory with straining in MICP modeling in soils. As such, there is a need to develop a model framework to calibrate parameters of MICP reactive transport model in large-scale setting for upscaling and design of field deployment protocols.

Towards this aim, the main objective is to scrutinize the extent of predicting the attached biomass distribution in both small- and field-scale tests using five proposed attachment models in literature; (a) constant rate, (b) nonlinear power-law distribution, (c) exponential distribution, (d) gamma distribution, and (e) the c_{str} based on the colloid attachment theory. The resulted calcium carbonate precipitations from these approaches were compared with experimental measurements to assess most efficient model. The c_{str} based on the colloid attachment theory, including straining, was concluded to be the most promising approach. The velocity-dependent and straining parameters from this theory were calibrated for MICP field-scale implementation in a new framework. Modeling has been conducted using COMSOL-multiphysics time-domain V5.5 (2020) and Finite Element Method (FEM) in conjunction with a MATLAB code. Modeling included coupling of embedded subsurface flow module for transport of diluted species and a system of PDEs for stationary components and soil modifications in a transient environment. The extent to which the post-treatment hydraulic conductivity and porosity change has been explored as well.

4.2. Model Development

4.2.1. The COMSOL-Multiphysics Framework

COMSOL-multiphysics time-domain V5.5 (2020) and Finite Element Method (FEM) in conjunction with a MATLAB code to optimize the model parameters were employed as the main modeling tool for this work for two reasons. COMSOL provides simultaneous coupling of embedded subsurface flow module for transport of diluted species and a system of PDEs for stationary components and soil modifications in a transient environment. COMSOL features allow

for capturing key processes of MICP while avoiding the complex chemical interactions incorporated within geochemistry models which restrict model tractability in 2D/3D simulations. The backward differentiation formulas (BDF solver) with the order of accuracy varying from one (backward Euler) to five was employed. Figure 1 shows flowchart of the model development and analyses in this study.

4.2.2. Bio-geochemical Process and Mathematical Model Development

Urease released by bacteria catalyzes urea hydrolysis to produce carbonate (CO_3^{2-}) and ammonium (NH_4) and CO_3^{2-} in the presence of calcium (Ca^{2+}) induce mineral bonds of CaCO_3 or calcite.

Richards' Flow model (Richards' 1931)

The Richards' equation is employed to simulate density-driven flow in saturated and unsaturated subsurface zones (Eq. 1).

$$\frac{\partial(\theta\rho)}{\partial t} + \nabla \cdot (\rho u) = Q_m, \quad \frac{\partial(\theta\rho)}{\partial t} = \rho \left(\frac{C_m}{\rho g} + S_e S \right) \frac{\partial p}{\partial t} \quad (1)$$

$$u = -\frac{k}{\mu} (\nabla p + \rho g \nabla z), \quad k = k_s k_r (S_e)$$

where θ denotes volume fraction of fluid (porosity in saturated), u is fluid velocity, S is storage coefficient (m^{-1}) defined with compressibility of fluid and matrix ($1/\text{Pa}$), p is pressure (Pa), t is time (s), ρ is fluid density (kg/m^3), μ is fluid dynamic viscosity (Pa.s), z is direction that represents vertical elevation (m), Q_m is fluid source or sink, S_e , C_m , and k_r are unsaturated parameters; residual saturation (equal to 1 in saturated), specific moisture capacity (zero in saturated), and relative permeability (1 in saturated), respectively.

Mass balance of chemical species transport (advection-dispersion-reaction) (Zhang and Klapper 2010, van Wijngaarden et al. 2011)

Chemical species transport model is given by Eq. 2 to simulate transport of dissolved species; urea, ammonium (NH_4), calcium (Ca^{2+}), and carbonate (CO_3^{2-}).

$$\frac{\partial(\theta C_i)}{\partial t} + \frac{\partial(\rho_b C_{p,i})}{\partial t} - \nabla \cdot (\theta D_i \nabla C_i) + \nabla \cdot (u C_i) = R_i \quad (2)$$

$$D_i = \alpha_{L,T} |u| + D_e, \quad R_i = m\theta r_{uh}$$

Where C_i is solute concentration (mol/m^3), D_i is dispersion tensor, $\alpha_{L,T}$ is longitudinal and transverse dispersivities, D_e is effective diffusion coefficient ($1 \times 10^{-9} \text{ m}^2/\text{s}$, van Wijngaarden et al. 2016), R_i is reaction term, a product of fluid volume fraction (θ), urea hydrolysis rate (r_{uh}), and

stoichiometry constants (m : -1 for urea and Ca^{2+} , 1 for CO_3^{2-} , and 2 for NH_4), $C_{p,i}$ is mass of absorbed species to solid particles (such as Langmuir or Freundlich models), and ρ_b is bulk density (kg/m^3).

Urea hydrolysis reaction kinetics (Barkouki et al. 2011, Minto et al. 2019)

The ureolysis rate in reaction term of Eq. (2) is defined on a basis of components following Michaelis-Menten kinetics per Eq. (3).

$$r_{uh} = K_u (S_{su} + S_{at}) \frac{C_{urea}}{K_m + C_{urea}} \cdot \frac{K_{NH4}}{K_{NH4} + C_{NH4}} \quad (3)$$

where S_{su} is suspended bacteria concentration (OD_{600}), S_{at} is bacteria attached to the surface known as biofilm (OD_{600}), K_u is specific rate of ureolysis (mol/l.s.OD), K_m is half-saturation rate constant (M), and K_{NH4} is optional ammonium inhibition (M).

Calcium carbonate precipitation kinetics (van Wijngaarden et al. 2011)

At low hydrolysis rates, precipitation occurs at relatively low supersaturation and the ureolysis rate and bulk precipitation rate are approximately equal van Paassen et al. (2009). Thus, the precipitation rate (r_p) in Eq. (4) is considered to be equal to ureolysis rate.

$$\frac{\partial \text{CaCO}_3}{\partial t} - m_{\text{CaCO}_3} \theta r_p = 0 \quad (4)$$

where m_{CaCO_3} is the molar mass of CaCO_3 (kg/mol).

Porosity and hydraulic conductivity modification (van Wijngaarden et al. 2011)

The pore space being filled with CaCO_3 precipitation results in porosity reduction. The porosity at each time increment is modified per Eq. (5).

$$\frac{\partial \theta}{\partial t} = - \frac{1}{\rho_{\text{CaCO}_3}} \frac{\partial \text{CaCO}_3}{\partial t} \quad (5)$$

In which ρ_{CaCO_3} is the bulk density of precipitated CaCO_3 .

Hydraulic conductivity (k_s) is updated following Kozeny-Carman style and new porosity per Eq. (6). k_0 represents initial hydraulic conductivity as function of mean particle size (d_m). n is a dimensionless scaling factor often assigned as 3 (vanWijngaarden 2011, Minto et al. 2019).

$$k_s = k_0 (d_m) \frac{\theta^n}{(1-\theta)^2} \quad (6)$$

4.2.3. Bacteria Transport, Attachment, Decay, and Encapsulation

During bacterial transport through porous medium, some suspended bacteria (S_{su}) are attached to soil particles and create biofilm on the particle surface (S_{at}). CaCO_3 then nucleates mainly in and on the biofilm that acts as nucleation sites at a supersaturation condition (Stockes-

Fischer et al. 1999, Zhang and Klapper 2010). The number of attached bacteria not only plays an important role in ureolysis and precipitation rates but also forms the CaCO₃ distribution within the subsurface domain. The inclusion of nutrient broth in the amendment solution, initial concentration of microbes, and retention period are important to achieve more uniform microbes and CaCO₃ distribution in an augmentation scheme (Martinez et al. 2012).

To simulate bacteria attachment, the previous studies have extensively used a typical first-order-rate model including a constant attachment rate coefficient (van Wijngaarden et al. 2012, Cuthbert et al. 2013). However, past colloidal transport studies have shown that the spatial distribution of retained microorganisms is not always consistent with a unique constant attachment coefficient (Swanton et al. 1995). The soil particles roughness, variability in colloid characteristics, soil size distribution, fluid velocity, and charge heterogeneity are influential factors governing the distribution behavior (Bradford et al. 2003, Mitchell and Santamarina 2005). Several studies showed that a more accurate model than constant rate attachment is needed to capture distribution of precipitation (Ebigbo et al. 2012, Hommel et al. 2015, Minto et al. 2019). (Barkouki et al. 2011, Martinez et al. 2014, Hommel et al. 2016) employed a specific ultimate distribution of bacteria in the model disregarding initial bacteria injected, transient transport and attachment process occurring in bio-augmentation. In the study presented herein, the models in the literature are used with modification. This modification is more appropriate to simulate bio-augmentation, whereas assigning the final distribution is more applicable to the bio-stimulation process where the distribution is not affected by transport. In closing, the most fitted model was found to be the c_{str} based on the colloid attachment theory with two important factors of attachment; velocity and location/depth dependence process. Even though colloidal transport studies used this model in the past (Harvey et al. 1993, Bradford et al. 2003, Tobler et al. 2014) to simulate colloid attachment process, little attention has been paid to this model in MICP model development. The past colloidal transport studies calibrate this model in small-scale column experiments (Bradford et al. 2003, 2004, 2006, and 2007), whereas the study presented herein will calibrate the model in both small- and large-scale MICP implementations and introduce a modification factor (c_{str}) into the model.

a) Constant rate attachment

The bacterial transport is a combination of advection-dispersion-retardation theory for solute transport given by Eq. (2), and bacteria attachment theory (Eq. 7, and 8). In Eq. (2), reaction rate (R_i) for suspended biomass is traditionally given by an irreversible first-order kinetic

relationship (Eq. (7)) in which K_{at} is a constant and the relationship predicts an exponential decrease in bacteria concentration with distance in porous medium (Harvey and Garabedian 1991, Murphy and Ginn 2000). Attached Bacteria cells can decay over time due to cell death or be inactivated due to encapsulation within CaCO_3 nucleus, as described in Eq. (8) per Minto et al. (2019) and van Wijngaarden et al. (2012).

$$R_{S_{su}} = -K_{at}\theta S_{su}, K_{at} \text{ is a constant attachment rate coefficient (1/s) can be noted as } K_{at1}. \quad (7)$$

The attached biomass S_{at} is driven by:

$$\frac{\partial S_{at}}{\partial t} = K_{at}\theta S_{su} - K_{decay}\theta S_{at} + \frac{CaCO_3}{K_{encapsulation}} S_{at} \quad (8)$$

where K_{decay} is decay rate coefficient (1/s), and $K_{encapsulation}$ is the encapsulation rate constant ($\text{kg}\cdot\text{m}^3\cdot\text{s}$). Note that in the simulations presented herein, encapsulation and decay are both modeled using decay term, as there no reliable data are found to calibrate $K_{encapsulation}$.

Four other approaches have been adopted from literature to modify bacterial attachment model. These four approaches, presented as follows, are in addition to a base model using constant attachment coefficient of K_{at} (Eq. (7) and (8)).

b) Nonlinear power-law distribution Function

The urease enzyme (ZH) is incorporated in ureolysis relationship (Eq. (9)) associated by the attached bacteria using a nonlinear power-law equation (Eq. (10)) following Ebigbo et al. (2012) and Hommel et al. (2015). Urease enzyme is released when bacterial cells rupture and catalyzes ureolysis. The bacteria amount in Eq. (3) has been replaced with ZH per Eq. (9) and (10) and K_{at} in Eq. (7) and (8) was upgraded to Eq. (11).

$$r_{uh} = K_u ZH \frac{C_{urea}}{K_m + C_{urea}} \cdot \frac{K_{NH_4}}{K_{NH_4} + C_{NH_4}} \quad (9)$$

$$ZH = K_{ZH} (S_{at})^{n_{ZH}} \quad (10)$$

$$K_{at} = K_{at1} * (c_{a,1} \cdot S_{at} + c_{a,2}) \quad (11)$$

where K_{ZH} , n_{ZH} , $c_{a,1}$, and $c_{a,2}$ are fitting parameters. K_{at1} is equal to the constant attachment coefficient in the base model. Table 1 shows the original relationships compared to the relationships used in this study.

c) Exponential distribution function

In another approach, K_{at} was updated as an exponential function (Eq. 12), following Barkouki et al. (2011) to capture temporally as well as spatially biomass distribution during the treatment time.

$$K_{at} = K_{at1} c_1 e^{-c_2 z} \quad (12)$$

where z is the distance from injection inlet, pre-multiplier c_1 and exponential coefficient c_2 are treated as fitting parameters.

Barkouki et al. (2011) employed ultimate distribution of bacteria in the model. The fixed urease enzyme $ZH_t(z)$ was simulated with a time-independent exponential relationship that is a function of distance from injection inlet (z) per Eq. (12*) in original formulation.

$$ZH_t(z) = c_1 e^{-c_2 z} \quad (12^*)$$

However, retention periods, decay and encapsulation may affect the bacterial distribution over the course of treatment was not considered in Eq. (12*), and c_1 and c_2 should be calibrated each time for any new bio-injection treatment schedule. In the present study, the attachment coefficient was modified based on exponential function to consider all these limitations in the model.

d) Gamma distribution function

The exponential function has been improved to gamma distribution expression per Eq. (13) following Martinez et al. (2014) to express random biomass distribution.

$$K_{at} = K_{at1} a z^{s-1} \frac{e^{-z/d}}{d^s \Gamma(s)} \quad z \geq 0, a, d > 0, \text{ and } s \geq 1 \quad (13)$$

Similar to previous method suggested by Barkouki et al. (2011), Martinez et al. (2014) incorporated the ultimate distribution of biomass in the simulations dismissing the alteration due to attachment/decay process over the treatment time (original formulation, Eq. (13*)).

$$ZH_t(z) = a z^{s-1} \frac{e^{-z/d}}{d^s \Gamma(s)} \quad (13^*)$$

where “a”, and “d” are scaling parameters and “s” is a shape factor. The gamma distribution shows the flexibility in the shape of a semi-log-linear distribution accounting for instances of bacterial detachment, which may occur at injection inlet, and move the maximum enzyme concentration to some distances from the injection source. In their studies, the parameters were calibrated to match their experimental results could not be extended to the future studies using different treatment solutions. To update their model, the attachment coefficient in this study was revised employing gamma distribution function (Eq. (13)).

e) The c_{str} based on colloid attachment theory

Two mechanisms have been observed during attachment process. The first is attachment of colloids on grain surfaces. Attachment occurs when colloids are retained at the solid–water

interface. The process depends on seepage velocity and force/torque balance that acts on the colloids. These forces include gravity and buoyancy, hydrodynamic drag and lift, electrical double-layer repulsion (or attraction), and London-van der Waals interaction (Cushing and Lawler 1998, Bradford et al. 2007). The other mechanism involves straining or filtering that occurs when colloid particles are entrapped at grain-grain contacts and pore throats that are too small to allow colloid passage (Ginn 1995, Cushing and Lawler 1998). Straining only occurs in a fraction of the soil pore space, and colloid transport can still occur in the larger portions of the continuous pore networks. Straining parameters depend on colloid (bacteria) size, porous medium size, textural interfaces, surface roughness, the system hydrodynamics, flow rates, solution chemistry, and ionic strength as presented in Bradford et al. (2003, 2004, 2006, and 2007).

A relationship with velocity-dependent attachment (Minto et al. 2019), and straining (Bradford et al. 2003) terms have been introduced per Eq. (14):

$$K_{at} = K_{att}U_z + K_{str}c_{str}y_{str} \quad (14)$$

$$U_z = \begin{cases} 1 & U < U_l \\ 1 - \frac{U-U_l}{U_u-U_l} & U_l \leq U \leq U_u \\ 0 & U > U_u \end{cases} \quad (15)$$

where K_{att} is a fitting attachment coefficient, and velocity-dependent factor (U_z) has been defined per Eq. (14) in which U is pore water velocity, U_u and U_l are upper and lower critical velocity limits, respectively. K_{str} is straining coefficient rate, y_{str} is a location-dependent power-law function, and c_{str} is a modification parameter introduced in the present study.

The first term in Eq. 13 is a function of velocity with no attachment above U_u , maximum attachment rate below U_l , and linear scaling of attachment between these limits (Minto et al. 2019). Previously, K_{att} has been correlated to pore water velocity, median porous medium grain diameter, collector efficiency, and colloid sticking efficiency (Logan et al. 1995, Bradford et al. 2003). The value of collector efficiency is calculated using a relationship incorporating various parameters such as Peclet number, London-van der Waals attractive forces number, and Happel correction factors. For the work presented herein, and to avoid many fitting parameters, a similar but simplified velocity-dependent term was employed following Minto et al. (2019).

Straining was incorporated in Eq. (13) using K_{str} , and y_{str} as was presented by Bradford et al. (2003) per Eq. 15.

$$y_{str} = \left(\frac{d_{50+r}}{d_{50}} \right)^{-\beta} \quad (16)$$

where β is a fitting parameter that controls the shape of the bacteria spatial distribution, and r is the least distance from the porous medium injection source or soil texture discontinuity. r is vertical distance (z) in 1-D column tests and squared root of horizontal and vertical distances ($\sqrt{x^2+z^2}$) in large-scale tests. The d_{50} is representative of pore length, while the quantity $(d_{50}+r)/d_{50}$ shows the number of pore lengths from injection source to the target point. The negative power in Eq. 16 shows increasing the number of pore lengths with distance from inlet decreases the straining.

Bradford et al. (2003) indicated that straining relationship assumes that colloids are accessible to all soil pores. We later show that a modification parameter c_{str} (Eq. 16) is needed in the straining term to account for inaccessible soil pores for straining in porous media. Bradford et al. (2003) assumed that all soil pores are colloids-accessible at the column inlet, thus the straining would be maximum at inlet ($y_{str}=1$ at inlet) and is expected to decrease with increasing distance. Simulated small- and large-scale experiments in this and previous study by the authors show peak straining occurs at some distances farther from inlet. Therefore, applied maximum straining at $z/L=0.14$ as indicated in Eq. (16) yielded the most fitted results (as will be shown later in results section.)

$$c_{str} = \begin{cases} 0 & \frac{z}{L} < 0.14 \\ 1 - \frac{\frac{z}{L} - 0.14}{1 - 0.14} & 0.14 \leq \frac{z}{L} \leq 1 \end{cases} \quad (17)$$

where z is the downgradient vertical distance from the inlet coordination, and L is total scale of specimen in vertical direction.

4.3. Application to small-scale experiments

Six column tests from Whiffin et al. (2007), Martinez et al. (2012) and (2014), Do et al. (2019), and Nafisi et al. (2020) were adopted to validate the reactive transport model used herein. Results from such validation are presented in Faeli et al. (2021). The main parameters of microbial activity were calibrated and a range was specified for the specific rate of ureolysis (K_u , mol/l.s.OD), bacterial attachment rate (K_{at} , 1/s), half-saturation (K_m , M), and decay rate coefficient (K_{decay} , 1/s) given the distributed mass of CaCO₃ and retained bacteria data. A sensitivity analysis was conducted to investigate the effects of 15 model parameters in four categories as follows: i. microbial activity and attachment parameters, ii. specimen preparation, iii. treatment procedure, and iv. column dimensions (Faeli et al. 2021).

Results from column test (triaxial testing) conducted by Do et al. (2019) were employed to explore attachment models in small-scale laboratory setup. Figure 2 shows the initial and boundary conditions of the numerical model. The soil type simulated in the analyses was poorly graded silica sand with $d_{50}=0.49$ mm, a minimum and maximum void ratio (e_{min} and e_{max}) of 0.61 and 0.91, respectively, and a relative density of approximately 30%. Transient piecewise functions were employed to simulate one bacteria inoculate injection followed by 42 steps simulating cementation treatment with 5–5–11 h retention times between those injection intervals. The mass source was located at the bottom boundary to prompt upward flow direction. A pressure of 10 kPa was applied as initial and boundary conditions. The detailed description of model parameters is presented in Table 1B.

4.4. Application to Large-scale Experiments

4.4.1. Large-scale Test - Montoya et al. (2021)

Large-scale test data reported by Montoya et al. (2021) were simulated herein. The MICP treatment was implemented within a soil box of 0.9 m x 0.9 m x 0.9 m through a central injection pipe ($D=0.05$ m). Figure 3(a) shows overall view of experiment configuration. The soil type is similar to that used in column test by Do et al. (2019), and described in previous section. The treatment was implemented in 6 batches each consisting of one set of biological and three sets of cementation solutions; therefore, a total of 6 biological and 18 cementation injections were utilized in the experiment. In first batch, the injection source was located at 2-4D below the surface and then lifted to a depth of 1-3D at the second batch and 0.2-2.2D at 3rd to 6th batches. The initial total head was 0.95 m and a head differential of 0.07 m was applied at the top of the pile to induce the

injection. At 3rd and 4th batches, the differential head was lowered to 0.05m with shorter injection times (2 h) to decrease applied seepage velocity and induce higher cementation near the injection source. The last two batches were implemented using a lower head of 0.03 m. The injections were conducted in 3 h-interval at 1st and 2nd batches and 2 h-interval at 3rd to 6th batches with one day retention time between injections, thus the treatment process was completed in 30 days. The biological solution consisted of 0.333 M urea, 0.374 M ammonium chloride (NH₄Cl), and bacterial suspension with optical density of 1 OD₆₀₀ ($2-5 \times 10^7$ cells/ml). The cementation solution consisted of 0.333 M urea, 0.374 M ammonium chloride, and 0.25 M calcium chloride (CaCl₂). The flow rate ranged from 1 to 10 cm³/s. The readers are referred to Montoya et al. (2021) for more details on experimental method.

The Schematic model of soil box is shown in Figure 3(b), with initial and boundary conditions displayed in Figure 4(a). The discretized model domain is presented in Figure 4(b). Constant head outflow boundaries were applied at the top and sidewalls set as $0.05+(0.9-z)$ m for $z \geq 0$. No-flow boundary was considered at the bottom of model domain. A transient head function was assigned to the central injection pile to induce flow at specified intervals (applied head differentials of 0.07-0.05-0.03 m for injection intervals and zero for no flow intervals) whereas the injection depth was varied from 0.2D to 4D during treatment steps (Figure 4(b)). Transient piecewise functions were used to apply the time-dependent injection boundaries.

The initial input parameters were selected based on experimental data (Table (1A)). The initial hydraulic conductivity was considered to be 0.01725 cm/s, porosity as 0.44, dispersivity as 0.3 m, and diffusion coefficient of 0.0001 cm²/s.

4.4.2. Meter-scale Biocementation Test-San Pablo et al. (2020)

A horizontal 3.7m long soil sample with square cross-section of 0.2 m × 0.2 m was bio-cemented by San Pablo et al. (2020); a cross-section of the setup is schematically shown in Figure 5(a). The injection process was applied through a PVC tube (ID= 26.6 mm) at the sample end in one flow direction to simulate a single stream path within a well-to-well half-space. The sandy soil was quarried from alluvial deposits of Concrete/Teichert Sand with $d_{10}=0.23$ mm, $d_{30}=0.54$, $d_{60}=1.54$, and relative density of 56-67 %. The initial porosity was considered to be 0.34. The treatment solution was injected in 1.5 PV (76 L) over 189 min at flow rate equal to 400 ml/min. The trough received a bio-injection consisting of 76 L of *Sporosarcina pasteurii* with cell density of 9.4×10^7 cells/ml in an isotonic saline solution. After augmentation, 4 cementation treatments

were applied to the sample once daily (189 min injection followed by 21 h retention time). Due to lower than expected observed ureolytic activity, a second augmentation treatment was applied after the fourth cementation injection. After the second bio-injection, five more cementations were implemented. The second augmentation injection consisted of 1.4×10^6 cells/ml. The cementation solution was urea-to-calcium ratios of 1:1 with a solution of yeast extract. The readers are referred to San Pablo et al. (2020) for more details on experimental method.

To develop a numerical model, a three-dimensional (3D) domain was employed including an injection source at one end and outlet at the other end (Figure 5(b)). The model parameters are described in Table 1A. The atmospheric boundary condition was assigned to the outlet. The hydrostatic pressure varying within depth was also applied within the domain as an initial condition. The treatment was simulated using piecewise transient functions applied at point mass source, at sample edge, as shown in Fig 5b, in a total duration of 13 days (2 bio injections, 9 cementations).

4.5. Results and Discussion

4.5.1. 1-D Column Testing

Spatial Distribution of Attached Biomass

Sensitivity analyses elucidated the main factors affecting CaCO_3 content and distribution are specific rate of ureolysis and attachment rate parameter, given the number of treatments. An increase in ureolysis and attachment rates by two orders of magnitude shifts average mass percentage of CaCO_3 by 13% and 6% within a column test (the size of conventional triaxial sample) respectively. The attached biomass is the most critical component governing the spatial distribution of CaCO_3 within specimen when treatment protocol, bacteria activity and scale of domain are all dictated by experimental setup. A constant first-order attachment rate (K_{at}) could yield average CaCO_3 within column tests if it is well calibrated; however, predicting exact distribution of the biomass and CaCO_3 is still shown to be a challenge using traditional constant attachment rate (Faelli et al. 2021).

Hence, the results from small-scale experiment by Do et al. (2019) were employed to assess spatially distributed attached biomass and the effect on the CaCO_3 distribution. Four different approaches were calibrated using optimization tool embedded in COMSOL-multiphysics in order to obtain the best fitted CaCO_3 distribution of the experimental results. Figure 6 shows distribution of precipitation mass using the c_{str} based on the colloid attachment theory. The parameters of (a)

non-linear power-law distribution function [K_{ZH} , n_{zh} , $c_{a,1}$, $c_{a,2}$ in Eq. (9) and (10)], (b) exponential distribution function [c_1 , and c_2 in Eq. (11)], (c) gamma distribution function [a , s , d in Eq. (12)], and (d) the c_{str} based on the colloid attachment theory [K_{att} , K_{str} , β , U_1 , U_u , Eqs. (13) to (16)] were calibrated for this experiment and the results are shown in Figure 7 and Table 2. To provide a criterion for decision on the best fitted model, statistical parameters of standard deviation (SD), coefficient of variation (COV), and bias for the results from each calibrated model were calculated. Note that K_{att1} in models (a) to (c) is equal to 1×10^{-4} 1/s from traditional constant rate model to give approximately 50% attached biomass within column. The results show the use of the colloid attachment theory was the most appropriate model to obtain spatial distribution of attached biomass and $CaCO_3$ with 68% improvement of *SD* and *COV* compared to the model using constant rate. Gamma distribution function with 44% improvement provided better results compared to exponential distribution function (3.22%) and non-linear power-law (no improvement).

Figures 7(a), 7(b), 7(c), and 7(d) present measured $CaCO_3$ versus simulated $CaCO_3$ for model using constant rate, as well as simulated $CaCO_3$ and attached biomass for each of the four distribution models. Martinez et al. (2014) extended exponential function used by Barkouki et al. (2011) (shown in Eq. 11) to better interpret their experimental results by using a probability gamma distribution function with more flexibility in shape (Eq. (12)). In column-tests by Martinez et al. (2014) the maximum $CaCO_3$ was observed at a distance of 15-16 cm from inlet within a column of 0.5 m height ($z/L \approx 0.3$). In Martinez et al. (2014) model, the scaling parameters “a, d” were constrained as positive within a wide range of 10^{-2} to 10^2 for the various column tests. The shape factor “s,” depending on the shape of distribution, calls for an exponential distribution for $s = 1$ or a gamma distribution for $s > 1$. Although simulation results showed a good agreement with experimental results (*SD*=0.4%, *COV*=8.28%,) conceptualization of the model parameters is needed to justify the components of relationship based on physical concepts.

According to Bradford et al. (2003), straining is probable when the ratio of the colloid diameter to the median grain diameter was greater than 0.005. In MICP applications, the average size of *S. pasteurii* is 2.8 μm (Tobler et al. 2014). Considering the d_{50} for a silica sand as 0.49 mm and for an Ottawa 50-70 sand as 0.22 mm, the ratio would be larger than 0.005. In colloid attachment theory, straining near the injection source or interfaces makes some pores become dead-ends, and the number of dead-end pores decreases with increasing distance from inlet. As explained by Bradford et al. (2003), size exclusion and limited transverse dispersivity tend to keep

colloids within the larger pore network avoiding colloids trapped in smaller pores. Hence, straining is expected to be greatest at the column inlet and then decrease with farther distance from inlet.

The simulated model using colloid attachment theory showed straining is the most influential factor for maximum accumulation of bacteria and induced CaCO_3 within a given area. However, results from column and large-scale testing reviewed herein showed maximum concentration occurred at a distance farther from injection source; a normalized distance (z/L) of 0.1 to 0.35 from inlet. Straining initiated at distances 2 to 10 cm from injection source at column and large-scale tests. The results from the large-scale experiment per van Paassen (2009) showed much less CaCO_3 within 10 cm of injection point where the velocity during injection exceeded 40 cm/hr (0.011 cm/s) (Minto et al. 2019). High fluid velocity at inlet can displace soil grains, prevent the formation of dead-end pores or having bacteria trapped in tight channels between soil particles. Noted that some observations (Silliman et al. 1995, Bradford et al. 2006) suggest that flow reversals can unclog pores containing colloids and liberate particles retained by straining, as was also observed in experiments by Nafisi et al. (2020). Figure 7 indicates maximum CaCO_3 measured at $z/L=0.2$. The straining term in Eq. (13) introduced by Bradford et al. (2003), was modified in this study using a c_{str} coefficient as defined in Eq. (16). The sensitivity analyses using optimization tool with a varied z/L within a range of 0.1-0.35 showed restricting straining at $z/L>0.14$ using c_{str} coefficient can yield the most fitted results for all simulated experiments in this work. Note that an optimization process is needed to match the location of maximum measured and simulated biomass and CaCO_3 contents using combination of all bacteria attachment, chemical transport and reaction processes as well as soil properties modifications. In addition, assigning the c_{str} parameter leads to distribution of biomass with steeper slope within depth and the better fit of the model results with the CaCO_3 experimental data. According to Figure 7(d), if c_{str} is not applied (i.e. $c_{str}=1$), statistical parameters of SD and COV will be 0.5%, and 10.2%, respectively, compared to SD and COV of 0.23%, and 4.79% using c_{str} as presented in Eq. (16).

4.5.2. Large-scale MICP Experiment

Spatial Distribution of Attached Biomass

The parameters for five attachment theories were calibrated for a large scale-test conducted by Montoya et al. (2021) as shown in Table 3. Figure 8(a) shows the results from using the c_{str} based on the colloid attachment theory (as presented in Eq. 16) and Figure 8(b) shows results for the constant rate model.

Figures 9(a) and 9(b) shows comparison between measured and calculated CaCO₃ content using the c_{str} based on the colloid attachment theory and constant rate model. To simulate the large-scale test, the domain was subdivided into two regions A (0-4D) representing the area in vicinity of injection source and region B (4-18D) (Figures 4(a) and 9(a)). D is the diameter of injection pile. Different calibrated parameters were obtained for regions A and B as shown in Table 3. To calibrate the models' parameters, each parameter was maintained constant while the other parameters varied within a pre-assumed range based on column tests results. The optimization tool in COMSOL was used for this calibration. Since there is wide range for all parameters of colloid theory, a MATLAB code was developed to optimize the model parameters comparing attachment rates with the ones from the model that used gamma distribution function and yielded well matched results.

The statistical parameters were indicated in Table 4. To better understand the process, each approach was assigned to one of regions A or B at a time, and parameters were calibrated for different combined models as shown in Tables 3 and 4. The results show improvement in SD by 21-53% and R^2 by 29-59% when using the c_{str} based on the colloid attachment theory compared to traditional constant attachment rate. Simulated model with gamma distribution function can improve SD by 13-32% and R^2 by 19-41%.

Large-scale test conducted by Montoya et al. (2021) has the same protocol as column test by Do et al. (2019). A question arises here as to how calibrated parameters in small-scale tests can be extended to a large-scale test. In large-scale test, specific ureolysis rate (K_u) was assigned as 2×10^{-6} mol/l.s.OD according to the calibrated parameters for column test.

Using gamma distribution function for region A, the function parameters were found based on column testing results.

$$d_1 = \frac{z_1 \times d_2}{z_2} = \frac{0.8 \times 0.1}{0.07} = 1.14, s_1 = s_2 = 1.5, a_1 = \frac{L_1 \times a_2}{L_2} = \frac{0.2 \times 0.24}{0.14} = 0.34 \approx 0.4 \quad (17)$$

where d_1 , s_1 , a_1 are gamma distribution t parameters for region A, z_1 is the elevation of center from bottom, and L_1 is the total height of region A. d_2 , s_2 , a_2 , z_2 , and L_2 are the corresponding parameters for column test (Table 3).

For region B, the same logic was followed, d was obtained using the correlation as above, but different values were calibrated for s and a (Table 3). The “ a ” value was 6 times higher than the value calculated by the mentioned approach (Eq. (17)).

In colloid theory model, the calibrated parameters were compared in Table 5. The results for horizontal trough are expanded in the next section. U_u and U_l in velocity-dependent terms of Eq. (13), (14) was the same for small- and large-scale tests. The attachment coefficient in velocity-dependent term (K_{att}) was calibrated within the same range as 7×10^{-5} and $4-6 \times 10^{-5}$ 1/s for column and large-scale tests, respectively. In straining term, β values were determined to be the same for small and large scale test, however, there is a significant difference in K_{str} by one order of magnitude between column and large-scale test. Table 5 compares calibrated parameters with ones per Bradford et al. (2003). In the study by Bradford et al. (2003), K_{str} was reported within a range by one magnitude difference based on colloid, and soil grain size, however, all the experiments were conducted in small column tests. The calibrated parameters herein show good agreement with the ones per Bradford et al. (2003), however, the straining has higher effects in large-scale test compared to small-scale experiment.

Higher introduced mass of bacteria in large-scale test can increase the potential of straining; The mass was introduced into the large-scale test with input flow rates 3 to 10 cm^3/s at 3 h for 6 times, whereas the mass was injected into column test with a flow rate of 0.167 cm^3/s at less than 1 h for one time at the beginning of the experiment. It is noted that the concentration is the same for column and large-scale tests (1 OD). Even though input flow rate in large-scale is higher than small-scale, the seepage velocity within large-scale body is lower particularly at the levels below injection source (region B).

On the other hand, it was also shown that hydrodynamic shearing forces could slowly funnel particles' path to the small pores at grain contacts and mobilize them in these locations. This could generate nonmonotonic attached bacteria profiles rather than hyperexponential so that exhibits a peak at some distance downgradient from the source (Cushing and Lawler 1998, Bradford et al. 2006). Nonmonotonic deposition profiles due to straining could be a function of pore water velocity (Tong et al. 2005, Bradford et al. 2006). Straining was predicted to increase with reducing approach velocity as a result of the lessened fluid drag force that acts on colloids in pores (Compere et al. 2001, Li et al. 2005, El Mountassir et al. 2014). Tobler et al. (2014) reported that colloid attachment theory that neglects straining failed to simulate breakthrough curves at various flow rates. An increase in *S. pasteurii* recovery (decrease in attachment) was observed with an increase in flow rate from 1 to 3 ml/min (6.7×10^{-3} and 2×10^{-2} cm/s, respectively) with 1 OD bacteria per Tobler et al. (2014) that was attributed to straining effects. Measurement and

simulation in column test herein showed seepage velocity of about 9.1×10^{-3} cm/s. Whereas, the simulation of large-scale test showed the seepage velocity was decreased from about 6.8×10^{-3} to 1.8×10^{-3} cm/s at the location of highest precipitation within region B during treatment. The precipitation in small-scale did not have considerable effects on the velocity within whole depth during treatment schedule, however, average seepage velocity at region B was 2×10^{-3} cm/s and 8×10^{-4} cm/s at first and last injection cycle, respectively. Porosity decreased from 0.44 to 0.35 in region B of large-scale test. The average seepage velocity at region A was calculated as 8×10^{-3} and 3×10^{-3} cm/s at first and last injection cycle, respectively. The seepage velocity exceeds 0.05 cm/s near injection source. Precipitation reduced seepage velocity and drag forces on bacteria entrapped in small pores. At the location of peak CaCO_3 concentration, deposition morphology may also influence subsequent retention. Attached bacteria and precipitation in a pore constriction reduce the effective size of the pore and increase number of collisions in small pores, therefore increase subsequent straining at this location (Bradford et al. 2007). In large-scale test, the induced head differential is dissipated throughout the domain, which the zone near the injection source (region A) tends to discharge higher injection volume compared to the zone below the injection source (region B) due to the distance of the flow path (Holtz et al. 1981).

Mechanical filtration and straining are also known to be strong functions of the flow direction (Silliman 1995). The downgradient flow in three directions at large-scale test (region B) can increase straining process in contrast to the upward flow direction in column test.

Chemistry, ionic strength (salinity of bacterial suspension), and PH of injected bacteria solution could be important factors affecting straining (Bradford et al. 2006, Harkes et al. 2010), however, the bacteria incubation and inoculating was followed by the same methods in both column and large-scale tests in this study (Do et al. 2019, Montoya et al. 2021).

The higher amount of CaCO_3 at lower part of large-scale tests can also be attributed to buoyancy-driven flow induced by the density differences between the injected fluids (van Paassen et al. 2009b). Viscosity and density vary during different phases in the process. Montoya et al. (2021) pointed to injected chemical density as 1076.7 kg/m^3 . An updated fluid density adopted from the relationship suggested by van Wijngaarden et al. (2011) was incorporated into the model in a separate simulation (not shown here). While fluid density can affect the peak CaCO_3 but such observed distribution pattern and highly mobilized precipitation measured at the lower level of large-scale test (region B) was not concluded to be a result of density variation. On the other hand,

the drastically increased concentration of CaCO_3 near the inlet in trough test (results shown in next section) cannot be attributed to the effect of density variation since the flow is in horizontal direction, thus the effect of straining can be highlighted.

Wang et al. (2021) also showed very high bacterial density (5.2×10^8 cells/ml~ 3 OD) results in large amount of unstable crystals of CaCO_3 with low density that may be transported with flow and locally clog the soil flow paths and affect the homogeneity of MICP treatment but they did not observe such unstable crystals at bacterial density of 6.0×10^7 cells/ml as low as bacteria density in small and large-scale experiments investigated by Do et al. (2019) and Montoya et al. (2021) ($2-5 \times 10^7$ cells/ml). Thus cell transport of unstable crystals is unlikely to be the primary reason for high CaCO_3 concentration in large-scale tests in this study. However, once the extent of precipitation increases (the pore throat space decreases), depending on the relative size of the suspended/unstable crystals and the pore space, this effect (filtering) may also contribute (Valdés and Santamarina 2006, DeJong et al. 2010).

In addition, Al Qabany and Soga (2013) observed the use of a high chemical concentration solution (urea- CaCl_2) as 1 M resulted in larger precipitation crystals, inhomogeneity in cementation and localized clogging inside the samples. Such clogging was not observed at low concentrations of 0.25 M. Using 0.333 M urea-0.25 CaCl_2 at simulated experiments herein reduces the possibility of clogging due to larger crystals and strengthens the effect of bacteria straining.

Note that the higher effect of straining was observed in region B, at a downgradient distance from source location at region A. Higher velocity and displaced location of injection source in region A prevent bacteria to be entrapped in soil pores. Removing straining from region A or very small values of K_{str} as indicated in Table 3 can yield the most fitted results. Figures 10(a) and 10(b) show the attachment and straining coefficients as a function of size of bacteria (d_p), mean soil particle size (d_{50}), sample diameter/width (D), sample height (L), injected bacteria ($PV_{bact.}$), and soil pore volume (PV_{soil}). A linear correlation was predicted for attachment coefficient ($K_{att} U_z$) considering the results per Bradford et al. (2003), and the present study. A polynomial correlation was fitted for straining coefficient (K_{str}).

Post-treatment Hydraulic conductivity and porosity

Hydraulic conductivity was calculated in subareas after treatment and compared with local measured values. In the conducted large-scale test higher hydraulic conductivities were derived compared to the measured values specifically at the locations of peak CaCO_3 . At the locations of

maximum CaCO_3 , the normalized hydraulic conductivity was obtained as 33% (Figure 11(a)) compared to the minimum normalized hydraulic conductivity of 22% obtained from measurements at laboratory. It is noted that these simulations do not reflect the concentration of inoculated bacteria and biofilm. Figure 11(b) indicates the reduction in normalized porosity up to 77% at peak CaCO_3 concentrations. Zamani and Montoya (2016) showed in specimens of fine Nevada sand ($d_{50}=0.13$ mm) when shear wave velocity increases from 80 m/s before treatment to 531 m/s after cementation, the hydraulic conductivity decreases by 28% (normalized k_f/k_0 is 28%). In large-scale test by Montoya et al. (2021) used in the simulation of this study, an increased shear wave velocity from 80 to more than 650 m/s was reported. Al Qabany and Soga (2013) observed that the normalized hydraulic conductivity was reduced to 10% (for 0.25 M urea) and 30% (1 M urea) when the amount of calcium carbonate precipitation became 2-8% of the sample weight. While the model can appropriately predict the hydraulic conductivity reductions consistent with the past studies, there are some discrepancies between calculation and measurements. A sensitivity analysis in this study showed the discrepancies between calculated and measured hydraulic conductivity did not have significant impact on the distributed biomass and CaCO_3 , however further measurements are needed to make a more precise relationship for hydraulic conductivity modification than Eq. (6). Whiffin et al. (2007) suggested that the reduction of hydraulic conductivity would be probably more affected by the nature of the treatment (the flowing of fluids through the material) than by the cementation process.

Damkohler number (Da)

Damkohler number (Da) is a dimensionless ratio of the reaction rate to the transport rate. Reaction and transport rates of Ca^{2+} can be derived from the model results at any time. Da parameter was computed during the time for regions A and B. The variation of Da with normalized shortest distance from injection source at time of the last injection cycle is depicted in Figure 12 within logarithmic scale. The distance was normalized with respect to the injection pile diameter (D). At last injection cycle, the velocity across region A varies from $\sim 10^{-2}$ cm/s to $\sim 2 \times 10^{-5}$ cm/s, while in the region B the variation was as $\sim 10^{-3}$ cm/s to $\sim 10^{-5}$ cm/s. The calculated Da from simulation can be used to control cementation patterns. The numbers were consistent with Da values from measurements per Montoya et al. (2021). Da generally increases as the distance from the injection source increases showing increased reaction rate. The highest Da was calculated across region B near the pile where the highest CaCO_3 content was achieved. The lowest Da was

calculated as zero at the location of zero reaction rate at a greater distance from the injection pile. Noted the value as low as 10^{-5} on the vertical axis was used to show zero Da at logarithmic scale. Montoya et al. (2021) concluded Da beyond distance of $5D$ is zero at the location with very low reaction rate and cementation, despite that the Da resulted from simulation herein showed a fluctuation between zero (10^{-5}) and values larger than 40 at distances beyond $8D$. At distances farther from injection source ($>8D$), velocities decrease, thus the corresponding transport rates reduce to 10^{-7} mol/(m³.s) and the reaction rates decrease to a range within 0 at boundaries of the domain to 10^{-5} mol/(m³.s) at general body at middle distances farther from pile compared to the reaction rates at the locations near injection source that are higher than 10^{-3} mol/(m³.s). Da parameter is zero where reaction rate is zero and is high value where reaction rate is about 10^{-5} at distances larger than $8D$ (due to significantly reduced transport rate). The boundaries of the domain generally show zero reaction rates and cementation.

4.5.3. Meter-Scale Biocementation Test

The results for simulated horizontal trough test conducted by San Pablo et al. (2020), are shown in Figures 13, and 14. Table 5 indicates calibrated parameters for this test. K_u was calibrated within a range of $1-2 \times 10^{-6}$ mol/l.s.OD according to measured ureolysis rates reported in their work. The results showed high effects of straining in this large-scale test. K_{str} was calibrated within the range $8 \times 10^{-4}-2 \times 10^{-3}$ 1/s corresponding to different K_u , comparable with achieved results from simulated tests by Do et al. (2019), and Montoya et al. (2021). However, a low value was fitted for K_{att} indicating the attachment can be highly influenced by different soil types and protocols used in the experiment. For this simulation, the c_{str} based on the colloid attachment theory was the most efficient approach to imitate the results of experiment. The peak concentration due to straining was found at inlet within 20 cm near injection source. The c_{str} was introduced in colloid attachment model (Eq. (13), (16)) to modify the model within the depth. Since the experiment was conducted in a horizontal trough, c_{str} was not applied in the simulation of the test at first ($c_{str}=1$). However, as shown in Figure 14, a defined c_{str} in horizontal direction (replaced z with x) leads to lower CaCO₃ content near the outlet and slightly improved SD . Similar to vertical column test, assigning this parameter caused distribution of biomass with steeper slope in horizontal flow direction (Figure 14). It is noted that the concentration of inoculation is close to the previous column and large-scale tests simulated herein (9.4×10^7 cells/ml).

4.6. Conclusion

A reactive transport model was developed to explore MICP reactive transport process in laboratory columns and large-scale tests for upscaling and design of field deployment protocols. The sensitivity analyses showed the main factor governing distribution of CaCO_3 content is the spatially distributed attached biomass within subsurface. Five approaches for biomass distribution were calibrated in small-and large-scale tests; (a) constant rate,(b) non-linear power-law distribution function, (c) exponential distribution function, (d) gamma distribution function, and (e) the c_{str} based on the colloid attachment theory. Specific findings are highlighted below.

- Of these simulated methods, “the c_{str} based on the colloid attachment theory” with straining component showed the most promising approach to better capture attached biomass and CaCO_3 distribution in small- and large-scale tests. Colloid attachment model involves two terms; attachment (velocity dependence) and straining terms (depth/location dependence). The attachment in velocity-dependent term occurs at grain surfaces controlled by pore water velocity and forces that act on the colloids. Whereas straining occurs when colloid particles (bacteria) are trapped in small pore throats. The previous studies in MICP did not account for straining in the attachment model, thus their predicted attachment coefficients have been found to be underestimated specifically for field deployment.
- The calibrated parameters in this study were within the range of values estimated by the past studies for colloids with similar size to *Sporosarcina pasteurii* bacteria used in MICP (Bradford et al. 2003 for colloids sizes of 2, 3.2 μm). Employing the c_{str} based on the colloid attachment theory, SD and COV for CaCO_3 mass distribution were improved by 68% in column tests compared to the model that used constant attachment rate (traditional model). In the large-scale test the improvement was by 21-53% in SD , and 29-59% in R^2 .
- Straining is a key parameter. A new parameter c_{str} was introduced in straining term (Eq. (13)) to account for inaccessible soil pores for straining in porous media. The coefficient c_{str} restricts straining at distances larger than 0.14 x targeted depth (vertical depth ~ 1 m in this study). Introduction of this parameter yields distribution of biomass with steeper slope in flow direction and the most fitted CaCO_3 mass with experiments. The flow direction, flow rate, and seepage velocity can affect the straining magnitude.
- For large-scale field deployment, the velocity-dependent parameters (K_{att} , U_l , U_u) can be estimated from calibrated parameters in laboratory small-scale tests. The shape of bacteria

distribution in straining term (β) can be derived from laboratory tests as well, however, straining coefficient rate (K_{str}) is shown to be one order of magnitude higher in large-scale tests compared to column tests. Downgradient flow path in three-dimensional and lower seepage velocity can enhance the effect of straining.

- Employed gamma distribution function with 44% improvement in column tests gained better results compared to constant rate model and placed in the second rank after colloid attachment theory while exponential distribution function with 3.22% and non-linear power-law with no improvement did not provide sufficient satisfaction with measurements at laboratory. Simulated large-scale model with gamma distribution function can improve SD by 13-32% and R^2 by 19-41%. However, the difficulty of parameter extrapolation from small-scale calibration to large scale makes challengeable the future prediction of this model in field implementation.

More experiments and simulations are needed to narrow down the range of straining coefficient rates for large-scale tests. Additionally, the model can yield valid post-treatment hydraulic conductivities in small-scale tests, even though computed hydraulic conductivity from the large-scale simulation was slightly higher than measurements in locations with maximum CaCO_3 . Further experimentally measurements are needed to improve the accuracy of model predictions for hydraulic conductivities.

Table 4.1 Comparison between the different biomass distribution approaches from literature and modified relationship used in this study.

Relationship function	The original relationship	References	The parameters	The proposed relationship in this study
Constant rate	$\frac{\partial S_{at}}{\partial t} = K_{at}\theta S_{Su}$	van Wijngaarden et al. (2012)	$K_{at}=K_{atl}$ is a constant. (decay and encapsulation are included as well.)	$\frac{\partial S_{at}}{\partial t} = K_{at}\theta S_{Su}$ $K_{at}=K_{atl}$
Power-law	$\rho_f \frac{\partial \phi_f}{\partial t} = k_a \phi S_w C_w^B$ $Z_{ub} = k_{ub} (\rho_f \phi_f)^{n_{ub}}$ $k_a = c_{a,1} \cdot \phi_f + c_{a,2}$	Ebigbo et al. (2012)	k_a : Attachment coefficient, ρ_f : Biofilm (bacteria) density, ϕ_f : Volume fraction of biofilm, ϕ : Porosity, C_w^B : Concentration of suspended biomass	$ZH = K_{ZH} (S_{at})^{n_{ZH}}$ $K_{at} = K_{at1} * (c_{a,1} \cdot S_{at} + c_{a,2})$
Exponential	$ZH_t(z) = c_1 e^{-c_2 z}$	Barkouki et al. (2011)	ZH_t : Total moles of the urease basis component	$K_{at} = K_{at1} c_1 e^{-c_2 z}$
Gamma Dist.	$ZH_t(z) = a z^{s-1} \frac{e^{-z/d}}{d^s \Gamma(s)}$	Martinez et al. (2014)	ZH_t : Total moles of the urease basis component	$K_{at} = K_{at1} a z^{s-1} \frac{e^{-z/d}}{d^s \Gamma(s)}$
The c_{str} based on colloid attachment theory	$K_a = k_{att} \Psi_{att} + k_{str} \Psi_{str}$ $k_{att} = \frac{3(1 - \theta_w)}{2 d_{50}} \eta \alpha v_w$ $\Psi_{str} = \left(\frac{d_{50} + z}{d_{50}}\right)^{-\beta}$	Bradford et al. (2003)	Ψ_{att} : Dimensionless colloid attachment function (1 for clean-bed conditions), η : Collector efficiency (defined by 6 dimensionless parameters), α : colloid sticking efficiency, Ψ_{str} : Dimensionless colloid straining function	$K_{at} = K_{att} U_z + K_{str} c_{str} y_{str}$ $U_z = \begin{cases} 1 & U < U_l \\ 1 - \frac{U - U_l}{U_u - U_l} & U_l \leq U \leq U_u \\ 0 & U > U_u \end{cases}$
	$K_a = K_{attach} U_{attach} + K_{str}$ $U_{attach} = \begin{cases} 1 & U < U_l \\ 1 - \frac{U - U_l}{U_u - U_l} & U_l \leq U \leq U_u \\ 0 & U > U_u \end{cases}$	Minto et al. (2019)	U_{attach} : Velocity dependence and K_{str} : Straining rate constant	$y_{str} = \left(\frac{d_{50} + r}{d_{50}}\right)^{-\beta}$ $c_{str} = \begin{cases} 0 & \frac{z}{L} < 0.14 \\ 1 - \frac{\frac{z}{L} - 0.14}{1 - 0.14} & 0.14 \leq \frac{z}{L} \leq 1 \end{cases}$

Table 4.2 Comparison between use of various bacteria attachment approaches using 1-D column test (experimental measurements per Do et al. 2019): calibrated and statistical parameters; mean CaCO₃, normalized hydraulic conductivity with initial one, and normalized attached biomass with initial injected bacteria.

Attached Biomass Distribution type	K _{att} (1/s)	Attached biomass distribution parameters				Mean normalized attached biomass with respect to injected biomass (%)	Mean normalized hydraulic conductivity with respect to initial hydraulic conductivity (%)	Mean CaCO ₃ (%)	SD (%) of simulated from measured CaCO ₃	COV (%) of simulated from measured CaCO ₃	Mean Bias compared to measured CaCO ₃	Improvement compared to the approach with constant rate (%)
Constant rate (K _{att})	1x10 ⁻⁴	-	-	-	-	51.40	76.20	4.83	0.71	14.70	0.99	
Nonlinear Power-Law distribution function	1x10 ⁻⁴	K _{ZH}	n _{ZH}	c _{a,1}	c _{a,2}							
		0.0315	1.5	1x10 ⁻⁴	9x10 ⁻¹	50.30	76.02	4.85	0.78	16.08	0.99	-9.41
Exponential distribution function	1x10 ⁻⁴	c ₁	c ₂	-	-							
		1.25	-0.03			51.39	76.05	4.85	0.69	14.23	1	3.22
Gamma distribution function	1x10 ⁻⁴	a	s	d	-							
		0.24	1.5	0.1		50.5	76.5	4.83	0.4	8.28	0.99	43.66
the c _{str} based on the colloid attachment theory	-	K _{att} (1/s)	K _{str} (1/s)	β	U _{it} -U _l (m/s)							
		7x10 ⁻⁵	6.5x10 ⁻⁴	0.4	1x10 ⁻⁴ 1x10 ⁻⁵	51.02	75.84	4.80	0.23	4.79	0.99	67.61

Table 4.3 Simulated large-scale test; comparison between calibrated parameters for different bacteria attachment approaches.

Model	Section	Dist. Func.	K_{att} (1/s)	Nonlinear Power Law				Exponential		Gamma			The c_{str} based on the colloid attachment theory				
				K_{ZH}	n_{ZH}	$c_{a,1}$	$c_{a,2}$	c_1	c_2	a	s	d	K_{att} (1/s)	K_{str} (1/s)	β	U_U (m/s)	U_L (m/s)
1	A	Constant rate	1.0×10^{-4}														
	B	Constant rate	1.0×10^{-4}														
2	A	Power Law	1.0×10^{-4}	0.03	1.50	1.0×10^{-4}	9.0×10^{-1}										
	B	Power Law	1.0×10^{-4}	0.05	1.50	1.0×10^{-4}	9.0×10^{-1}										
3	A	Constant rate	1.0×10^{-4}														
	B	Power Law	1.0×10^{-4}	0.05	1.50	1.0×10^{-4}	9.0×10^{-1}										
4	A	Power Law	1.0×10^{-4}	0.03	1.50	1.0×10^{-4}	9.0×10^{-1}										
	B	Constant rate	1.0×10^{-4}														
5	A	Exponential	1.0×10^{-4}					0.80	0.263								
	B	Exponential	1.0×10^{-4}					5.00	0.60								
6	A	Exponential	1.0×10^{-4}					2.50	0.263								
	B	Exponential	1.0×10^{-4}					2.50	0.60								
7	A	Exponential	1.0×10^{-4}					2.50	0.47								
	B	Exponential	1.0×10^{-4}					2.50	0.47								
8	A	Constant rate	1.0×10^{-4}														
	B	Exponential	1.0×10^{-4}					5.00	0.60								
9	A	Exponential	1.0×10^{-4}					0.80	0.263								
	B	Constant rate	1.0×10^{-4}														
10	A	Gamma	1.0×10^{-4}							0.40	1.50	1.14					
	B	Gamma	1.0×10^{-4}							6.00	2.00	0.50					
11	A	Gamma	1.0×10^{-4}							3.00	2.00	1.14					
	B	Gamma	1.0×10^{-4}							3.00	2.00	0.50					
12	A	Gamma	1.0×10^{-4}							3.00	1.75	1.14					

Model	Section	Dist. Func.	K_{att} (1/s)	Nonlinear Power Law				Exponential		Gamma			The c_{str} based on the colloid attachment theory				
				K_{ZH}	n_{ZH}	$c_{a,1}$	$c_{a,2}$	c_1	c_2	a	s	d	K_{att} (1/s)	K_{str} (1/s)	β	U_U (m/s)	U_L (m/s)
	B	Gamma	1.0×10^{-4}							3.00	1.75	0.50					
13	A	Constant rate	1.0×10^{-4}														
	B	Gamma	1.0×10^{-4}							6.00	2.00	0.50					
14	A	Gamma	1.0×10^{-4}							0.40	1.50	1.14					
	B	Constant rate	1.0×10^{-4}														
15	A	Colloid Theory											4.0×10^{-5}	$< 2.0 \times 10^{-4}$	0.4	1×10^{-4}	1×10^{-5}
	B	Colloid Theory											4.0×10^{-5}	5.0×10^{-3}	0.4	1×10^{-4}	1×10^{-5}
16	A	Colloid Theory											6.0×10^{-5}	$< 2.0 \times 10^{-4}$	0.4	1×10^{-4}	1×10^{-5}
	B	Colloid Theory											6.0×10^{-5}	5.0×10^{-3}	0.4	1×10^{-4}	1×10^{-5}
17	A	Constant rate	1.0×10^{-4}														
	B	Colloid Theory											4.0×10^{-5}	5.0×10^{-3}	0.4	1×10^{-4}	1×10^{-5}
18	A	Colloid Theory											4.0×10^{-5}	$< 2.0 \times 10^{-4}$	0.4	1×10^{-4}	1×10^{-5}
	B	Constant rate	1.0×10^{-4}														
1(Subarea)	A	Constant rate	1.0×10^{-4}														
	B	Constant rate	1.0×10^{-4}														
2(Subarea)	A	Colloid Theory											4.0×10^{-5}	$< 2.0 \times 10^{-4}$	0.4	1×10^{-4}	1×10^{-5}
	B	Colloid Theory											4.0×10^{-5}	5.0×10^{-3}	0.4	1×10^{-4}	1×10^{-5}

Table 4.4 Simulated large-scale test; comparison between different bacteria attachment approaches, mean CaCO₃ (%), and statistical parameters for each approach.

Model	Section	Biomass Distribution approach	Mean (%)	SD (%)	COV (%)	R ² (%)	Improved SD (%)	Improved R ² (%)
1	A	Constant rate	2.53	3.06	120.70	0.24		
	B	Constant rate						
2	A	Power Law	2.90	2.01	69.24	0.67	34	43
	B	Power Law						
3	A	Constant rate	3.11	2.26	72.82	0.58	26	34
	B	Power Law						
4	A	Power Law	2.30	2.83	122.98	0.35	8	11
	B	Constant rate						
5	A	Exponential	3.04	2.06	67.59	0.64	33	40
	B	Exponential						
6	A	Exponential	3.31	3.68	111.21	0.00	-20	-24
	B	Exponential						
7	A	Exponential	3.21	3.36	104.71	0.09	-10	-15
	B	Exponential						
8	A	Constant rate	3.22	2.34	72.84	0.56	24	32
	B	Exponential						
9	A	Exponential	2.33	2.78	119.40	0.37	9	13
	B	Constant rate						
10	A	Gamma	3.20	2.07	64.83	0.65	32	41
	B	Gamma						
11	A	Gamma	2.86	2.45	85.60	0.51	20	27
	B	Gamma						
12	A	Gamma	2.99	2.59	86.66	0.46	15	22
	B	Gamma						
13	A	Constant rate	3.40	2.38	69.95	0.54	22	30
	B	Gamma						
14	A	Gamma	2.23	2.66	119.33	0.43	13	19
	B	Constant rate						
15	A	Colloid theory	2.93	1.43	48.81	0.83	53	59
	B	Colloid theory						
16	A	Colloid theory	3.02	1.52	50.33	0.81	50	57
	B	Colloid theory						
17	A	Constant rate	3.30	2.10	63.64	0.63	31	39
	B	Colloid theory						
18	A	Colloid theory	2.55	2.41	94.51	0.53	21	29
	B	Constant rate						
1 (Subarea)	A	Constant rate	1.81	1.67	92.27	0.44		
	B	Constant rate						
2 (Subarea)	A	Colloid theory	2.10	1.10	52.38	0.76	34	32
	B	Colloid theory						

Table 4.5 Calibrated parameters for small- and large-scale tests modeled with the c_{str} based on the colloid attachment theory compared to the calibrated parameters by Bradford et al. (2003) for different soil grain sizes ($d_{50}=0.15, 0.24, 0.36, 0.74$ mm) and colloids' size ($d_p=2, 3.2$ μm). Average size for *S. pasteurii* used in MICP (d_p) is 2.8 μm .

	Small-scale Column test	Large-scale test	Large-scale Horizontal trough	Bradford et al. (2003)			
d_{50} (mm)	0.49	0.49	1	0.15	0.24	0.36	0.74
K_{att} (1/s)	7.0×10^{-5}	(4.0- 6.0) $\times 10^{-5}$	1.0×10^{-6}	(1.1-1.28) $\times 10^{-4}$	(2.5-3.3) $\times 10^{-5}$	(5-7) $\times 10^{-5}$	(4-7) $\times 10^{-5}$
K_{str} (1/s)	6.5×10^{-4}	5.0×10^{-3}	8.0×10^{-4} - 2.0×10^{-3}	6.1×10^{-3} - 1.9×10^{-2}	5.1×10^{-3} - 1.9×10^{-2}	1.6×10^{-3} - 1.4×10^{-2}	5.0×10^{-4} - 2.1×10^{-3}
β	0.4	0.4	0.75	(0.34-0.58)	(0.43-0.6)	(0.23-0.78)	(0.18-0.43)
U_u (m/s)	1×10^{-4}	1×10^{-4}	1×10^{-4}	-	-	-	-
U_l (m/s)	1×10^{-5}	1×10^{-5}	1×10^{-5}	-	-	-	-

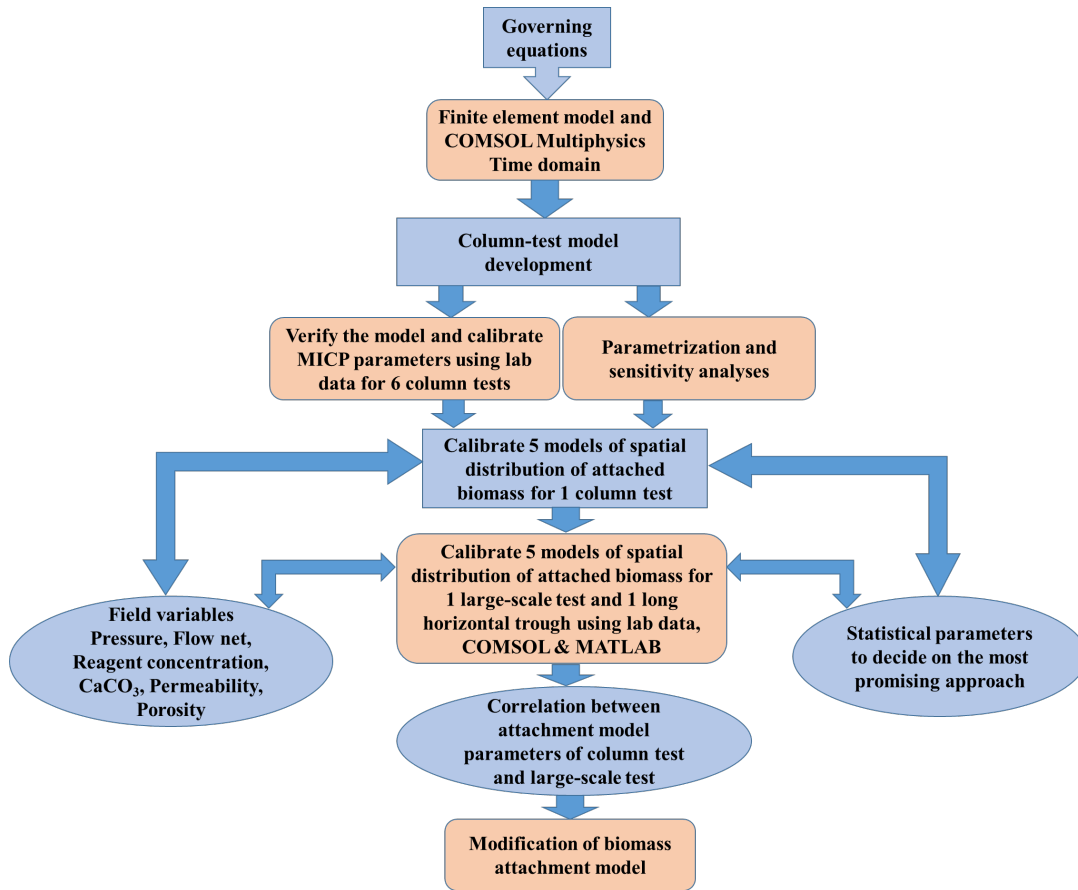


Figure 4.1 Flowchart of model development and analyses in this study.

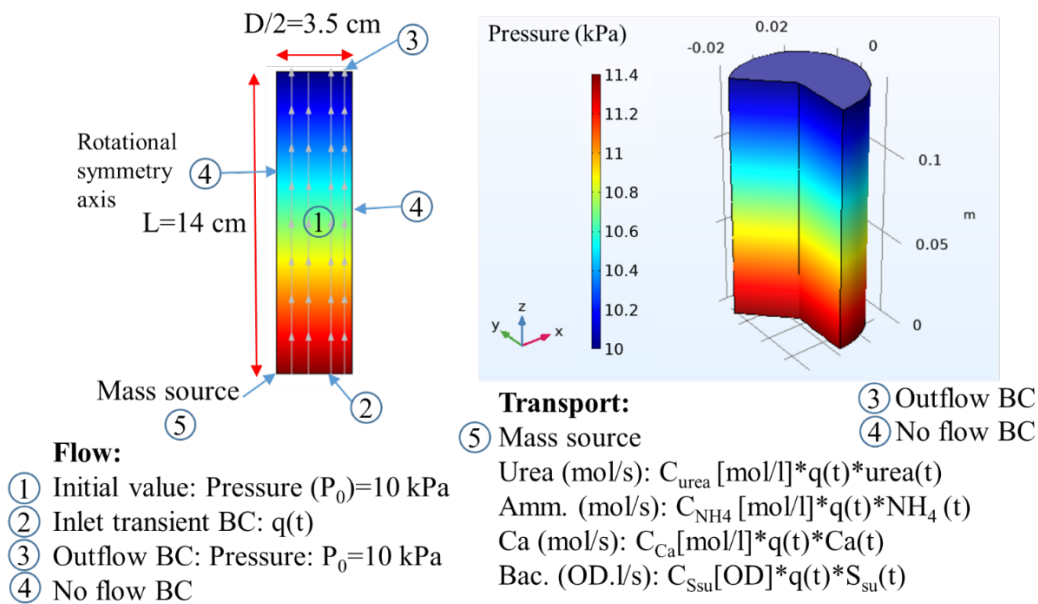
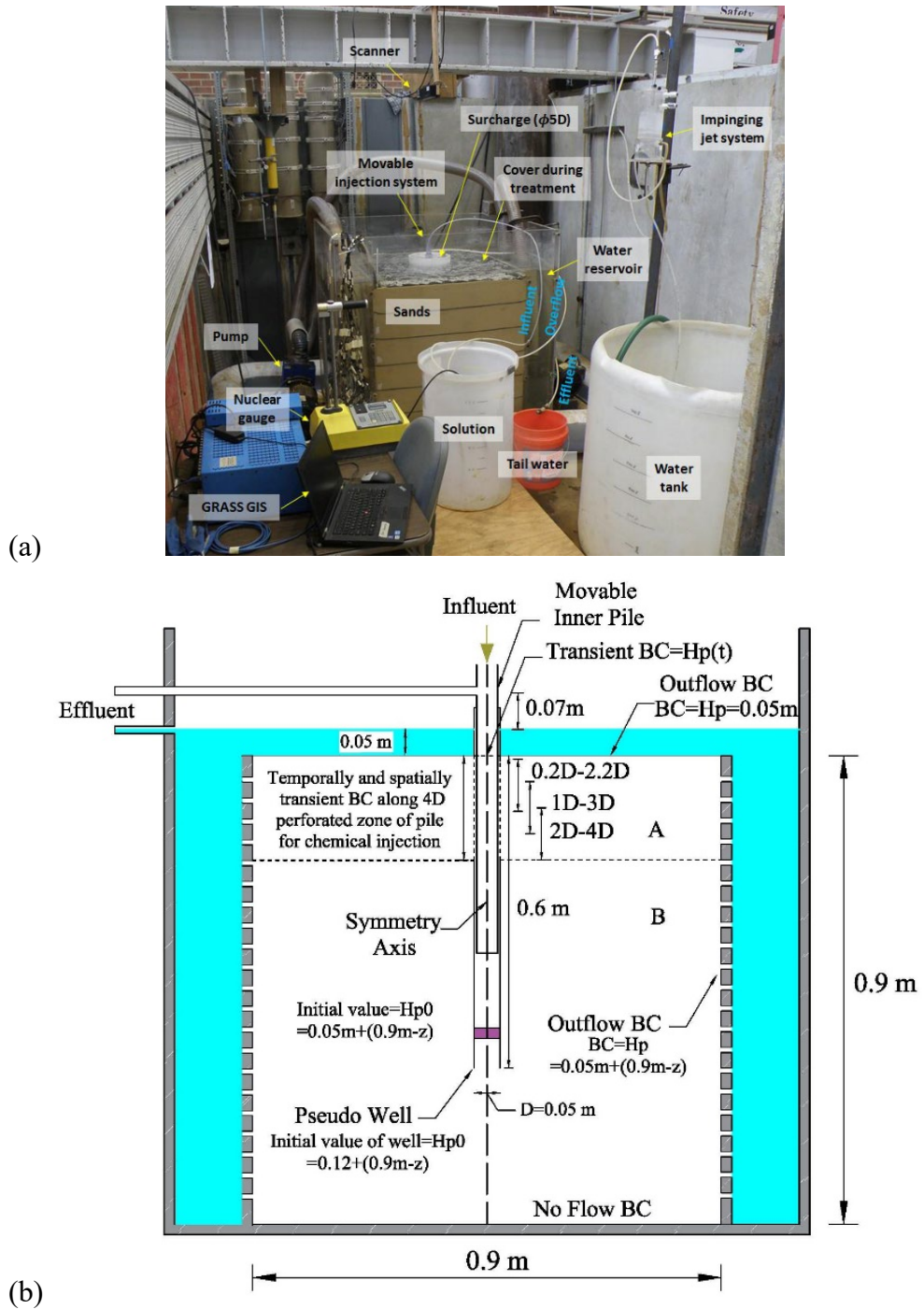


Figure 4.2 Initial and boundary conditions in simulated small-scale column test.



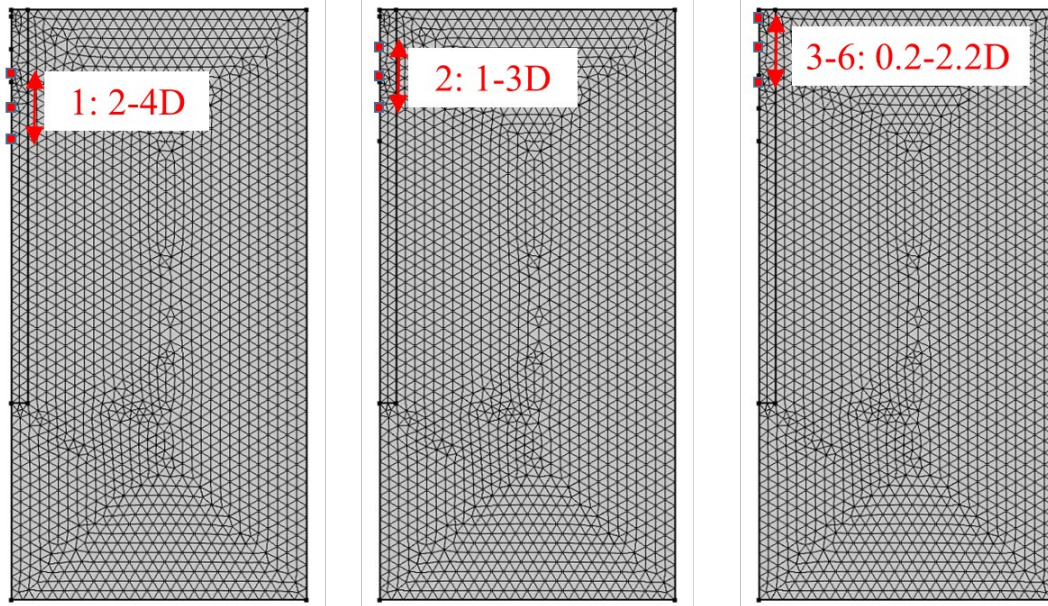
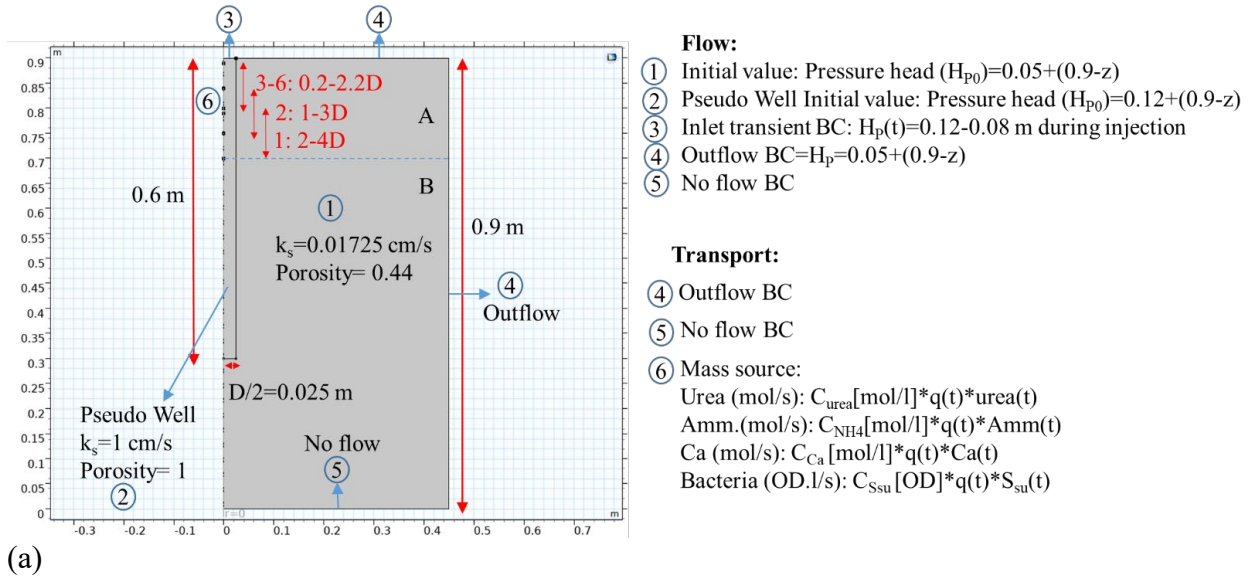
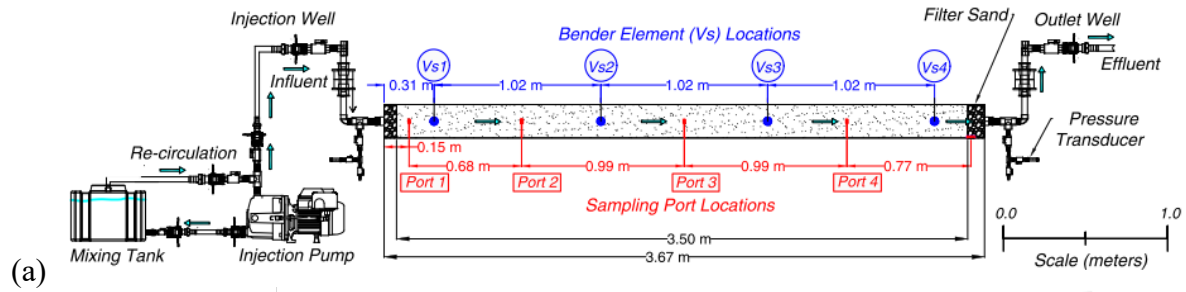
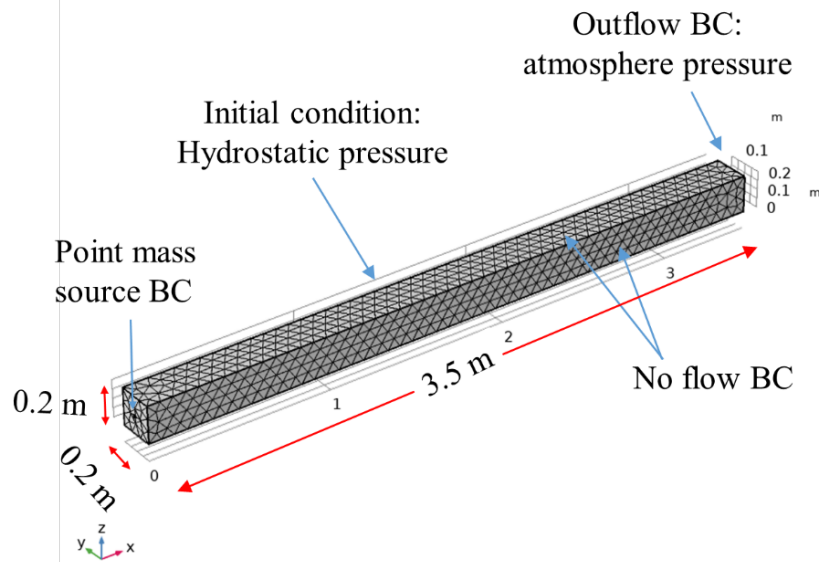


Figure 4.4 Model development of large-scale soil box, (a) initial and boundary conditions (b) discretized model domain, and the location of injection source during experiments.



(a)



(b)

Figure 4.5 (a) Horizontal long trough (San Pablo et al. 2020) (b) discretized Model domain, initial and boundary conditions.

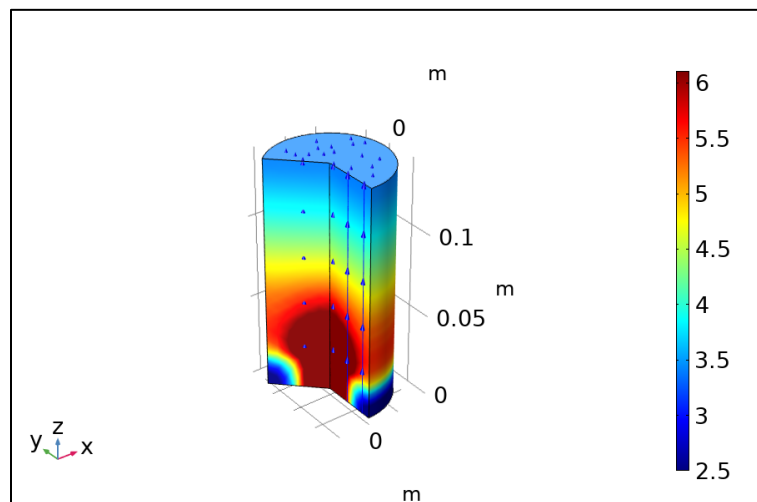


Figure 4.6 Mass of CaCO_3 with the c_{str} based on the colloid attachment theory in simulated column test.

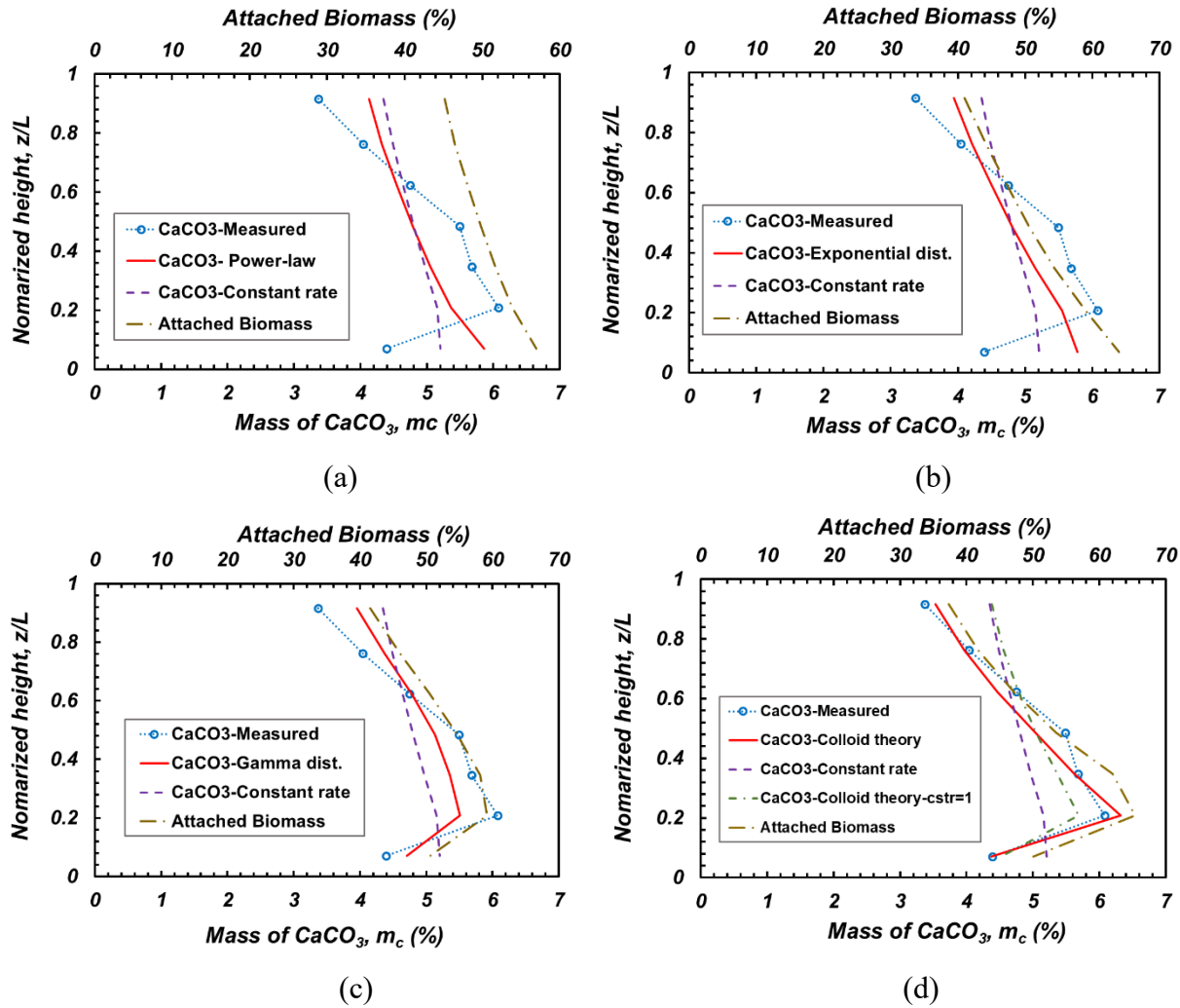


Figure 4.7 Simulated 1-D column test (experimental measured CaCO_3 per Do et al. 2019); CaCO_3 content and attached biomass within depth resulted from different bacteria attachment functions compared to constant rate (a) Nonlinear power-law distribution function, (b) Exponential distribution function, (c) Gamma distribution function, (d) the c_{str} based on the colloid attachment theory (the graph labeled with $c_{str}=1$ shows the results when this coefficient is not applied).

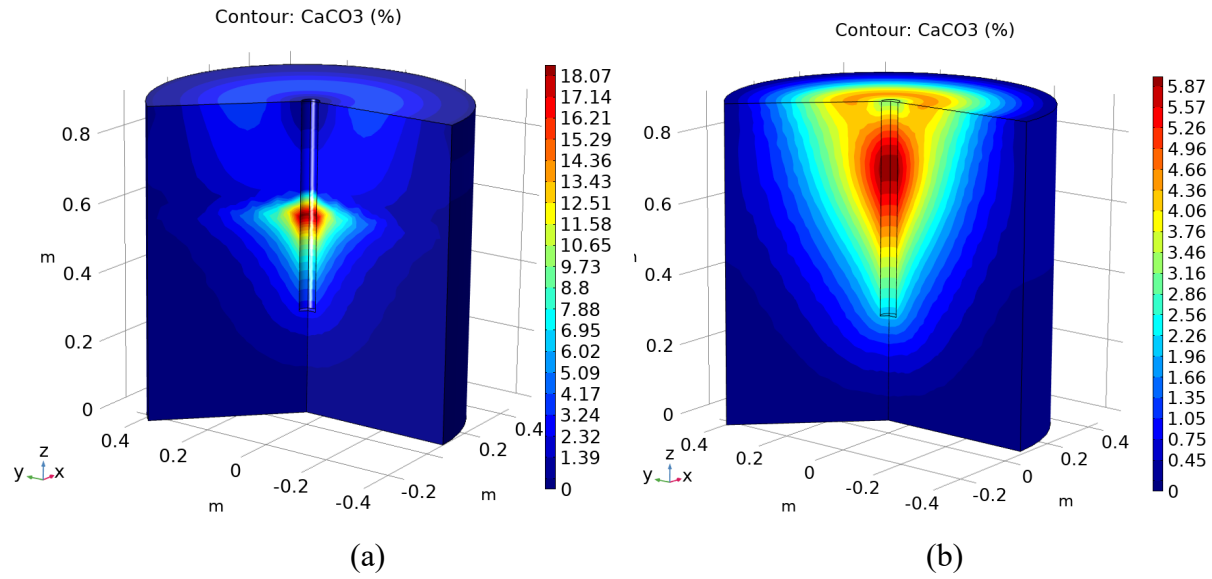
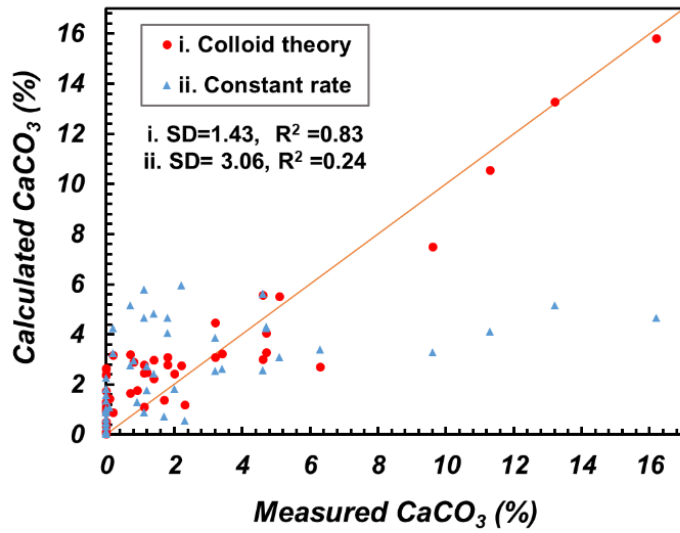
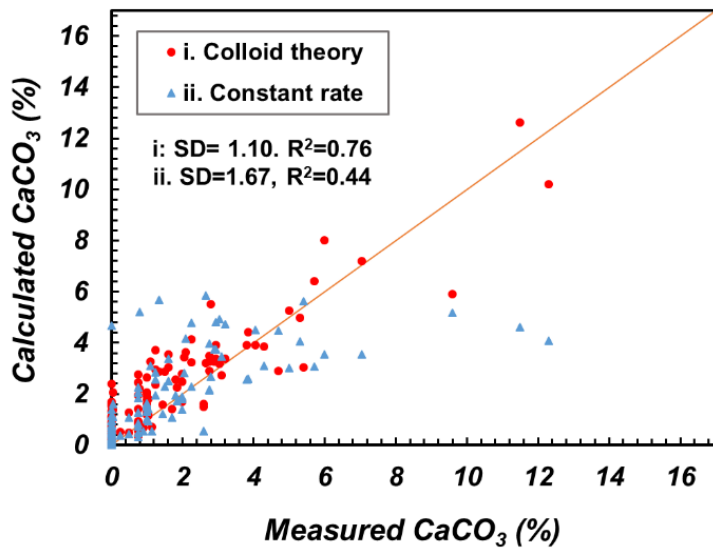
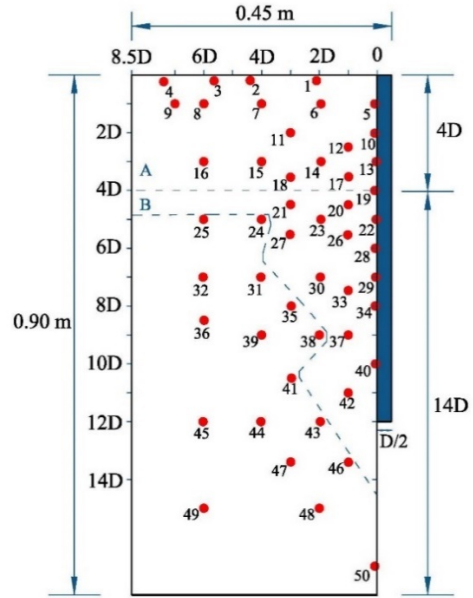


Figure 4.8 Simulated Large-scale test (a) mass of CaCO_3 (%) using the c_{str} based on the colloid attachment theory, (b) mass of CaCO_3 (%) using constant rate.



(a)



(b)

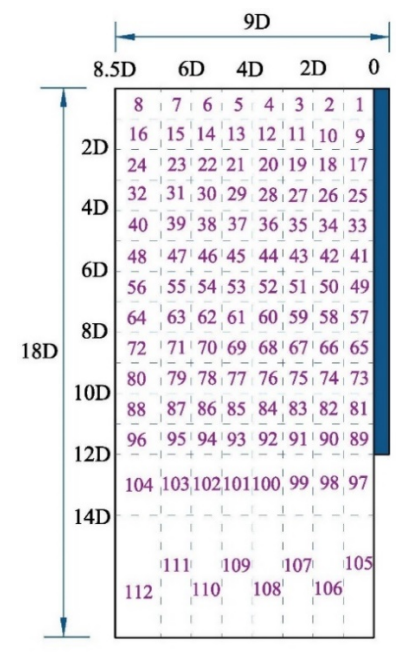
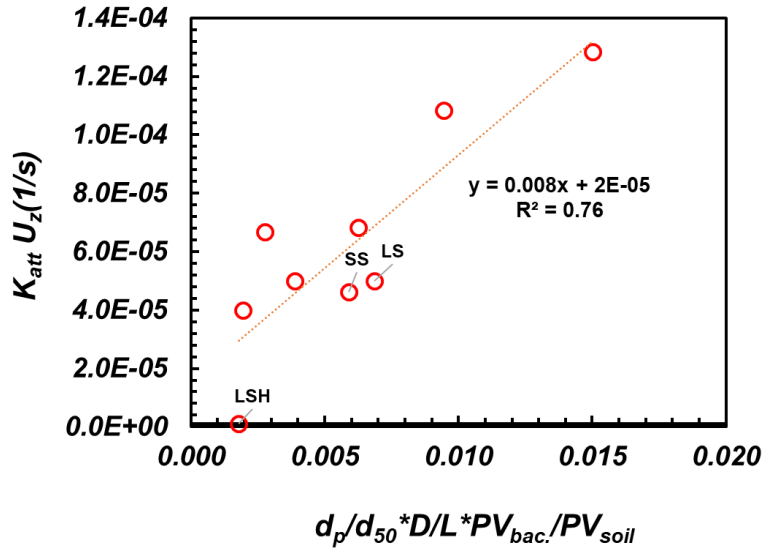
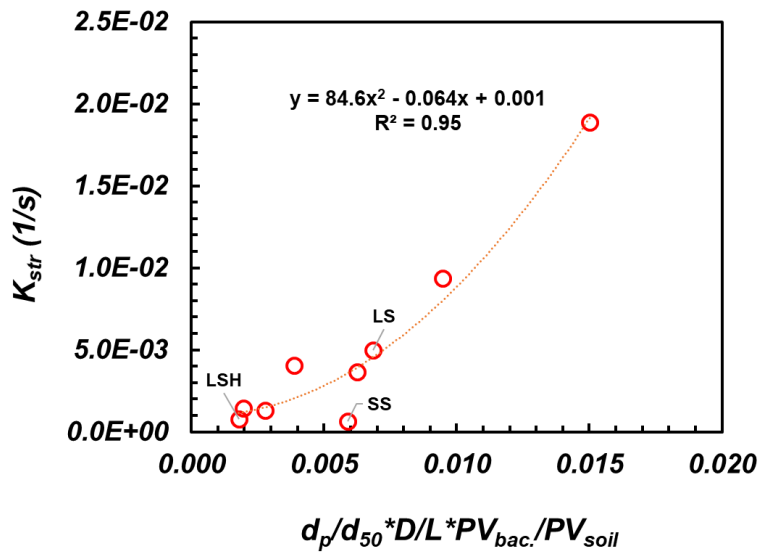


Figure 4.9 Simulated large-scale test (experimental measurements per Montoya et al. 2021); comparison between measured and calculated CaCO_3 content using the c_{str} based on the colloid attachment theory and constant rate, (a) mass of CaCO_3 (%) at nodal locations, (b) averaged mass of CaCO_3 (%) at subareas.



(a)



(b)

Figure 4.10 A plot of fitted attachment and straining coefficients as a function of size of bacteria (d_p), mean soil particle size (d_{50}), sample diameter/width (D), sample height (L), injected bacteria ($PV_{bac.}$), and soil pore volume (PV_{soil}), a) $K_{att} U_z$, b) K_{str} .

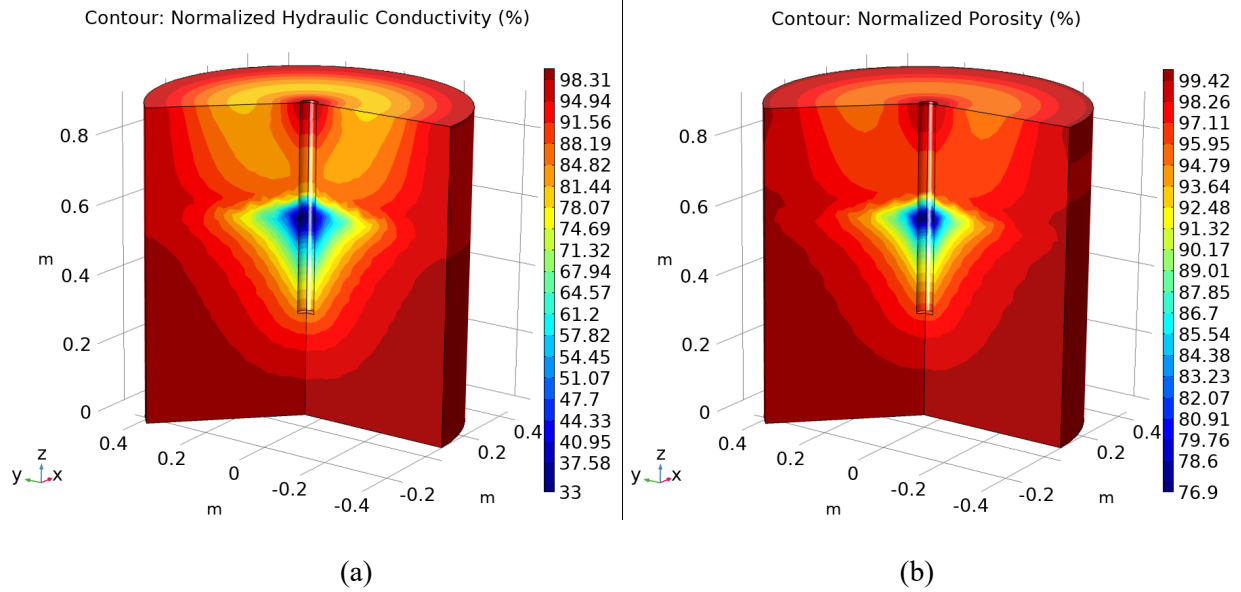


Figure 4.11 Simulated Large-scale test (experimental measurements per Montoya et al. 2021) using the c_{str} based on the colloid attachment theory (a) normalized hydraulic conductivity (%) with respect to initial hydraulic conductivity, (b) normalized porosity (%) with respect to initial porosity.

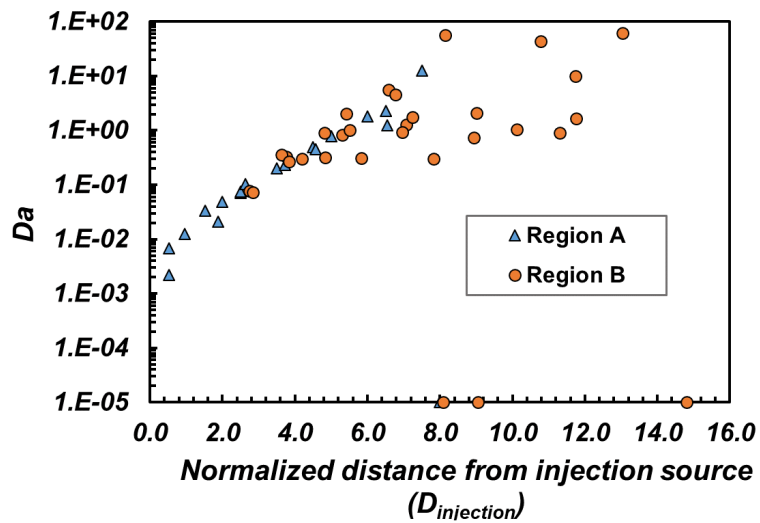


Figure 4.12 Simulated large-scale test; Da number with distance from injection source.

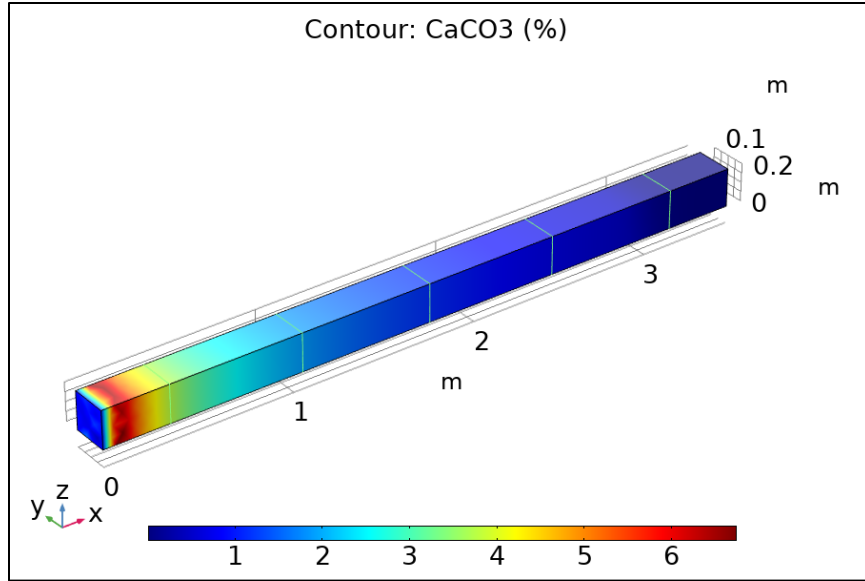


Figure 4.13 Simulated horizontal trough test using colloid attachment theory, mass of CaCO_3 (%), $K_u = 1 \times 10^{-6} \text{ mol/l.s.OD}$, $K_{att} = 1 \times 10^{-6} \text{ 1/s}$, $\beta = 0.75$, $K_{str} = 2 \times 10^{-3} \text{ 1/s}$.

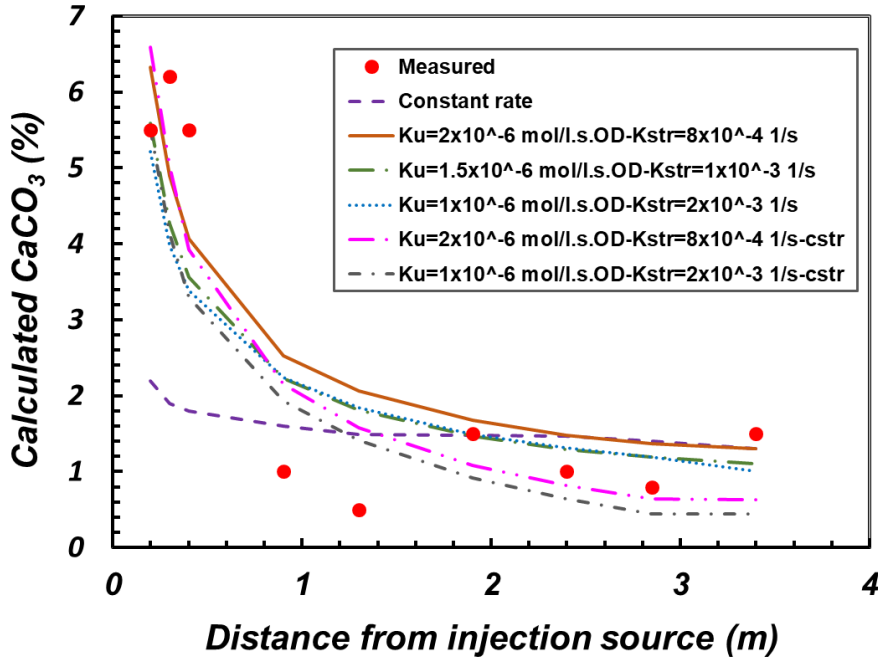


Figure 4.14 Simulated horizontal trough test, CaCO_3 content along horizontal trough resulted from the c_{str} based on the colloid attachment theory compared to constant rate. In all colloid theory models $K_{att} = 1 \times 10^{-6} \text{ 1/s}$ and $\beta = 0.75$. In constant rate model $K_{at} = 3 \times 10^{-6} \text{ 1/s}$. The c_{str} coefficient was defined in horizontal direction for the graph labeled with c_{str} as Eq. (16).

CHAPTER 5. Development of a Reactive Transport Model for Microbial Induced Calcium Carbonate Precipitation in Unsaturated Conditions

Abstract

Microbial induced calcium carbonate precipitation (MICP) offers a sustainable biological technique to improve geologic properties of onshore and offshore subsurface areas of engineering structures. The applications involve soil strength, scour mitigation, concrete/rock fracture sealing, contaminant immobilization, and permeability controls. Previous studies have discussed fundamental processes during MICP and implementation in lab- and field-scale. However, most of these studies were examined in saturated conditions despite many MICP applications of engineering soil embankments and slopes on coastal and riverside areas in unsaturated conditions. The purpose of this study is to develop a reactive transport model framework that captures key physicochemical and biological processes of MICP in unsaturated soils. Using COMSOL multiphysics and numerical analyses, a continuum 3D scale model was developed to couple unsaturated flow and transport with biological and chemical reactions in variably saturated conditions. The paper compares mass percentage of calcium carbonate at various degrees of saturation 20, 40, 80 with fully saturated condition in sandy soil media. The results indicate the bacteria attachment coefficient (K_{at}) increases about 3 times by lowering the degree of saturation from 100% to 20%. The higher negative pressure and suction at lower saturation degrees may improve bacteria fixation within the pores and reduce the possibility of detachment.

Keywords: COMSOL Multiphysics, Microbial induced calcium carbonate precipitation (MICP), Numerical analyses, Reactive transport model, Unsaturated soil.

5.1. Introduction

Microbial induced calcium carbonate precipitation (MICP) is a reactive chemical transport method with sustainably bioremediation and soil reinforcement applications. MICP method harnesses microbial metabolism and low-cost substrate to provide cohesive bonds of calcium carbonate (CaCO_3) between soil particles in bio-augmented and bio-stimulation pathways. Controlling the MICP process and predicting the resulting material properties at field-scale are essential in improving the engineering properties of porous soil materials. However, the most previous studies have been done on fully saturated soils while the field-scale application of MICP is mostly governed by unsaturated conditions. Not much studies have been found on partially

saturated MICP whether in numerical or experimental efforts. Cheng et al. (2013) assessed the effect of degree of saturation on MICP process efficiency and treated soil strength. Their results verified the improved mechanical characteristics of bio-cemented partially saturated soils in terms of cohesion, friction angle, and unconfined compressive strength (UCS) compared to MICP at a fully saturated condition. Fewer calcite crystals produced similar soil strength at partially saturated soils compared to fully saturated (Cheng et al. 2013). In other words, treatment under low saturated conditions exhibited higher strength at similar CaCO_3 levels (Cheng and Cord-Ruwisch 2012) enabling bio-cemented soils to be produced more economically due to lower requirement of the microbes, urease enzyme, and substrate. Mathematical Models for predicting MICP processes in saturated soils have been developed by coupling reaction kinetics of chemical variants and fluid transport (Faeli et al. 2021). Several studies experimentally have assessed the soil-water characteristic and hydraulic behavior of artificially cemented sands using cement mixtures and vegetation (Yan and Zhang 2015; Cardoso 2017), however, the effects of MICP on unsaturated parameters is still unknown.

The objective of the work herein is to develop a reactive transport model to assess the MICP process in unsaturated conditions. The model has been calibrated to yield experimental measurements at 20%, 40%, 80%, and 100% saturation degrees done per Cheng et al. (2013). The simulation results describe the effects of saturation degrees and unsaturated parameters of retention model on attachment coefficient (K_{at}) and CaCO_3 precipitation of coarse sand materials. Additionally, the effects of drying and wetting branches of soil-water characteristic curves (SWCCs) have been compared. The changes in hydraulic conductivity, porosity and unsaturated parameters of treated medium have been assessed. The model framework can be extended and applied to similar situations of field trials and prompt comprehensive understanding of MICP reactive transport model in variably saturated conditions.

5.2. Model Development

5.2.1. Constitutive Model

The governing equations for unsaturated flow and transport are solved simultaneously using finite element method and COMSOL Multiphysics.

Richards' equation model describes the storage and retention models in variably saturated porous media.

$$\rho \left(\frac{c_m}{\rho g} + S_e S \right) \frac{\partial p}{\partial t} + \nabla \cdot \rho \left(-\frac{k_s}{\mu} k_r (\nabla p + \rho g \nabla z) \right) = Q_m \quad (1)$$

where C_m denotes specific moisture capacity (m^{-1}), S_e is the effective saturation of the soil (dimensionless), S is storage coefficient (m^{-1}), pressure p is the dependent variable (Pa) proportional to pressure head H_p , t is time (s), ρ is the fluid density (kg/m^3), k_s gives the hydraulic conductivity (m/s), μ is the fluid dynamic viscosity (Pa.s), k_r is the relative permeability, z is the direction of gravity (m), and Q_m is the fluid source (positive) or sink (negative).

The fluid velocity across the faces of an infinitesimally small surface is defined as follows.

$$u = -\frac{k_s}{\mu} k_r (\nabla p + \rho g \nabla z) \quad (2)$$

Nonlinearities arise due to variation of hydraulic properties θ , S_e , C_m , and k_r in unsaturated conditions, for example, negative pressures reach a pressure of zero or above saturation. The volume liquid fraction per porous medium volume, θ , ranges from a small residual value θ_r to the total porosity θ_s in a constitutive relation model. The effective saturation, S_e , is normalized θ with a maximum value of 1. The specific moisture capacity, C_m , is the slope θ versus pressure describes the change in θ as the simulation run progresses. The relative permeability, k_r , increases with moisture content to its maximum value at saturation, which shows that the fluid moves more readily when the porous media is fully saturated.

The van Genuchten retention model is used to define S_e , θ , C_m , and k_r . This model represents the saturation when the fluid pressure is atmospheric ($H_p = 0$) or a positive value. The analytical solution requires data for the saturated θ_s and residual θ_r liquid volume fractions as well as constants α , n , m , and l , which specify a particular medium type.

The retention model is expressed as:

$$\theta = \begin{cases} \theta_r + S_e (\theta_s - \theta_r) & H_p < 0 \\ \theta_s & H_p \geq 0 \end{cases}, S_e = \begin{cases} \frac{1}{[1 + |\alpha H_p|^n]^m} & H_p < 0 \\ 1 & H_p \geq 0 \end{cases} \quad (3)$$

$$C_m = \begin{cases} \frac{\alpha m}{1-m} (\theta_s - \theta_r) S_e^{\frac{1}{m}} (1 - S_e^{\frac{1}{m}})^m & H_p < 0 \\ 0 & H_p \geq 0 \end{cases}, k_r = \begin{cases} S_e^l \left[1 - \left(1 - S_e^{\frac{1}{m}} \right)^m \right]^2 & H_p < 0 \\ 1 & H_p \geq 0 \end{cases}$$

The transport model is described per Faeli et al. (2021) and summarized in Table 1.

In Eqs. (4) to (8), D_i denotes dispersion tensor, α_L / α_T is longitudinal and transverse dispersivities. D_e is effective diffusion coefficient (1×10^{-9} m²/s for fluid, van Wijngaarden et al. 2016, 1×10^{-5} m²/s for gas). ρ_b is bulk density (kg/m^3), R_i is reaction term, a product of fluid volume fraction (θ), urea hydrolysis rate (r_{uh}), and stoichiometry constants (m : -1 for urea and Ca^{2+} , 1 for CO_3^{2-} , and 2 for NH_4).

The rate of urea hydrolysis is defined with S_{su} that is suspended bacteria concentration (OD600), S_{at} that is bacteria attached to the surface known as biofilm (OD600), K_u is specific rate of ureolysis (mol/l.s.OD), K_m is half-saturation rate constant (M), K_{NH4} is optional ammonium inhibition (M). The r_p (mol/l.s) is precipitation rate and is considered equal to urea hydrolysis rate (r_{uh}) per van Paassen et al. (2009). The ρ_{CaCO_3} and m_{CaCO_3} are bulk density and molar mass of $CaCO_3$ (kg/mol), respectively. Hydraulic conductivity (k_s) is modified using a Kozeny-Carmen style incorporating initial k_0 as function of mean particle size (dm), and constant factor that is often assigned 3 per van Wijngaarden et al. (2011).

It is important to note that in saturated model volumetric water content (θ) is equal to porosity (ε) and both terms are denoted by θ in equations (4) to (8), however, the unsaturated model differentiates between these two terms. The transport model in Eq. (4) uses the solute concentrations and reaction rates per water content volume and θ is defined as a product of porosity (ε) and degree of saturation (S_r) (Eq. 4). The porosity is updated per time step as a result of pore space being occupied by $CaCO_3$ precipitation (Eq. 7). The θ_s in retention model (Eqs. 3) is the porosity (ε) will be modified with $CaCO_3$ precipitation.

5.2.2. Material Properties

A pure silica sand tested by Cheng et al. (2013) was employed to calibrate the model. The soil is classified as poorly graded sand (SP) to reflect undesirable engineering behavior of geotechnical applications. Cheng et al. (2013) employed two different soil types; coarse and fine sand. The study herein uses coarse sand in analyses due to the availability of required data and experimental results for this type. The grain-size distribution of coarse sand is shown in Figure 1. Figure 2 presents soil-water characteristic curves (SWCCs) of materials. Comparing D_{60} , D_{30} , D_{10} , gravel and Fine contents estimated from soil size distribution, two SWCCs per Yang et al. (2004) were selected denoted by coarse sand and coarse sand II in Figure 2. The objective of using two SWCCs is to assess the effects of different unsaturated properties on the results. Additionally, a fine material that is mostly loess and clay (CL) was selected from Hu et al. (2021) for further analysis. Table 2 indicates soil properties used in analyses.

5.2.3. Model Configuration

The samples were prepared in polyvinyl chloride (PVC) columns of 55 mm inner diameter and 160 mm height. In order to avoid solution accumulation at the bottom of the columns by gravity and obtain more homogeneous precipitation, the columns have been placed horizontally

during curing. The simulated 3D horizontal columns with discretized mesh are shown in Figure 3. Initial pressure within domain is defined based on degree of saturation and SWCCs of Figure 2. Point mass source and inlet velocity have been used as one boundary condition at one end of column and outlet pressure has been used in another end. The outlet pressure is atmosphere in the most of cases as percolation has been prompted by inflow rate. However, as stated per Cheng et al. (2013) a vacuum pump suction was connected to the bottom of column to collect excess solution. In some experiments (ex. 20% saturated clay with high negative pressure) a negative pressure of -1 kPa was used at outlet pressure to keep outflow equal to inflow rates and a constant degree of saturation during injections. Table 3 presents MICP model parameters used in simulations. The optical density of the harvested bacterial suspension varied between 1.5 to 2.0 OD₆₀₀, and the bacteria activity was approximately 10 U/ml (1U=1 mol urea hydrolyzed per minute) that is converted to 1.67×10^{-4} mol/l.s.OD₆₀₀ for consistency of units in the simulations. The cementation solution consisted of 1 mol/l urea and 1 mol/l CaCl₂.

At 20% degree of saturation about 3 to 12 treatments were implemented for low to high CaCO₃ contents. When the degree of saturation increased to 40%, 80%, and 100%, for low to high CaCO₃, 3 to 8 treatments have been applied. Transient piecewise functions were employed to simulate treatment schedule, one bio injection with inflow rate of 1 l/h. The injection time is calculated using inflow rate and injected volume. The volume of injections varies from one column test to another depending on degree of saturation. The total volume of introduced solutions in each injection has been same as volume of water content in soil matrix to keep a constant degree of saturation during the experiment. The curing period of 12 h after treatments allowed bacterial attachment as well as CaCO₃ precipitation. The protocol followed in this series of experiments and used in simulation process are summarized in Table 4.

5.3. Results and Discussion

Efficient axisymmetric model

The CaCO₃ content (%) within column at 40% saturation degree after 8 treatments is shown in Figure 4. Figure 6 shows inlet and outlet velocity during treatments that are controlled to keep equal extraction and injection volumes when simulation progresses. As noted before, in some experiments a low negative pressure is required at the boundary. An axisymmetric model was developed with similar boundary and initial conditions. The models' results have been compared with 3D horizontal cylinder in Figure 5 showing good agreement between a 3D and axisymmetric

model. The justification behind aforementioned developed axisymmetric model is that the simulation running time for a 3D model is 10 times more than the axisymmetric one and to improve model efficiency, an axisymmetric domain was replaced to implement further analyses.

Model calibration

The variations of CaCO₃ content per experimental results of Cheng et al. (2013) were used to calibrate the unsaturated reactive transport model at 20, 40, 80, 100 % saturations for sand column tests. The maximum number of treatments has been 12 at 20%, while it was 8 at the higher saturation degrees.

Figure 7 shows the agreement between simulation and experimental results using unsaturated properties of coarse sand. The injected volume increases with degree of saturation as it is equal to volumetric water content. The injection fluid volumes (V_f) are normalized with initial fluid within the domain ($V_{fi}=V_v \cdot S_r$). After the same number of treatments, the CaCO₃ content is significantly affected by the degree of saturation in different ways. Firstly, the saturation degree affects the injected volume of solution, and additionally, changes suction pressure, fluid flow, and transport. At the same V_f/V_{fi} , higher degree of saturation induced more CaCO₃ (Figure 7(a)). Higher degree of saturation requires higher volume of bio and cementation solution to keep the saturation degree constant, thereby increasing CaCO₃ precipitation. At lower degree of saturation and lower volume of injection more discontinuous, residual pores (pendular) are formed and it may lack continuous fluid net (continuous capillary or funicular zone) within the domain. When degree of saturation and the corresponding volume of the injection solution decrease, the injected fluid may exclude from the pores within residual zone and hence, decreases CaCO₃ precipitation within that zone. The higher degree of saturation and increased corresponding water content enhance the accessibility of bacteria and cementation solutions to more pores and grain contacts and induce more precipitation. However, when CaCO₃ content is depicted versus injected volume without normalizing, the results at various degrees of saturation have been lined up with each other as shown in Figure 7(b), emphasizing the effects of injected volumetric solution in experimental results per Cheng et al. (2013). The calibrated attachment coefficient increases from 5×10^{-4} 1/s at 80 and 100% saturations to 1.5×10^{-3} 1/s at 20 and 40% saturation (Figures 7(a) and (b)). The higher negative pressure and suction at lower saturation degrees may improve bacteria fixation within the pores and reduce the possibility of detachment.

In addition, Figure 7 shows drying branch of SWCC induces higher CaCO_3 content than when wetting front is used, however, this is not a significant effect and the effect reduces with increasing degree of saturation. The similar results are shown for coarse sand type II that is similar in saturated properties (θ_s , k_s) while having different unsaturated properties and SWCC (Figure 2 and Table 2). The simulation results of coarse sand type II were not fitted into experimental results as much as the first type of coarse sand. The agreement decreased mainly in lower degrees of saturation. Therefore, using various SWCCs in simulation of treated coarse sand that is similar in other soil properties and treatment protocol may yield different results. These results highlight the effects of unsaturated parameters used in simulations and emphasize the importance of SWCC measurement for unsaturated soil before treatment in order to have more exact predictions in simulation process. The calibrated unsaturated parameters of soil used in experiments of Cheng et al. (2013) match more with the coarse sand (first type) as presented in Table 2.

For clay material, lower attachment coefficients of 2×10^{-4} 1/s at 40% saturation and 4×10^{-4} 1/s at 80% saturation have been obtained to give the same CaCO_3 content as the coarse sand at the same degree of saturation with similar treatment protocol.

Unsaturated properties of treated sand

The hydraulic conductivity and porosity change during the treatment. The hydraulic conductivity decreases from 4.47×10^{-4} m/s to 3.51×10^{-4} , 2.58×10^{-4} , 1.91×10^{-4} , and 1.68×10^{-4} at 20%, 40%, 80%, and 100% saturation, after 8 treatments, respectively (Figure 9). Similarly, Figure 10 shows that the porosity decreases from 0.39 to 0.358, 0.341, 0.317, and 0.3 at 20, 40, 80, and 100% saturation, respectively. The reduction has similar trend with hydraulic conductivity measurements per Cheng et al. (2013) at 30, 65, and 100% saturation. For 30% saturation, the least hydraulic conductivity resulting from precipitation is $1.70\text{--}2.1 \times 10^{-4}$ at 10% CaCO_3 , for 65% saturation the least hydraulic conductivity is 2.4×10^{-4} at 8% CaCO_3 , and for fully saturated soil is 1.5×10^{-4} at 12% and 1.0×10^{-4} at 14% CaCO_3 .

The hydraulic conductivity and porosity change during CaCO_3 precipitation and the final unsaturated properties tend to be similar to properties of finer sand as well. A fine sand with reduced k and θ as low as treated sand at 40% saturation after 8 treatments is used in simulations. The SWCC is depicted in Figure 2 (grey curve) and Table 2 presents unsaturated parameters which is given for a similar fine sand per Peters et al. (2021). Figure 11 shows the fine sand with reduced k and θ and revised SWCC has better agreement with measurements specifically at higher CaCO_3

content. The attachment coefficient decreases from 1.5×10^{-3} to 1×10^{-3} 1/s as well. As the model can capture variations in porosity and hydraulic conductivity during experiment, this result reflects the possibility of change in unsaturated properties and attachment coefficients during treatment process.

5.4. Conclusion

A model framework has been developed and calibrated to capture MICP process in variably saturated conditions. The model properly captures the variation of hydraulic conductivity and porosity in domain.

The calibration of model with column tests indicates the attachment coefficient (K_{at}) increases about 3 times by lowering the degree of saturation from 100% to 20%. The higher negative pressure and suction at lower saturation degrees may improve bacteria fixation within the pores and reduces the possibility of detachment.

The drying branch of SWCC yields higher CaCO_3 than wetting front under the same normalized volumetric injection fluid.

The hydraulic conductivity reduces during treatment within the range of 38%-to-80% and porosity reduction would be 79%-to-94% of initial ones after 8 treatments at various degrees of saturation indicating the unsaturated hydraulic parameters of material can subsequently change during the treatment process as well.

Table 5.1 Summary of numerical equations implemented in model development.

Equation	Description	Reference
$\frac{\partial(\theta C_i)}{\partial t} + \frac{\partial(\rho_b C_{p,i})}{\partial t} - \nabla \cdot (\theta D_i \nabla C_i) + \nabla \cdot (\mathbf{u} C_i) = R_i$ $R_i = m\theta r_{uh}$ $\theta = \varepsilon \cdot S_r$ $D_i = \alpha_{L,T} \mathbf{u} + D_e$	(4) Mass balance of chemical species transport for C_i that is solute concentration of bacteria, urea, NH_4 , Ca^{2+} , CO_3^{2-} . (advection-dispersion-reaction)	Zhang and Klapper (2010), van Wijngaarden et al. (2011)
$r_{uh} = K_u (S_{su} + S_{at}) \frac{C_{urea}}{K_m + C_{urea}} \cdot \frac{K_{NH4}}{K_{NH4} + C_{NH4}}$	(5) Urea hydrolysis reaction kinetics	Barkouki et al. (2011), Minto et al. (2019)
$\frac{\partial CaCO_3}{\partial t} - m_{CaCO_3} \theta r_p = 0$	(6) Calcium carbonate precipitation kinetics	van Wijngaarden et al. (2011)
$\frac{\partial \varepsilon}{\partial t} = - \frac{1}{\rho_{CaCO_3}} \frac{\partial CaCO_3}{\partial t}$	(7) Porosity modification	van Wijngaarden et al. (2011)
$k_s = k_0 (d_m) \frac{\varepsilon^n}{(1-\varepsilon)^2}$	(8) Hydraulic conductivity modification	van Wijngaarden et al. (2011)

Table 5.2 SWCC and Retention model.

Description	Symbol	Coarse Sand	Coarse Sand II	Clay	Fine sand
Reference		Yang et al. (2004)	Yang et al. (2004)	Hu et al. (2021)	Peters et al. (2021)
Saturated volumetric water content or Porosity	θ_s (ϵ)	0.39	0.39	0.43	0.34
Hydraulic conductivity (m/s)	ks	4.47×10^{-4}	4.47×10^{-4}	2.2×10^{-7}	1.5×10^{-4}
Drying curve					
Residual volumetric water content	θ_r	0.04	0.035	0.137	0.07
unsaturated parametres	α (kPa ⁻¹)	0.816	0.408	0.105	0.37
	n	1.9	3.3	1.586	2.1
	m	0.474	0.697	0.369	0.524
	l	0.5	0.5	0.5	0.5
Wetting curve					
Volumetric water content at Ψ_w	θ_w	0.0205	6.07×10^{-5}		
unsaturated parametres	α (kPa ⁻¹)	2.34	0.7135		
	n	2	4.5		
	m	0.5	0.778		
	l	0.5	0.5		

Table 5.3 MICP model parameters.

Model Parameter	Symbol	Unit	Value	Reference
Column Dimension	H x D	m	0.16 x 0.055	Cheng et al. (2013)
Pore volume	V _v	ml	Caorse sand:148- Clay:163	Cheng et al. (2013)
Specific ureolysis rate	K_u	mol/l.s.OD 600	1.67×10^{-4}	Cheng et al. (2013)
Attachment rate coefficient	K_{at}	1/s	2×10^{-4} - 1.5×10^{-3}	Calibrated
Half-saturation rate Constant	K_m	mol/l (M)	1×10^{-2}	Faeli et al. (2021)
Decay rate coefficient	K_{decay}	1/s	1.15×10^{-7}	Faeli et al. (2021)
Dispersivity	$\alpha_L = \alpha_t$	m	0.01	Calculated
Diffusion coefficient of fluid	D_e	m ² /s	1×10^{-9}	van Wijngaarden et al. (2016)
Diffusion coefficient of gas	D_e	m ² /s	1×10^{-5}	Faeli et al. (2021)
Sand Dry Density	γ_d	kg/m ³	1630	Cheng et al. (2013)
Clay Dry Density	γ_d	kg/m ³	1500	Hu et al. (2021)
fluid density	γ_f	kg/m ³	1000	
Injection flow rates	Q_i	ml/h	1000	Cheng et al. (2013)
Outlet pressure	p_o	kPa	Atmosphere (or pump suction -1 kPa)	Cheng et al. (2013)
Compressibility of fluid	X_f	1/Pa	4.4×10^{-10}	Storage
Matrix Effective compressibility	X_p	1/Pa	1×10^{-8}	Storage
Dynamic Fluid viscosity	μ	Pa.s	8.9×10^{-4}	
Molar mass of CaCO ₃	m_{CaCO_3}	g/mol	100.087	
Molar mass of NH ₄	m_{NH_4}	g/mol	18.039	
CaCO ₃ bulk density	ρ_{CaCO_3}	kg/m ³	2710	

Table 5.4 Bio-injection and cementation treatments in simulated tests.

Bacterial solution	<i>Bacteria</i>	OD ₆₀₀	1.5-2
Cementation solution	<i>Urea-CaCl₂</i>	M-M	1-1
Bacteria Injection volume	V_i		$V_v * S_r / 2$
Cementation Injection volume			1st treatment: $V_v * S_r / 2$; 2-12: $V_v * S_r$
Injection time		h	V_i / Q_i
Retention time		h	12 (No retention time after bacteria)
No. treatment			3-12
Treatment duration (No. treatment)		d	1.5 (3)- 4 (8)- 6 (12)

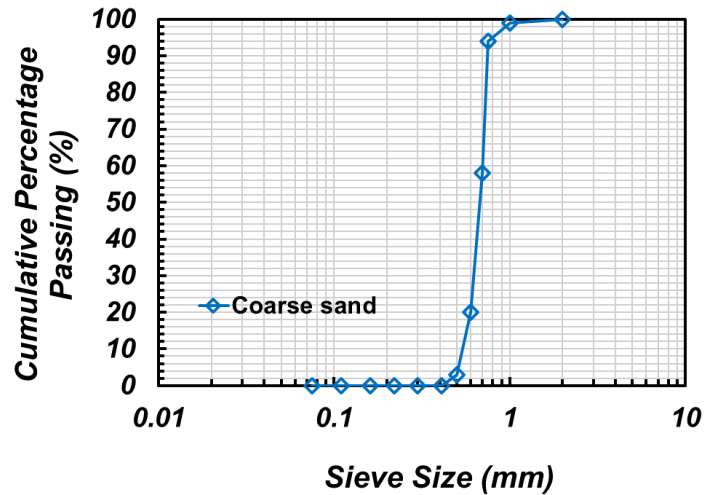


Figure 5.1 Grain size distribution for coarse sand (Cheng et al. 2013).

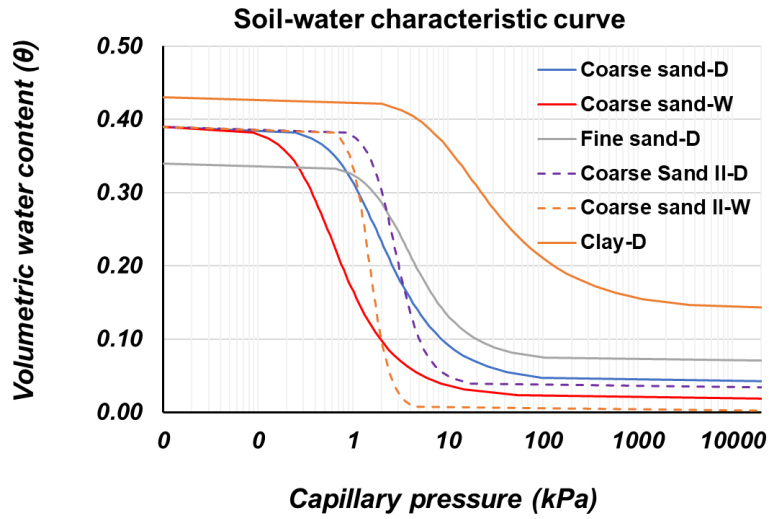


Figure 5.2 Soil-Water characteristic curves of materials.

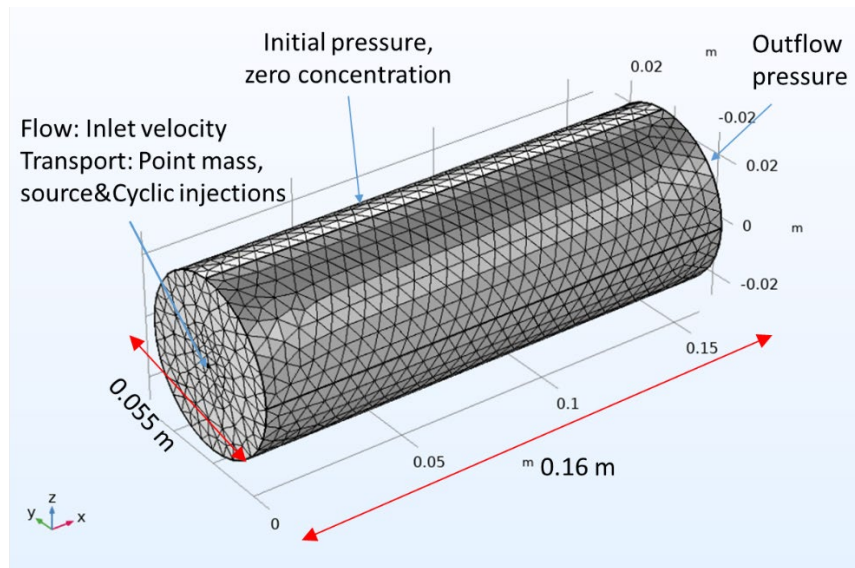


Figure 5.3 Column model and discretized mesh domain.

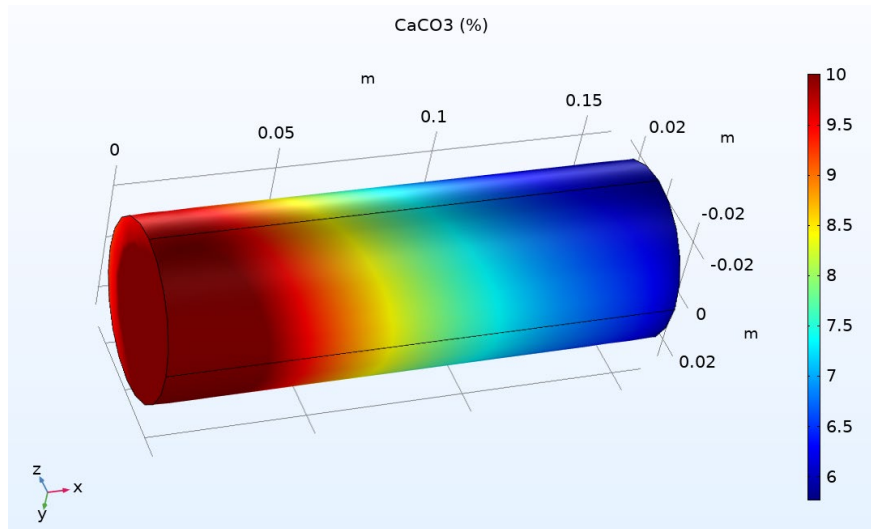


Figure 5.4 CaCO₃ content- S:40%-No. of treatment: 8

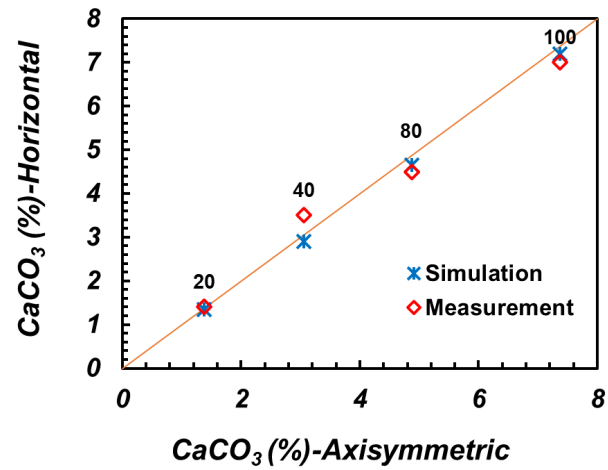


Figure 5.5 Comparison between 3D horizontal and axisymmetric columns after 3 treatments for 20, 40, 80% and 4 treatments at saturated condition.

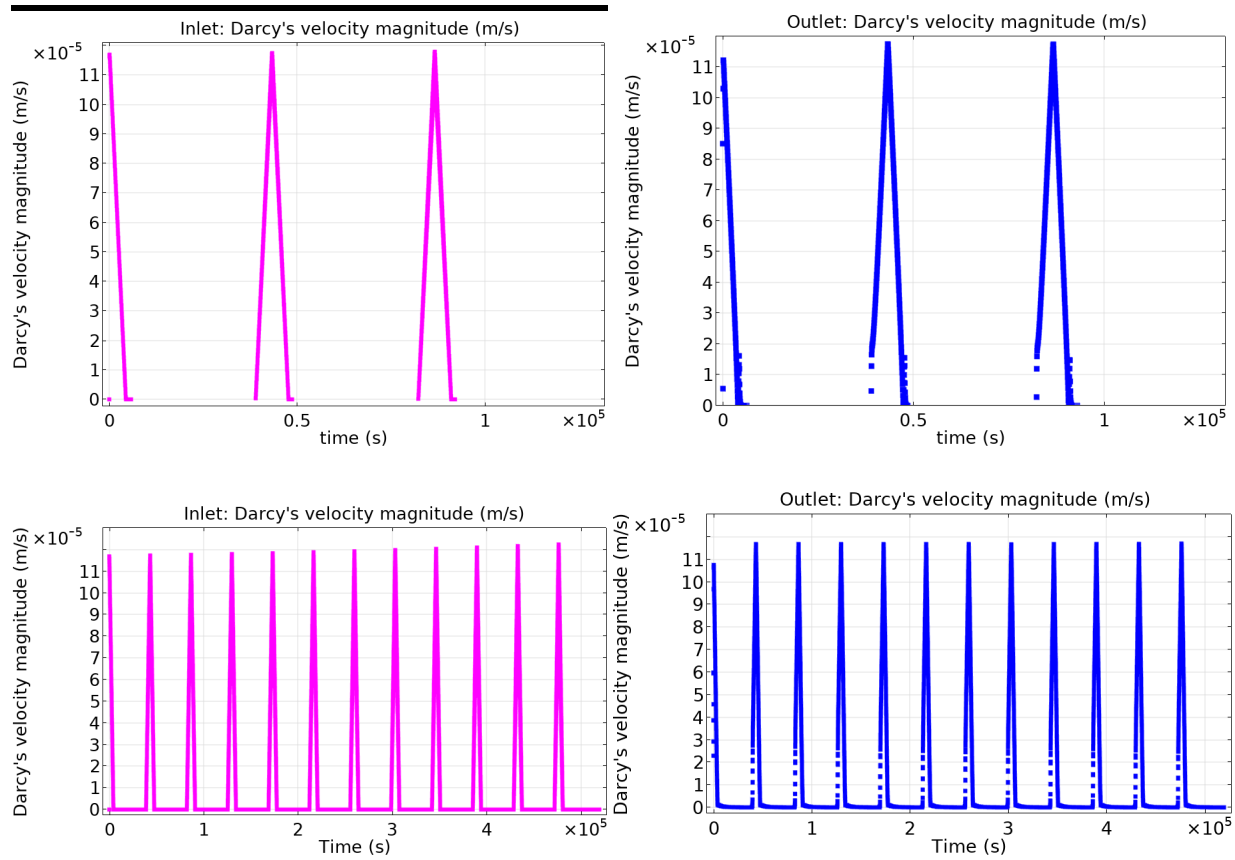
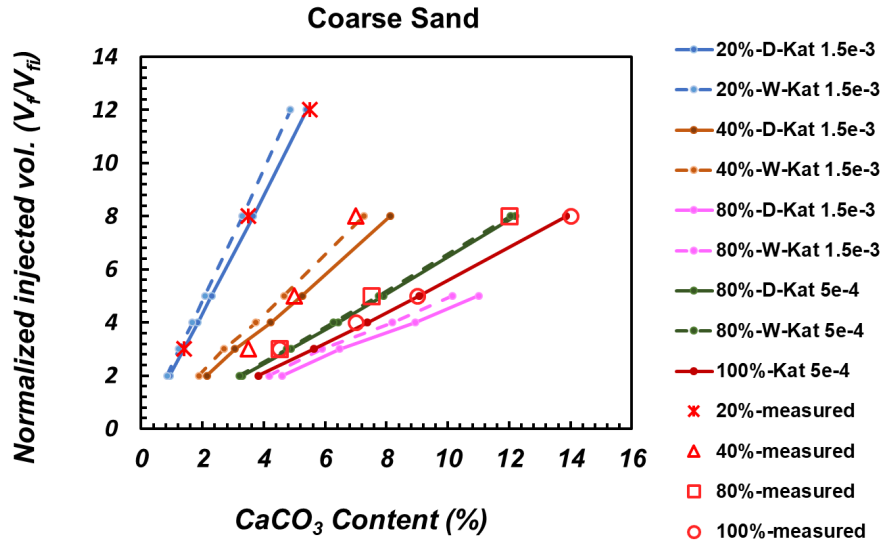
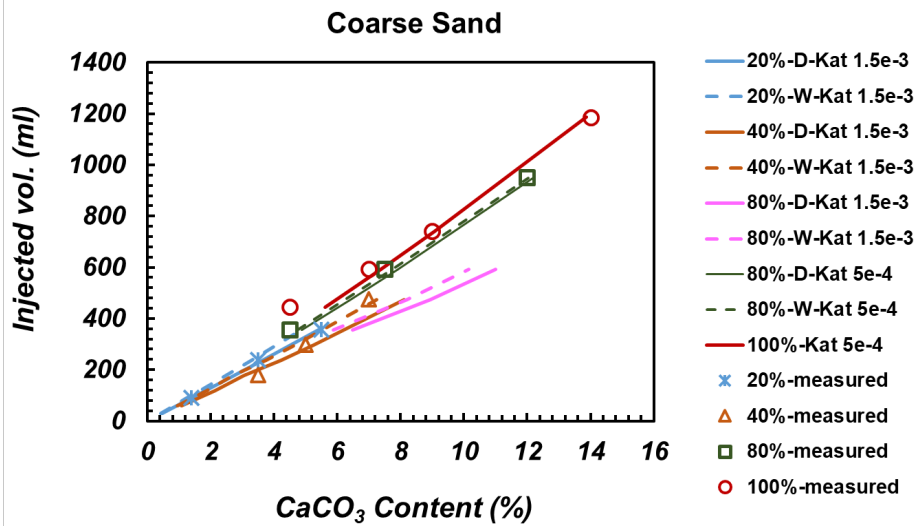


Figure 5.6 Inlet and outlet velocity during treatment.



(a)



(b)

Figure 5.7 $CaCO_3$ content at different degree of saturations, drying and wetting branches of SWCC for coarse sand compared with laboratory measurements (a) $CaCO_3$ content with normalized injected volumes (b) $CaCO_3$ content with injected volumes.

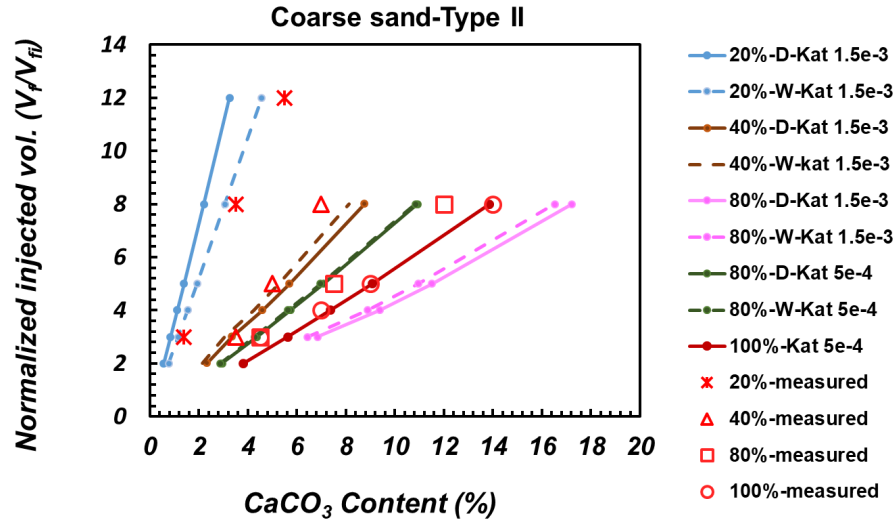


Figure 5.8 CaCO₃ content at different degree of saturations, various normalized injected volumes, drying and wetting branches of SWCC for coarse sand-type II compared with laboratory measurements.

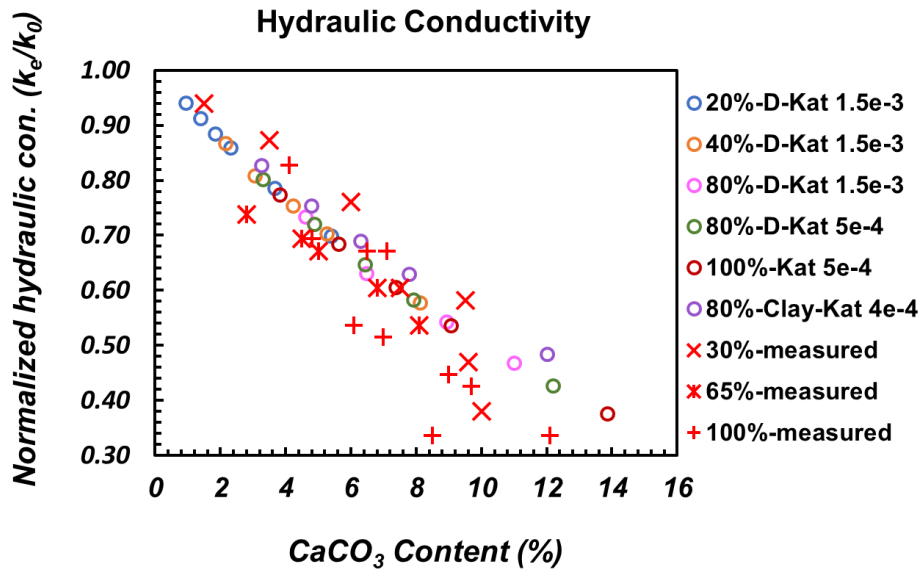


Figure 5.9 Hydraulic conductivity variations with CaCO₃ precipitation at different degrees of saturation, $k_0=4.47 \times 10^{-4}$ m/s for sand, $k_0=2.20 \times 10^{-7}$ m/s for clay.

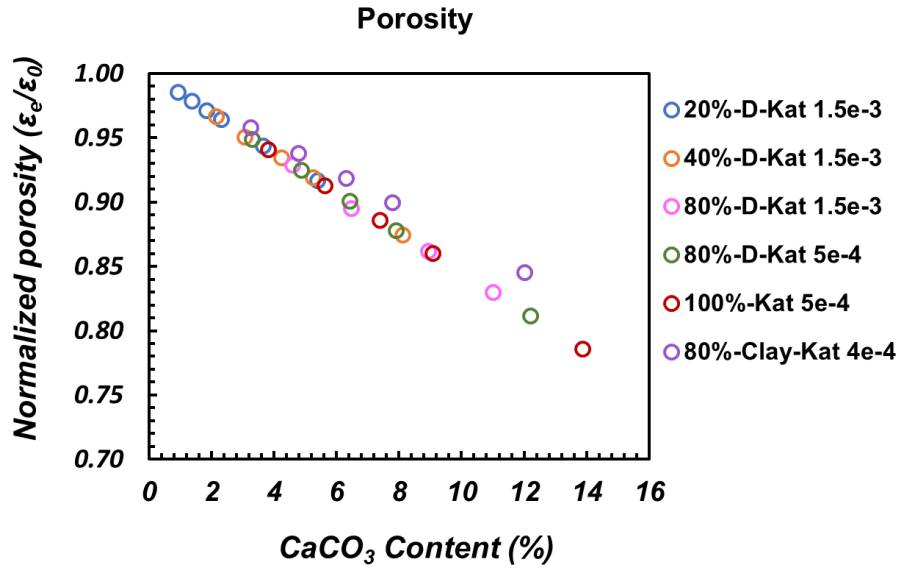


Figure 5.10 Porosity variations with CaCO_3 precipitation at different degrees of saturation, $\epsilon_0=0.39$ for sand, $\epsilon_0=0.43$ for clay.

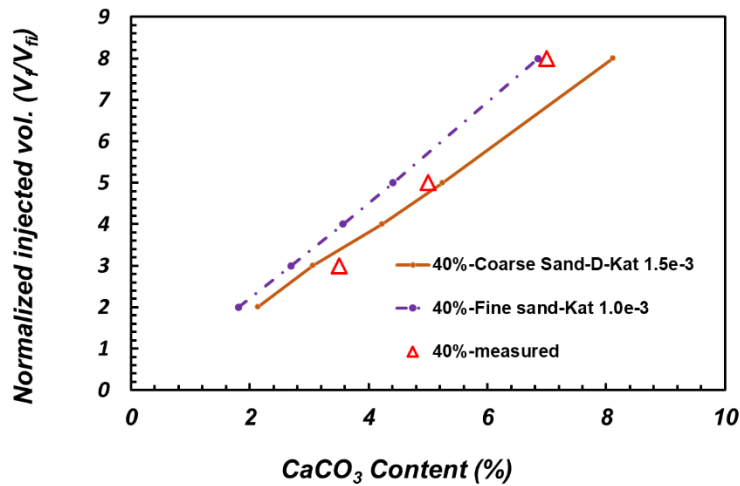


Figure 5.11 Comparison between coarse and fine sands indicating changes in unsaturated properties of coarse sand during treatment. Fine sand has the permeability and porosity equal to the ones for the treated coarse sand after 8 treatment cycles.

CHAPTER 6. Benzene Migration in Unsaturated Profile with Subsurface Drainage Concrete Pipe

This chapter has been previously published in ASCE publications in *Geo-Congress* 2020.

Abstract

The impact of benzene leakage on underlying unsaturated zone and nearby subsurface drainage concrete pipe is investigated. Work in the paper considers mass transfer into subsurface concrete pipe located in unsaturated profile. The 3-D numerical simulations were implemented using the T2VOC code with the Petrasim2018 graphical user interface to analyze multiphase migration in the vadose zone and the impact on the concrete pipeline installed in a trench. The contaminant's gas, aqueous and free product phases are assessed based on the model physical properties of soil and concrete materials. A case study is presented with data from a site located in the coastal plain physiographic region of North Carolina (NC). The site is a gas station located near the town of Jacksonville, NC. The analyses consider the effect of depth to groundwater table and volatilization into the atmosphere. The results illustrate the transport of the three phases in unsaturated soil domain and the potential of having the gas and aqueous phases breakthrough the subsurface concrete pipe.

6.1. Introduction

Leakage from permanently closed, or in service, underground storage tanks (UST) and pipelines as well as from disposal area practices dry cleaning facilities leads to contamination of the vadose zone and subsurface utilities. Volatile organic compounds (VOCs) such as hydrocarbon fuels (gasoline, diesel, BTEX), or Trichloroethene (TCE) can migrate through the unsaturated surface profile and breakthrough subsurface utilities such as culverts and water/drainage pipes; thereby contaminate surface and groundwater.

In the unsaturated zone, transport of the contaminant can occur as solute in the water (or aqueous phase), vapors in the gas phase, and as unaltered constituents in the NAPL (nonaqueous phase liquid). The mechanisms of interphase mass transfer include evaporation of the NAPL, dissolution into the liquid water phase, and equilibrium partitioning of the organic chemical between the gas, water, and solid phases (Falta et al. 1992). In some scenarios, it is possible for vapor transport, rather than the slowly percolating dissolved-phase plume, to be largely responsible for VOC transport to the underlying layers (Rivett et al. 2011). The transport of VOCs in the gas

phase may occur due to both advection and diffusion and is influenced by phase partitioning into the water and solid phases.

In a field investigation by Hinchee and Reisinger (1985), lateral diffusive transport in an unsaturated zone was suggested as a main mechanism for hydrocarbon contamination of soil and groundwater some distance away from a leaking gasoline storage tank (Baehr 1987). Through partition into water and air phases, the vapors can also migrate into aquifers and the inner space of subsurface utilities with the potential of transport over large horizontal distances. Small concentrations of petroleum products render groundwater unfit for domestic use (Baehr 1987).

Past studies that focused on contaminant migration in unsaturated soil can be categorized into two groups; i) Literature on governing equations and parameters (Jury et al. 1983, Sleep and Skyes 1989) of the transport phenomena and soil media, and ii) Literature on different scenarios of contaminant migration in simulated field situations. These for example include work investigating water table fluctuation by Yang et al. (2012) and the effects of episodic NAPL releases and land cover by Dafny (2017). However, there is dearth of information on contaminant transport through unsaturated zones having installed subsurface utilities such as concrete drainage pipes, for example. Specifically, data in literature related to the potential of contaminant breakthrough subsurface concrete pipes (common in subsurface drainage applications) in unsaturated profiles are scarce.

Work presented herein is focused on investigating the potential transport of benzene as VOC with high vapor pressure through unsaturated zone and into the subsurface concrete utility pipes with polymeric gaskets. The numerical analyses are conducted using T2VOC code with the Petrasim2018 graphical user interface. A site in Jacksonville, North Carolina is used as a case study. Two water table levels and unsaturated properties of the various materials incorporated in the model. The effect of depth to groundwater table, and volatilization into the atmosphere, on contaminant migration into subsurface concrete pipe is assessed and discussed.

6.2. Governing Equations

In a nonisothermal system containing three mass components of air, water and an organic chemical and three flowing phases, gas, aqueous, and NAPL, three mass balance equations and an energy balance equation are needed to fully describe the system (Falta et al. 1992). These are summarized as follows:

$$\frac{d}{dt} \int_{V_l} M^K dV_l = \int_{T_l} F^K \cdot n dT_l + \int_{V_l} q^K dV_l \quad (\text{K: a: air; w: water; c: chemical; h: heat}) \quad (1)$$

where M^K is component mass per unit porous medium volume, F^K is the mass flux of component K into V_1 (net flux), n is outward unit normal vector, q^K is rate of mass generation of component K per unit volume at source.

The mass accumulation terms, including linear equilibrium adsorption, is presented as:

$$M^K = \phi \sum_{\beta} S_{\beta} \rho_{\beta} \omega_{\beta}^K + \rho_b \rho_w \omega_w^C K_D \quad (2)$$

where ϕ is porosity, S_{β} is the β phase saturation, ρ_{β} is the β phase density, and ω_{β}^K is the mass fraction of component K in phase β , ρ_b is the dry bulk density of the soil, and K_D is the soil water distribution coefficient for the organic chemical (Freeze and Cherry, 1979).

The mass flux of each component in the aqueous and NAPL phases is calculated by considering only advection. The mass flux of each component in the gas phase considers advection and diffusion and is expressed as follows:

$$F_g^K = \frac{-k k_{r\beta} \rho_g}{\mu_g} \omega_g^K (\nabla P_{\beta} - \rho_g g) + J_g^K \quad (3)$$

where k is the absolute permeability tensor, $k_{r\beta}$ is the β phase relative permeability, μ_{β} is the β phase dynamic viscosity, P_{β} is β phase pressure, g is the gravitational acceleration vector, and J_g^K is the diffusive mass flux of component K in the gas phase.

The diffusive Mass fluxes of water and organic chemical vapor J_g^W & J_g^C are calculated as follows:

$$J_g^K = -\phi S_g \tau_g D_g^K \rho_g \nabla \omega_g^K \quad \left(\frac{kg}{m^2.s} \right), K = C, W \quad (4)$$

where S_g is gas saturation, ϕ is porosity, ρ_g is gas phase density and ω_g^K is the mass fraction of component K in gas phase, D_g^K is the molecular diffusion coefficient of component K in the gas phase and τ_g is the gas phase tortuosity calculated from Millington and Quirk (1961) equation.

In order to determine the thermodynamic state of four components (air, water, NAPL, heat) and establish the local thermal and chemical phase equilibrium, four primary variables (S_w , S_g , P , T) and a complete set of secondary variables are needed. The secondary variables include thermodynamic and transport properties such as concentration, mole or mass fractions, relative permeabilities, capillary pressure, viscosities, densities, water and chemical molecular diffusivity, tortuosity and enthalpies (Falta et al., 1992).

6.3. Site Description

The study site is an operating gas station where gasoline leakage was detected near a subsurface concrete drainage pipe. This leakage led to contamination of underlying soil layers with soil contamination level above MSCCs (MSCC=0.0056 mg/kg) (Terracon, 2018). As shown in Figure 1, the nearby subsurface drainage concrete pipe is installed in a trench located adjacent to the gasoline station.

The site information presented herein is from reports by Delta (2000), Antea (2016) and Terracon (2018). Soils at the subject location consist of silt, silty and sandy clay. Results from slug testing indicated the hydraulic conductivity ranges from 6.24×10^{-5} cm/s to 9.07×10^{-5} cm/s with an average of 7.33×10^{-5} cm/s (Delta 2000). The groundwater flow direction is northeast with an average hydraulic gradient of 1%. Most of the utilities are located at depth 0.6-1.7m below ground surface. As presented in the reports by Antea (2016) and Terracon (2018), benzene persisted at concentrations above the standard levels from 1998. They reported petroleum hydrocarbon as free product thickness of 0.47 m at MW-12. The model domain dimensions utilized herein are indicated on the Figure 1 as simulated in this analysis.

6.4. Model Development

6.4.1. Domain Configuration

The discretized analysis model domain with rectilinear elements is shown in Figure 2. The domain dimensions are 30 m \times 15 m \times 6 m. The concrete pipe is taken as 0.5 m in diameter and is located at 1.5 m below the ground surface, as indicated on the site plan.

For the initial analyses, ground water table in the model is located at the lowest possible level at the site, \sim 3m, from ground surface. The flow gradient is taken as 1%. In a second scenario, the water table is raised to 2.1 m to consider the effect of depth to groundwater table on benzene phase distribution. Water flow within the saturated zone, depending on the scenario being analyzed, was introduced to account for the possible effect of hydraulic gradient on the propagation of benzene in the unsaturated zone through mass transfer between the saturated and unsaturated zones. The model domain's horizontal dimension of 30m is large enough to include sampling wells MW-4 and MW-12, which encompass an area having the highest contaminant concentrations (based on ground water monitoring report by Antea, 2016). As pipe gaskets are located at 2.5m from each other, the distance of 15m along z direction (horizontal axis along pipe) includes five joints or gaskets. In the vertical direction (y axis), the depth of 6m encompasses the contaminated

area, as field sampling showed the vertical extent of benzene doesn't exceed 6 m from the surface in MW-4 (Delta Group, 2000). The discretized domain and pipe as well as gaskets are shown in Figures 3 and 4, respectively. To eliminate effect of mesh size on simulation results, a series of mesh sensitivity analyses were implemented to optimize dimensions and discretized mesh.

6.4.2. Model Parameters

The subsurface sequence, pipe and specific properties used in the numerical model are presented in Tables 1 and 2. The native soil in the domain is mostly sandy clay with intrinsic permeability of $6.4 \times 10^{-14} \text{ m}^2$ ($K = 6.24 \times 10^{-5} \text{ cm/s}$, Delta 2000). The hydraulic conductivity in vertical direction is assumed equal to half of the value in the horizontal direction. The pipe is located in a trench with 0.15 m sandy gravel as the bedding material, overlain by 0.9 m initial backfill that is mostly sandy soil, and 0.9 m final top backfill, from the native soil as shown in Figure 2b. The capillary pressure parameters of pipe material and gasket materials are defined based on Van Genuchten parameters (α_{gw} and n) (Pour-Ghaz et al. 2016 and Kumar 2010). As these parameters are determined for a two-phase water-gas system, the scaling factors are needed to calculate α_{gn} and α_{nw} from α_{gw} (Table 2).

The gaskets are assumed to be in good condition with their hydraulic conductivity equal to that of concrete. Table 3 shows the parameters of diffusion used in the analyses to define D_g^k in equation (4). Adsorption of chemical onto the solid phase is defined by soil-water distribution coefficient for organic chemical (K_d). The K_d is estimated by multiplying the organic carbon partition coefficient (K_{oc}) and organic carbon fraction in the soil (f_{oc}). As shown in Table 3, in this study, k_{oc} is considered as $0.085 \text{ m}^3/\text{kg}$ (Shores et al 2017). The organic carbon fraction of soil was reported as 0.04-1.4 % for soils within the coastal plain regions of North Carolina where the Jacksonville site is located (Deiss et al., 2017). By using an organic carbon fraction of 0.1%, and K_{oc} of $0.085 \text{ m}^3/\text{kg}$, K_d is estimated as equal to $8.5 \times 10^{-5} \text{ m}^3/\text{kg}$.

6.4.3. Boundary Conditions

No manufactured ground cover is assumed for the soil near the surface (ie the top soil allows gas exchange with the atmosphere.) To consider gaseous emissions to the atmosphere, the top layer of the domain is set as fixed state with capillary pressure as zero (ie the top surface represents the atmospheric boundary condition.), and gas relative permeability as “=1” and liquid permeability near zero. By assigning a water saturation smaller than residual liquid saturation, liquid relative permeability would be nearly zero, preventing liquid flow into the soil and allowing

the gas evaporation to the atmosphere, representing a worst-case scenario. The water table level is set with fixed head at right and left side boundaries (Y-Z planes). The saturated cells along left and right sides represent a constant hydraulic head of 2.85 m and 3.15 m from surface to induce a hydraulic gradient of 1%. In case of a raised water table scenario, the saturated cells are located at 2 m at left side and 2.3 m at right side. Two fixed boundary conditions with constant pressure (atmospheric pressure) are considered at the two ends of the pipe. These boundary conditions represent half full pipe with a higher head in one side to set flow inside the pipe from the back to the front face. No flow boundary condition is assumed for the remaining boundaries of the model domain.

6.4.5. Simulation Process

The initial gravity-capillary equilibrium within the subsurface domain is first established in the simulation before contamination release. The governing equations of capillary pressure (Parker et al. 1987) and relative hydraulic conductivity of the soil (Stone, 1970) are specified to define the soil-water characteristic curve (suction head or capillary pressure vs degree of saturation) for the model domain. Figure 5 displays the soil-water characteristic curves (SWCCs) for native soil, the trench material, and, water retention curve (WRC) for concrete pipe material. The initial water saturation and pressures are defined based on these diagrams. The whole domain is analyzed for equilibrium one time without the pipe but with the groundwater gradient, then followed by analysis second time with the pipe included in the domain.

Because of high capillary pressure of concrete, the pipe walls become completely saturated, with the trench around the pipe having the lowest saturation level within the domain. After establishing equilibrium, contaminants are released in a specific area and long term redistribution of the contaminants with time and the potential transport to the concrete pipe are assessed. The area used as a source of released contamination is assigned based on data in Antea (2016). Benzene saturation as NAPL phase is released into the domain as percentage of maximum detected BTEX (3207 mg/kg) at 1.2 m to 1.8 m below the ground surface (degree of saturation of benzene as NAPL phase (S_n) = 0.1).

The source domain of contamination covers an area of 4×10.5 m around MW12 location where the free product was discovered (see Figure 2 and Figure 3). After assigning source term, verification analyses are carried out at the location of MW4 where data are available on benzene concentration in groundwater samples. The model results show the concentration in aqueous phase

at 1.2m depth at the location of MW4 ranged from 16450 to 18500 $\mu\text{g/l}$ for six years after release. These values agree with concentration in aqueous phase obtained from field sampling results that were reported by Antea (2016).

6.5. Results and Discussion

Several simulation runs were conducted to study the benzene migration breakthrough the pipe and the effect of depth to groundwater table. Since the NAPL plume was defined as a finite volume in a specific region, it cannot develop much further from the source and reach the pipe location. The model results indicated that the initial free product NAPL saturation is depleted after two and half years from release. The results indicate the lateral mass transfer through unsaturated profile is more dominated by gas phase diffusion rather than advection in gaseous, aqueous or NAPL phases. VOC diffusion coefficients in the gas phase are up to 4 orders of magnitude higher than the coefficients for the aqueous phases (Rivett et al. 2011). When raising the water table level, concentration and mass inside the pipe decrease significantly due to low lateral diffusive gas phase spreading as the water content in the unsaturated domain increases. The Figure 6 shows the breakthrough concentration in aqueous and gaseous phases inside the pipe for the two water table levels of 3m and 2.1m (from ground surface) used herein. The peak value of concentration along the pipe reaches 11.3 $\mu\text{g/l}$ (aqueous phase) and 2.2 $\mu\text{g/l}$ (gas phase) when water table level at pipe location is 3m from ground surface and these peak values decrease respectively to 0.7 $\mu\text{g/l}$ and 0.13 $\mu\text{g/l}$ when the water table level raises to 2.1m from the top surface. For a comparative reference, these concentrations are above 5 $\mu\text{g/l}$ (MCL , EPA, 2002) and 1.2×10^{-4} $\mu\text{g/l}$ (AAL, NCDEQ 2018).

The cumulative mass of benzene breaking through the pipe in aqueous and gaseous phases are computed by adding up the gas and aqueous fluxes at individual cells of the pipe multiplied by the specific time increment in which those fluxes were calculated. The mass calculations are shown in Figure 7 for the two water table levels. The main point inferred from this figure is that although the lateral gas diffusion is responsible for contaminant transport from source to the trench, most of the accumulated mass in the trench breaks through the pipe as aqueous fluxes (and then partitions into the gas phase inside the pipe since the pipe was assumed half full.) The initial total mass released as free product in the domain is 840×10^6 mg from which 2355 mg and 237 mg breakthrough the pipe in aqueous phase during simulation time for water table levels of 3m and 2.1m, respectively. The mass ingress in gas phase is 19 mg and 2 mg for water table at 3m and

2.1m, respectively. The lower mass fluxes in gas phase are reasonable given the high water content in pores of the concrete pipe wall minimizing gas diffusion through the pipe wall. After contaminant breaking through the pipe, it is partitioned in both aqueous and gas phases as the concentrations are in equilibrium with each other. As results show, the concentration in the gas phase can locally reach greater values than allowable ones along the pipe.

6.6. Summary and Conclusion

Numerical analyses are conducted to study the potential breakthrough of benzene into concrete pipe located in unsaturated media. A case study is presented herein with data from a site located in the coastal plain physiographic region of North Carolina. The site is a gas station located near the town of Jacksonville. The released NAPL is partitioned into adsorbed mass, aqueous and gas phases and is transported by diffusion in gas phase and advection in NAPL, aqueous and gas phases. Based on the results from the numerical analyses, the following conclusions are made:

i. The results indicate that Benzene as NAPL plume in the modeled unsaturated soil does not develop much further from source and after being partitioned into adsorbed, aqueous and gas phases spread through the domain to the trench where the pipe is located in.

ii. The water table level has significant effect on mass breaking through the pipe. The mechanism of lateral transport in an unsaturated domain in this case was dominated by vapor phase diffusion. When the water table was raised to 2.1m below the surface, the concentrations inside the pipe decrease due to lower lateral diffusive gas phase as a result of increased water content in the vadose zone. As the gas and aqueous phases are in equilibrium, there will be a decrease in the aqueous phase concentration that is laterally transported as well.

iii. The mass calculations show that the most of transported benzene breaks through the pipe as aqueous fluxes. However, the concentrations inside the pipe in both phases are in equilibrium and once aqueous phase breakthrough is partition back to the gas phase as the pipe was assumed to flow only half full in these analyses.

iv. Atmosphere layer simulated the top boundary of the model domain has a significant role in VOC dissipation from the system through volatilization. Such effect mitigates the level of benzene reaching the pipe. The results show the 140,000 g of benzene benzene lost to the atmosphere after one year in case of water table at 3m.

Table 6.1 Main properties of soil and concrete domain.

Soil type	Rock density	K_v	K_h	Intrinsic K_v	Intrinsic K_h	Porosity
	kg/m ³	cm/s	cm/s	m ²	m ²	
Native soil (sandy clay)	2700	3.12×10^{-5}	6.24×10^{-5}	3.20×10^{-14}	6.40×10^{-14}	0.37
Final backfill (sandy clay)	2700	4.68×10^{-5}	9.36×10^{-5}	4.80×10^{-14}	9.60×10^{-14}	0.38
Initial backfill	2700	7.5×10^{-2}	1.5×10^{-1}	7.70×10^{-11}	1.54×10^{-10}	0.34
Bedding material	2900	5×10^{-1}	1	5.13×10^{-10}	1.03×10^{-9}	0.32
Pipe material	2800	3.90×10^{-9}	3.90×10^{-9}	4.00×10^{-18}	4.00×10^{-18}	0.125
Undamaged gasket	1500	3.90×10^{-9}	3.90×10^{-9}	4.00×10^{-18}	4.00×10^{-18}	0.1
Flow	2700	10	10	1.00×10^{-8}	1.00×10^{-8}	0.999
Atm.	2700	1	1	1.00×10^{-9}	1.00×10^{-9}	0.999

Table 6.2 Capillary pressure and relative permeability of soil and concrete.

Soil type	S_m	n	α_{gn}	α_{nw}	α_{gw}	Swr	Snr	Sgr	n	Reference
			(m ⁻¹)	(m ⁻¹)	(m ⁻¹)					
Native soil	0.36	1.86	10.8	6	3.2	0.38	0.07	0.01	3	CP (Parker 1987)
Final backfill	0.36	1.86	10.8	6	3.2	0.38	0.07	0.01	3	RP (Battistelli 2008)
Initial backfill	0	1.84	10	11	5.2	0.15	0.05	0.01	3	CP (Parker 1987)
Bedding material	0	1.84	10	11	5.2	0.15	0.05	0.01	3	RP (Battistelli 2008)
Pipe material	0	1.5	1.7×10^{-3}	1.3×10^{-3}	7.4×10^{-4}	0.1	0.05	0.01	3	(Pour-Ghaz et al. 2016), (Kumar 2010)
Undamaged gasket	0	1.5	1.7×10^{-3}	1.3×10^{-3}	7.4×10^{-4}	0.1	0.05	0.01	3	
Flow	0	1.8	0.5	0.25	0.17	0.1	0.05	0.01	3	
Atm.			No capillary pressure			0.6	0.01	0	3	(Pruess, Battistelli, 2002)

Table 6.3 Diffusion and adsorption parameters used in simulations.

Parameter		unit	value
Reference diffusion coefficient for vapor-air mixtures	D_g^{awR}	m^2/s	2.13×10^{-5}
Reference binary diffusivity of VOC in air	D_g^{acR}	m^2/s	7.7×10^{-6}
vapor-air diffusivity exponent	θ_{aw}	-	1.8
chemical diffusivity exponent	θ_{ca}	-	1.52
organic carbon partition coefficient	K_{oc}	m^3/kg	0.085
organic carbon fraction	f_{oc}	%	0.1
Soil-water distribution coefficient for organic chemical	K_d	m^3/kg	8.5×10^{-5}

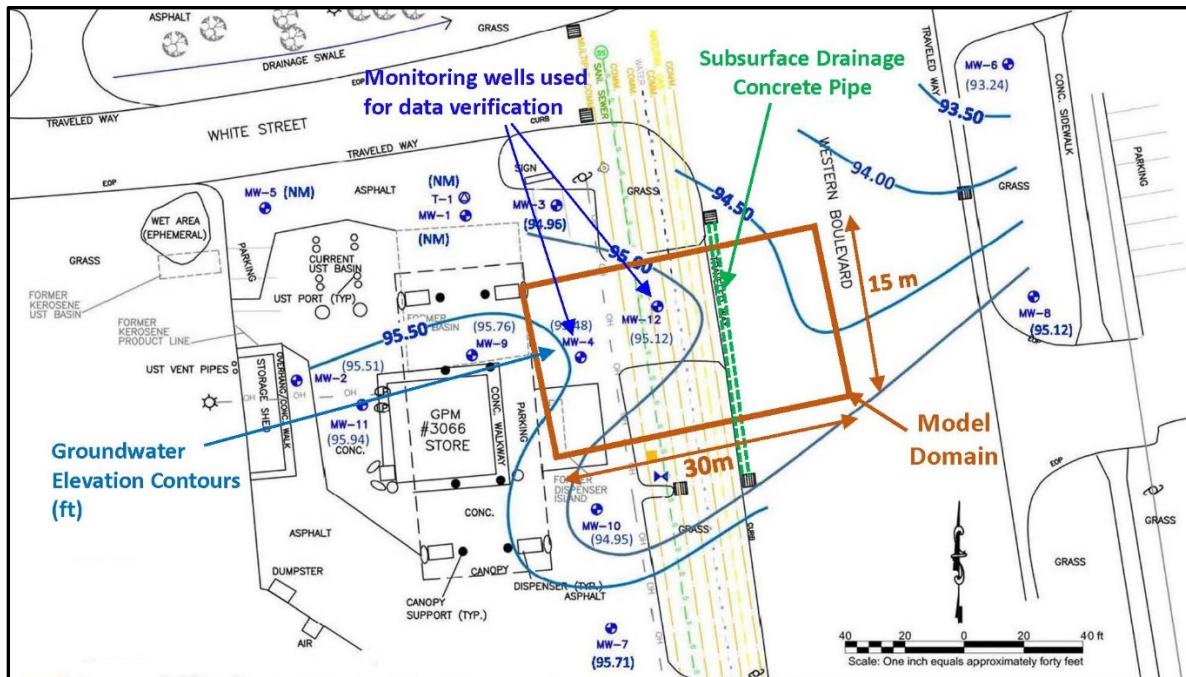
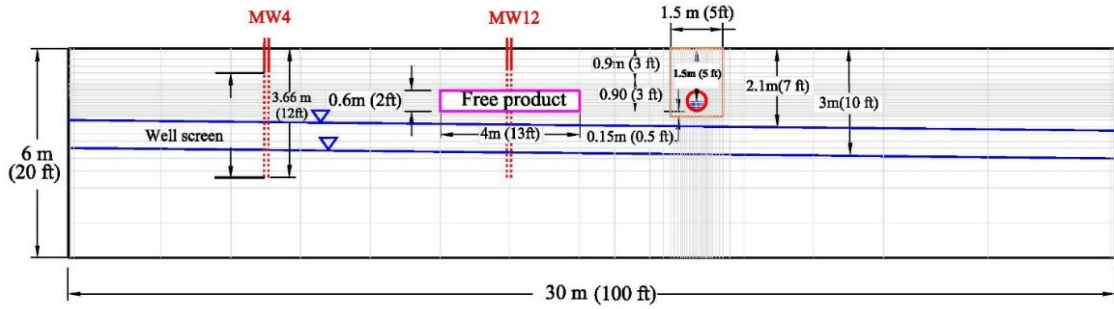
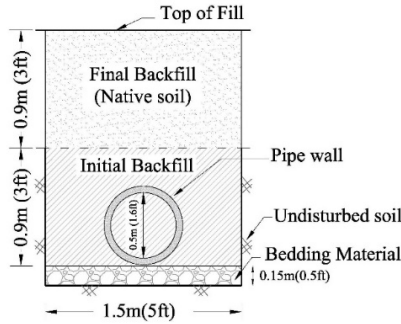


Figure 6.1 Jacksonville site map with monitoring wells locations and area utilized as model domain (site map from Antea, 2016).



a) Cross section view



b) Section detail view-Installed pipe in trench

Figure 6.2 Schematic sketch of Model.

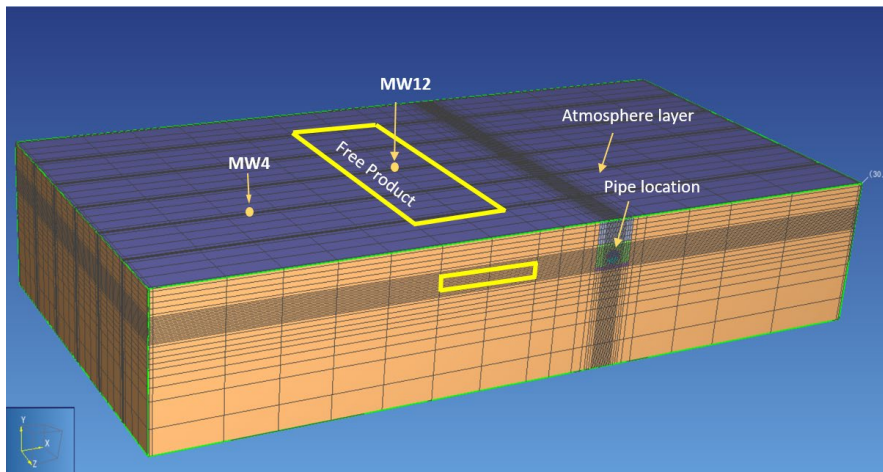


Figure 6.3 The Model and created Mesh (pipe and trench are located above water table level in unsaturated zone).

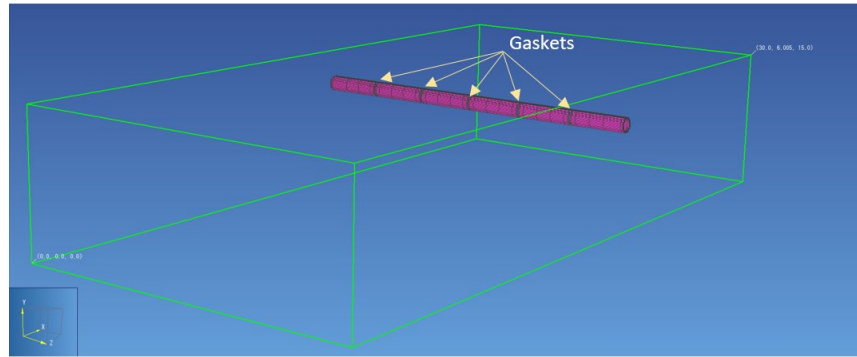


Figure 6.4 The discretized mesh with pipe and gaskets (Distances of gaskets are 2.5 m).

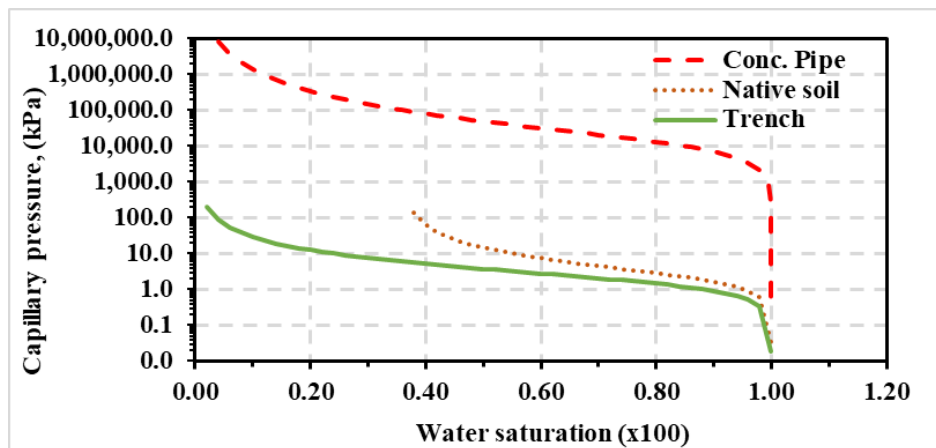
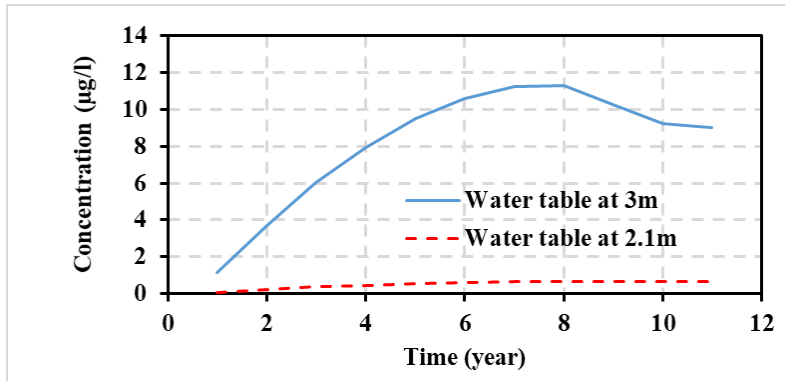
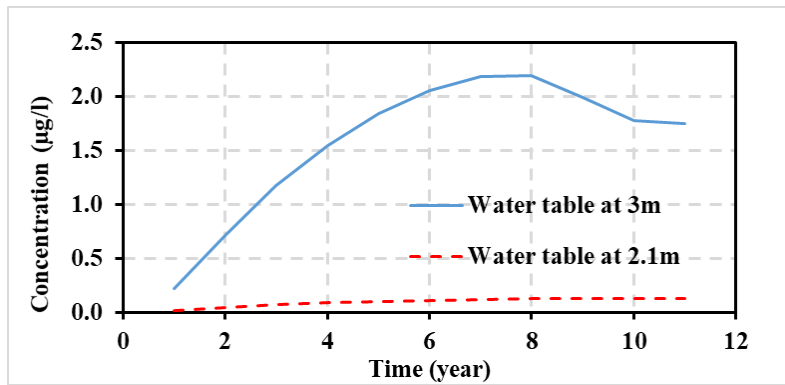


Figure 6.5 Water Retention Curves and SWCCs used in simulations.

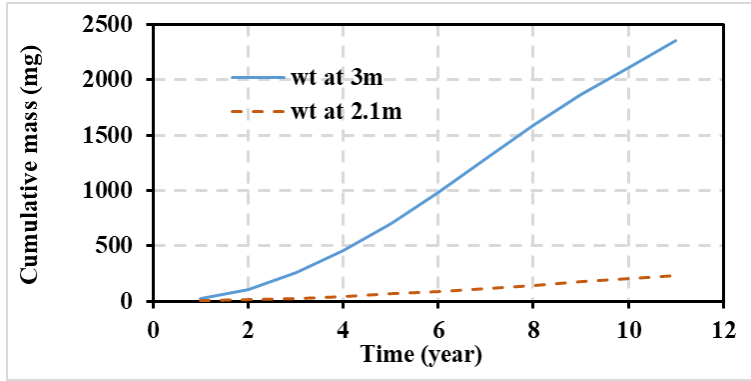


a)

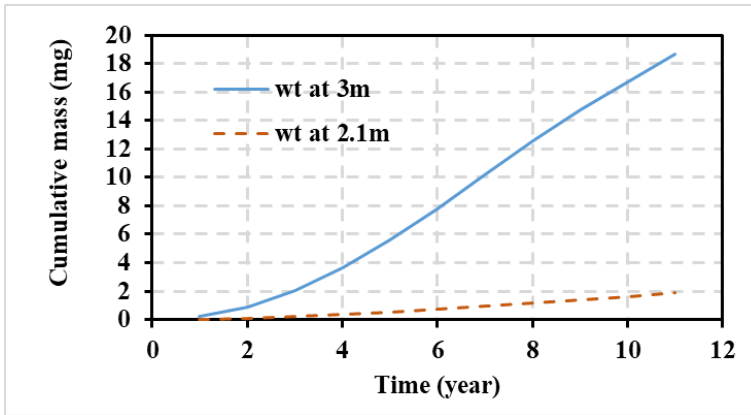


b)

Figure 6.6 Benzene concentration inside the pipe for two water table levels a) Aqueous phase b) Gas phase.



a)



b)

Figure 6.7 Cumulative mass breaking through the pipe for two water table levels a) Aqueous, phase and b) Gas phase.

CHAPTER 7. Factors Affecting Multiphase Benzene Breakthrough into Drainage Concrete Pipe in the Unsaturated Subsurface Profile

This chapter has been previously published in *Journal of Pipeline Systems Engineering and Practice*.

Abstract

Analyses presented herein explore transport aspects related to benzene breakthrough into gasketed subsurface concrete pipe embedded in unsaturated soil profile. A series of three-dimensional numerical analyses were conducted using T2VOC code. The simulations yielded results on multiphase multicomponent transport providing insights onto the effect of pipe material and gasket conditions, subsurface soil saturated and unsaturated properties, volatilization to atmosphere, and the thickness of initial contamination at the source on rate and magnitude of the transported mass. Results showed that the use of lower pipe concrete material quality led to increasing mass transport into the pipe by more than 60%. The use of damaged gasket also allowed for a considerable breakthrough of the contaminant into the pipe with two orders of magnitude higher mass compared to the use of an intact gasket. While the main mechanism of contaminant migration in vadose zone is vapor diffusion, benzene transport in the aqueous phase was the main phase breaking through the pipe walls, given the initial matric suction of the concrete pipe wall that leads to the near saturation of the pipe walls once water flow commences. The thickness of the Non-Aqueous Phase Liquid at source has relatively a secondary effect on the mass transfer into the pipe. Considering coarse-type soil material versus the sandy clay as the native soil where the pipe is located led to an increase in the concentrations in both aqueous and gas phases inside the pipe by a factor of 6 after one year.

Keywords: Concrete, Diffusion, Non-Aqueous Phase Liquid (NAPL), Numerical analyses, Pipes, Unsaturated, Utilities, Volatilization.

7.1. Introduction

Water mains and drainage pipes installed in the vadose and saturated zones may be exposed to contaminant permeation at sites with leaking Underground Storage Tanks (USTs) or with previously unregulated disposal practices. Reports of drinking water contamination in the United States revealed that petroleum products (diesel and gasoline) were involved in 89% of the incidents of permeation to the subsurface mains (US Environmental Protection Agency (EPA) 2002).

Volatile Organic Compounds (VOCs) of hydrocarbon fuels such as Benzene, Toluene, Ethylbenzene, and Xylene (BTEX) are significant environmental contaminants that can lead to high levels of toxicity upon exposure even at low concentrations. Benzene is of particular concern as it has been classified by the Department of Health and Human Services (DHHS) as Group A of known human carcinogens causing leukemia (Cornelius et al. 2013). Upon release into the environment, benzene can migrate through unsaturated soil profiles, break through the subsurface utilities, and consequently contaminates the groundwater. Benzene has significant partial vapor pressure and an aqueous phase solubility that can exceed the standard limits of drinking water by more than five orders of magnitude (Sleep and Skyes 1989).

In the unsaturated zone, contaminants can flow as solutes in the aqueous phase, as vapors in the gas phase, and as immiscible Non-Aqueous Phase Liquid (NAPL) or free product. Interphase mass transfer is controlled by mechanisms of the NAPL evaporation, the NAPL dissolution into the liquid water phase, and equilibrium partitioning of the VOC between the gas, water, and solid phases (Falta et al. 1992). The processes governing contaminant flow in unsaturated soil zone include advection, diffusion, and phase partitioning into the water, gas and solid phases. In situations with higher mobility of the gas phase, compared to the water phase (as in unsaturated soil zones), volatilization and vapor diffusion are primarily responsible for increased contamination some distances away from the source (Sleep and Skyes 1989; Rivett et al. 2011).

Previous studies have assessed contaminant migration in the unsaturated soil to i) develop models describing simultaneous three-phase transport of chemicals (e.g., Baehr et al. 1987; Van Geel 1994; Class et al. 2002) and ii) explore various scenarios of field situations and the effects of contaminant transport on the soil and groundwater (Yang et al. 2012; Pasha et al. 2014; Dafny 2017). The contaminant migration in a vadose zone with the presence of subsurface utilities has received little attention in the literature. Water mains, storm sewers, and gasketed drainage pipes provide potential pathways to transport NAPL, aqueous and vapor phase contaminations along the inside of the pipe and contaminate downstream water resources and water supply networks. If the existing characteristics of the project site are not fully understood, engineering mitigation methods may not be implemented effectively (EPA 2002).

Several laboratory studies were conducted to evaluate contaminant permeation into the different types of polymeric pipes (e.g., Holsen et al. 1991; Ong et al. 2008; Mao et al. 2010, 2011).

Mao et al. (2010) conducted Pipe-bottle tests to investigate the permeation of BTEX through high-density polyethylene (HDPE) pipe exposed to gasoline-contaminated soil; results indicated diffusion coefficients on the order of 2 to 9 $\times 10^{-9}$ cm^2/s . Through curve fitting the permeation data with a diffusion model, Mao et al. (2011) calculated the permeation rate (0.38-0.73 mg/joint/day) and diffusion coefficients of BTEX through PVC pipe joints equipped different Rieber gaskets exposed to various levels of gasoline contamination (6×10^{-8} - 1.1×10^{-7} cm^2/s).

Even though, we have not been able to find studies in the literature that specifically simulate and quantify the field-scale contaminant breakthrough into the subsurface concrete pipe installed within a vadose zone. Work by Faeli et al. (2020) revealed that the mechanism of transport in an unsaturated zone is dominated by vapor phase diffusion of VOCs. Assuming initially uncontaminated groundwater, raising the water table level leads to a significant reduction in concentration and mass breaking through the pipe. This is due to low lateral diffusive gas phase spreading as the water content in the unsaturated domain increases. Alhomair et al. (2020) assessed the efficacy of mitigation measures to minimize the contaminant ingress into subsurface concrete pipes placed under groundwater table in saturated soil conditions. Results showed the use of flowable fill in the pipe trench to be highly effective in reducing the level of contaminant breakthrough the pipeline. Hosseini et al. (2020) investigated durability and degradation rates of rubber gasket materials commonly used in stormwater drains exposed to benzene and tetrachloroethylene (PCE), proposed degradation model for such material.

The objective of the work presented herein is to quantitatively contribute the following: i. Assessment of benzene phase partitioning and the rate and magnitude of mass transport through the unsaturated media, and into the pipe trench in both gaseous and aqueous phases, ii. Demonstration of the rate and magnitude of benzene breakthrough into the different material classes of concrete pipes using data from field case study, iii. Quantifying effect of various parameters on the transport and breakthrough of benzene within the domain. These factors include pipe material quality levels, gaskets condition, volume and depth of NAPL in the domain, the presence of fine or coarse soil types, and the magnitude of volatilization to the atmosphere. The variation of the input parameters and the outcome of each analysis set are presented in a comparative manner. The numerical simulations were conducted using T2VOC code and Petrasim 2018 Graphical User Interface (GUI). Parameters from a site in North Carolina was used as a case study where the gasoline leakage from the USTs was detected.

7.2. Multiphase Transport of VOC in Subsurface

Contaminant transport in the unsaturated domain has been recognized as a complex multiphase multicomponent process. Falta et al. (1992) developed finite difference code “T2VOC” for modeling of steam displacement of the NAPL in shallow subsurface systems. The code considers three-phase flow; gas, aqueous, and NAPL and three mass components; the air, water, and an organic chemical as well as an energy heat component.

Four primary variables (water saturation, gas saturation, pressure, and temperature) are used to determine the thermodynamic state of four components (air, water, chemical, and heat) such that the local thermal and chemical phases equilibrium are established. Within the unsaturated domain, a gas phase pressure value equal to the atmospheric pressure ($P_g = P_{atm}$) is assigned as an initial pressure (P). Aqueous, NAPL and gas phase pressures are then related by gas-water and gas-NAPL capillary pressures ($P_w = P_g + P_{cgw}$; $P_n = P_g + P_{cgn}$). Through the course of steady state attainment, the gas pressure is composed of several components that include air, water vapor and NAPL vapor pressures ($P_g = P_g^a + P_g^w + P_g^n$). The initial pressures within the saturated zone below the groundwater level are computed based on the hydraulic gradient and assigned to the boundaries and several sections along the water table gradient. These initial conditions approximate the steady state solution, so facilitate the convergence.

A set of secondary variables are also needed to solve four coupled balance equations. The secondary variables include thermodynamic and transport properties, such as concentration, mole fractions, relative permeabilities, capillary pressure, viscosities, densities, molecular diffusivity, tortuosity, and enthalpies; refer to Falta et al. (1992) for more details.

A nonisothermal system containing three mass components, three mass balances, and energy balance terms, as shown in equation (1), fully describes the system.

$$\frac{d}{dt} \int_{V_l} M^K dV_l = \int_{T_l} F^K \cdot n_l dT_l + \int_{V_l} q^K dV_l \quad (1)$$

where M^K is the component mass per unit porous medium volume (K assumes the following: a =air; w = water; c = chemical; h = heat), F^K is the mass flux of component K into V_l (net flux), V_l is flow region having a surface area of T_l , n_l is outward unit normal vector, and q^K is the rate of mass generation of component K per unit volume at the source.

The mass accumulation terms, including linear equilibrium adsorption, is presented as:

$$M^K = \varphi \sum_b S_b \rho_b \omega_b^K + \rho_{bulk} \rho_w \omega_w^c K_d \quad (2)$$

where φ is porosity, S_b is b phase saturation, ρ_b is b phase density, and ω_b^K is the mass fraction of component K in b phase, ρ_{bulk} is the dry bulk density of the soil, and K_d is the soil-water distribution coefficient for the organic chemical (Freeze and Cherry 1979).

The mass flux of each component in the gas phase, included in equation (1) considers advection and diffusion:

$$F_g^K = \frac{-k k_{rg} \rho_g}{\mu_g} \omega_g^K (\nabla P_g - \rho_g g) + J_g^K, \quad J_g^K = -\varphi S_g \tau_g D_g^K \rho_g \nabla \omega_g^K \quad \left(\frac{kg}{m^2.s} \right), \quad K = c, w \quad (3)$$

where k is the intrinsic permeability, k_{rg} is the gas phase relative permeability, μ_g is dynamic viscosity, P_g is the pressure, g is the gravitational acceleration vector, and J_g^K is the diffusive mass flux of component K in the gas phase. D_g^K is the molecular diffusion coefficient of component K in the gas phase in the absence of porous medium, and τ_g is the gas phase tortuosity defined by $\tau_g = \varphi^{1/3} S_g^{7/3}$.

The mass flux in other phases considers only advection ignoring the second term, J_g^K in equation (3).

The VOC concentration as the gas phase is a secondary variable obtained from equation (1) defined as a function of primary variables as follows. We determine VOC concentration throughout the domain and inside the pipe.

$$C_g^c = \frac{P_g^c M_{wt}^c}{RT} \quad (\text{mass/volume}) \quad \left(C_g^c = \frac{m_g^c}{V_g} \right) \quad (4)$$

where M_{wt}^c is the molecular weight of chemical (g/mol), R is the universal gas constant, T is temperature, and P_g^c is the partial pressure of chemical or VOC that is defined as saturated vapor pressure in the presence of the NAPL and partial pressure in the absence of the NAPL phase.

Under conditions of local chemical equilibrium, the concentration of a compound in a phase is related to the concentration in another phase by a constant. The second term in equation (2), defined as the adsorbed concentration C_s^c , is related to concentration in the aqueous phase (C_w^c) by a coefficient (K_d) as shown in equation (5).

$$C_s^c = \rho_{bulk} K_d C_w^c, \quad K_d = K_{oc} f_{oc} \quad (5)$$

where f_{oc} is the amount of organic carbon present in the soil, and K_{oc} is the Organic carbon partition coefficient.

The equilibrium expression for the gas-liquid distribution of a dilute compound is known as Henry's law as:

$$P_g^K = H_{gw}^K X_w^K \quad K = a, c \quad (6)$$

where P_g^K is the partial pressure of component K in the gas phase, X_w^K is the mole fraction of component K in the aqueous phase, and H_{gw}^K is Henry's constant.

The multicomponent diffusivities expressed in equation (3) for water and chemical vapor in the gas phase are formulated as:

$$D_g^w = \frac{(1-X_g^w)}{\left(\frac{x_g^a}{D_g^{aw}} + \frac{x_g^c}{D_g^{cw}}\right)} \quad \text{and} \quad D_g^c = \frac{(1-X_g^c)}{\left(\frac{x_g^w}{D_g^{cw}} + \frac{x_g^a}{D_g^{ac}}\right)} \quad (7)$$

where X_g^K is the mole fraction of component K in the gas phase, and D_g^K is the multicomponent molecular diffusion coefficient of component K in the gas phase when no porous medium is present and calculated by using binary diffusivity (air-water and air-chemical diffusivities) as below:

$$D_g^{ij} = D_g^{ijR} (P_R/P_g) (T/T_R)^{\theta_{ij}} \quad (8)$$

where D_g^{ijR} (Reference binary diffusivity) is the experimentally determined i-j binary diffusivity at a temperature T_R and pressure of P_R , and θ_{ij} is an experimentally determined constant. D_g^{cw} or water-chemical diffusivity is calculated using Wilke and Lee empirical correlation (Reid et al. 1987).

The capillary pressure relationships from Parker et al. (1987) and relative permeabilities from Stone (1970) are determined as secondary variables. The secondary variables are needed to solve the mass balance equations (1) and (3). The parameters needed for defining capillary pressure relationships are residual water saturation (S_m), and fitting parameters (n , α_{gn} , α_{nw}). The parameters needed to define relative permeabilities are residual saturations (S_{wr} , S_{nr} , S_{gr}) and fitting parameter (n). The approach utilized herein extends the capillary pressure–saturation functions for a two-phase system by Van Genuchten (1980) to define a three-phase system using scaling factors. The scaling factors are determined using the interfacial tension (σ) per Parker et al. (1987) approach.

Primary variables (initial input) permanently switched during simulations based on the type and number of phases existed in the system. For example in a three-phase system, when $S_g + S_w \geq 1$ the NAPL phase disappears and the two-phase water-gas system is substituted for the previous three-phase setting and primary variables are switched from (S_w , S_g , P , T) to (S_w , X_g^C , P , T). In such

a fashion, the three-phase system transforms to two-phase NAPL-water if $S_g < 0$, two-phase water-gas transforms to single-phase water when $S_w > 1$, single-phase water to two-phase water-NAPL (or two-phase water-gas to three-phase) if $X_w^C > \underline{X}_w^C$ (solubility limit at prevailing temperature), single-phase water to two-phase water-gas (or two-phase water-NAPL to three-phase) if $P_g > P_{hydrostatic} + P_{atm}$ as presented by Pruess et al. (2002).

7.3. Case Study

7.3.1. Site Description

The case study site has a gas station with nearby subsurface utilities on the west side of the right-of-way adjacent to the gas station, as shown in Figure 1. The site includes natural gas, water, sewer, stormwater and communication lines. A release from the USTs was discovered after the gas station permanently closed in 1998 and the tank was filled with flowable fill. The facility currently operates new gasoline USTs. Recovered soil sampling revealed soil contamination above Maximum Soil Contaminant Concentrations (MSCC) (Terracon 2018). The MSCC value along with the allowable benzene concentrations in various media is shown in Table 1. Water lines are measured to be at 0.9 m deep while sewer lines are located 1.2 m in depth. Most of the utilities are located at depth 0.6-1.7m below the ground surface. The focus of the analyses herein is on the rate and magnitude of benzene breaking through subsurface drainage concrete pipe adjacent to leaking underground storage tanks where benzene, an LNAPL, is present due to such leakage. The present work explores the transport of benzene phases through unsaturated porous media and the breakthrough of such phases onto field-scale concrete pipes. Such data which specifically address the placement of concrete pipes within contaminated and unsaturated subsurface domain and the corresponding transport of benzene phases is lacking in literature.

The subsurface soil layers are found to be moderately to well-drained silt and silty clay to a depth of approximately 0.9 m below the ground surface underlain by clay to a depth of about 2.4 m and then sandy clay, clayey sand or silty clay to a depth of about 3 m. The permeability ranges from 6.24×10^{-7} m/s to 9.07×10^{-7} m/s with an average of 7.33×10^{-7} m/s (Delta 2000). The average hydraulic gradient of groundwater flow is 1% with northeast direction.

The site map is shown in Figure 1, locating the gas station, the monitoring wells, model domain and groundwater flow direction. Benzene persisted at concentrations in excess of regulatory limits and a NAPL thickness of about 0.5 m was detected in 2016 at Monitoring Well-

12 (MW-12) located nearby the storm drain (Figure 1). BTEX was reported with a concentration of 3207 mg/kg at boring P43-SB-05 near the drainage pipe (Antea 2016; Terracon 2018).

7.3.2. Model Development

The numerical model was used to simulate the released benzene as the NAPL with an adjacent subsurface concrete pipe under unsaturated soil conditions. The model domain has been selected based on the extent of the plume, pipe joints distance, boundaries, and monitoring well locations. The 3D domain was simulated using dimensions of 30 m × 15 m × 6 m. A schematic sketch of the model domain is shown in Figure 2. A pipe 0.5 m in diameter (OD=0.6 m, ID=0.5m), embedded 1.5 m below the ground surface, was simulated in the model. The distance of 1.5 m was determined from spring line of the pipe. The domain's horizontal distance (x-direction) was large enough to contain MW-4 and MW-12; these are two sampling wells with the highest contaminant concentrations (Antea 2016). The other horizontal distance of 15m (z-direction) was chosen considering pipe gasket locations at 2.5m from each other. The model included five gaskets along the pipe. In the vertical direction (y-axis), the model depth encompassed the extent of benzene contamination, which did not exceed 6 m from the surface according to the monitoring wells data (MW-4 data, Delta 2000).

Figure 3 exhibits model configuration and discretized domain and pipe. The mesh was constructed of 76,140 cells with grid size refined toward the location of the pipe.

The groundwater table was set at ~ 3 m from the surface with a flow gradient as 1% (0.3 m difference in depth between left and right boundaries). This represented the possible lowest groundwater level considering seasonal changes.

A top boundary layer that is 0.005 m in thickness was applied to model atmospheric layer boundary condition. To simulate the conditions representative of the atmosphere layer, the uppermost layer was assigned as fixed atmospheric pressure and temperature. Moreover, the capillary pressure was set as zero at this layer. In addition, the layer was assigned a water saturation smaller than residual water saturation, liquid relative permeability as zero, and gas relative permeability as '1'; thereby, allowing for gaseous emission to the atmosphere. The water table gradient was established by fixed hydrostatic pressures at right and left side boundaries. Two fixed boundary conditions with near atmospheric pressure were applied at two ends of the pipe, while half full flow was assumed inside the pipe from back to the front face. No-flow boundary condition has been assumed for the remaining boundaries.

7.3.3. Model Parameters

The native subsurface soil is mostly sandy clay with intrinsic permeability of $6.4 \times 10^{-14} \text{ m}^2$ (permeability as $6.24 \times 10^{-7} \text{ m/s}$, Delta 2000). The permeability in the vertical direction was considered as half of the value in the horizontal direction (Bagarello et al. 2009; Qiu et al. 2015). To define capillary pressure and relative permeability of subsurface materials, the governing equations from Parker's three-phase functions (Parker et al. 1987) and Stone's three-phase equations (Stone 1970), were used, respectively. The trench where the pipe was located comprised of 0.15 m sandy gravel as the bedding material, overlain by 0.9 m sandy soil as initial backfill, and 0.9 m native soil as the final top backfill. The properties of materials used in the model are presented in Table 2 and Table 3. The zones to which these properties are assigned are schematically depicted in Figure 2 and Figure 3. To study different scenarios, sandy soil from UNSODA database (Nemes et al. 2015, USDA website) with a higher intrinsic permeability of $2.05 \times 10^{-12} \text{ m}^2$ (permeability as $2.00 \times 10^{-5} \text{ m/s}$) was used as representative of the native soil 2 and two-phase fitting parameters, α_{gw} and n were determined using RETC code (Released date 1994, EPA website).

Two-phase parameters, α_{gw} and n were obtained from the references noted in Table 3. For native soil 2, in a second scenario, and pipe materials used in the simulations (Table 3), only two-phase parameters were available; hence, scaling factors were used to determine three-phase parameters; α_{gn} , α_{nw} and α_{gw} . The α_{gn} and α_{nw} are computed as product of scaling factors and α_{gw} . The scaling factors have been calculated by equation (9).

$$\beta_{gn} = \frac{\sigma_{nw} + \sigma_{gn}}{\sigma_{gn}} = \frac{0.029 + 0.035}{0.029} = 2.2 \quad , \quad \beta_{nw} = \frac{\sigma_{nw} + \sigma_{gn}}{\sigma_{nw}} = \frac{0.029 + 0.035}{0.035} = 1.82 \quad (9)$$

where $\sigma_{nw} = 0.035 \text{ Nm}^{-1}$ and $\sigma_{gn} = 0.029 \text{ Nm}^{-1}$ are the interfacial tension and surface tension for benzene, respectively, at $20 \text{ }^\circ\text{C}$ (Mercer & Cohen 1990). Parameters $\beta_{gn} = 2.2$ and $\beta_{nw} = 1.82$ are in agreement with scaling factors from Van Genuchten regression analyses (Parker et al. 1987).

Three different conditions for concrete pipe materials (high-, medium-, and low-quality) and two gasket conditions of "intact" (undamaged) and "damaged" were considered in the analyses. According to the ASTM C76 and C14, all concrete used for reinforced or non-reinforced concrete pipes should have a water-cementitious materials ratio not exceeding 0.53 by weight. If w/c ratio higher than 0.53 is used, it must be demonstrated that the quality and performance of the

pipe meet the test and design requirements of these standards. The high, medium, and low-quality concrete, as defined herein, correspond to w/c ratios within ranges of [0.4-0.45], [0.45-0.5], and [0.55-0.6], respectively. The w/c of the concrete used in manufacturing concrete pipe in this case study was 0.42.

For the intact (undamaged) gasket, permeability was considered to be the same as concrete material, and for the damaged gasket, higher permeability than that of concrete was assumed (i.e., value similar to the permeability of the soil; see Table 2 and Table 3 for values). It is noteworthy to mention that neither advection nor diffusion-defined permeability values of the gasket material are available in the literature.

Mechanical dispersion was neglected and only molecular diffusion in the gas phase was considered in addition to advection in gas and liquid phases. However, T2VOC produces a velocity-dependent numerical dispersion using upstream weighting for stability. The computation of the diffusivities for water vapor and the vapor phase of benzene is carried out using equations (7) and (8) and the binary diffusivities are summarized in Table 4. In such a manner, the molecular diffusion coefficients of D_g^c and D_g^w are calculated as 8.65×10^{-6} m²/s and 2.13×10^{-5} m²/s, respectively; however, these values do not account for the presence of the porous media. According to equation (3), diffusion coefficients in porous media account for gas saturation, porosity, and tortuosity. The gas saturation within the native soil varies from 9% above the capillary fringe to 56% near the top surface. Accordingly, in native soil where gas saturation is 50%, the diffusion coefficient of vapor benzene is determined to be as 2.3×10^{-7} m²/s. However, in trench materials with gas saturation about 85%, the diffusion coefficient of vapor benzene is 1.2×10^{-6} m²/s, and for the concrete, the diffusion coefficient is calculated as 1.18×10^{-11} m²/s (equation (3)).

Chemical partitioning into the solid phase was defined by the adsorption coefficient (K_d) as defined in the equation (5). Degree of organic chemicals adsorption (C_s^c) is mainly dependent on the quantity of organic carbon in the soil (f_{oc}). The soil organic carbon content was specified in a range of 0.4-13.9 g per kg of soil (0.04-1.4 %) depending on the soil textures and depth within coastal plain regions of North Carolina (Deiss et al. 2017). Delle et al. (2001) measured K_d for benzene transport for different soil textures and with different organic carbon fractions. According to their studies, f_{oc} was in the range of 0.2-12% for clayey sand and 0.006-0.2% for sandy materials. Since the types of sand commonly used as backfill material in the pipe trench have very low organic carbon content, compared to the native soil (EPA 2002), f_{oc} as 0.1% was assumed for the

whole domain. K_d was estimated to be equal to $8.5 \times 10^{-5} \text{ m}^3/\text{kg}$ while k_{oc} was assigned as $0.085 \text{ m}^3/\text{kg}$ (Delle et al. 2001), as shown in Table 4.

7.3.4. Simulation Approach

The simulations were implemented following several steps. An initial run was made to establish the static gravity-capillary equilibrium of the water saturation profile within the subsurface domain before contamination release. Due to substantial differences between capillary properties of the subsurface materials, including concrete, equilibrium convergence was reached through sequential simulation runs; one time without pipe but including groundwater gradient, then the second time with the concrete pipe introduced in the domain. The initial water saturation and pressures were defined based on Soil-Water Characteristic Curves (SWCCs) for soil materials, and Water Retention Curves (WRCs) for the concrete pipe materials (Figure 4). When groundwater table level changes, different initial water saturations and soil matric suctions were defined based on the new elevation of the water table. Because of the high capillary pressure of concrete, the pipe walls remained mostly saturated, while the trench around the pipe had the lowest water content in the domain.

After establishing equilibrium, contaminants were released into the domain, and the long-term redistribution of contaminant with time and the transport to the subsurface concrete pipe were examined. Benzene was released as the NAPL and as a percentage of maximum detected BTEX (3207 mg/kg) with the degree of saturation of benzene as the NAPL phase (S_n)= 10 % at 1.2 m to 1.8 m from the ground surface over an area of $4 \text{ m} \times 10.5 \text{ m}$ around MW-12. This is the location where the NAPL phase was detected (data from Antea 2016). The area of benzene plume is delineated in Figure 2 and Figure 3. After the source domain had been assigned, the long-term redistribution of benzene in different phases was allowed. The flowchart presented in Figure 5 summarizes the simulation approach.

7.3.5. Sensitivity Analyses of Domain and Mesh Size

A series of mesh sensitivity analyses were executed to assess the proper dimensions and ascertain no effect of the mesh size on the outcome. Since this study was focused on the lateral transport of contamination from the source to the pipe, five simulations with 15, 20, 27, 30, and 33 m distances in x-direction along with the direction of laterally transport of benzene were carried out. Figure 6a shows two of the five model configurations with 15 m and 33 m in horizontal distances. The contaminant transport into the pipe was quantified within two years after the initial

contaminant release at the source, as shown in Figure 6b. Results indicated no discernible effect on the concentrations infiltrating into the pipe by increasing the horizontal dimensions beyond 30 m. Therefore, 30 m of horizontal dimension was used in the model domain. The grid mesh size increasing from 0.8 m to 2 m within the domain, except for the pipe and the trench area, did not affect the transport calculations. Consequently, the coarser mesh was used in the domain outside of the trench location.

7.3.6. Model Verification

The benzene concentrations of groundwater samples measured by Antea group (2016), as shown in Table 5, were compared to the benzene concentrations calculated by the model at the same location and depth. Figure 7 shows the benzene concentrations as the aqueous phase at the location of MW-4, as obtained from the model results. The assessment of these simulations is started from 2016 when the NAPL was observed at the site. As indicated by data in Table 5, the concentration was reported to be 17,900 $\mu\text{g/l}$ at MW-4 in 2016, while it was measured to be in a range of 13,000 -17,000 $\mu\text{g/l}$ in 2013.

The simulation analyses indicated that the aqueous phase concentration at MW-4 reached to 17,900 $\mu\text{g/l}$ at the end of the second year of simulation after the release. The concentration increased to 18,500 $\mu\text{g/l}$ at the end of the third year, after which it decreased to 15,000 $\mu\text{g/l}$ in the seventh year. The lower concentration of 14000 $\mu\text{g/l}$ in the first year relates to the delay in contaminant transport from the initial NAPL phase at MW-12 to the location of MW-4. The extent of agreement between the concentrations in the aqueous phase obtained from the model in seven years after the release (14,000-18,500 $\mu\text{g/l}$) and from the monitored data by Antea (2016) (13,000 to 19,000 $\mu\text{g/l}$) is revealed by comparing the results from Table 5 and Figure 7 at the location of MW-4. The concentrations at the right side of the model domain were obtained to be lower than 1 $\mu\text{g/l}$ in agreement with the monitored data from MW-6 and MW-8, as shown in Table 5.

7.4. Results and discussion

Investigated factors affecting multiphase contaminant infiltration into the drainage concrete pipe in the unsaturated subsurface profile included the pipe material quality, damaged and undamaged gaskets, soil parameters, the NAPL thickness at the source location, and evaporation to the atmosphere. Since the NAPL plume was introduced as a finite mass in a specific area, it could not move much further from the source zone and reach the pipe location. Previous

studies verify this observation for the contaminant development toward the water table (Sleep and Skyes 1989).

Results indicated that the initial NAPL saturation ($S_n=0.1$) at the source location around MW-12 is depleted through partitioning into the gas and aqueous phases within seven years after release in the case of the water table at 3 m from surface and the NAPL thickness of 0.6 m. If the NAPL thickness decreases to 0.3 m, it takes about two and half years for the NAPL to partition into different phases and disappear from the domain. The relatively fast time to depletion is explained by the initial condition of the un-contaminated subsurface profile except for the location of the initial benzene release. Phase partitioning and contaminant transport continue until the equilibrium will be set in the domain. When the groundwater table rises toward the surface, gaseous transport and evaporation to the atmosphere decrease, and as a result, the NAPL phase depletion decelerates as well. Figures 8a and 8b show gas and aqueous fluxes in the domain.

7.4.1. Pipe Material Quality

The unsaturated transport properties of concrete materials are dependent on the mixture proportions, water-to-cement (w/c) ratio of the binder, and the presence of microcracks. Kumar et al. (2010) estimated Van Genuchten capillary pressure parameters for different w/c ratios of concrete specimens using vapor equilibrium experiments (i.e., sorption isotherms). Results by Kumar et al. indicated that variations in the mixture proportions and w/c ratio affect the saturated permeability, water retention, and relative permeability. In general, at a given capillary suction, the degree of saturation is higher for concrete with a lower w/c ratio. This higher degree of saturation is due to the presence of a smaller size of pores in lower w/c ratio concrete mixes as compared to high w/c concrete. The presence of microcracks in the concrete is recognized as a major factor affecting the transport properties of concrete. Ghasemzadeh et al. (2015) studied the effects of distributed microcracks on the transport properties of concrete. Their findings indicated that the saturated permeability of concrete can increase by two orders of magnitude with the presence of cracks.

To study the effect of the pipe material quality on the contaminant breakthrough into the pipe, we implemented simulations by considering different concrete qualities (corresponding to different w/c), which affect the saturated and unsaturated properties of concrete.

The three different concrete qualities are qualitatively denoted by “high,” “medium”, and “low” with the corresponding numerical properties shown in Table 2 and Table 3. The

corresponding w/c ratios fall within ranges of [0.4-0.45], [0.45-0.5], and [0.55-0.6], respectively for high, medium and low qualities. In this study, the saturated permeability and unsaturated properties were obtained from Kumar et al. (2010) and Smyl et al. (2016) based on mixture proportions. These properties were modified by scaling factors (see equation (9)) to be used in multiphase multicomponent transport. The capillary pressures of pipe materials (note α_{ij} in Table 3) are three to four orders of magnitudes higher than the soil materials (Leech et al. 2006; Bao et al. 2017). This significant difference could be explained by the microstructure of concrete, distribution of pore size diameter, tortuosity, and connectivity (Kumar et al. 2010). As indicated in Table 3, the residual saturation of concrete mixtures was assumed to be 0.2 (Kumar et al. 2010). In all simulations, the water table level was located at 3.0 m below the ground surface.

Our analyses indicate that the fitting parameters defining the unsaturated properties of concrete for low, medium, and high quality significantly impact the contaminant breakthrough the pipes. As shown in Figure 9a and Figure 9b, the benzene concentrations in aqueous and gas phases inside the pipe reach peak values after eight years and gradually decrease thereafter to reach the rate of breakthrough equal or less than 0.3 $\mu\text{g/l}$ per year in the eleventh year. Rates of breakthrough with time indicate that the rate in the aqueous phase for medium- and low-quality concrete materials are 2.5 and 4 $\mu\text{g/l}$, respectively, per year in the first year and 0.19 and 0.3 $\mu\text{g/l}$ per year, respectively, in the eleventh year. The rates in the gas phase are less than 0.05 $\mu\text{g/l}$ per year in the eleventh year. The peak concentrations along the pipe in the aqueous phase are 18.7, 11.3 and 2.6 $\mu\text{g/l}$ and in the gas phase are 3.6, 2.2 and 0.5 $\mu\text{g/l}$ for low, medium and high-quality concrete materials, respectively. These concentrations are above the thresholds of 5 $\mu\text{g/l}$ (Maximum Contaminant Level, MCL) and 1.2×10^{-4} $\mu\text{g/l}$ (Acceptable Ambient Levels, AAL). The allowable benzene concentrations are shown in Table 1. The high-quality pipe with w/c=0.4-0.45 leads to having peak concentrations inside the pipe below MCL in the aqueous phase. Breakthrough concentrations into the medium and low-quality pipes are lower than MCL up to two years after release; however, as the contamination is redistributed the peak concentration increases to the higher levels than the standard concentration of MCL. The concentrations in the gas phase for all cases exceed AAL.

We computed the cumulative mass of benzene breaking through the pipe in aqueous and gaseous phases per equation (10) using gas and aqueous fluxes at individual model cells of the pipe. The analyses are done per time increments and are shown in Figures 10a and 10b.

$$\text{Cumulative mass} = \sum_{t=1}^n (\text{time periods}) \text{ Flux of VOC in gas or water } \left(\frac{\text{mass}}{\text{time}} \right) \times \Delta t (\text{time}) \quad (10)$$

The total released NAPL (8.4×10^8 mg) has been partitioned into the adsorbed mass to the soil, aqueous, gas, and NAPL phases from which aqueous and gas phases permeate into the pipe. Mass calculations using equation (10) show 5,031 mg in the aqueous phase breaks through the pipe in case of low-quality material, and 2,355 mg and 811 mg for medium- and high-quality materials, respectively (Figures 10a and 10b). The breakthrough mass in the gas phase is calculated as 40, 19, 6 mg for low, medium, high quality, respectively. Using the medium-quality material of pipe as a “base case” with $w/c=0.45-0.5$, the peak concentrations in both aqueous and gas phases inside the pipe increase by 65% in case of low-quality material and decrease by 77% in case of high-quality pipe. The cumulative mass penetrating the pipe increases by 114% and decreases by 65% and in case of low and high-quality materials, respectively, compared to the base case.

The VOC diffusion coefficients in the gas phase are up to 4 orders of magnitude higher than the coefficients for the aqueous phases (Rivett et al. 2011) and gaseous diffusion is identified as the main factor of the lateral transport in the unsaturated soil. However, the cumulative mass ingress into the pipe is dominated by aqueous fluxes instead of the gaseous ones. This predominance of aqueous transport through the concrete wall of the pipe is explained by the close-to-saturation state of concrete material as a result of high initial matric suction of the concrete. Once the pipe walls are saturated, the gas phase diffusion into the pipe is limited. Although the gas diffusion in the second term of equation (3) does not account for the microstructure of concrete, much lower gaseous saturation of concrete suppresses the gas diffusion term. The relative permeability of the gas phase (K_{rg}) in the first term of equation (3) for concrete is equal to zero, ignoring gaseous advective fluxes while it is about 0.8 within the trench materials. However, the concentrations inside the pipe in both phases are in equilibrium and can go beyond the limits suggested by standard guidelines.

7.4.2. Gasket Material Quality

Mass transfer surface area associated with the gasket is considerably smaller than that associated with the concrete pipe. As such, gaskets usually are not primary pathways for the permeation (EPA 2002). However, if gaskets lose their functionality due to damage or incorrect installation, then there is a potential of contaminant transport.

When damage occurs in the gaskets, the contaminants within the trench may break through the pipe with higher fluxes compared to the breakthrough the undamaged gasketed pipes. The contaminant transport in two scenarios of severe-damaged and undamaged gaskets are compared herein in terms of aqueous and gaseous phases breaking through the pipe. The properties of damaged and undamaged gaskets are indicated in Table 2 and Table 3.

In the case of damaged gasket, the benzene peak concentration inside the pipe reaches 2800 $\mu\text{g/l}$ in the aqueous phase as shown, in Figure 11a and 550 $\mu\text{g/l}$ in the gas phase, as indicated in Figure 11b within 2 years after release. In comparison, a maximum concentration of 11.3 $\mu\text{g/l}$ in the aqueous phase and 2.2 $\mu\text{g/l}$ in the gas phase gradually accumulate over eight years in the case of undamaged-condition gaskets. Furthermore, the cumulative mass infiltrating into the pipe in the case of the damaged gaskets is compared with the undamaged ones as indicated in Figure 12a and Figure 12b. In the case of damaged gaskets, the cumulative mass inside the pipe increases to 284,000 mg in the aqueous phase and 2,245 mg in the gas phase. In comparison, in the case of the undamaged gaskets, these values are 2,355 mg and 19 mg in aqueous and gas phases, respectively.

7.4.3. The NAPL Phase Thickness at the Source

The thickness of the NAPL found in MW-12 was reported to be about 0.5 m. The NAPL thickness measured in a monitoring well usually exceeds the NAPL-saturated formation thickness in the surrounding ground by a factor between 2 and 10 (Mercer and Cohen 1990). However, as the groundwater table (and therefore also the NAPL) fluctuates, the residual NAPL will remain in parts of the pore spaces which it initially occupied. The residual NAPL entrapment in the pores may result in reduced migration when the water table rises to the ground surface and eventually lead to a decrease in the NAPL thickness monitored in the wells (Fetter 1999).

The observed NAPL thickness in the monitoring wells may not be a representative of the NAPL thickness in the entire contaminated area; thus, two scenarios assuming the NAPL thickness as 0.3 m and as 0.6 m were used in the analyses. In these analyses, medium-quality pipe material and undamaged gaskets were assumed. Results indicated that by reducing the thickness of initial NAPL benzene at the source, the concentrations inside the pipe decreased by 13% after three years in both aqueous and gas phases, as shown in Figures 13a and 13b. The peak concentrations reduced from 11.3 $\mu\text{g/l}$ to 9.8 $\mu\text{g/l}$ in the aqueous phase and from 2.2 to 1.9 $\mu\text{g/l}$ in the gas phase along the pipe. Using the NAPL thickness of 0.6 m, data in Figures 14a and 14b show that the cumulative mass flow in the pipe decreased to 1,889 mg in the aqueous phase and to 15 mg in the gas phase.

These values represent a decrease in mass transport by 20% compared to the 2,355 mg and 19 mg in aqueous and gas phases, respectively, when the initial NAPL thickness of 0.6 m was assumed.

7.4.4. Native Soil Material

The analyses were conducted using a sandy soil material as the native soil with a permeability two orders of magnitude higher than the one for original sandy clay native soil, as shown in Table 2. The unsaturated properties are indicated in Table 3, as well. The soil was selected from the UNSODA database (Nemes et al. 2015, USDA website), and the unsaturated parameters were determined using RETC code (Released date 1994, EPA website). The scaling factors described in the model parametrization were used to obtain the unsaturated soil properties.

Results indicate that coarse materials with lower water content facilitate the gas phase diffusion. When permeability of the native soil was increased by two orders of magnitude, the concentrations inside the pipe in both aqueous and gas phases increased by approximately factor of 6. The concentrations inside the pipe rise to 10 $\mu\text{g/l}$ in the aqueous phase and 2 $\mu\text{g/l}$ in the gas phase one year after release compared to the 1.7 and 0.32 $\mu\text{g/l}$ in aqueous and gas phases, respectively when the native soil is sandy clay with two orders of magnitude lower permeability value.

7.4.5. Emission to the Atmosphere Layer and Adsorption

The cumulative mass emitted to the atmosphere was calculated by using mass fluxes in the gas phase at the top boundary layer. Data in Table 6 show the total mass partitioned into the different phases within the domain, including emitted vapor phase to the atmosphere. By comparing the mass exiting the system at each period to cumulative mass volatilized to the atmosphere after 11 years of simulations, results indicate that more than 98% of the mass loss from the system occurs through emission to the atmosphere (note Table 6). The total mass of VOC remained in the system after eleven years was estimated to be 1.5×10^6 mg compared to the initially released mass equal to 8.40×10^8 mg. During the first year after release, 16% of released mass emits to the atmosphere, which limits contaminant transport into the pipe. Most of the initial mass evaporated into the atmosphere after 11 years of simulation is in general agreement with the previous studies. Dafny (2017) found at the end of the disposal period of 10 years, the cumulative mass emitted to the atmosphere consists of 80%–86% of the total released VOC. Considering various types of land covers, it was shown that the atmosphere layer has the most impact on

lowering the VOC evolution in the subsurface leading to a reduction of transfer to the groundwater by an order of magnitude (Dafny 2017).

Adsorption to the soil mass impedes the benzene migration in the presence of fractional amounts of organic carbon of 0.1%. Normalized adsorbed mass as a percentage of total remained mass at the end of each simulation year is shown in Table 6. The percentage of adsorbed mass compared to the total mass remaining in the domain can vary from 4-5% in the first year to 34% in the eleventh year. These findings are in concert with results presented by Holsen et al. (1991), which indicated that under identical conditions, the pipes buried in a soil of high organic carbon content were permeated more slowly than pipe buried in a soil of low organic carbon content.

7.5. Conclusions

The effect of the pipe material quality and the associated unsaturated properties on the transport of benzene in the unsaturated domain and contaminant breakthrough concrete pipes were investigated. The main mechanism of contaminant transport in the vadose zone is through vapor phase diffusion. However, given the initial suction level of the concrete pipe wall, and the fact that the pipe wall is mostly saturated, the aqueous phase of benzene is the main phase breaking through the pipe surface area, while the gas phase is the main phase breaking through the gasket if the gasket is damaged (i.e., has high permeance). Based on the results of the analyses presented herein, the following conclusions are advanced:

i. After two and half to seven years from the release, and depending on the NAPL phase thickness within the domain, the contamination mass source will disappear through partitioning into the solid, aqueous and gas phases. In such case, the contaminant is transported to the location of the pipe by diffusion in the gas phase or advection in both aqueous and gaseous phases.

ii. The simulations for three levels of concrete pipe quality indicate that the peak concentrations inside the pipe increase by 65% for low-quality pipe and decrease by 77% for high-quality pipe compared to the concentrations estimated for the medium-quality pipe (base case).

iii. The analyses results show that most of the transported benzene mass is breaking through the pipe as the aqueous flux through the pipe surface rather than gaseous fluxes. The high capillary pressure, in addition to the high saturation level of concrete, in this case, hinders the gas diffusion. However, the concentrations inside the pipe in both gas and aqueous phases are in equilibrium and there is potential for gaseous concentrations to exceed Acceptable Ambient Levels. The

cumulative mass penetrating the pipe decreases by 65% and increases by 114% in the case of high- and low-quality concrete materials, respectively, compared to the base case.

iii. The analyses for the damaged versus undamaged gaskets indicates that severe-damaged gaskets, as defined herein, can increase the concentrations and mass transfer into the pipe in both gas and aqueous phases by more than two orders of magnitude. The high contaminant concentrations accumulated in the pipe trench percolate into the pipe within two years after the NAPL release.

iv. The thickness of the NAPL at the source has relatively a secondary effect on the concentration and mass transfer into the pipe. Reducing the NAPL phase thickness at the source by a factor of two, led to the decrease in the peak concentrations in both aqueous and gas phases by 13% and reduction in the mass transported into the pipe by 20%.

v. Considering the coarse-type soil material versus the sandy clay as the native soil, where the pipe is located, an increase in the soil permeability by two orders of magnitude led to an increase in the concentrations in both aqueous and gas phases inside the pipe by approximately 6 times after one year.

vi. Benzene is lost through volatilization to an atmospheric layer at the top of the system domain, and, as such, lessened the contaminant transfer into the pipe. The results indicate that 16% of benzene is emitted to the atmosphere after one year and most of it dissipates after eleven years.

The investigations in the present paper are limited to reinforced concrete pipe without embedded steel cylinder. Embedded steel cylinders are used in water distribution networks and the presence of steel cylinder changes their transport properties significantly. The findings of the present work do not apply to concrete pipes with embedded cylinder (e.g., pressure pipes).

Table 7.1 Allowable benzene concentration.

Criteria	Unit	Allowable for benzene	Reference
Acceptable Ambient Levels (AAL) (Concentration in air)	µg/l	1.2×10^{-4}	NC DEQ, 15A NCAC 02D.1104 toxic air pollutant guidelines, (2018)
Maximum allowable concentration in groundwater suitable for drinking	µg/l	1	NC DEQ, 15A NCAC 2L .0202 Groundwater quality standards (2016)
Maximum Contaminant Level (MCL) (concentration in drinking water)	µg/l	5	EPA (2002)
Maximum Soil Contaminant Concentration (MSCC)	mg/kg	0.0056	NC DEQ, 15A NCAC 02L .0411 Maximum soil contaminant concentrations (2007)

Table 7.2 Main petro-physical properties of soil and concrete materials.

Soil type	Density	K_v	K_h	Intrinsic k_v	Intrinsic k_h	Porosity
	kg/m ³	m/s	m/s	m ²	m ²	
Native soil 1 (sandy clay)	2700	3.12×10^{-7}	6.24×10^{-7}	3.20×10^{-14}	6.40×10^{-14}	0.37
Final backfill (sandy clay)	2700	4.68×10^{-7}	9.36×10^{-7}	4.80×10^{-14}	9.60×10^{-14}	0.38
Native soil 2 (sand)	2700	1.00×10^{-5}	2.00×10^{-5}	1.025×10^{-12}	2.05×10^{-12}	0.34
Initial backfill	2700	7.50×10^{-4}	1.50×10^{-3}	7.70×10^{-11}	1.54×10^{-10}	0.34
Bedding material	2900	5.00×10^{-3}	1.00×10^{-2}	5.13×10^{-10}	1.03×10^{-9}	0.32
High qual. pipe	2800	2.10×10^{-11}	2.10×10^{-11}	2.16×10^{-18}	2.16×10^{-18}	0.121
Med. qual. pipe	2800	3.90×10^{-11}	3.90×10^{-11}	4.00×10^{-18}	4.00×10^{-18}	0.125
Low qual. pipe	2800	5.85×10^{-11}	5.85×10^{-11}	6.00×10^{-18}	6.00×10^{-18}	0.131
Undamaged gasket	1500	3.90×10^{-11}	3.90×10^{-11}	4.00×10^{-18}	4.00×10^{-18}	0.1
Damaged gasket	1500	3.90×10^{-7}	3.90×10^{-7}	4.00×10^{-14}	4.00×10^{-14}	0.1
Flow	2700	1.00×10^{-1}	1.00×10^{-1}	1.00×10^{-8}	1.00×10^{-8}	0.999
Atm.	2700	1.00×10^{-2}	1.00×10^{-2}	1.00×10^{-9}	1.00×10^{-9}	0.999

Table 7.3 Capillary pressure and relative permeability of different soils and concrete.

Soil type	S_m	n	α_{gn} (m^{-1})	α_{nw} (m^{-1})	α_{gw} (m^{-1})	S_{wr}	S_{nr}	S_{gr}	n	Reference
Native soil 1 (sandy clay)	0.36	1.86	10.8	6	3.2	0.38	0.07	0.01	3	CP (Parker 1987)
Final backfill sandy clay	0.36	1.86	10.8	6	3.2	0.38	0.07	0.01	3	RP (Battistelli 2008)
Native soil 2 (sand)	0	1.56	9.6	7.94	4.35	0.15	0.05	0.01	3	UNSODA , RETC Code
Initial backfill	0	1.84	10	11	5.2	0.15	0.05	0.01	3	CP (Parker 1987)
Bedding material	0	1.84	10	11	5.2	0.15	0.05	0.01	3	RP (Battistelli 2008)
High qual. pipe	0.2	1.51	1.14×10^{-3}	9.4×10^{-4}	5.16×10^{-4}	0.2	0.05	0.01	3	(Smyl et al. 2016), (Kumar 2010)
Med. qual. pipe	0.2	1.5	1.7×10^{-3}	1.3×10^{-3}	7.4×10^{-4}	0.2	0.05	0.01	3	
Low qual. pipe	0.2	1.48	2×10^{-3}	1.65×10^{-3}	9.04×10^{-4}	0.2	0.05	0.01	3	
Undamaged gasket	0.2	1.5	1.7×10^{-3}	1.3×10^{-3}	7.4×10^{-4}	0.2	0.05	0.01	3	
Damaged gasket	0.2	1.5	1.7×10^{-3}	1.3×10^{-3}	7.4×10^{-4}	0.2	0.05	0.01	3	
Flow	0	1.8	0.5	0.25	0.17	0.1	0.05	0.01	3	
Atm.			no capillary pressure			0.6	0.01	0	3	(Pruess, Battistelli 2002)

Table 7.4 Diffusion and adsorption parameters of benzene.

Parameter		unit	value
Reference diffusion coefficient for vapor-air mixtures	D_g^{awR}	m^2/s	2.13×10^{-5}
Reference binary diffusivity of VOC in air	D_g^{acR}	m^2/s	7.7×10^{-6}
vapor-air diffusivity exponent	θ_{aw}	-	1.8
chemical diffusivity exponent	θ_{ca}	-	1.52
organic carbon partition coefficient	K_{oc}	m^3/kg	0.085
organic carbon fraction	f_{oc}	%	0.1
Soil-water distribution coefficient for organic chemical	K_d	m^3/kg	8.5×10^{-5}

Source: Reprinted from Faeli et al. (2020) © ASCE

Table 7.5 Benzene Concentrations in groundwater samples (Antea 2016).

Date	MW1	MW 2	MW 3	MW 4	MW 5	MW 6	MW 7	MW 8	MW 9	MW 10	MW 11	MW 12
4/30/1998	3200											
8/12/1998	2100	20	410	12000								
12/4/1998	2700											
1/5/1999	1600											
10/14/1999	1820	141	813	19100	<10	<0.5	<0.5	<0.5				
8/31/2012	250	1700	620	14000	5.1	<1	<1	<1				
12/18/2012	130	1400	1400	16000	3.3	<1	<1	<1				
6/25/2013	100	670	540	13000	0.72	<1	<1	<1	9000	360	600 0	14000
12/18/2013	170	1400	730	17000		<1	<1	<1	10000	380	630 0	~0.3cm NAPL (@1.4 m)
7/20/2016	well covered by asphalt	2970	1790	17900	not sampled	<0.5	<0.5	<0.5	7440	960	482 0	~0.5m NAPL (@1.2m)

Table 7.6 Total benzene mass in different phases in the domain including volatilized and normalized adsorbed mass (as % of remained mass).

Time	Gas	Aqueous	NAPL	Adsorbed	Total	Volatilized to Atmosphere	Normalized adsorbed
year	kg	kg	kg	kg	kg	kg	%
Initial					840		
1	7.16	48.09	602.76	35.33	693.34	141.82	5.1
2	7.15	49.80	451.00	35.89	543.84	148.01	6.6
3	6.75	47.80	321.58	34.10	410.23	132.15	8.3
4	6.22	44.66	209.60	31.60	292.07	116.38	10.8
5	5.63	41.00	111.00	28.79	186.42	103.54	15.4
6	4.78	35.40	32.70	24.60	97.48	86.27	25.2
7	2.29	18.80	0.00	12.55	33.64	61.41	37.3
8	0.74	6.89	0.00	4.40	12.03	20.75	36.6
9	0.31	3.42	0.00	2.07	5.80	5.92	35.7
10	0.15	1.94	0.00	1.13	3.22	2.45	35.1
11	0.07	0.92	0.00	0.52	1.51	1.60	34.2

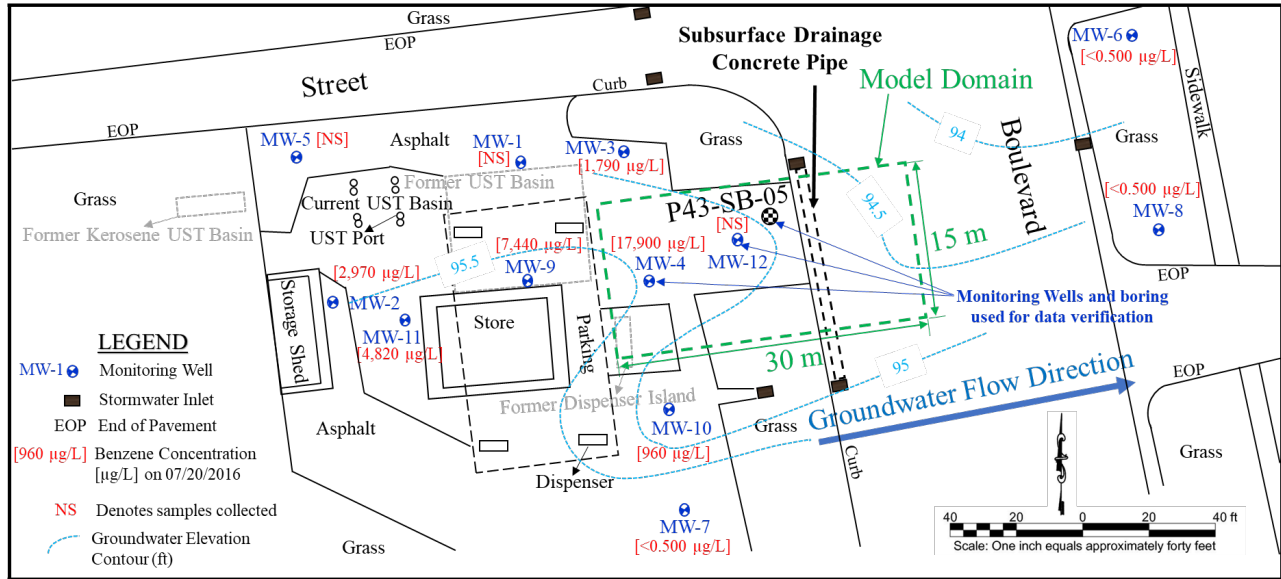


Figure 7.1 Site map with the gas station location, model domain, the monitoring well locations, and the groundwater flow direction (Antea 2016).

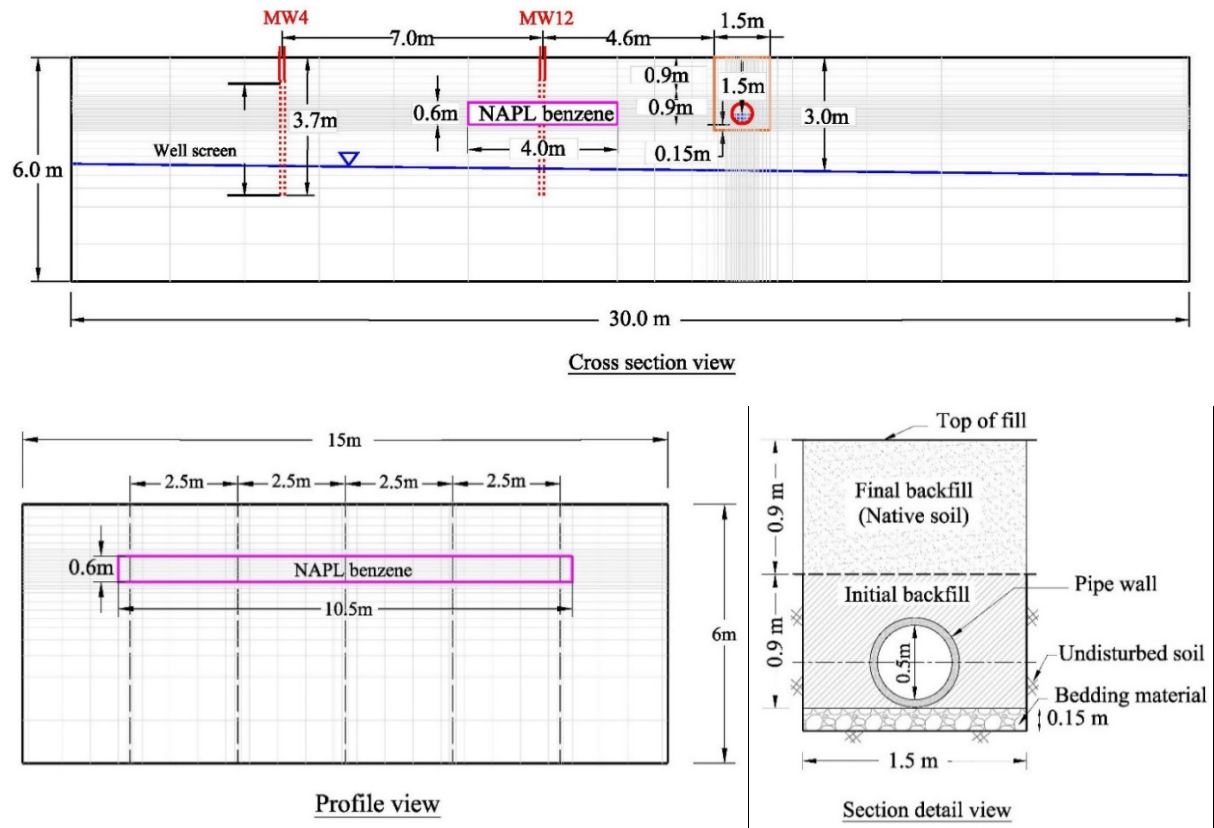


Figure 7.2 Schematic sketch of model.

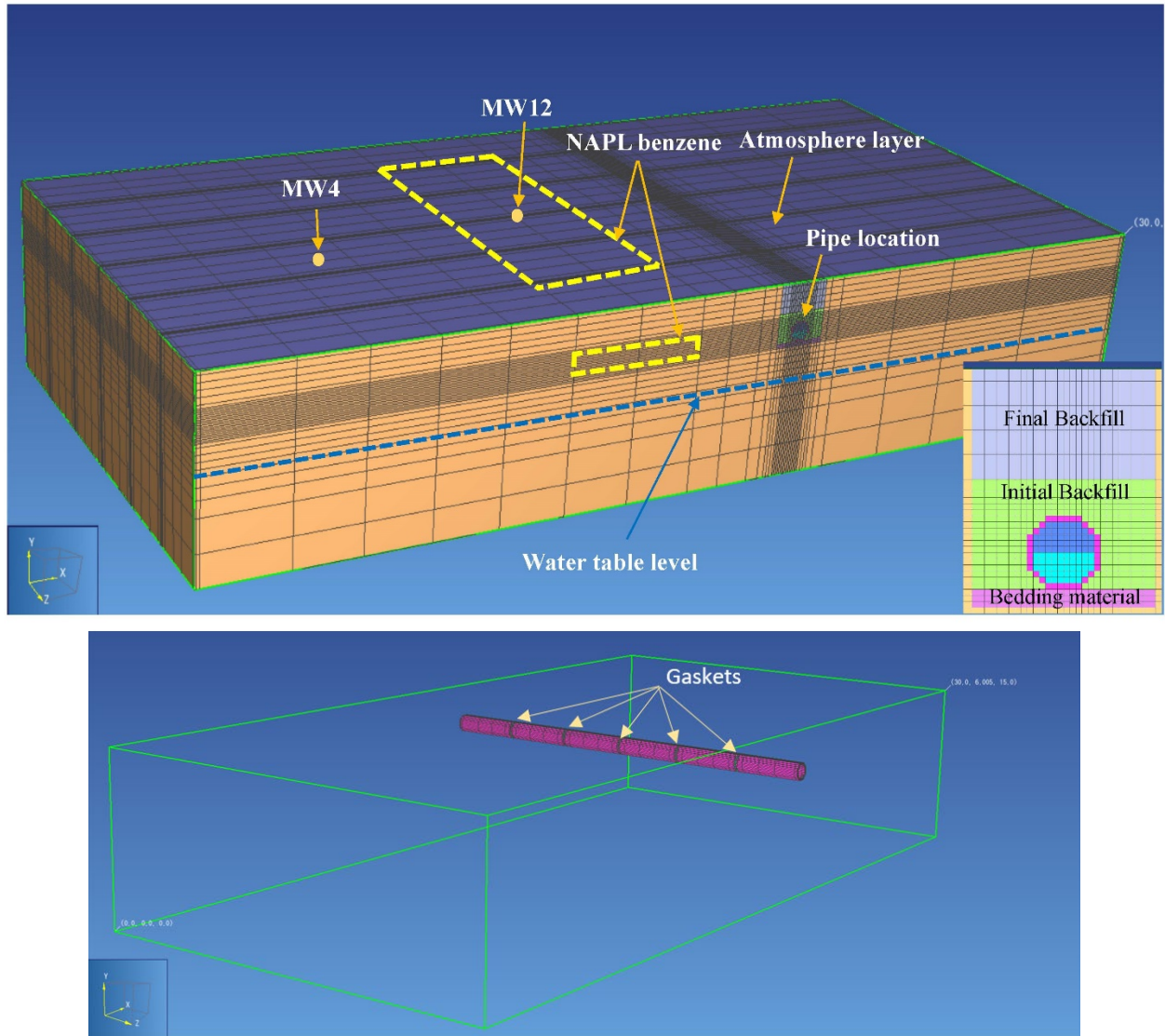


Figure 7.3 The Discretized model domain and pipe located in the unsaturated soil.

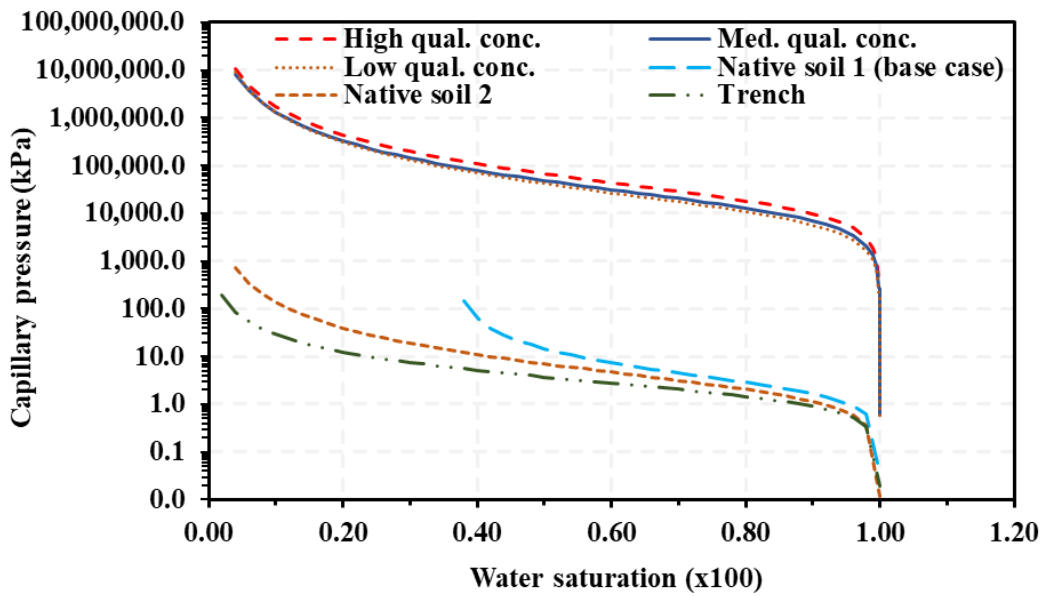


Figure 7.4 Water Retention Curves (WRCs) and Soil Water Characteristic Curves (SWCCs) used in analyses.

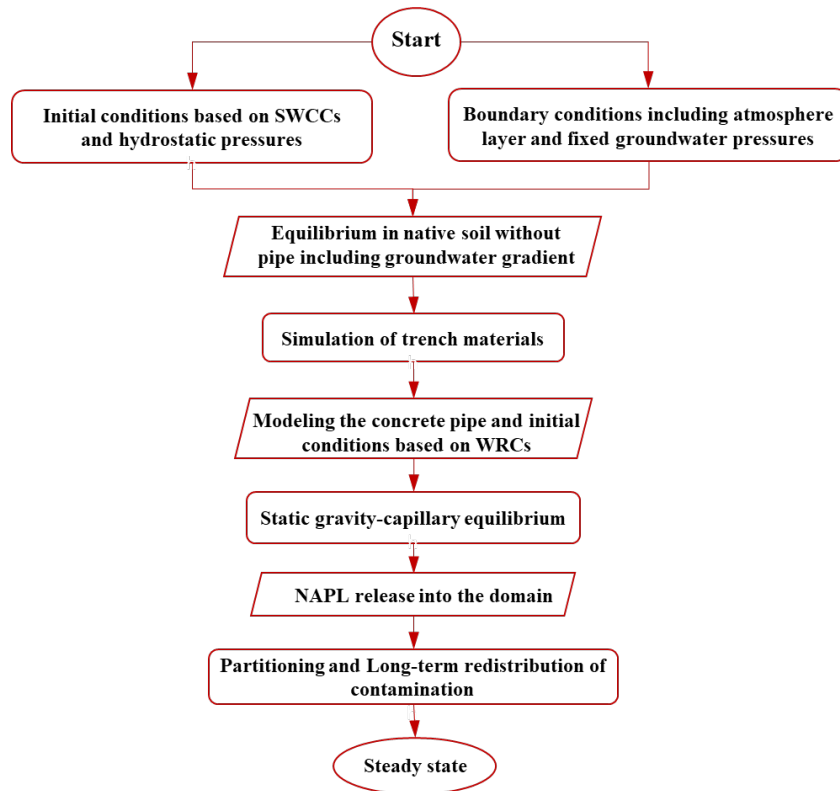
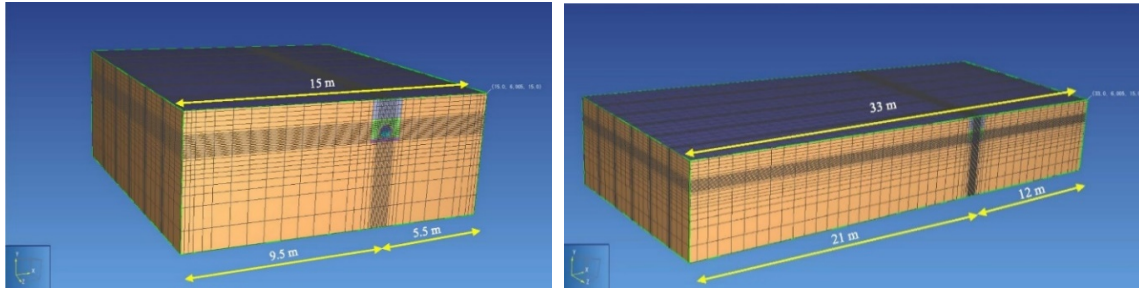
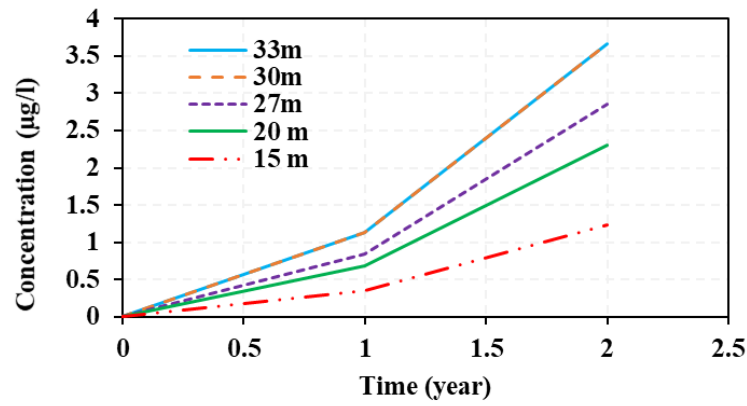


Figure 7.5 Simulation flowchart.



a)



b)

Figure 7.6 Size and mesh sensitivity analyses, a) Simulations for 15 m and 33 m horizontal distances. b) Concentrations in the aqueous phase inside the pipe for different model dimensions.

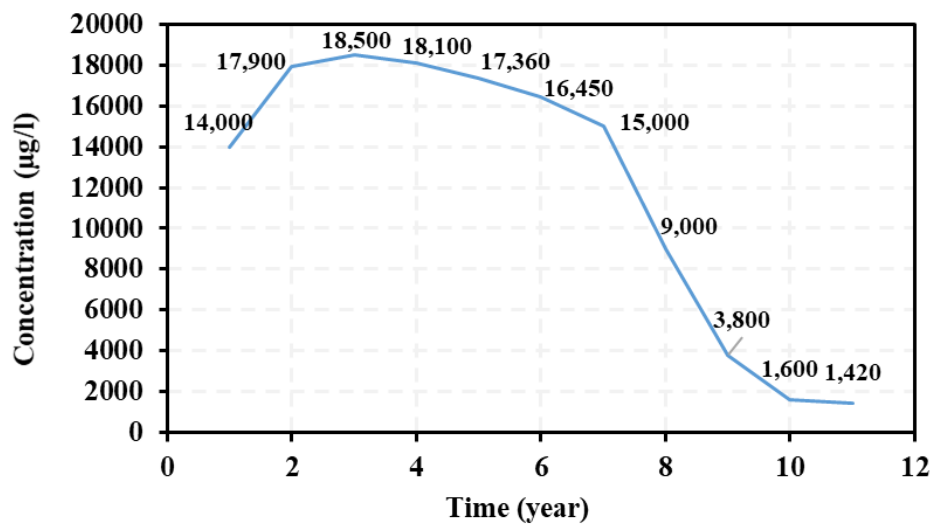


Figure 7.7 Estimation of benzene concentration in the aqueous phase in MW-4 location.

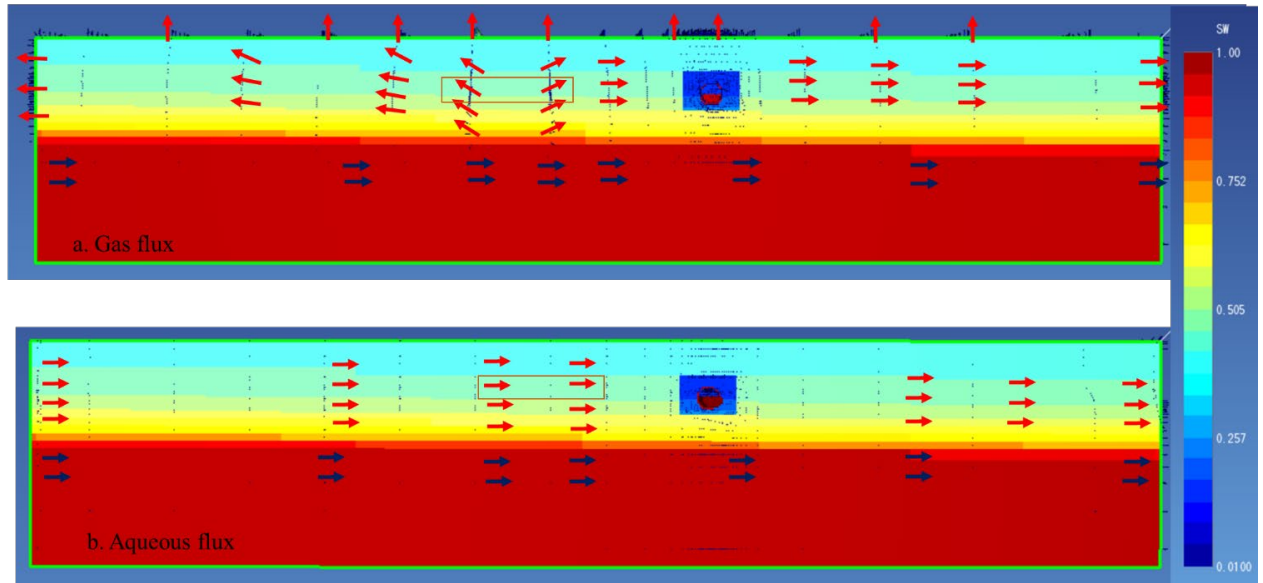
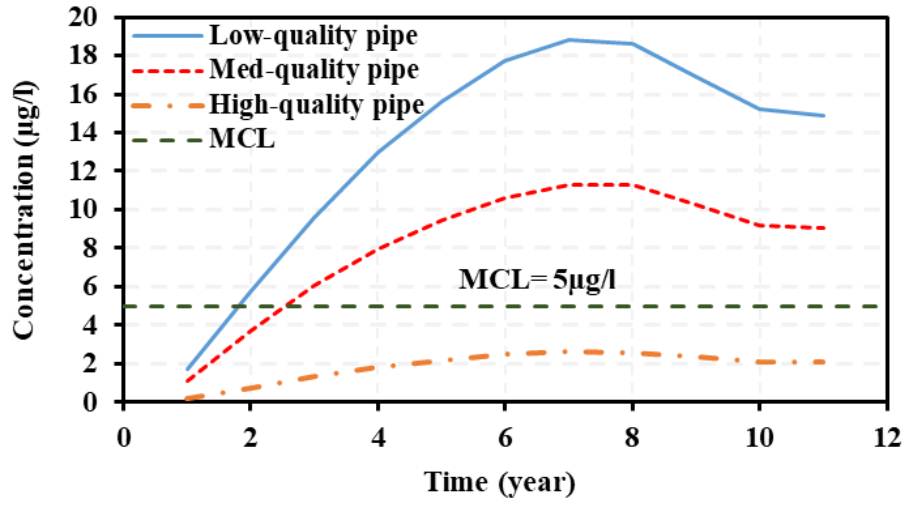
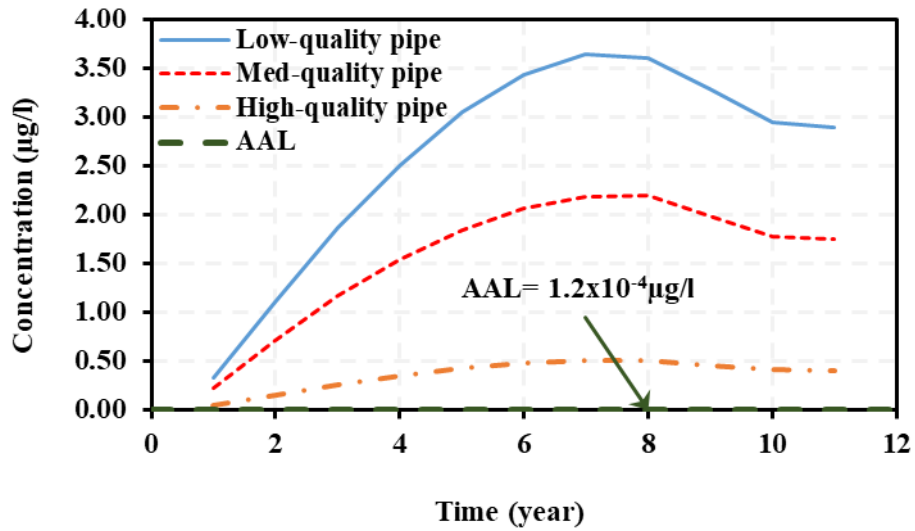


Figure 7.8 Water saturation within the depth and flux directions in the domain, a) Gas fluxes, b) Aqueous fluxes.

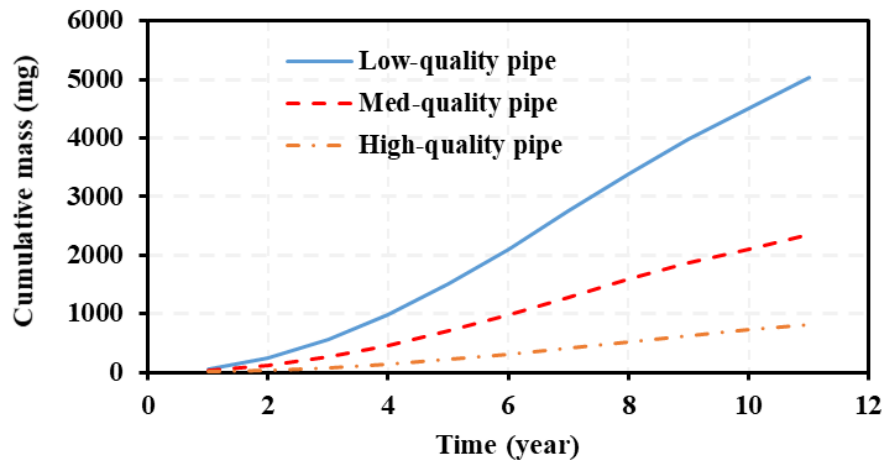


a)

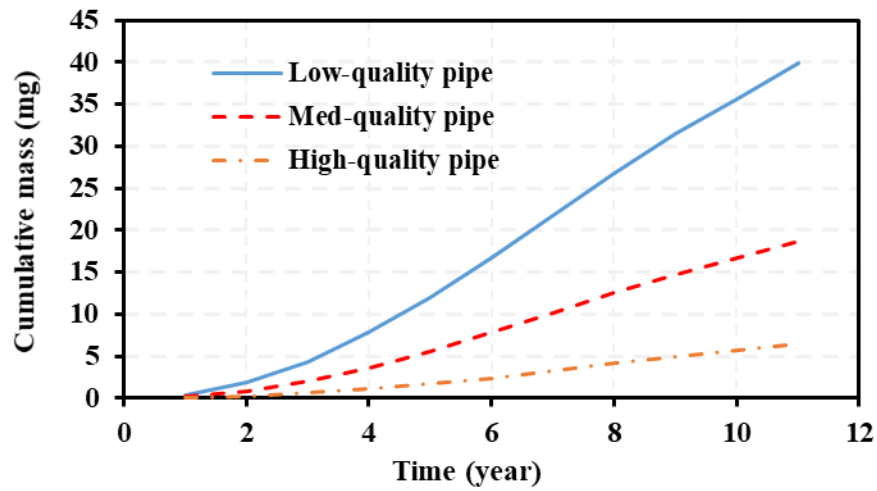


b)

Figure 7.9 Benzene quantity inside the pipe for different pipe material qualities, a) Peak concentration in the aqueous phase, b) Peak concentration in the gas phase.

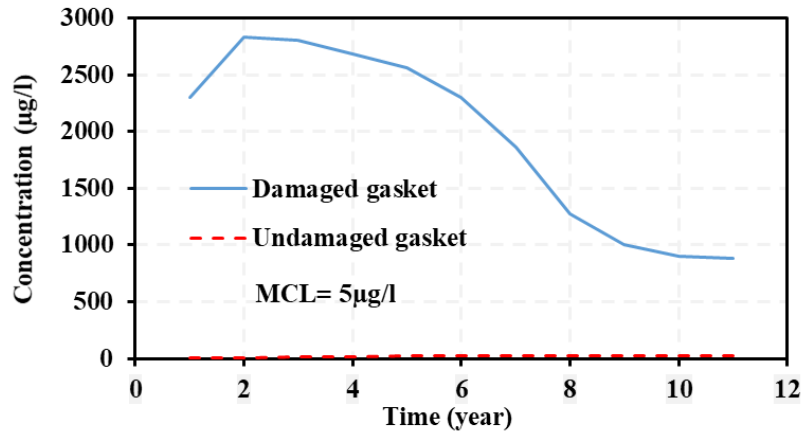


a)

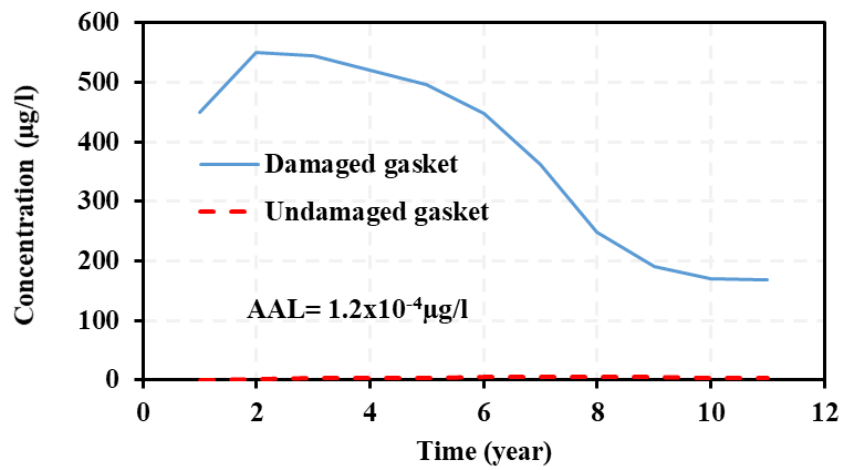


b)

Figure 7.10 Benzene mass breaking through the pipe for different pipe material qualities, a) Cumulative mass breaking through the pipe in the aqueous phase, b) Cumulative mass breaking through the pipe in the gas phase.

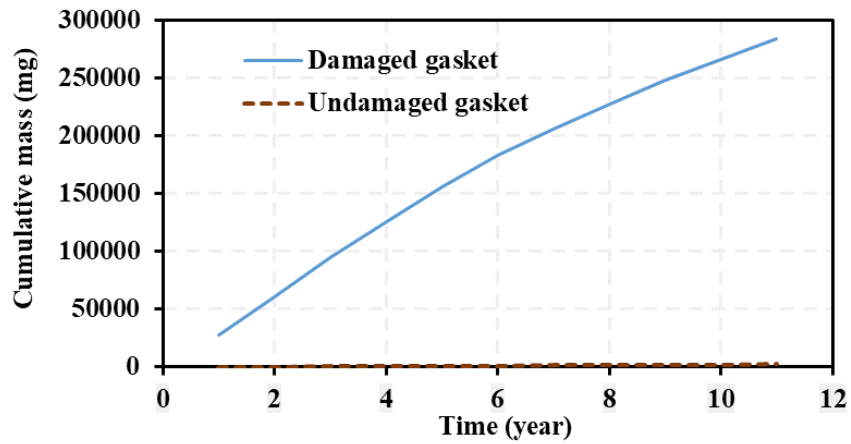


a)

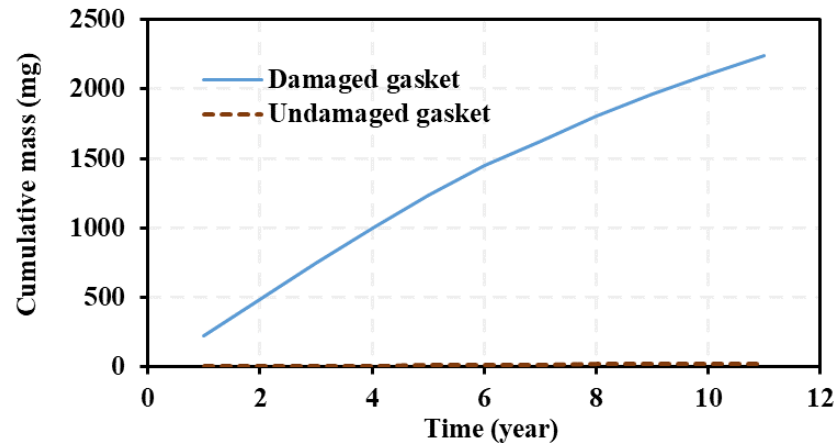


b)

Figure 7.11 Benzene quantity inside the pipe in the case of damaged and undamaged gaskets, a) Peak concentration in the aqueous phase, b) Peak concentration in the gas phase.

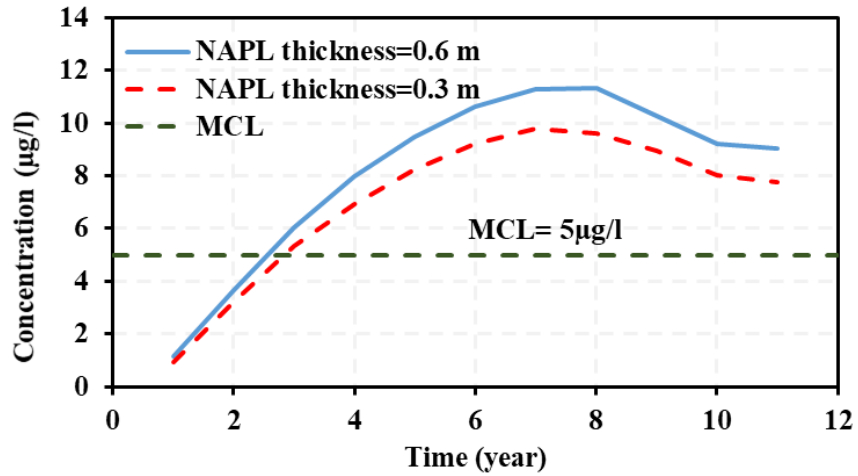


a)

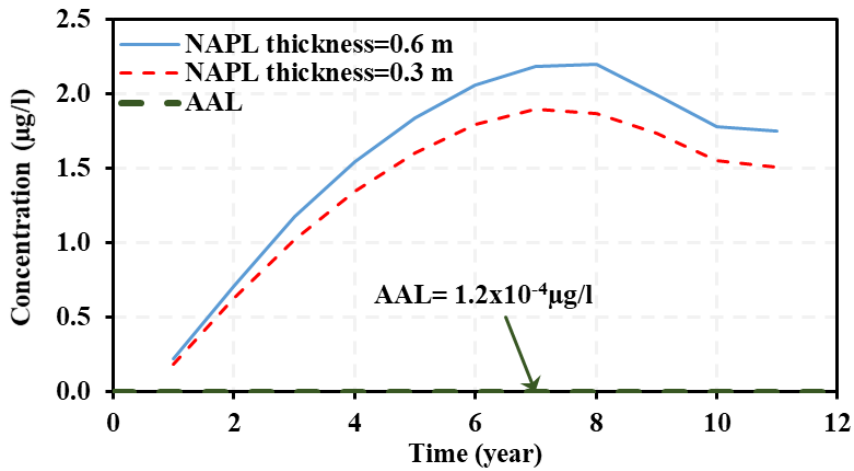


b)

Figure 7.12 Benzene permeation into the pipe in the case of damaged and undamaged gaskets, a) Cumulative mass breaking through the pipe in the aqueous phase, b) Cumulative mass breaking through the pipe in the gas phase.

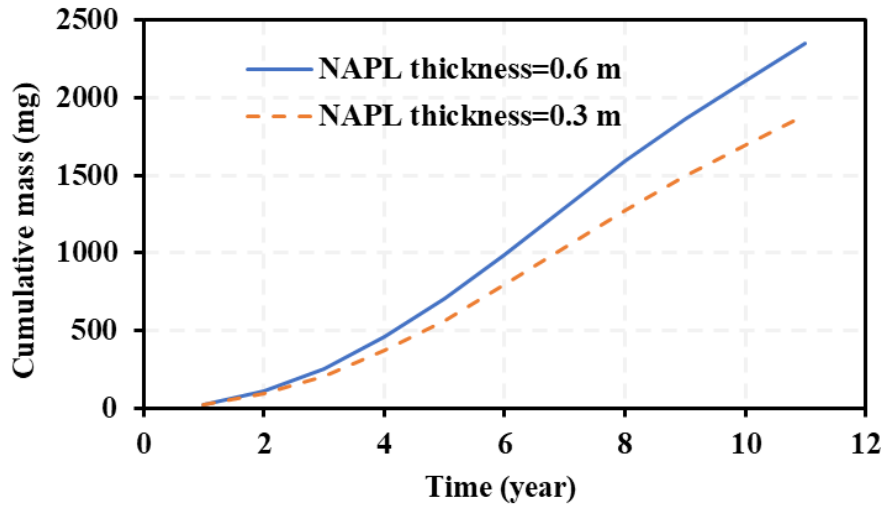


a)

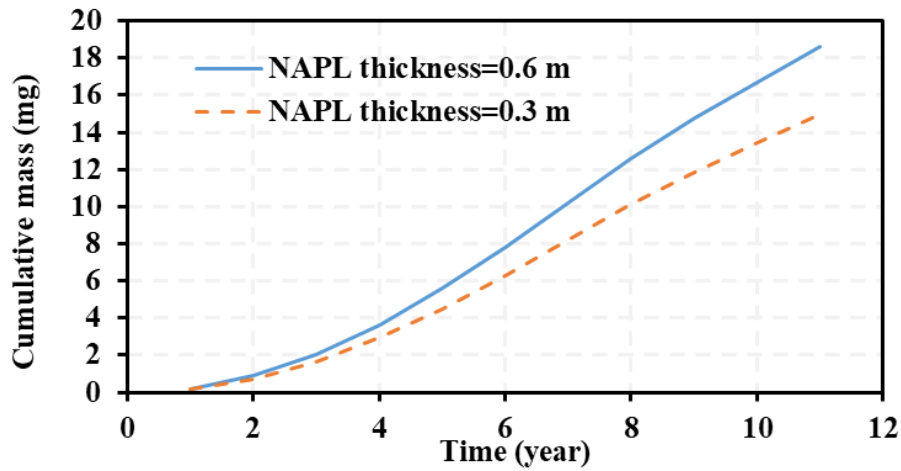


b)

Figure 7.13 Benzene quantity inside the pipe for different NAPL phase thicknesses at the source, a) Peak concentration in the aqueous phase, b) Peak concentration in the gas phase.



a)



b)

Figure 7.14 Benzene mass breaking through the pipe for different NAPL phase thicknesses at source, a) Cumulative mass breaking through the pipe in the aqueous phase, b) Cumulative mass breaking through the pipe in the gas phase.

CHAPTER 8. A New Monitoring Approach for Sustainability Assessment of Subsurface Utilities Gasket Materials Against Gasoline and Chlorinated Solvents: Field Evaluation and Model Development

Abstract

A new pipe material monitoring capsule (PMMC) has been designed to evaluate volatile organic compounds (VOCs) and chlorinated solvents (CS) breakthrough three types of pipe materials; Neoprene, Buna-N, and Viton. Three contaminated sites (two gasoline and one CS contaminated sites) were selected to deploy PMMCs. A 3D field-domain model has been developed for each site to calibrate hydraulic parameters of PMMC (k_e , D) and develop protocols for installing/retrieval of PMMCs. According to the recommended protocol, benzene breaking through the Neoprene and Buna-N more than 70% and 60% of the monitoring well concentration after 4 months, respectively. The corresponding value for PCE breakthrough after 4 months will be 60% for both the Neoprene and Buna-N. Both gasket materials of Neoprene and Buna-N showed similar performances, including higher rate of contaminant breakthrough compared to Viton. The fluctuation of concentrations in monitoring well due to seasonal rainfall and changes in groundwater level can affect model prediction results.

8.1. Introduction

The idea of pipe material monitoring capsule (PMMC) development can be correlated to passive integrative samplers in groundwater studies with similarities in components but different application. The conventional time-discrete grab sampling provides a snapshot of pollutants only at the time and place of sampling, failing to account for episodic contamination events. Integrative sampling is introduced as an alternative option to discrete-sampling for identifying wide range of volatile and semivolatile micropollutants over extended timeframes, from hours to months (Vrana et al. 2001).

Integrative samplers require mechanical work on the environment to transfer the contaminant-bearing phase to the sampling phase are referred to as ‘active’, while those relying on diffusion or environmental advection are termed ‘passive’ (Roll and Halden 2016, Lohmann et al., 2012, Vrana et al. 2001, 2005).

Previous studies have shown continuous active samplers can successfully detect analytes in water (Ellis et al., 2009, Coes et al. 2014, Roll and Halden 2016). Coes et al. (2014) used a

continuous low-level aquatic monitoring (CLAM) sampler consisting of a nylon body containing a low-flow pump and two extraction disks that continuously draws water through solid-phase extraction media. The active samplers were deployed four times for a duration of 19-23 h with a period of 7 days between deployments. The passive samplers consisted of solid-phase sorbent contained between two sheets of polyethersulfone membrane were submerged for the duration of the 29-day deployment period. By comparing continuous active sampling method, continuous passive, and discrete sampling methods for the sampling of trace organic compounds (TOCs) in water, Coes et al. (2014) found a greater number of TOCs detected in active samplers, but lower concentrations than the other methods. The variability in the results between the three methods was affected by variability in stream discharge and possibly constituent loading. Roll and Halden (2016) suggested that active samplers have the potential to reduce more sampling rate and analyte uptake errors, by applying high-precision mechanical pumps, instead passive samplers can increase the number of replicates due to much lower cost, thereby increase spatial coverage of environmental monitoring. Furthermore, some studies reported that peak concentrations pass the monitoring well may not be noticed in active sampling because this kind of monitoring is not continuous (Verreydt et al. 2010).

Passive sampling methods have shown promise as tools for measuring aqueous concentrations of a wide range of priority pollutants. Depending on sampler design, the mass of pollutant accumulated by a sampler can reflect either the in-situ concentration with which the tool is at equilibrium or yield time-weighted averages of concentrations in water over the period of deployment. Passive tools have been invented for monitoring air quality since the early 1970s. Later, the principles were applied in monitoring in aqueous environments (Vrana et al. 2005). The passive samplers are low-cost and suitable to use at remote sites without vandalism (Vrana et al. 2001).

Passive samplers, generally, consist of a receiving phase enclosed within a permeable housing or membrane bags and used to measure dissolved gases and volatile organic compounds (VOCs) in groundwater at contaminated sites (Hatfield et al. 2004, Namiesnik et al. 2005). The receiving phase can be solvents, solid-phase extraction sorbent, chemical reagent or even distilled water (Verreydt et al. 2010). Passive samplers in some other design approaches consist of a sealed container with a semipermeable membrane material at the top (Divine and Mccray 2004, Ma et al., 2013). Vrana et al. (2001) used a passive sampler consisting of a stir bar coated with poly

dimethylsiloxane (PDMS) enclosed in a membrane bag that acts as a receiving organic phase. Upon exposure to solution with constant concentrations, Vrana et al. (2001) derived sampling rate of system using an overall mass-transfer coefficient, membrane surface area, and porosity. They correlated mass-transfer coefficient to diffusion coefficient, thickness of membrane and sampler-water partition coefficients. Divine and Mccray (2004) employed passive samplers to estimate equilibration times for several dissolved gas and common VOC. To predict equilibration times, diffusion coefficients (D_m) of low-density polyethylene membranes (LDPE) employed in samplers were estimated analytically and experimentally. Additionally, a numerical model was developed to evaluate the “lag time” for conditions in which in situ concentrations are temporally variable. Studies have shown that trace organic compounds (TOC) detected by passive samplers are strongly controlled by sampling rate for the TOC, which can be difficult to define because of many variables, including water velocity, water temperature, and biofouling (Alvarez 2010, Morin et al. 2012, Coes et al. 2014). The passive samplers can be classified as i) diffusion-based passive samplers in which the transport of the contaminants through the housing membrane of the sampler is diffusion-limited and advective transport through the housing is inhibited, and ii) permeation-based passive samplers in which the groundwater flow gradient is the driving force that induces the advective transport of the contaminant through the housing (KotWasik et al. 2007). Using diffusion-based samplers, the Fick’s first law is used to calculate uptake rate, while variations in water level and groundwater flow rate can still influence the uptake rate and may not be considered using Fick’s first law.

In situ concentration measurements can vary substantially because of the spatial and temporal variability of the source mass, natural gradient, the pathway patterns of biogeochemical processes, degradation, sorption, desorption, dissolution, as well as human activities (Verreydt et al., 2010). Ma et al., (2013) used a passive diffusion bag (PDB) sampler filled with deionized water in low-density polyethylene (LDPE) tubes to evaluate equilibration time and partitioning of VOCs between the sampler and the water sample. They compared VOC soluble phase from PDB samplers after 14 days. They measured diffusion coefficient of sampler (D_m) by using time required to reach 90% equilibration of sampling ($t_{90\%}$) in the laboratory. The diffusion coefficient of benzene through LDPE membrane with 100 μm thickness was measured to be $2.84\text{--}8.34 \times 10^{-10} \text{ cm}^2/\text{s}$.

In the present study, the PMMC tools are developed based on the idea of passive samplers to evaluate the sustainability of pipe materials. A sample of pipe gasket material was installed at the top of sealed aluminum cases, then deployed over pre-scheduled time slots in monitoring wells located in solvent chlorinated and gasoline contaminated sites. The resident analytes flow from the surrounding media and break through across the pipe material during the sampling period. Afterward, the PMMCs are retrieved and the analytes of benzene and PCE inside and outside of the PMMCs are measured. The potential differences between concentrations of two media inside the PMMC and monitoring well, as well as hydraulic gradient in site prompt the rate of break through the pipe materials. The PMMCs were calibrated using the measurement data and the hydraulic parameters of pipe materials have been determined. Afterward, the calibrated parameters were used to predict the rate of breakthrough and a protocol was recommended for installing/retrieval of PMMCs to monitor PCE and benzene breakthrough rate.

8.2. Methods

8.2.1. PMMC Design

The PMMCs have been designed and fabricated at the Constructed Facilities Laboratory (CFL) of North Carolina State University (NCSSU) shown in Figure 1. and deployed on three chlorinated solvent and gasoline contaminated sites in North Carolina. The PMMC consists of an aluminum alloy cup filled with ultrapure water and three gasket materials (Neoprene, Buna-N, and Viton) being installed and fixed with hollow grooved cap at the top (Figure 1). The pipe material sheet has 2.54 cm (1 in) diameter and 3.2 mm (0.125 in) thickness. The capsule has the similar inside diameter as pipe material as 2.54 cm and the height of 7.8 cm (~3 in). For each contaminated site twelve capsules were deployed including three for each gasket material, and three more cups enclosed and sealed at both ends for quality control (QC) assessment of designed tool.

8.2.2. Deployment/Retrieval Strategies

The PMMCs have been deployed in equal-distance-increments in three batches per monitoring well (three replicates for each gasket material and three more for blank QC monitoring) to represent breakthrough-weighted concentrations of an impacted cross-section. Total number of 72 PMMCs have been deployed in all sites and for the whole exposure time. Table 1 shows deployment/retrieval schedule for each monitoring well.

8.2.3. Field sites

Three sites have been identified for field evaluation of PMMCs; i. Nash county maintenance depot in Nashville, NC (gasoline contaminated site), ii. NCDOT maintenance facility project in Newton, NC (gasoline contaminated site), and iii. Triangle Laundromat in Durham, NC (chlorinated solvent contaminated site). Benzene and Tetrachloroethylene (PCE) have been assessed as the dominant concentrations in gasoline and chlorinated solvent contaminated sites, respectively.

i. Nashville gasoline contaminated site

Figure 2 shows a plan view of the Nashville site map including monitoring well locations and benzene plume distribution (Wood Inc., 2019). The subject site includes vehicle and equipment storage, maintenance, and vehicle fueling station. The gradient of groundwater flow is to the southwest of the site with an approximate average hydraulic gradient of 0.01 ft/ft. Historical data show fluctuations in groundwater elevation over time, and the largest fluctuation was observed in MW-12 at approximately 7.8 ft (Wood Inc. 2019). Several geological borings were advanced to a depth of 16 ft bgs to investigate soil types and properties. According to geologic cross-sections (ATEC Inc. 2012) and soil sampling reports (AMEC Inc. 2013) native soils generally consisted of red to brown clayey silt, sand and sandy silt at the impacted site.

The soil contamination was observed for the first time in 1990, when seven 1000-10000 gal capacity gasoline and diesel underground storage tanks (USTs) were removed from a fueling pavilion at the site. Accordingly, between 1991 to 2016, 17 monitoring wells (MW-1-17) were installed and screened to a maximum depth of 35 ft below ground surface (bgs) (Wood Inc. 2019). Benzene, toluene, ethylbenzene, xylenes (BTEX), methyl-tert-butyl-ether (MTBE), and diisopropyl ether (DPE) concentrations were detected in groundwater samples in excess of the North Carolina groundwater quality standards (2L Standards). Benzene has been the dominant contaminant with a highly detected concentration in MW-3, thereby the PMMCs were deployed in this monitoring well at site in March 2020. Table 2 indicates MW-3 characteristics and gathered data during PMMC first deployment. Although contaminant concentrations have fluctuated, the lateral extent of the groundwater impact has remained comparatively unchanged since 1991 and does not migrate down gradient. Three in situ chemical oxidation (ISCO) pilot tests were performed by Wood Inc. in 2016, 2018 and, 2019 which reduced concentrations significantly,

however, concentrations remained in excess of the gross contamination levels (GCLs) in some of impacted monitoring wells (Wood Inc. 2019).

ii. Newton gasoline contaminated site

The Newton site map, including the location of monitoring wells, the extent of benzene plume and the model domain is shown in Figure 3. The subject site is used as a maintenance and equipment facility yard for NCDOT. The site is placed within the Piedmont area of North Carolina. The soil layers consist of sandy to silty clay fill from the surface to a depth of 5 to 10 ft. The fill soils are generally underlain by sandy silts to a depth of approximately 60 ft, where the partially weathered rock was encountered. Results from the slug test indicated hydraulic conductivity at the site ranging from approximately 0.005 ft/d to 0.35 ft/d with an average hydraulic conductivity of 0.06 ft/d (2×10^{-7} m/s). The horizontal gradient is 0.01 ft/ft to the northwest, and based on the hydraulic conductivity of 0.06 ft/d, and assumed porosity of 0.25, the groundwater seepage velocity is estimated to be approximately 0.88 ft/yr. The hydraulic gradient in the domain is 1% toward the west. The PMMCs were installed in MW-3. The source area is mainly located around MW-6 where the former gasoline USTs and dispensers have been installed.

According to Hart & Hickman, PC. (2018), contaminated soils were detected in 2003 due to gasoline release from the former UST system in the area. Free gasoline product was observed in MW-6 (Figure 3) with groundwater sampling revealing VOC contamination. The detected contamination included benzene at concentrations up to 35,000 $\mu\text{g/l}$. Benzene was detected in shallow groundwater at concentrations up to 35,000 $\mu\text{g/l}$, which exceeded the groundwater standard of 1 $\mu\text{g/l}$ and the Gross Contamination Level (GCL) of 5,000 $\mu\text{g/l}$. Ethylene dibromide (EDB) and 1,2-dichloroethane (DCA) were also detected at concentrations exceeding GCLs (50, 400 $\mu\text{g/l}$). Free product recovery and soil treatment systems were initiated from 2004 by using soil vapor extraction remediation system (SVE) (2004), a free product recovery system (2008), in-well aeration system (IWS) (2011), and re-installation of a free product removal pump in MW-6 (2012). The remediation system is currently active.

Sampling of monitoring wells commenced in 2013 and continues to the present time. Free product thickness at MW-6 was measured as rebounding to 0.6 ft in 2018 while it was decreased to 0.01 ft in thickness during product recovery in the past years. Petroleum-impacted groundwater extends from the previous UST domain (around MW-6) primarily to the west, and slightly to the north. The highest concentrations were detected in monitoring well MW-3, which is located down-

gradient of the source area. In March 2020, the groundwater level and concentrations were updated in MW-3 immediately before PMMC installation. The results are shown in Table 1.

iii. Durham chlorinated solvent contaminated site

Figure 4 shows a plan view of Durham site map which indicates the extent of chlorinated solvent distribution and monitoring wells. The subject site includes dry cleaning facility and laundromat which has utilized PCE in its dry cleaning operations since its inception in 1984 (URS 2015). The site stratigraphy, hydrogeology and aquifer characterization data from preliminary site assessment reports have been gathered in the site assessment reported by URS Corporation (2015). The soil layers consist of dark red to reddish-brown silty clay to a depth of 27 ft which gradually transitioned to sandstone/mudstone at 27 to 65 ft. The flow direction is toward south-southeast with a very low hydraulic gradient (<1%). The average hydraulic conductivity from slug test data is 125.5 cm/yr (4×10^{-8} m/s). The groundwater level fluctuates between 0.5 to 26.8 ft bgs.

The PCE, Trichloroethylene (TCE), and 1,2-dichloroethylene (1,2-DCE) were detected at monitoring wells which PCE was at the highest levels above the North Carolina 2L Standard of 0.7 $\mu\text{g/l}$ and GCL 700 $\mu\text{g/l}$. The GCL for TCE, and 1,2-DCE are 3000, and 60000 $\mu\text{g/l}$, respectively. Among the monitoring wells in the vicinity of dry cleaner facility, RW-2 was chosen to deploy PMMCs. PCE was the dominant contamination with 88000 $\mu\text{g/l}$ detected in RW-2 in 2008. The monitoring well concentrations were updated during PMMC deployments indicated in Table 1.

8.2.4. Measurements of retrieved PMMC

Table 3 shows the results of testing for PMMC measurements retrieved from the monitoring wells at all three sites.

8.3. Model Development

i. Nashville gasoline contaminated site

A 3-dimensional model domain has been developed using finite difference method incorporated in GMS transient mass-transport domain. Figure 5(a) shows simulated model domain with dimensions 30 m \times 15 m \times 5 m (98.4 ft \times 49.2 ft \times 16.4 ft) based on the extent of benzene plume. The dimensions were chosen to cover field concentrations more than 50 ppb as delineated on the site map in Figure 2. The total number of grids is 310,000 with grid size of 0.25 m far from the location of PMMC becoming as fine as 0.002 m towards the monitoring well where PMMC has been deployed. The hydraulic gradient in the domain is 1% toward the southwest (right to the

left in the model) simulated with constant head boundaries. To avoid complexity, the impact of groundwater level fluctuation on flow regime and hydraulic gradient was not considered in the model, however, the fluctuation in monitoring well's concentration has been applied using transient functions. Figure 5(b) presents a plan view of the model developed herein while the distribution of the initial soil and groundwater contamination was assigned based on the field measurements of monitoring wells and borings (Wood Inc. 2019, Pace analytical services report 2020, 2021). An area of 1.75 m around monitoring and purge wells were selected to define high concentrations at PW-3 (18200 ppb), PW-1 (3700 ppb) and MW-4 (12600 ppb). Section A-A' shown in plan view is displayed in Figure 5(c). The PMMCs have been deployed in MW-3. The location of MW3 is also shown along with benzene distribution throughout the domain depth. A PMMC with 2.54 cm diameter and 7.8 cm height was simulated at 75 cm below the groundwater level in MW-3 with 5.0 cm diameter (Figure 5(c)). The test sample on the top of the capsule is 3.2 mm thickness and an initial concentration of zero is assumed inside the capsule. Groundwater table level and benzene concentration are not constant with seasonal changes and fluctuate during PMMCs deployment period which is shown in the hydrograph of Figure 6(a). A hydrograph is presented for PW-3 which is the closest monitoring well to the location of PMMCs and has been used to deploy some pipe material samples to assess samples' tensile strength. Accordingly, transient sources have been defined in MW-3 and PW-3 to account for these fluctuations with time.

Table 4 presents the model flow and transport parameters used in modeling required to simulate advection, dispersion/diffusion, chemical reaction/adsorption, and degradation. The diffusion coefficient (D) and equivalent hydraulic conductivity (k_e) of samples are unknown and will be calibrated using the simulation (presented in results section). The material properties of the study site are shown in Table 5. Adsorption of the organic chemical onto the solid-phase is defined by linear equilibrium-controlled sorption isotherm and the soil-water partition coefficient (K_d). The partitioning of chemicals onto the soil particles is a function of the organic carbon fraction (f_{oc}) present in the soil (Table 5) that is defined based on-site assessment and soil sampling reports illustrated in field sites description. The first-order reaction rate of dissolved phase (K_1) and sorbed phase (K_2) are employed to account for the decay or degradation of the contaminant due to natural biochemical attenuation. The diffusion coefficient, adsorption/degradation parameters of benzene, as long as the rationale for dispersivity have been described in the previous studies developed by

these authors (Faedi et al. 2021, Alhomai et al. 2021). Different adsorption and degradation parameters have been considered for Durham site which is PCE contaminated than the other sites with benzene and gasoline contamination (Aronson and Howard 1997). The diffusion coefficient value of benzene and PCE in water (D) was assigned as $9.5 \times 10^{-5} \text{ m}^2/\text{d}$ ($1.1 \times 10^{-9} \text{ m}^2/\text{s}$) and $8.8 \times 10^{-5} \text{ m}^2/\text{d}$ ($1.0 \times 10^{-9} \text{ m}^2/\text{s}$), respectively (GSI Environmental 2014). The longitudinal dispersivity parameter (α_x) was estimated based on Neuman (1990) ($\alpha_x = 0.0175 \times L^{1.46}$, L is domain size in the x-direction). The transverse (α_y) and vertical dispersivity (α_z) have been assumed 30% and 5% of α_x as recommended per ASTM (1994).

ii. Newton gasoline contaminated site

To assess the performance of PMMC at another gasoline contaminated site, a 3-D domain was developed for Newton site shown in Figure 7(a) with the similar approach as used for Nashville site. The model dimensions are $80 \text{ m} \times 50 \text{ m} \times 10 \text{ m}$ selected based on the plume extent shown in Figure 3. Figures 7(b) and 7(c) show a plan view and cross-section views A-A', B-B', and C-C' of the model developed herein. The contamination distribution was assigned according to Hart & Hickman (2018), Pace analytical services report (2020), and measurements during this study. The extent of plume in depth is considered to be 4 m that is more than Nashville site (3 m). The total number of grids is 1,123,000 with grid size of 0.5 m far from the location of PMMC becoming finer as 0.002 m towards the monitoring well where PMMC has been deployed. The hydraulic gradient in the domain is 1% toward the west (right to the left in the model). A PMMC is located 75 cm below the groundwater level in MW-3 (diameter of 5.0 cm) shown in Figure 7. The location of MW-6 is shown in Figures 7(b) and (c) where USTs have been formerly installed. Due to the presence of free product in MW-6 and possible interference with the measurements in this study, this monitoring well was not selected for PMMC deployment. The model flow and transport parameters of Newton site are defined following the same approach as described for Nashville and presented in Table 4 while the specific soil parameters of Newton site are presented in Table 5. A transient benzene concentration was defined in MW-3 according to the hydrograph shown in Figure 8. The hydrograph represents benzene fluctuation during PMMCs deployment period in this study.

iii. Durham chlorinated solvent contaminated site

The 3D model domain, plan view, cross-section view, and the PMMC configuration in the developed model of Durham site are shown in Figures 9(a), 9(b), and 9(c). The dimensions of

model domain are 50 m × 37.5 m × 10 m as shown in Figure 4. The PCE concentrations in monitoring wells are defined according to the plan view of Figure 4 (URS 2015), Pace analytical services report (2020), and measurements during this study. The PMMC is deployed in RW-2 with 10 cm well diameter. A hydraulic gradient of 1% in the direction of plume extent was simulated using constant head boundaries at right and left sides of the model domain. The total number of grids is 320,000 with grid size of 0.5 m far from the location of PMMC becoming finer towards the monitoring well and PMMC location. Transient PCE source has been simulated in RW-2 according to the measured hydrograph of Figure 10. The model parameters and site material properties are indicated in Tables 4 and 5, respectively.

8.4. Model Calibration

The parameters of D and k_e of gasket samples, Neoprene and Buna-N, and Viton against benzene and PCE were calibrated through inverse analyses. 1-D convection-diffusion equation, or second Fick's law, within a MATLAB code, has been employed to obtain a first estimation of diffusion coefficient. The first estimation was used as an input into the field simulation, thereby both unknown hydraulic parameters D and K_p were narrowed down following the approach shown in flowchart of Figure 11. The parameters have been updated after each retrieval or field measurement.

8.5. Results and Discussion

8.5.1. Benzene Contaminated Sites

The hydraulic parameters of gasket materials (D , k_e) were calibrated after each measurement during the retrievals and indicated in Table 6. The average or best estimation based on field conditions were presented as finalized hydraulic parameters of each gasket material in Table 7. The data used in the study included site material properties, plume distribution, as well as the PMMC concentration measurements (C_c) at the retrievals and monitoring well concentrations (C_w) at deployment/retrievals. The calibrated parameters are used in the developed model of each site to predict the benzene and PCE breaking through gasket materials with time.

Benzene breakthrough the sample installed in PMMC can be determined per each time increment. The results are shown in Figure 12 for Neoprene sample as an example, after one, two, three, and four months at Nashville site. Figures 13 and 14 show benzene concentration normalized with respect to maximum concentration in monitoring well at the Newton and Nashville sites.

The measured concentrations at the site (denoted as star symbols) have been compared with the simulation results in Figure 13 at each retrieval using the calibrated parameters in Table 7. The comparison shows good agreement between results from the model and measurements. At Nashville site, the simulation run was continued after the first retrieval (dashed lines) and the results have been compared with the results of the second deployment and field measurements. The rate of breakthrough at the Nashville site was higher at the beginning of the second deployment compared to the rate of breakthrough at the beginning of the first deployment due to higher concentrations present within the monitoring well during the second deployment (see Figure 13).

At Newton site, the first deployment indicates that both Neoprene and Buna-N have 100% breakthrough after 9 months, while Neoprene has higher breakthrough rate compared to Buna-N. The model results from the second deployment show that even though the concentration of MW-3 decreases, the breakthrough will be 50-62% of monitoring well concentration, after two months which is similar to the breakthrough after first two months of the first deployment (2% differences). These results indicate for a given period, the average magnitude of the fluctuated concentrations in monitoring wells (the amount of MW concentration) affects the breakthrough rate and concentration inside the PMMC more than the trend of increasing/decreasing chemical concentration in monitoring well. Similar to the results of Nashville site, comparing the simulation results of first and second deployments show that the rate of breakthrough was higher at the beginning of the second deployment and then decreases in parallel to the decreasing monitoring well concentrations. The rate of breakthrough was lower at the beginning of the first deployment and then increases within first two months. However, after two months of both first and second deployments, the rate of benzene breakthrough approaches a similar value as explained before with average concentration of monitoring well during two months (Figure 14). As described in description of Newton contaminated site, a removal pump has been installed in MW-6 as a remediation method. A pumping rate of 700 cm³/d was estimated according to the remediation system data. When pump is operated the maximum reduction in normalized concentration is 9% (ex. C_c/C_{wmax} decreases from 93 to 84) as shown in Figure 14 with purple markers.

The concentrations have been normalized with respect to the monitoring well concentrations at each time slot in order to develop a protocol for installing/retrieval of the PMMC in future field deployments (Figures 15 and 16). The field measurement data and simulation results indicated the breakthrough of contaminant for each gasket material depends on the VOCs

fluctuation within the field. Table 8 provides the error estimation of calibrated model, indicating good agreements between model predictions and field measurements. The minimum normalized concentrations at each time step, and comparison between two sites of Nashville and Newton as well as comparison between the rates of breakthrough at each deployment, have been used to develop the protocol presented in Table 9. The model predicts benzene breaking through the Neoprene and Buna-N will reach more than 69% and 64%, respectively, of the monitoring well concentration after 4 months. Since the PMMCs were installed in the monitoring wells under the water level and assuming constant hydraulic gradient across the site, the obtained results represent the upper bound values, or the “worst case scenario.” Likely, a pipe will be located in a zone of fluctuating water level, and at a site with transient hydraulic flow gradient. These two factors will likely lessen the potential for contaminant breakthrough the gasket materials.

8.5.2. PCE Contaminated Site

Figure 17 shows PCE concentration normalized with respect to maximum concentration in the monitoring well (15400 $\mu\text{g/l}$) at the Durham site. Since the measured concentrations within the PMMCs at first retrieval (17920 and 13970 $\mu\text{g/l}$) were higher than monitoring well concentration (9900 $\mu\text{g/l}$), it is hypothesized the contaminant concentration within the monitoring well fluctuated with time. It is noted that the purging processes during groundwater sample collection from monitoring wells yield aquifer concentration at the time of PMMC retrieval and these concentrations could be exposed to any rise or drop in prior months. The fluctuation of concentrations in monitoring well can be due to seasonal rainfall and changes in groundwater level. Furthermore, the spatially and temporally varying hydrologic conditions in heterogeneous sites pose significant variations in contaminant fluxes during interval periods, accordingly, higher uncertainty may arise from sampler measurements in prediction analyses (Verreydt et al. 2010). The main objective of this study is to set a protocol based on the data collected from different sites with various characteristics and numerical analysis. The measurements at various time intervals allow seasonal fluctuations to be taken into account. For modeling purposes, it is assumed that both Neoprene and Buna-N gained 100% of monitoring well concentration at first retrieval, accordingly, the k_e was obtained to be 4.3×10^{-11} m/s for both materials at first retrieval. The results from the 3D numerical model of the contaminated site in Durham have been updated by incorporating the data of the second retrieval. Lower values were calibrated for k_e and D of Neoprene and Buna during 9 months exposure at second deployment, as presented in Table 6. Due

to the lower concentration detected in PMMC with Neoprene, the k_e and D of Neoprene is slightly smaller than the corresponding values for Buna-N. However, this slightly less concentration can be due to environmental conditions such as seasonal rainfall, temperature fluctuation, as well as multi-species diffusion, or even accuracy of the measured lab analyses of the water samples. Thus the results herein should be viewed with caution as these do not necessarily reflect a better performance of Neoprene over Buna-N. The calibrated parameters are used in the developed model to predict the PCE breaking through gasket materials with time. Figure 17 confirms similar trends of contaminant breakthrough with time for both Neoprene and Buna using calibrated parameters.

Figure 18 shows normalized PCE breakthrough the gasket materials with respect to monitoring well concentration at each time slot. The minimum normalized concentrations at each time step for Neoprene and Buna, as well as comparison between the rates of breakthrough at each deployment, have been used to develop the protocol presented in Table 10. The model predicts PCE breaking through the Neoprene and Buna-N will reach around 59% of the monitoring well concentration after 4 months. Due to the similar performance of Neoprene and Buna, the same protocol for installing/retrieval of both materials is suggested. It is noted that due to small concentrations detected in PMMC with Viton (not detected), the parameters of this gasket type were not well calibrated, however, the results indicate Viton performance against PCE and benzene significantly surpasses that of Neoprene and Buna-N.

The Peclet numbers are used to determine the domination of advective flux. Hatfield et al. (2004) indicated one order of magnitude relative difference between advective and diffusive transport processes (i.e. Peclet number=10) is needed to ensure advective dominated flux transport. Permeation-based samplers are typically used to directly measure contaminant mass flux (Verreydt et al. 2010). Hatfield et al. (2004) used a passive flux meter (PMF) to quantify cumulative contaminant mass flux. The Peclet numbers in experiments of PMF ranged from 43 to 415, hence indicated advective dominated transport. The Peclet number in this study is calculated in the range of 24 -to- 50 as shown in Table 11. The Peclet numbers indicate in the simulation approach used in this study to calibrate the PMMCs, advective transport dominates diffusive flux. Therefore, the simulation results are sensitive to the groundwater flow rate, hydraulic gradient and equivalent hydraulic conductivities of pipe samples.

8.6. Conclusion

A new monitoring tool named PMMC was designed to evaluate volatile organic compounds (VOCs) and chlorinated solvents (CS) breakthrough the pipe materials; Neoprene, Buna-N, and Viton mostly used as gasket materials of pipe joints. This monitoring tool can be of considerable value in the risk-based assessment and management of subsurface utility materials.

3D field-domain models have been developed for the sites of study to calibrate hydraulic parameters of PMMC (k_e , D). The diffusion coefficient (D) and equivalent hydraulic conductivities (k_e) of Neoprene and Buna-N against benzene and PCE were calibrated as Table 7. A very low value was calibrated for diffusion coefficient of Viton in the case of benzene breakthrough.

After calibration the model has been used for prediction of benzene and PCE breakthrough the gasket materials at the field scale. The breakthrough of contaminant for each gasket material depends on the field condition and contaminant fluctuation within the domain.

The model predicts benzene breaking through the Neoprene and Buna-N will reach more than 70% and 60% of the monitoring well concentration after 4 months, respectively. The model predicts PCE breaking through the Neoprene and Buna-N will reach around 60% of the monitoring well concentration after 4 months. A recommended protocol for installing/retrieval of PMMCs to monitor breakthrough rate is presented in Tables 9 and 10.

Both gasket materials of Neoprene and Buna-N showed a higher rate of contaminant breakthrough compared to Viton.

The fluctuation of concentrations in monitoring well due to seasonal rainfall and changes in groundwater level, temperature fluctuation, multi-species diffusion, or even accuracy of the measured lab analyses of the liquid samples are important factors affecting model calibration and hydraulic parameters of PMMC.

Table 8.1 Deployment/retrieval schedule of PMMCs.

Site	MW ID	1st deployment	1st retrieval/2nd deployment	2nd retrieval
Nashville	MW-3	Mar-20	Jul-20	Feb-21
Newton	MW-3	Mar-20	Dec-20	Jan-21
Durham	RW-2	Mar-20	Sep-20	Jun-21

Table 8.2 Monitoring well characteristics and detected VOC concentration history before and during PMMC deployment.

Site	Nashville	Newton	Durham
Monitoring well ID (PMMC location)	MW-3	MW-3	RW-2
Depth (m)	6.30	10.60	7.60
Depth to groundwater (m)	4.47	6.55	1.70
Analyte	Benzene	Benzene	PCE
Well concentration before 1 st deployment (ppb) in 2019	19400	350	88000*
Well concentration at 1 st deployment (ppb) in 2020	506	1380	7120
Well concentration at 2 nd deployment/1 st retrieval (ppb) in 2020	8990	1600	9900
Well concentration at 2 nd retrieval (ppb) in 2021	18200	1230	15400

* The last reported concentration for this well before study commencement in 2020 was on Nov. 2008.

Table 8.3 Results of PMMC measurements.

Site	Analyte	Gasket Material	1 st retrieval			2 nd retrieval		
			Exposure time (d)	Concentration (PPb or µg/l)	COV (%)	Exposure time (d)	Concentration (PPb or µg/l)	COV (%)
Nashville	Benzene	Neoprene	135	7068	2.1	211	15863	3.9
		Buna-N	135	4949	1.4	211	17151	3.4
		Viton	135	63	5.7	211	ND (< 5 µg/L)	ND
		QC	135	3	31.4	211	ND (< 5 µg/L)	ND
Newton	Benzene	Neoprene	273	1120	1.3	59	1730	2.2
		Buna-N	273	680	3.6	59	1690	0.7
		Viton	273	ND (< 5 µg/L)	ND*	59	210	4.9
		QC	273	ND (< 5 µg/L)	ND	59	ND (< 5 µg/L)	ND
Durham	PCE	Neoprene	183	17923	0.3	272	9550	0.6
		Buna-N	183	13790	0.6	272	10550	4.9
		Viton	183	4	10.9	272	ND (< 5 µg/L)	ND
		QC	183	ND (< 5 µg/L)	ND	272	ND (< 5 µg/L)	ND

*ND: Not determined.

Table 8.4 Model flow and transport parameters.

Parameter/Material	Symbol	Native soil	Sample	Capsule	Capsule inside	Well
Horizontal Hydraulic conductivity(m/s)	$kh_x=kh_y$	Site material	Calibrated	1×10^{-20}	1×10^{-2}	1×10^{-4}
Hydraulic conductivity ratio	kh_x/k_v	2	1	1	1	1
Porosity	n_e	Site material	1×10^{-2}	1×10^{-10}	0.99	0.99
Diffusion (m^2/s)	D	1.0- 1.1×10^{-9}	Calibrated	1×10^{-20}	1.0- 1.1×10^{-9}	1.0- 1.1×10^{-9}
Longitudinal Dispersion (m)	α_x	2	1×10^{-3}	1×10^{-3}	1×10^{-3}	2
Horizontal/Longitudinal disp.	α_y/α_x	0.3	0.3	0.3	0.3	0.3
Vertical/Longitudinal disp.	α_z/α_x	0.05	0.05	0.05	0.05	0.05
Density (kg/m^3)	ρ_b	Site material	1300	2700	1000	1000

Table 8.5 Site material flow and transport parameters.

Parameter/Site	Symbol	Newton	Nashville	Durham
Soil type		Silty Clay- Sandy silt	Sandy Silt	Silty Clay
Horizontal Hydraulic conductivity(m/s)	$kh_x=kh_y$	2×10^{-7}	1×10^{-6}	4×10^{-8}
Porosity	n_e	0.25	0.22	0.27
Density (kg/m^3)	ρ_b	1600	1700	1710
Organic carbon fraction (%)	f_{oc}	0.1	0.1	2.4
Partition coefficient (m^3/mg)	K_d	8.5×10^{-11}	8.5×10^{-11}	1.1×10^{-10}
The first-order reaction rate of the dissolved (mobile) phase (d^{-1})	K_1	1×10^{-5}	1×10^{-5}	1.9×10^{-4}
The first-order reaction rate of the sorbed (immobile phase) (d^{-1})	K_2	1×10^{-5}	1×10^{-5}	1.9×10^{-4}

Table 8.6 Calibrated hydraulic parameters of gasket samples (D and k_e) for each site and after each deployment/retrieval.

Site	Analyte	Sample	Exposure duration	D	k_e	Exposure duration	D	k_e
			(m)	(m^2/s)	(m/s)	(m)	(m^2/s)	(m/s)
Nashville	Benzene	Neoprene	4.5	3.89×10^{-13}	4.55×10^{-11}	7	3.78×10^{-13}	1.10×10^{-11}
		Buna-N		2.12×10^{-13}	1.00×10^{-12}		ND	3.70×10^{-11}
		Viton		3.40×10^{-14}	ND		ND	ND
Newton	Benzene	Neoprene	9	ND	1.40×10^{-11}	2	1.23×10^{-12}	4.50×10^{-11}
		Buna-N		ND	1.30×10^{-12}		4.54×10^{-13}	7.00×10^{-12}
		Viton		4.04×10^{-14}	ND		ND	ND
Durham	PCE	Neoprene	6	ND	ND	9	1.22×10^{-13}	9.0×10^{-12}
		Buna-N		ND	ND		1.32×10^{-13}	1.1×10^{-11}
		Viton		1.45×10^{-14}	ND		ND	ND

Table 8.7 Calibrated hydraulic parameters of gasket samples (D and k_e) for benzene and PCE used in prediction studies.

Analyte	Sample	k_e	D
		(m/s)	(m^2/s)
Benzene	Neoprene	2.89×10^{-11}	3.85×10^{-13}
	Buna-N	1.45×10^{-11}	2.12×10^{-13}
	Viton	ND	3.40×10^{-14}
PCE	Neoprene	9.0×10^{-12}	1.22×10^{-13}
	Buna-N	1.1×10^{-11}	1.32×10^{-13}
	Viton	ND	1.45×10^{-14}

Table 8.8 Error estimation of calibrated model.

Site	Sample	Normalized Measured	Normalized Predicted	Normalized Measured	Normalized Predicted	Error 1 st	Error 2 nd	Average Error (%)
		1 st retrieval	1 st retrieval	2 nd retrieval	2 nd retrieval	retrieval (%)	retrieval (%)	
Nashville	Neoprene	79	73	87	92	7	5	10
	Buna-N	55	67	94	88	18	7	
Newton	Neoprene	108	100	91	80	8	12	
	Buna-N	106	100	55	66	5	16	

Table 8.9 Recommended protocol for installing/retrieval of gasket-capsules to monitor Benzene breakthrough rate.

Normalized benzene breakthrough concentration with monitoring well concentration (%) (C_c/C_{wi})- predicted by field simulation				
	Sample/time	2 months	4 months	6 months
Minimum 2 sites	Neoprene	50	69	90
	Buna-N	43	64	85

Table 8.10 Recommended protocol for installing/retrieval of gasket-capsules to monitor PCE breakthrough rate.

Normalized PCE breakthrough concentration with monitoring well concentration (%) (C_c/C_{wi})- predicted by field simulation				
	Sample/time	2 months	4 months	6 months
Durham	Neoprene	42	59	64
	Buna-N	42	59	64

Table 8.11 Calculated Peclet number for benzene and PCE breakthrough the gasket materials installed in PMMC.

Sample/Site	Peclet Number		
	Newton	Nashville	Durham
Neoprene	26.14	36.30	49.73
Buna-N	23.83	33.89	27.38



Figure 8.1 The pipe material monitoring capsule (PMMC) designed at the lab and deployed on the contaminated sites. The components include stainless cup open at one end, ultrapure water as liquid receiving phase, pipe material sheet fixed at open end, and sealing hollow grooved cap.

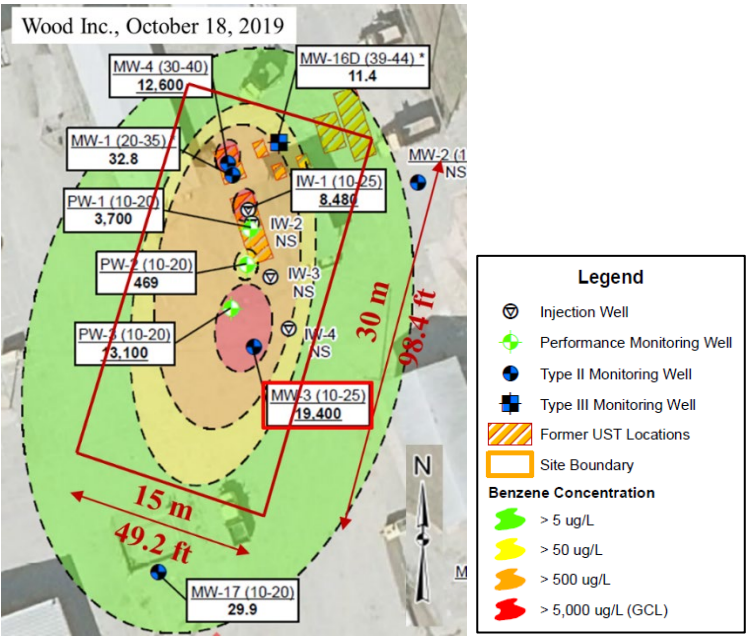


Figure 8.2 Nashville site map and model domain (after Wood, 2019).

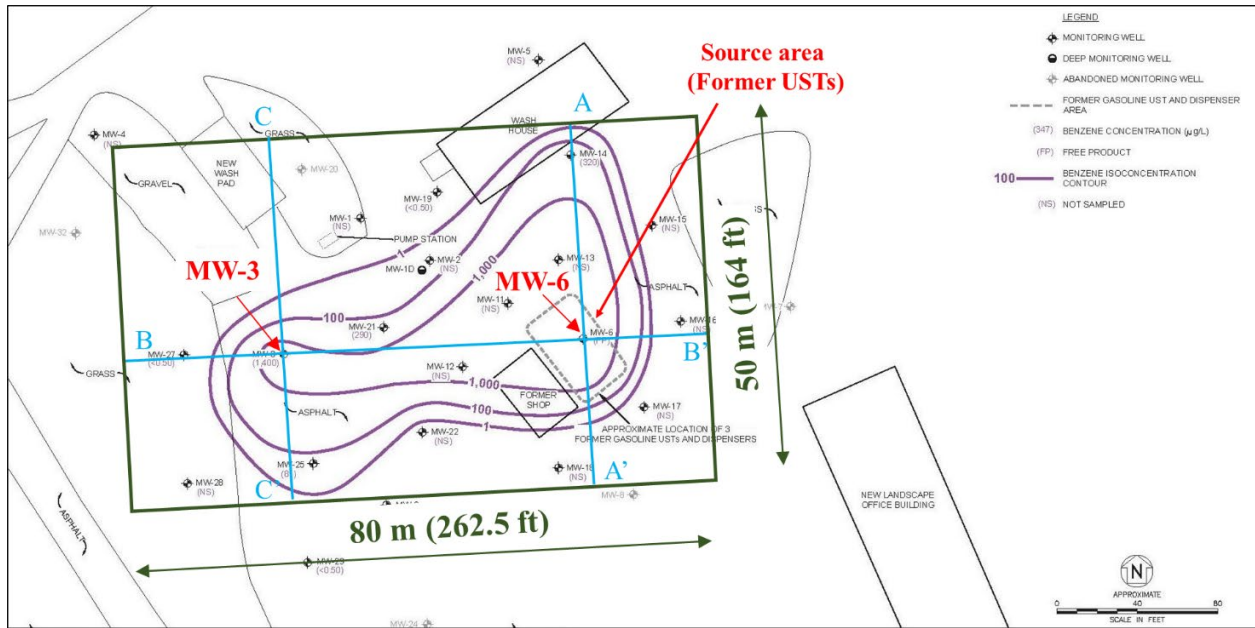


Figure 8.3 Newton site map and model domain (after Hart & Hickman 2018, Pace analytical services report 2020).

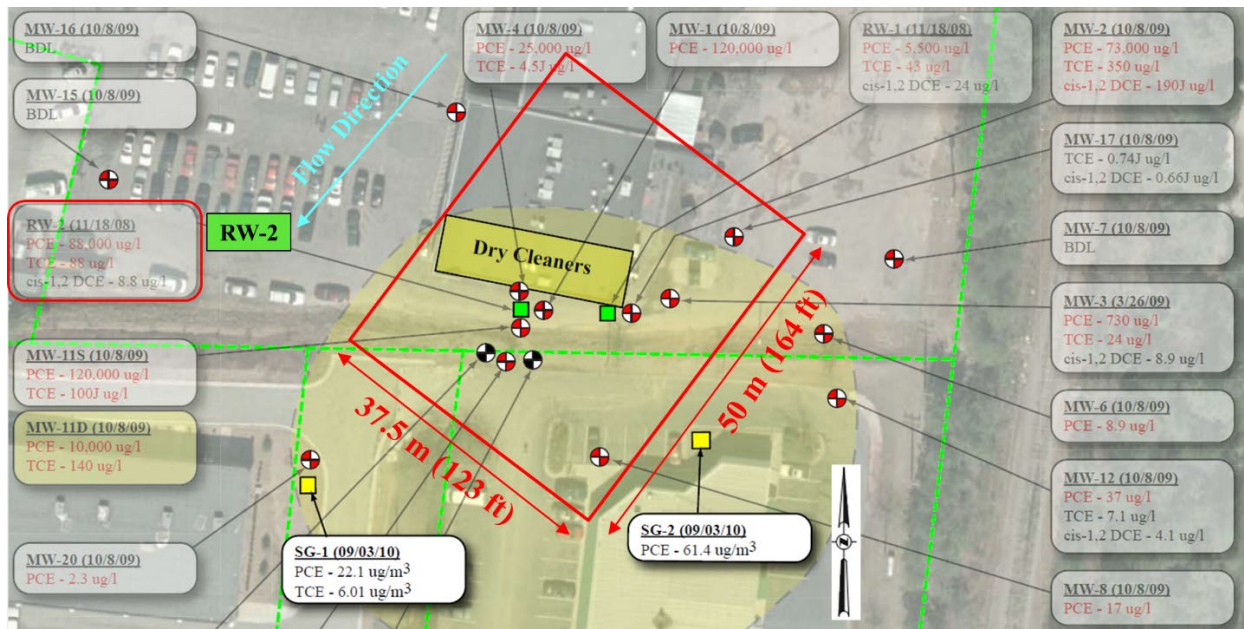
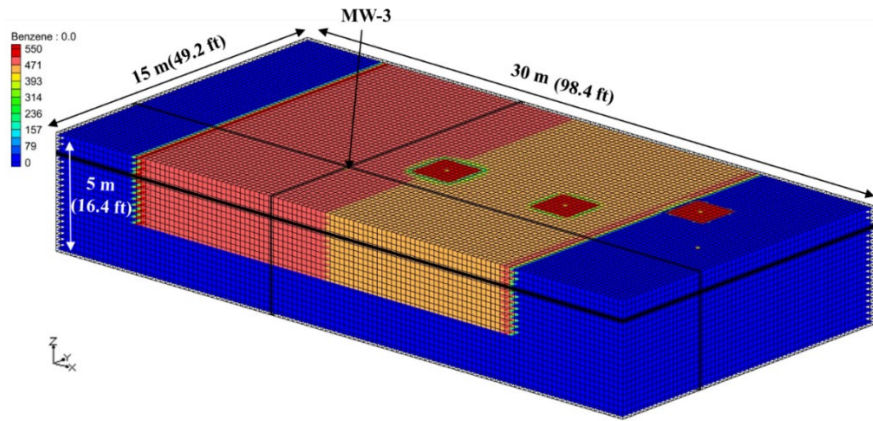
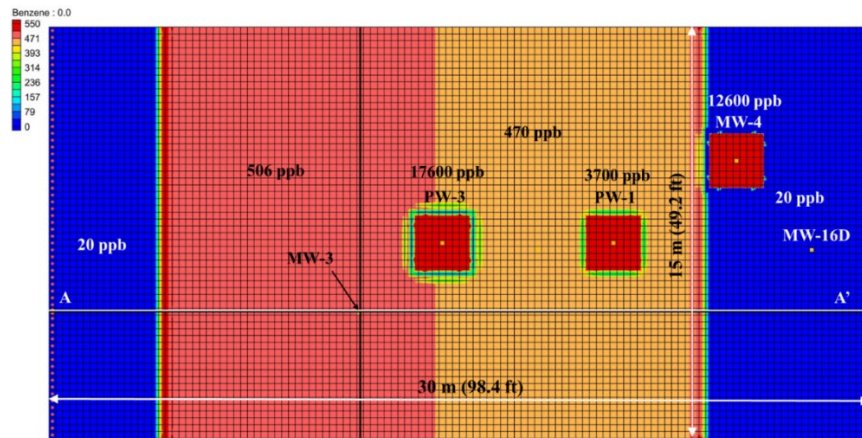


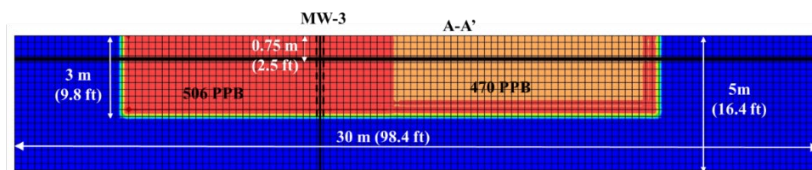
Figure 8.4 Durham site map and model domain (After URS 2015).



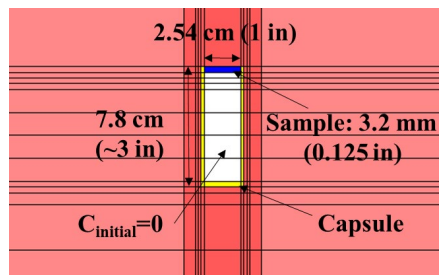
(a)



(b)

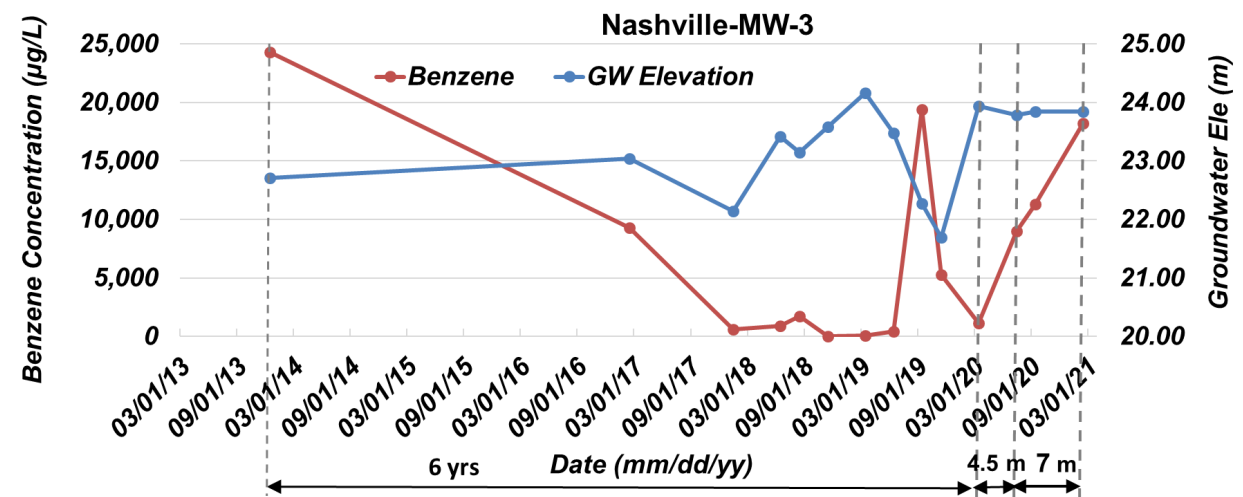


(c)

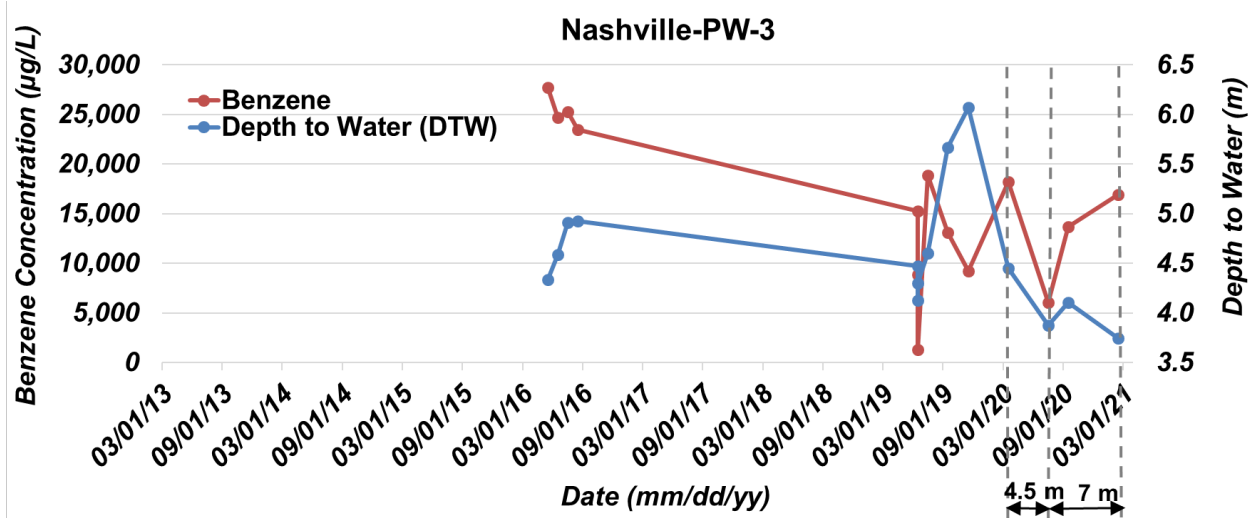


(d)

Figure 8.5 Model development of Nashville site, (a) 3D domain, (b) Plan view, (c) Cross section view of the simulated model and (d) the PMMC being simulated in MW3.

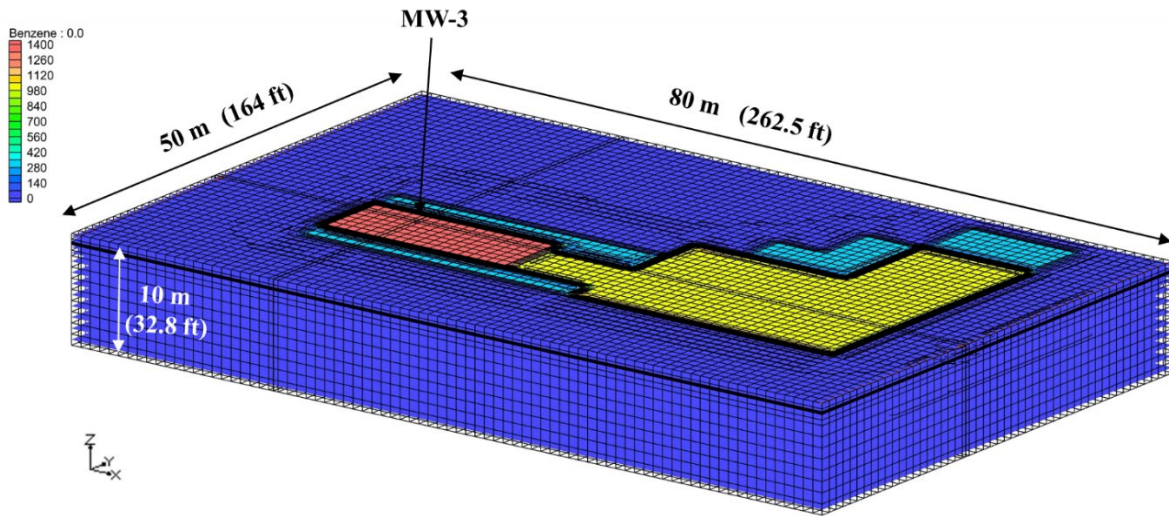


(a)

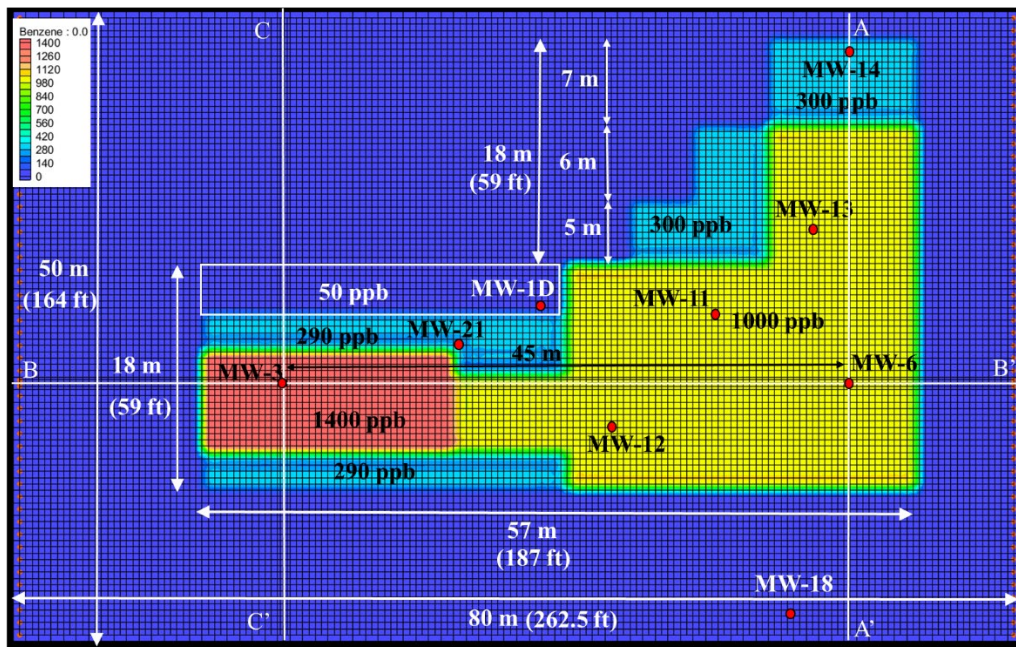


(b)

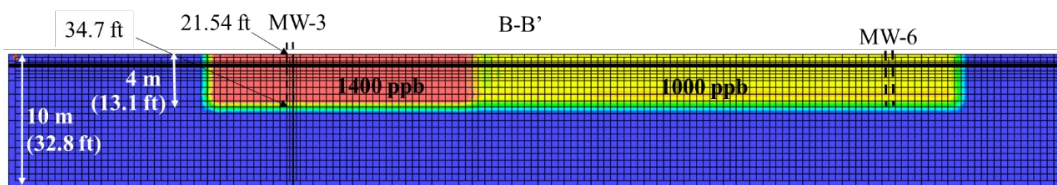
Figure 8.6 (a) The hydrograph of monitoring well (MW-3) where the PMMCs have been deployed in Nashville site, (b) the hydrograph of monitoring well PW-3 located near MW-3 indicating groundwater level and benzene fluctuation (after Wood Inc., 2021).



(a)



(b)



(c)

Figure 8.7 Model development of Newton site, (a) 3D domain, (b) Plan view, (c) Cross section view of the simulated model.

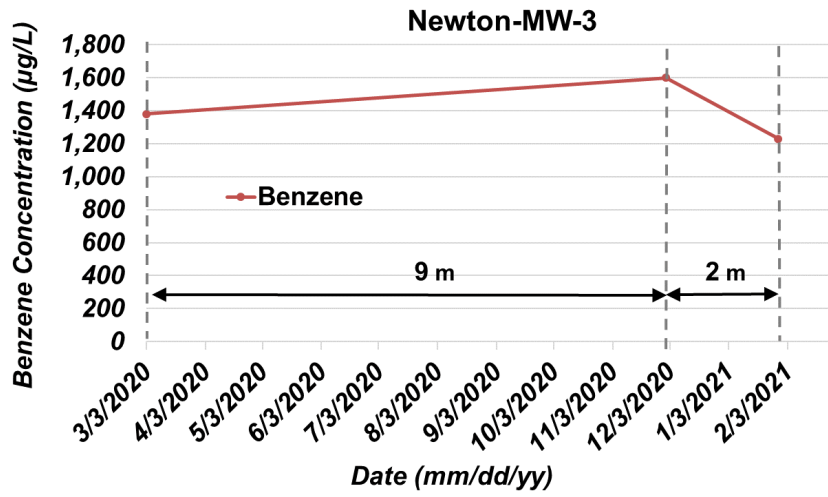
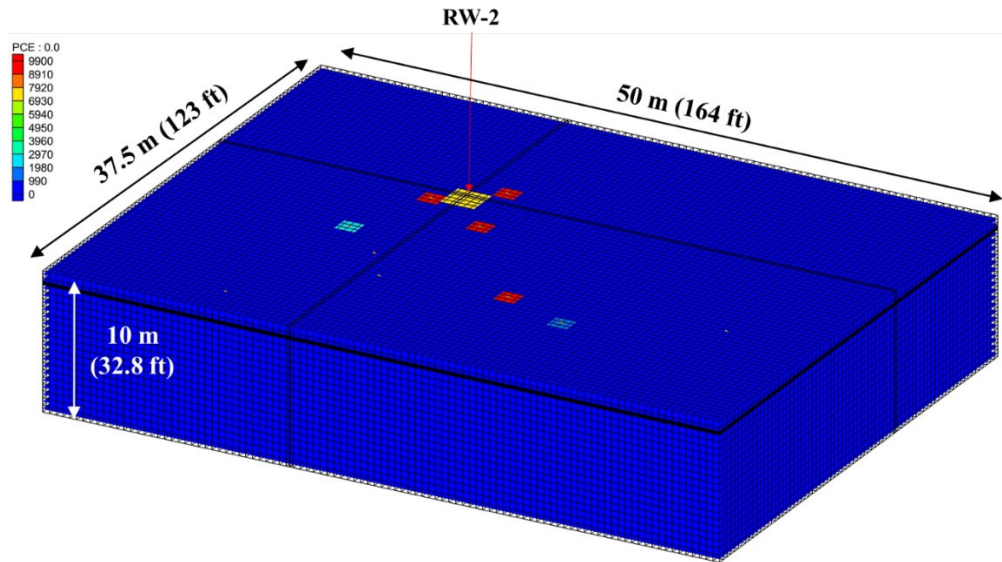
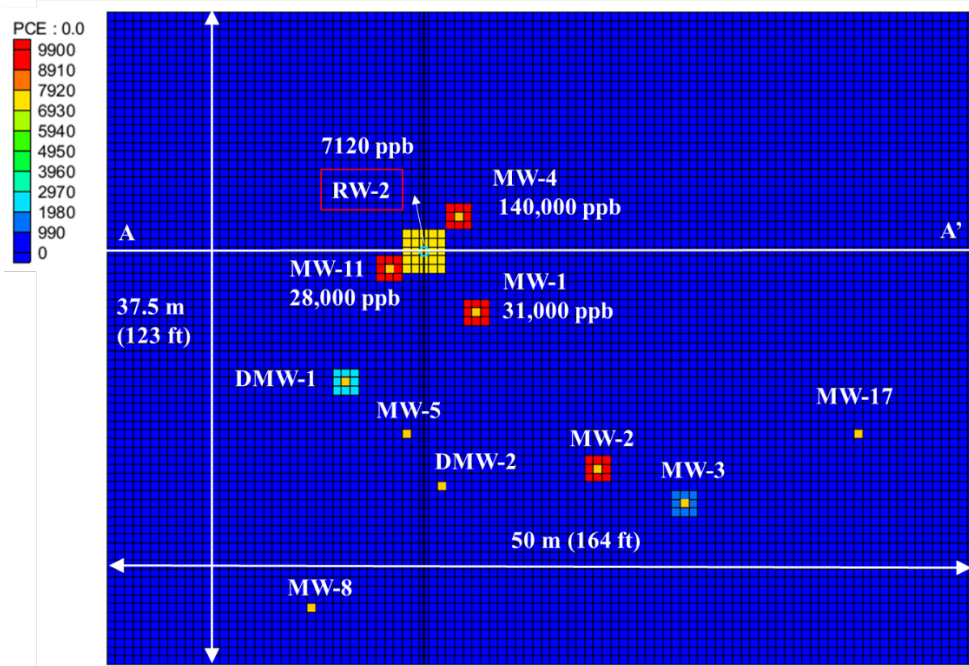


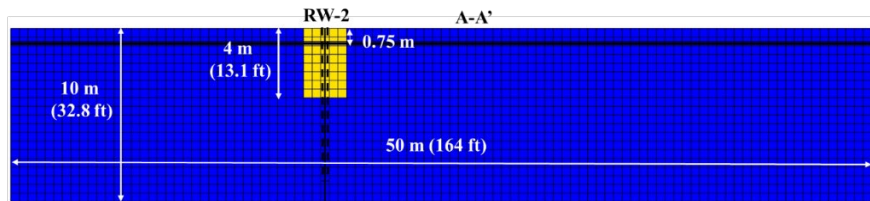
Figure 8.8 The hydrograph of monitoring well (MW-3) where the PMMCs have been deployed in Newton site, indicating benzene fluctuation during deployment.



(a)



(b)



(c)

Figure 8.9 Model development of Newton site, (a) 3D domain, (b) Plan view, (c) Cross section view of the simulated model and the capsule being simulated in MW3.

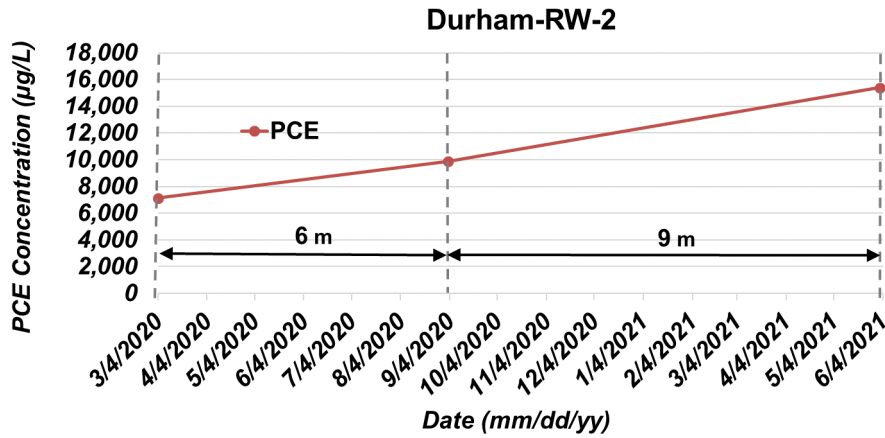


Figure 8.10 The hydrograph of monitoring well (Rw-2) where the PMMCs have been deployed in Newton site, indicating benzene fluctuation during deployment.

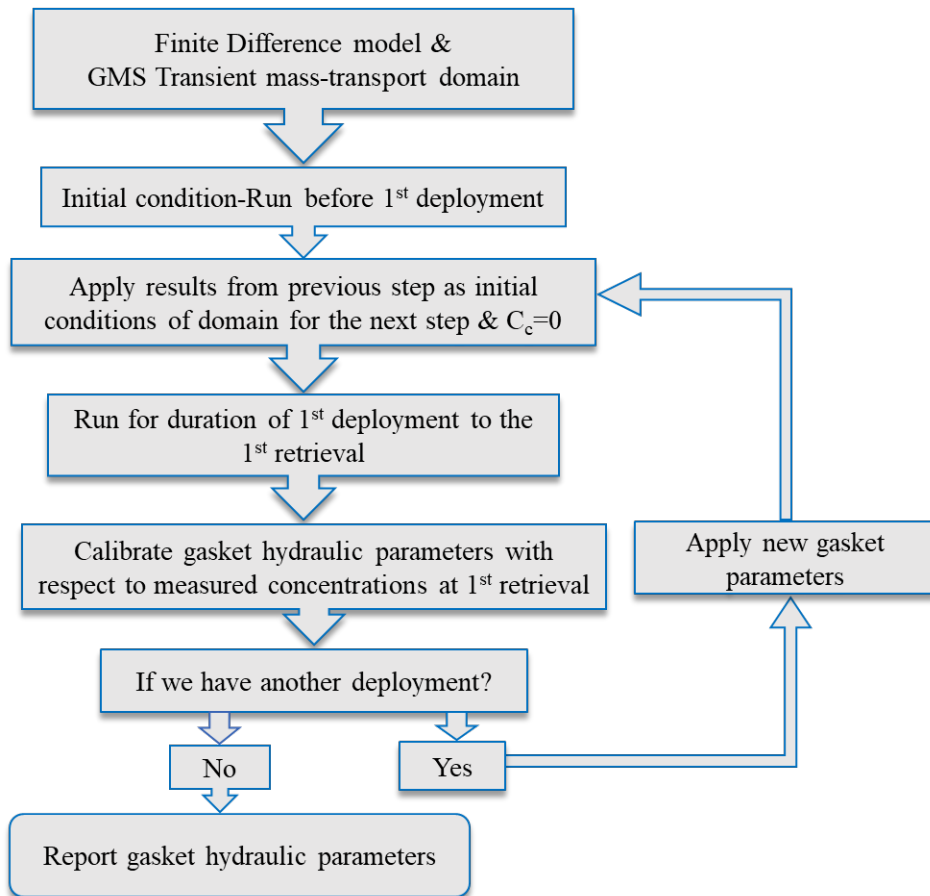


Figure 8.11 Calibration flowchart (Cc: PMMC measurement).

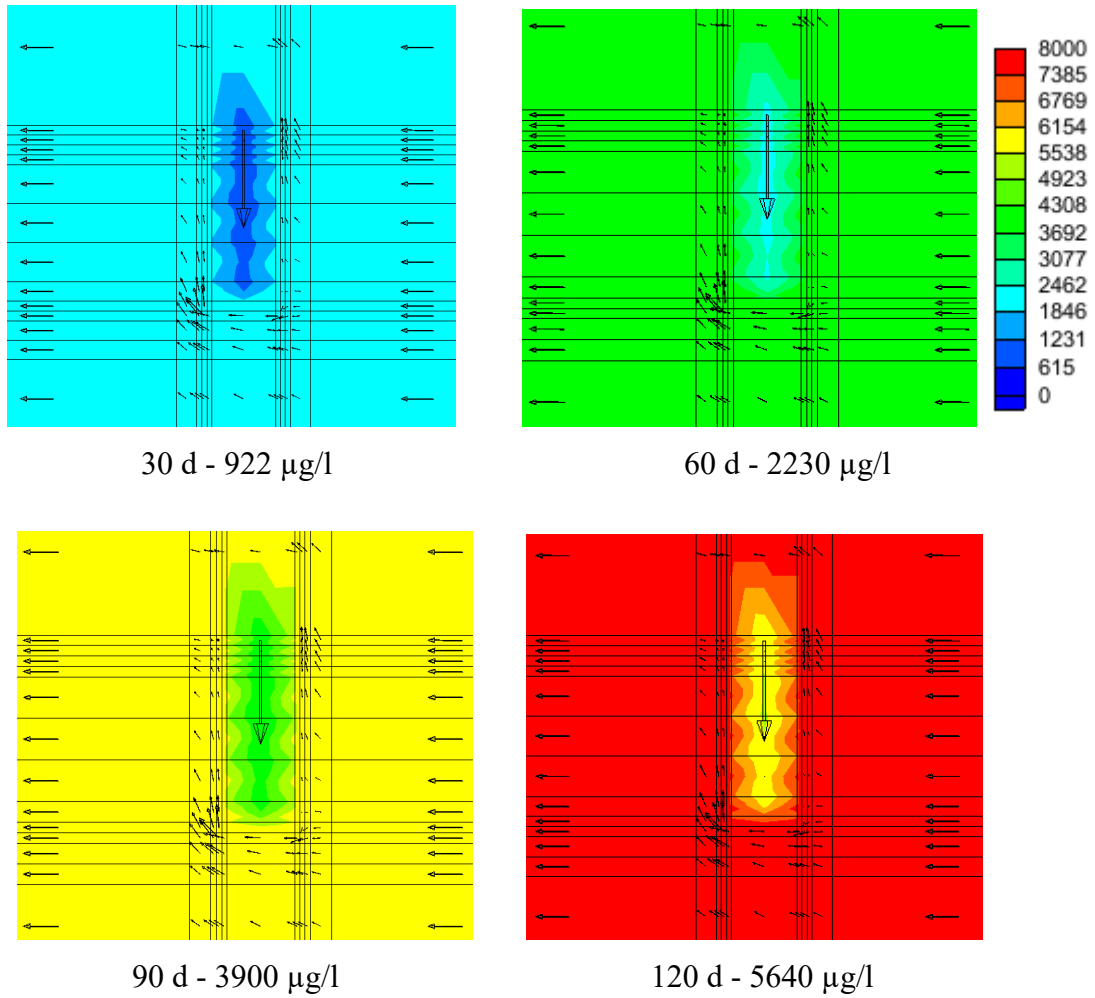


Figure 8.12 Benzene breakthrough the sample (Neoprene) installed at the top of the PMMC after one, two, three, and four months at Nashville site. The direction and relative magnitude of velocity vectors are shown here.

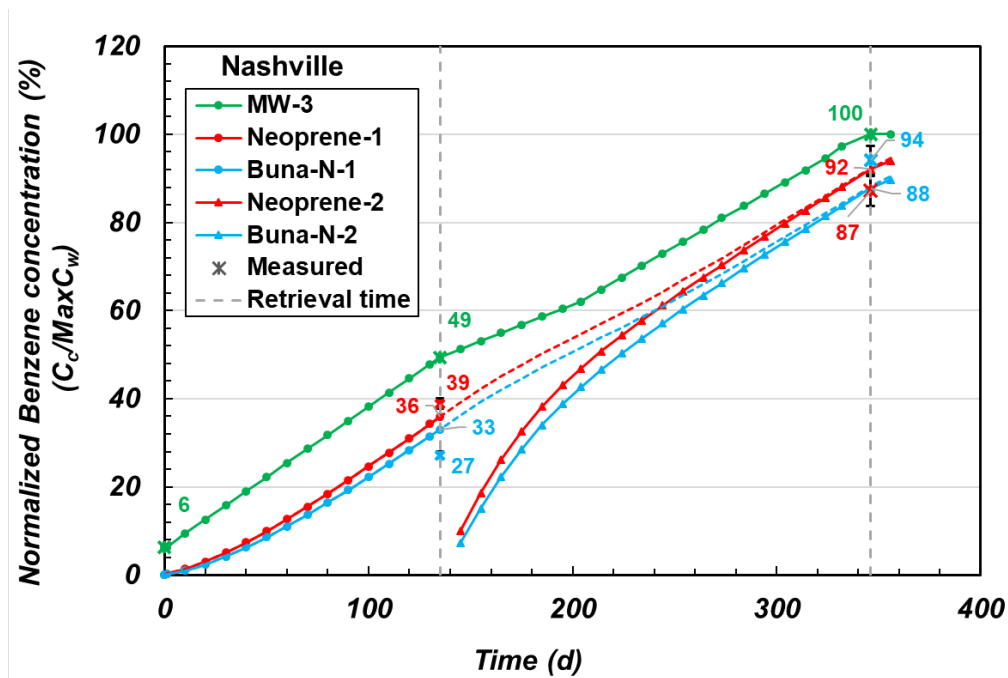


Figure 8.13 Normalized benzene breakthrough concentration in Nashville site using calibrated parameters of both gasoline contaminated sites.

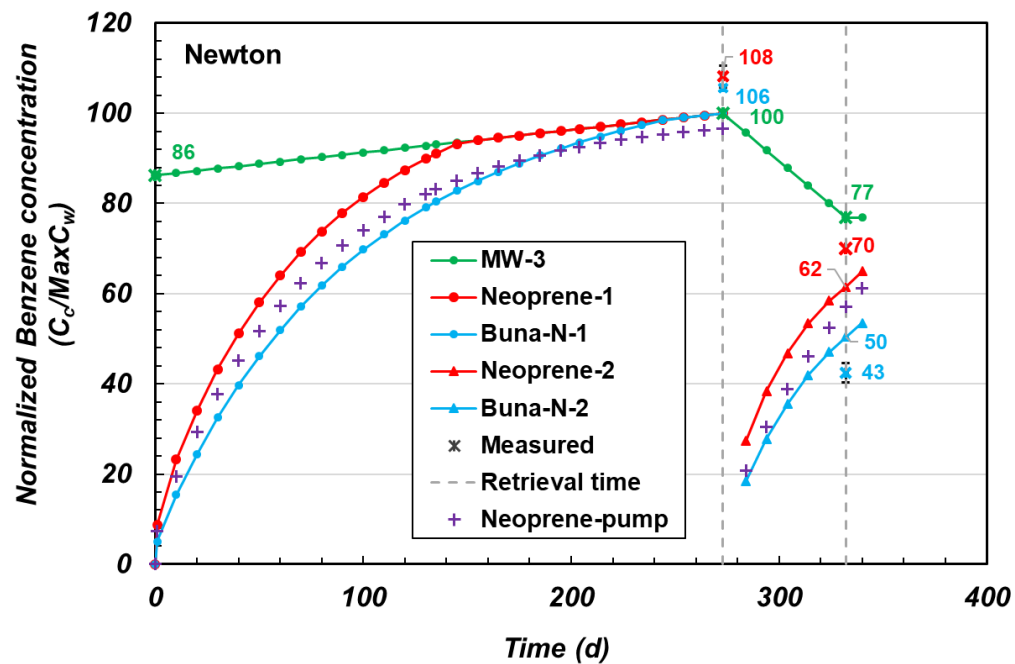


Figure 8.14 Normalized benzene breakthrough concentration in Newton site using calibrated parameters of both gasoline contaminated sites.

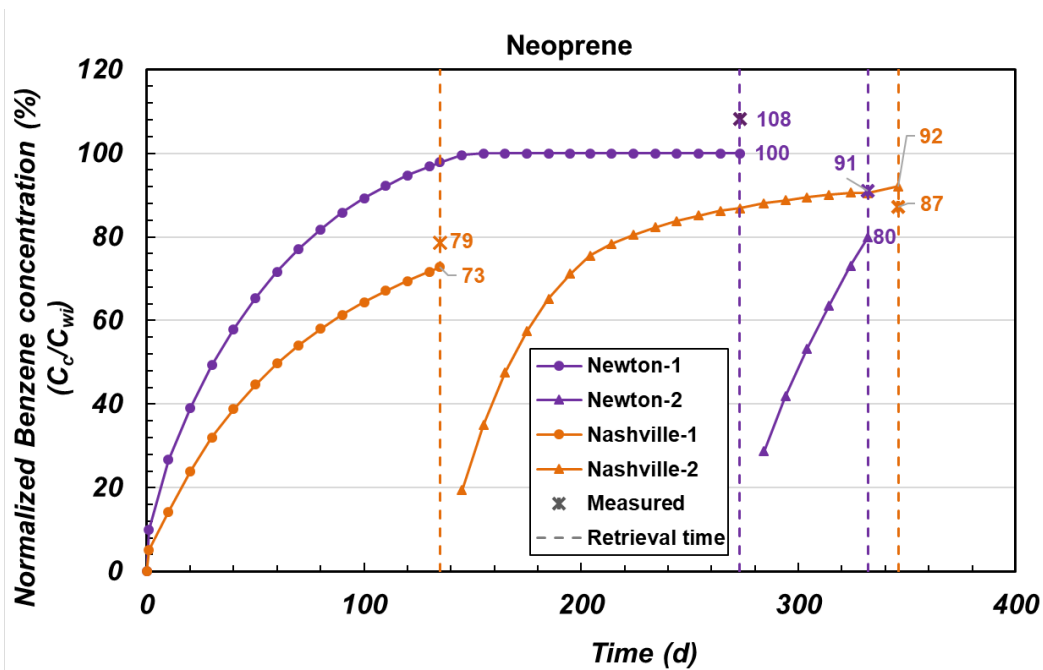


Figure 8.15 Benzene breakthrough rate for Neoprene comparing two sites and two deployment/retrieval (C_{wi} : concentration measured in monitoring well at each time slot).

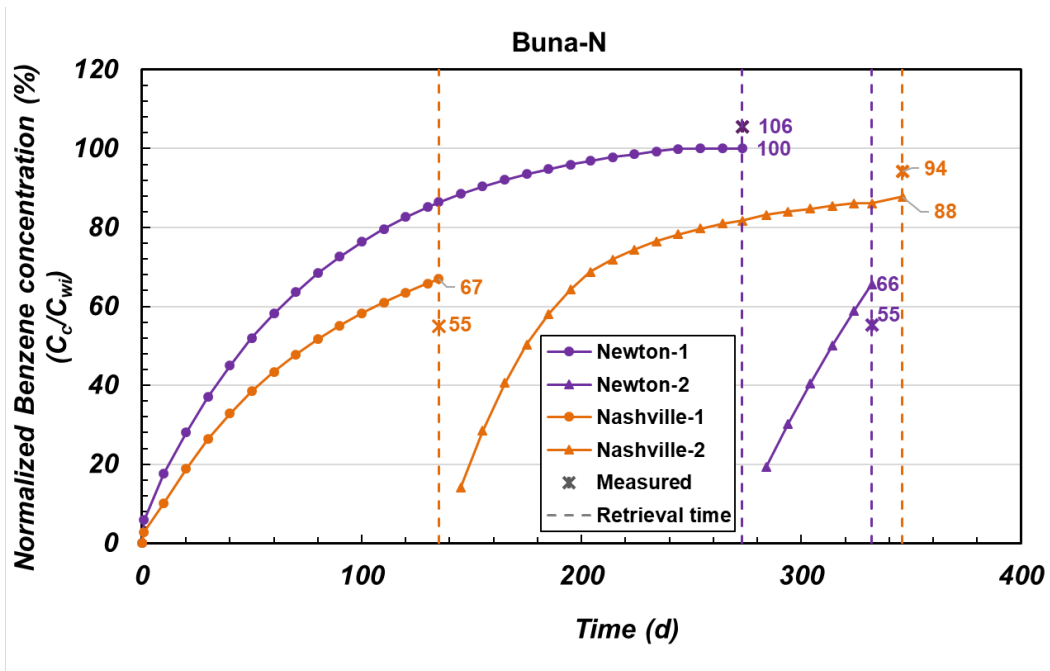


Figure 8.16 Benzene breakthrough rate for Buna-N comparing two sites and two deployment/retrieval (C_{wi} : concentration measured in monitoring well at each time slot).

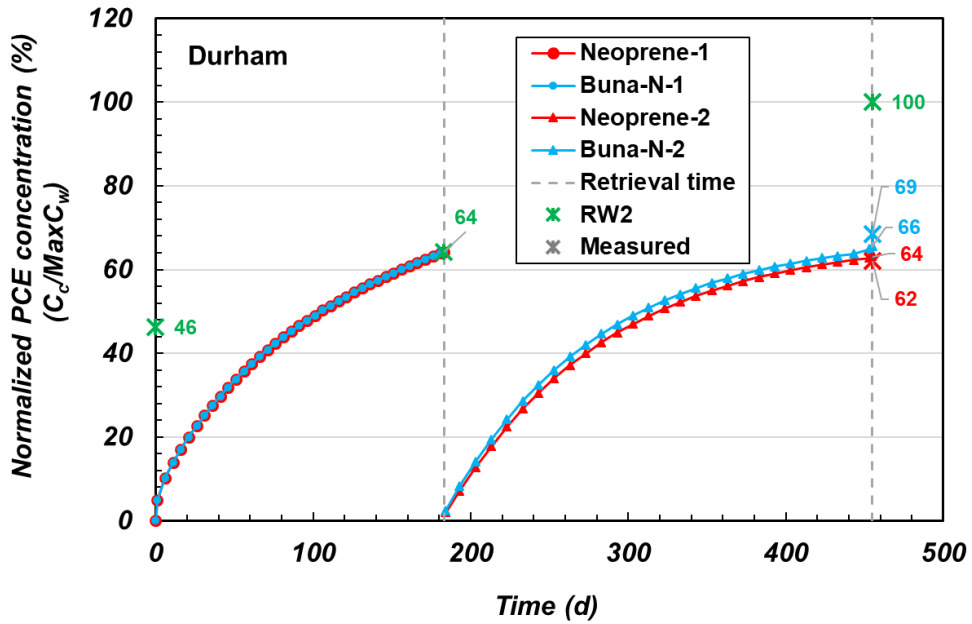


Figure 8.17 Normalized PCE breakthrough concentration in Durham site using calibrated parameters of PCE contaminated site.

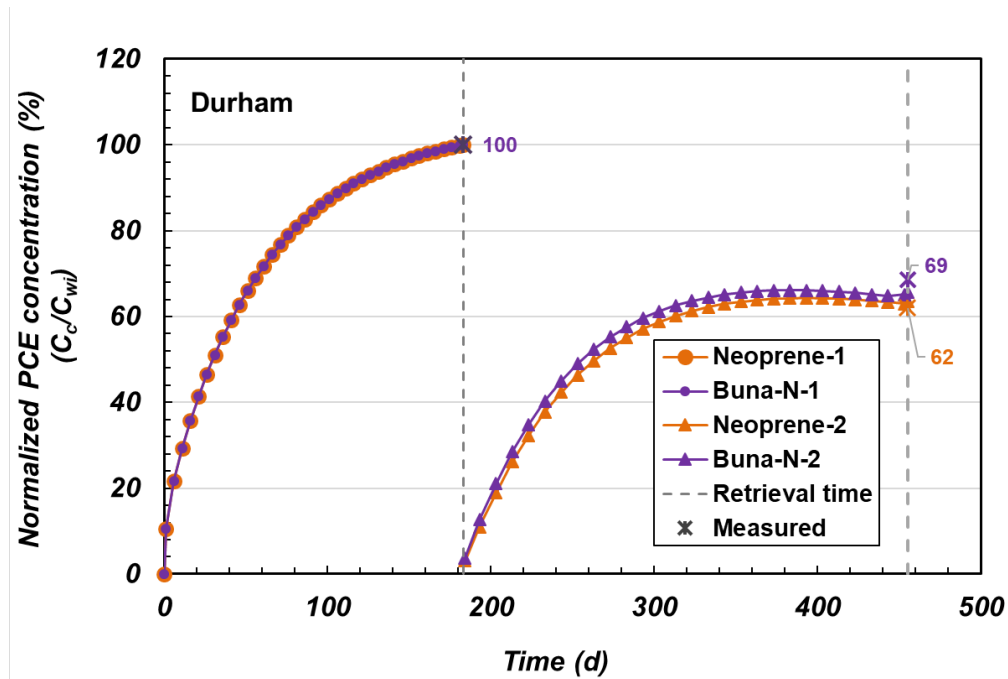


Figure 8.18 PCE breakthrough rate for Neoprene and Buna-N comparing two deployment/retrieval normalized with concentration at each time slot (C_{wi} : concentration measured in monitoring well at each time slot).

CHAPTER 9. Contributions and Future works

9.1. Contribution

Reactive transport analyses have been conducted to explore MICP process in subsurface profile and contaminant breakthrough into gasketed concrete pipes. The main contributions in this study are as follows:

- A model framework has been developed to calibrate parameters of MICP reactive transport model in small- and large-scale tests for upscaling and design of field deployment protocols.
- A range for important model parameters; specific ureolysis rate, microbial attachment model parameters and decay rate coefficients has been calibrated.
- The variations in mass percentage and distribution of CaCO_3 were determined with varying model parameters within calibrated range or the range derived from literature.
- All effective features of MICP model have been assessed through sensitivity analyses. The results emphasized the effects of principal factors of microbial activity, microbial attachment efficiency, and number of treatment (among all 15 assessed parameters) on the precipitation content and distribution.
- Little attention has been paid to biomass and calcium carbonate distribution in large-scale trials (surface and depth distribution) which can affect consistency of bio-cemented soil and local failures. Five approaches for biomass distribution were calibrated in small-and large-scale tests; (a) constant rate, (b) non-linear power-law distribution function, (c) exponential distribution function, (d) gamma distribution function, and (e) the c_{str} based on the colloid attachment theory.
- It was shown that constant attachment rate model which is traditionally used in literature is incapable of simulating exact distribution of calcium carbonate within surface and more important, within the depth but is useful to determine average mass of calcium carbonate within a specific subarea.
- Of these simulated methods, “the c_{str} based on the colloid attachment theory” with straining component showed the most promising approach to better capture attached biomass and CaCO_3 distribution in small- and large-scale tests. Employing this theory to predict CaCO_3 mass content, the statistical parameters (SD and COV) for CaCO_3 mass distribution were improved by 68% in column tests compared to the model that used constant attachment rate.

In other words, the theory shows 68% improvement in simulation predictions compared to traditional models. In the large-scale test the improvement was by 21-53% in SD , and 29-59% in R^2 .

- Various layouts and configurations of injection wells have been explored in deployment of MICP at field condition and the most promising design was determined in terms of continuity and level of cementation as well as associated by-products. Under the same flow rate and injected volumetric solutions, increasing the number of wells beyond 4 does not necessarily improve treatment extent.
- MICP model has been calibrated at various saturation degrees. The attachment coefficient (K_{at}) increases about 3 times with lowering the degree of saturation from 100% to 20%. The higher negative pressure and suction at lower saturation degrees may improve bacteria fixation within the pores and reduces the possibility of detachment.
- A model framework has been developed to evaluate factors affecting multiphase benzene breakthrough the concrete subsurface utilities with polymeric gaskets in unsaturated subsurface profile. The rate and magnitude of transported mass have been determined in both gaseous and aqueous phases.
- The simulations provide insights onto the effect of pipe material and gasket conditions, subsurface soil saturated and unsaturated properties, volatilization to atmosphere, and the thickness of initial contamination at the source on rate and magnitude of the transported mass. The use of lower-quality pipe concrete material led to increasing mass transport into the pipe by more than 60%.
- The analyses results show main mechanism of contaminant transport in the vadose zone is through vapor phase diffusion. However, due to SWCC of concrete materials, the pipe wall placed above groundwater level is mostly saturated and hinders gas diffusion, while the gas phase is the main phase breaking through the gasket if the gasket is damaged.
- The analyses for the damaged versus undamaged gaskets indicates that severe-damaged gaskets, can increase the concentrations and mass transfer into the pipe in both gas and aqueous phases by more than two orders of magnitude.
- A new monitoring tool named PMMC was designed and calibrated to evaluate volatile organic compounds (VOCs) and chlorinated solvents (CS) breakthrough the pipe materials; Neoprene, Buna-N, and Viton mostly used as gasket materials of pipe joints. This monitoring

tool can be of considerable value in the risk-based assessment and management of subsurface utilities materials.

- The hydraulic properties of pipe gasket materials (Neoprene, Buna-N, Viton gaskets) such as hydraulic conductivity and diffusion coefficient have been calibrated.
- A protocol was recommended for installing/retrieval of PMMCs to monitor breakthrough rate of benzene and PCE.

9.2. Future Work

- Conducting more experiments and simulations to verify the bacteria attachment model and narrow down the range of straining coefficient rates for large-scale tests.
- Implementing further experimentally measurements to improve the accuracy of model predictions (Kozeny-Carman) for hydraulic conductivities of cemented soils.
- Assessing biogeochemical kinetics and reaction rates at pore-scale and using pore-scale models along with macro-scale model presented in this work to having deep understanding of biomass attachment in pore throat or particle surface and verify the accuracy of macro-scale models.
- Measuring material properties needed as input data into simulation such as SWCC curves for cemented sands in MICP, or SWCC curves for concrete pipe or pipe trench materials in contaminant breakthrough models.
- Conducting MICP experiments at variable degrees of saturation and verifying the model in these conditions.
- The precipitation rate in this study was considered to be similar to ureolysis rate. Measurements of precipitation rates and determining $A_{c,t}$ (the total average crystal surface area) used in precipitation rate can be helpful.
- Coupling strength-reactive transport models to make predictions of calcium carbonate content based on shear wave velocity measurements during precipitation in large- and field scale trials.

Limitations

Results of the modeling were performed for laboratory-scale MICP experiments whether small- or large-scale and these samples are prepared under controlled conditions to extend the modeling results and calibrate parameters per field. Calibrations are needed to be performed using soil conditions encountered in the field.

REFERENCES

- Alhomair S., Z. Faeli, P. Hosseini, M. Gabr, M. Pour-Ghaz and C. Parker. 2020. "Assessment of mitigation measures against benzene breakthrough into subsurface concrete pipe", *Journal of Pipeline Systems Engineering and Practice*, 10.1061/(ASCE)PS.1949-1204.0000512.
- Al Qabany, A., K. Soga, and J. C. Santamarina. 2012. "Factors affecting efficiency of microbially induced calcite precipitation" *J. Geotech. Geoenviron. Engineering*, 138(8): 992–1001.
- Al Qabany, A., and K. Soga. 2013. "Effect of chemical treatment used in MICP on engineering properties of cemented soils." *Géotechnique*, 63(4): 331–339.
- Antea USA of North Carolina, Inc. 2016. "Groundwater monitoring report of 267 Western Boulevard project, Jacksonville, NC." Scotchman 3066, Project No. NC30661601.
- ASTM C14 2020. Standard specification for nonreinforced concrete sewer, storm drain, and culvert pipe, 10.1520/C0014-20.
- ASTM C76. 2019. Standard specification for reinforced concrete culvert, storm drain, and sewer pipe, 10.1520/C0076-19B.
- Baehr, A.L. 1987. "Selective transport of hydrocarbons in the unsaturated zone due to aqueous and vapor phase partitioning." *Water Resources Research*, 23(10), 1926-1938. <https://doi.org/10.1029/WR023i010p01926>.
- Bagarello, V., S. Sferlazza , and A. Sgroi. 2009. "Testing laboratory methods to determine the anisotropy of saturated hydraulic conductivity in a sandy-loam soil." *Geoderma*, 154, 52-58. <https://doi.org/10.1016/j.geoderma.2009.09.012>.
- Bao, J., and L. Wang. 2017. "Empirical estimation of the hydraulic diffusivity and sorptivity of unsaturated concrete subjected to sustained compressive loading." *Journal of Materials in Civil Engineering*, 29(12):04017242. [https://doi.org/10.1061/\(ASCE\)MT.1943-5533.0002104](https://doi.org/10.1061/(ASCE)MT.1943-5533.0002104).
- Barkouki, T., Martinez, B., Mortensen, B., Weathers, T., DeJong, J, and N. Spycher. 2011. "Forward and inverse bio-geochemical modeling of microbially induced calcium carbonate precipitation in half-meter column experiments." *Transport Porous Med*, 90:23–9.
- Battisteli, A. 2008. "Modeling multiphase Organic Spills in Coastal Sites with TMVOC V.2.0." *Vadose zone journal*, 7(1), 316-324. <https://doi.org/10.2136/vzj2006.0119>.
- Bolster, C. H., Mills, A. L., Hornberger, G. M. and J. S. Herman. 1999. "Spatial distribution of deposited bacteria following miscible displacement experiments in intact cores." *Water Resour. Res.*, 35:1797–1807.

- Bouwer, E., Rijnaarts, H., Cunningham, A., and R. Gerlach. 2000. "Biofilms II: process analysis and applications." Wiley- Liss, Inc., chapter Biofilms in Porous Media, 123–158.
- Bradford, S.A., Simunek, J., Bettahar, M., Van Genuchten, M. TH., and S.R.Yates. 2003. "Modeling colloid attachment, straining, and exclusion in saturated porous media." *Environ. Sci. Technol.*, 37(10): 2242-2250.
- Bradford, S.A., Bettahar, M., Simunek, J., and M. TH., Van Genuchten. 2004. "Straining and attachment of colloids in physically heterogeneous porous media." *Vadose Zone Journal* 3:384–394.
- Bradford, S. A., Simunek, J., Bettahar, M., van Genuchten, M. T., and S. R. Yates. 2006. "Significance of straining in colloid deposition: Evidence and implications." *Water Resources Research*, 42: W12S15, <https://doi.org/10.1029/2005WR004791>.
- Bradford, S. A., Torkzaban, S., and S. L. Walker. 2007. "Coupling of physical and chemical mechanisms of colloid straining in saturated porous media." *Water Research*, 41: 3012–3024.
- Cheng, L., R. Cord-Ruwisch, and M. A. Shahin. 2013. "Cementation of sand soil by microbially induced calcite precipitation at various degrees of saturation." *Can. Geotech. J.* 50 (1): 81–90. <https://doi.org/10.1139/cgj-2012-0023>.
- Class, H., R. Helmig, and P. Bastian. 2002. "Numerical simulation of non-Isothermal multiphase multicomponent processes in porous media, 1-An efficient solution technique." *Advances in Water Resources*, 25, 533-550. [https://doi.org/10.1016/S0309-1708\(02\)00014-3](https://doi.org/10.1016/S0309-1708(02)00014-3).
- Cornelius, W. 2013. "Ambient air quality report." Ambient monitoring section report #2013.01, U.S. Department of Environmental and Natural Resources, Division of Air Quality, Raleigh, North Carolina. <https://files.nc.gov/ncdeq/Air%20Quality/monitor/reports/2013-01.pdf>.
- Compere, F., Porel, G. and F. Delay .2001. "Transport and retention of clay particles in saturated porous media: Influence of ionic strength and pore velocity." *J. Contam. Hydrol.*, 49: 1–21.
- COMSOL, Multiphysics® v. 5.5. www.comsol.com, COMSOL AB, Stockholm, Sweden, 2020.
- Cunningham, A.B., Sharp, R.R., Caccavo, F., and R. Gerlach. 2007. "Effects of starvation on bacterial transport through porous media." *Adv. Water Resource*, 30: 1583–1592.
- Cushing, R.S., and D.F., Lawler. 1998. "Depth filtration: fundamental investigation through three-dimensional trajectory analysis." *Environ. Sci. Technol.* 32: 3793–3801.
- Cuthbert, M. O., McMillan, L. A., Handley-Sidhu, S., Riley, M. S., Tobler, D. J., and V. R. Phoenix. 2013. "A field and modeling study of fractured rock permeability reduction using microbially induced calcite precipitation." *Environmental Science & Technology*.

- 47(23):13637–13643. <https://doi.org/10.1021/es402601g>.
- DeJong, J. T., M. B. Fritzges, and K. Nüsslein. 2006. “Microbially induced cementation to control sand response to undrained shear.” *J. Geotech. Geoenviron. Eng.* 132 (11): 1381–1392. [https://doi.org/10.1061/\(ASCE\)1090-0241\(2006\)132:11\(1381\)](https://doi.org/10.1061/(ASCE)1090-0241(2006)132:11(1381)).
- Dafny, E. 2017. “TCE longevity in the vadose zone and loading to the groundwater-The case of episodic NAPL releases from near-surface source.” *Environmental Technology and Innovation*, 7: 128-140. <https://doi.org/10.1016/j.eti.2016.12.007>.
- Deiss, L., A. J. Franzluebbbers , A. Amoozegar, , D. Hesterberg , M. Polizzotto, , and F. W. Cabbage. 2017. “Soil carbon fractions from an alluvial soil texture gradient in North Carolina.” *Soil Science Society of America Journal*, 81(5), 1096-1106. <https://doi.org/10.2136/sssaj2016.09.0304>.
- DeJong, J.T, Mortensen, B.M., Martinez, B.M., and D.C. Nelson. 2010. “Bio-mediated soil improvement.” *Ecological Eng.* 36: 197–210. <https://doi.org/10.1016/j.ecoleng.2008.12.029>.
- Delle Site, A. 2001. “Factors affecting sorption of organic compounds in natural sorbent/water systems and sorption coefficients for selected pollutants.” *Journal of Physical Chemistry, Ref. Data*, 30(1),188-439. <https://doi.org/10.1063/1.1347984>.
- Delta Environmental Consultants. 2000. “Comprehensive site assessment of 267 Western Boulevard project, Jacksonville, NC.” Scotchman #66, Project No. X0NC-110.
- Do J., B.M. Montoya, and M.A. Gabr. 2019. “Debonding of microbially induced carbonate precipitation-stabilized sand by shearing and erosion.” *Geomechanics and Engineering*, 17(5): 429-438. <https://doi.org/10.12989/gae.2019.17.5.429>.
- Ebigbo, A., Phillips, A., Gerlach, R., Helmig, R., Cunningham, A. B., Class, H., and L. H. Spangler. 2012. “Darcy-scale modeling of microbially induced carbonate mineral precipitation in sand columns.” *Water Resources Research*, 48, W07519, <https://doi.org/10.1029/2011WR011714>.
- El Mountassir, G., Lunn, R. J., Moir, H., and E. MacLachlan. 2014. “Hydrodynamic coupling in microbially mediated fracture mineralization: Formation of self-organized groundwater flow channels.” *Water Resources Research*, 50:1–16, <https://doi.org/10.1002/2013WR013578>.
- EPA (Environmental Protection Agency). 2002. *Permeation and Leaching*. Washington DC.
- Faeli Z., B. Montoya, and M. Gabr. 2022. “Reactive Transport Modeling of Microbial Induced Calcium Carbonate Precipitation Utilizing Various Configurations of Injection Wells”, GeoCongress, Charlotte, North Carolina.

- Faeli Z., S. Alhomair, M. Gabr, M. Pour-Ghaz, and C. Parker. 2020. "Benzene migration in unsaturated profile with subsurface drainage concrete pipe." Geo-Congress, Minneapolis, MN, February 25-28, 2020, ASCE. <https://doi.org/10.1061/9780784482827.020>.
- Faeli Z., S. Alhomair, P. Hosseini, M. Gabr, and M. Pour-Ghaz. 2021. "Factors affecting multiphase benzene breakthrough into drainage concrete pipe in the unsaturated subsurface profile", *Journal of Pipeline Systems Engineering and Practice*. [https://doi.org/10.1061/\(ASCE\)PS.1949-1204.0000554](https://doi.org/10.1061/(ASCE)PS.1949-1204.0000554).
- Falta, R. W., K. Pruess, I. Javandel, and P. A. Witherspoon. 1992. "Numerical modeling of steam injection for the removal of non aqueous phase liquids from the subsurface, 1. Numerical formulation." *Water Resources Research*, 28(2), 433-449. <https://doi.org/10.1029/91WR02526>.
- Fetter, C. W. 1999. *Contaminant hydrogeology* (second ed.). Upper Saddle River, New Jersey, United States of America: Prentice Hall Inc., Simon & Schuster.
- Freeze, R.A., and J.A. Cherry. 1979. "Groundwater; Prentice-Hall Inc.: Englewood Cliffs." NJ, USA, Volume 7632, p. 604.
- Ghasemzadeh, F., and M. Pour-Ghaz. 2015. "Effect of damage on moisture transport in Concrete." *Journal of Materials in Civil Engineering*, 27(9): 04014242. [https://doi.org/10.1061/\(ASCE\)MT.1943-5533.0001211](https://doi.org/10.1061/(ASCE)MT.1943-5533.0001211).
- Ginn, T.R. 1995. "A brief review of bacterial transport in natural porous media." Pacific Northwest National Laboratory, Richland, WA, PNL-10876, ON: DE96003607. <https://doi.org/10.2172/197807>.
- Ginn, T.R., Wood B.D., Nelson K, Scheibe T.D., Murphy E.M., and T.P. Clement. 2002. "Processes in microbial transport in the natural subsurface." *Adv. Water Resource*, 25(8-12):1017-42.
- Gomez, M. G., Anderson, C. M., Graddy, C. M. R., DeJong, J. T., Nelson, D. C., and T. R. Ginn. 2017. "Large-scale comparison of bioaugmentation and biostimulation approaches for biocementation of sands." *J. Geotech. Geoenviron. Eng.* 143(5). [https://doi.org/10.1061/\(ASCE\)GT.1943-5606.0001640](https://doi.org/10.1061/(ASCE)GT.1943-5606.0001640).
- Harkes, M. P., Van Paassen, L. A., Booster, J. L., Whiffin, V. S., and M. C. van Loosdrecht. 2010. "Fixation and distribution of bacterial activity in sand to induce carbonate precipitation for ground reinforcement." *Ecol. Eng.*, 36(2): 112-117.
- Harvey, R.W., and SP. Garabedian. 1991. "Use of colloid filtration theory in modeling movement of bacteria through a contaminated sandy aquifer." *Environ Sci Technol*, 25 :178-185.
- Harvey, R. W., Kinner, N. E., MacDonald, D., Metge, D. W., and A. Bunn. 1993. "Role of physical heterogeneity in the interpretation of small-scale laboratory and field observations of bacteria, microbial-sized microsphere, and bromide transport through aquifer sediments." *Water Resources Research*, 29: 2713-2721.

- Holsen, T. M., J. K. Park, L. Bontoux, D. Jenkins, and R. E. Selleck. 1991. "The effect of soils on the permeation of plastic pipes by organic chemicals." *Journal of the American Water Works Association JAWWA* 5, 83 (11), 85-91. <https://www.jstor.org/stable/41293557>.
- Hosseini P., S. Alhomair, Z. Faeli, M. Gabr, M. Pour-Ghaz, D. Knappe. 2020. "Degradation model for the tensile strength of PVC and Rubber gasket materials exposed to benzene and PCE-Saturated Aqueous Solutions", *Transport Research Record* , 2674 (2), 274–283. <https://doi.org/10.1177/0361198120906126>.
- Holtz, R. D., Kovacs, W. D., and T. C. Sheahan. 1981. "An introduction to geotechnical engineering." Prentice-Hall, Englewood Cliffs, NJ.
- Hommel, J., Lauchnor, E., Phillips, A., Gerlach, R., Cunningham, A.B., Helmig, R., Ebigbo, A., and H. Class. 2015. "A revised model for microbially induced calcite precipitation: Improvements and new insights based on recent experiments." *Water Resources Research*, 51:3695–3715, <https://doi.org/10.1002/2014WR016503>.
- Hommel, J., Lauchnor, Gerlach, R., A., Cunningham, A.B., Ebigbo, A., Helmig, R., and H. Class. 2016. "Investigating the influence of the initial biomass distribution and injection strategies on biofilm-mediated calcite precipitation in porous media." *Transp Porous Med*, 114:557–579.
- Kumar, A. 2010. "Water flow and transport of chloride in unsaturated concrete." M.Sc. thesis Department of Civil and Geological Engineering, University of Saskatchewan, Canada. <http://hdl.handle.net/10388/etd-07132010-144542>.
- Leech, C., D. Lockington, and R. Dough Hooton. 2006. "Estimation of water retention curve from mercury intrusion porosimetry and Van Genuchten model." *ACI Structural Journal*. 103(2), 291-295.
- Li, X., Zhang, P., Lin, C. L., and W. P. Johnson .2005. "Role of hydrodynamic drag on microsphere deposition and re-entrainment in porous media under unfavorable conditions." *Environ. Sci. Technol.*, 39: 4012– 4020.
- Logan, B. E., Jewett, D. G., Arnold, R. G., Bouwer, E. J., and C. R. O'Melia. 1995. "Clarification of clean-bed filtration models." *J. Environ. Eng.*, 121 (12): 869-873, [https://dx.doi.org/10.1061/\(ASCE\)0733-9372\(1995\)121:12\(869\)](https://dx.doi.org/10.1061/(ASCE)0733-9372(1995)121:12(869)).
- Mao, F., J. A. Gaunt, C. L. Cheng, and S.K. Ong. 2010. "Permeation of BTEX compounds through HDPE pipes under simulated field conditions." *Journal American Water Works Association*, 102(3),107-118. <https://doi.org/10.1002/j.1551-8833.2010.tb10077>.
- Mao, F., J. A. Gaunt, C. L. Cheng, and S.K. Ong. 2011. "Permeation of Petroleum-Based Hydrocarbons through PVC Pipe Joints with Rieber Gasket Systems." *Journal of Environmental Engineering*, 137(12),1128-1135.[https://doi.org/10.1061/\(ASCE\)EE.1943-](https://doi.org/10.1061/(ASCE)EE.1943-)

7870.0000431.

- Martinez, B.C. 2012. "Up-Scaling of Microbial Induced Calcite Precipitation in Sands for Geotechnical Ground Improvement." Ph.D. Dissertation, University of California, Davis.
- Martinez, B.C., DeJong, J.T., and T.R. Ginn. 2014. "Bio-geochemical reactive transport modeling of microbial induced calcite precipitation to predict the treatment of sand in one-dimensional flow." *Computers and Geotechnics*, 58:1–13, <http://dx.doi.org/10.1016/j.compgeo.2014.01.013>.
- Mercer, J. W., and R. M. Cohen. 1990. "A Review of immiscible fluids in the subsurface: properties, models, characterization and remediation." *Journal of Contaminant Hydrology*, 6(2), 107-163. [https://doi.org/10.1016/0169-7722\(90\)90043-G](https://doi.org/10.1016/0169-7722(90)90043-G).
- Minto, J.M., Lunn, R.J., and G. El Mountassir. 2019. "Development of a reactive transport model for field-Scale simulation of microbially induced carbonate precipitation." *Water Resources Research*, 55:7229–7245. <https://doi.org/10.1029/2019WR025153>.
- Mitchell, J.K., and J.C., Santamarina. 2005. "Biological considerations in geotechnical engineering." *J. Geotech. Geoenviron. Eng.*, 131(10): 1222–1233.
- Montoya, B.M., Do, J., and M.A. Gabr. 2021. "Distribution and Properties of Microbially Induced Carbonate Precipitation in Underwater Sand Bed." *J. Geotech. Geoenviron. Eng.* (In press).
- Murphy, E.M., and T. Ginn. 2000. "Modeling microbial processes in porous media." *Hydrogeology Journal*, 8:142–158.
- Nafisi, A., Montoya, B.M., and Evans, T.M. 2020. "Shear Strength Envelopes of biocemented sands with varying particle size and cementation level." *J. Geotech. Geoenviron. Eng.* 146(3): 04020002, [https://doi.org/10.1061/\(ASCE\)GT.1943-5606.0002201](https://doi.org/10.1061/(ASCE)GT.1943-5606.0002201).
- Nassar, M.K., Gurung, D., Bastani, M., Ginn, T.R., Shafei, B., Gomez, M.G., Graddy, C.M.R., Nelson, D.C., and J.T. DeJong. 2018. "Large-Scale experiments in microbially induced calcite precipitation (MICP): Reactive transport model development and prediction." *Water Resources Research*, 54: 480–500. <https://doi.org/10.1002/2017WR021488>.
- NC DEQ. 2016. Groundwater Quality Standards. 15ANCAC 2L .0202. <https://deq.nc.gov/documents/nc-stds-groundwater-02l-0202>.
- NC DEQ. 2007. Maximum Soil Contaminant Concentrations. 15A NCAC 02L .0411. <https://files.nc.gov/ncdeq/Waste%20Management/DWM/UST/NonUST/NURP%20Guidelines%20tables%20%20062912%20FINAL.pdf>.
- NC DEQ. 2018. Toxic Air Pollutant Guidelines. 15A NCAC 02D.1104. <https://files.nc.gov/ncdeq/Air%20Quality/rules/rules/D1104.pdf>.

- Nemes, A., M. Schaap, F. J. Leij, and J. H. M. Wösten. 2015. "UNSODA 2.0: Unsaturated Soil Hydraulic Database. Database and program for indirect methods of estimating unsaturated hydraulic properties." US Salinity Laboratory - ARS. Accessed 31 January 2020. <https://doi.org/10.15482/USDA.ADC/1173246>.
- Ong, S. K., J. A. Gaunt, F. Mao, C.L. Cheng, L. Esteve-Agelet, and C.R. Hurburgh. 2008. "Impact of petroleum-based hydrocarbons on PE/PVC pipes and pipe gaskets." Order No. 91204, Awwa Res. Fdn., Denver. 32(3).
- Parker, J. C., R. J. Lenhard, and T. Kuppasamy. 1987. "A parametric model for constitutive properties governing multiphase flow in porous media." *Water Resources Research*, 23(4), 618-624. <https://doi.org/10.1029/WR023i004p00618>.
- Pasha, A., L. Hu, and J. Meegoda. 2014. "Numerical simulations of a light non aqueous phase liquid (LNAPL) movement in variably saturated soils with capillary hysteresis." *Canadian Geotechnical Journal*, 51(9), 1046–1062. <https://doi.org/10.1139/cgj-2012-0165>.
- Petrasim User Manual, Rockware Inc. 2018. www.thunderheadeng.com.
- Pruess, K., and A. Battistelli. 2002. "TMVOC, a numerical simulator for three-phase non-isothermal flows of multicomponent hydrocarbon mixtures in saturated- unsaturated heterogeneous media." LBNL-49375 Lawrence Berkeley National Lab.: Berkeley, CA, USA.
- Qiu Z., and J. Wang. 2015. "Experimental study on the anisotropic hydraulic conductivity of a sandstone–mudstone particle mixture." *Journal of Hydrological Engineering*, 20(11): 04015029. [https://doi.org/10.1061/\(ASCE\)HE.1943-5584.0001220](https://doi.org/10.1061/(ASCE)HE.1943-5584.0001220).
- Reid, R. C., J. M. Prausnitz, and B. E. Poling. 1987. *The properties of gases and liquids*. McGraw-Hill, New York.
- Rivett, M. O., G. P. Wealthall, and R. A. Dearden. 2011. "Review of unsaturated-zone transport and attenuation of volatile organic compound (VOC) plumes leached from shallow source zones." *Journal of Contaminant Hydrology*, 123 (3-4), 130-156. <https://doi.org/10.1016/j.jconhyd.2010.12.013>.
- Richards, L.A. 1931. "Capillary conduction of liquids through porous mediums." *Physics*, 1 (5): 318–333.
- San Pablo, A.C. M., Lee, M., Graddy, C.M.R., Kolbus, C.M., Khan M., Zamani, A., Martin, N., Acuff, C., DeJong, J.T., Gomez, M.G., and D.C. Nelson. 2020. "Meter-Scale biocementation experiments to advance process control and reduce impacts: examining spatial control, ammonium by-product removal, and chemical reductions." *J. Geotech. Geoenviron. Eng.*, 146(11): 04020125, [https://doi.org/10.1061/\(ASCE\)GT.1943-5606.0002377](https://doi.org/10.1061/(ASCE)GT.1943-5606.0002377).

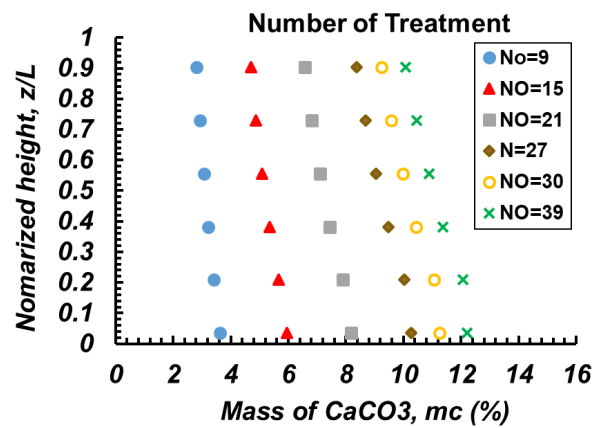
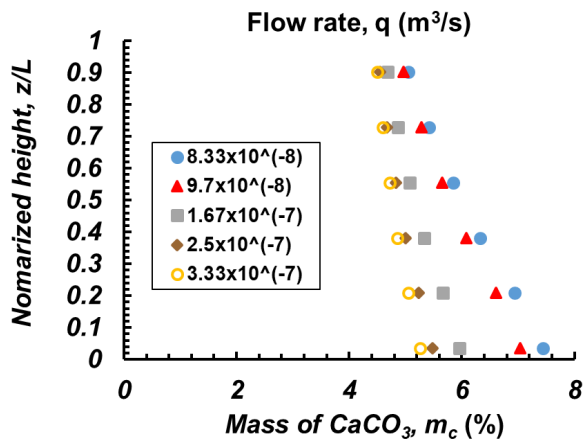
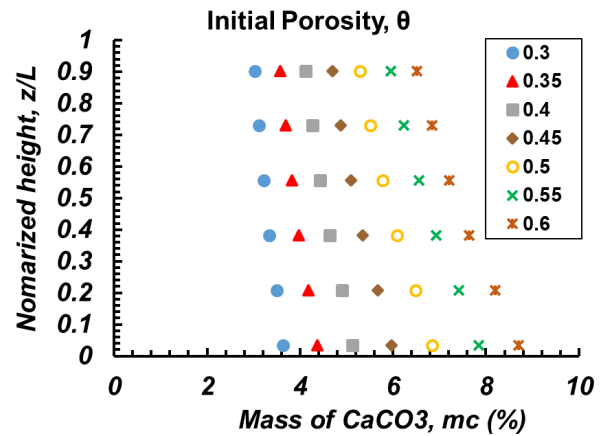
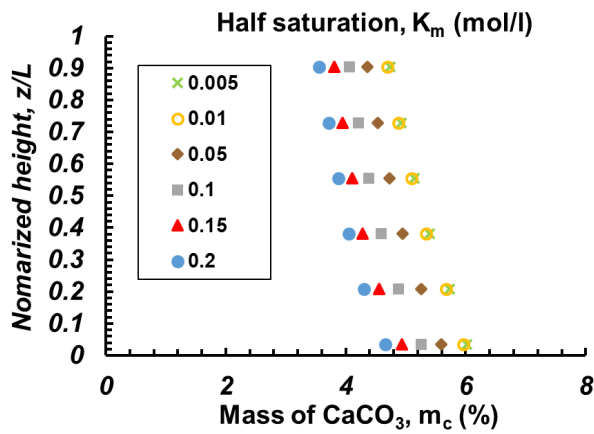
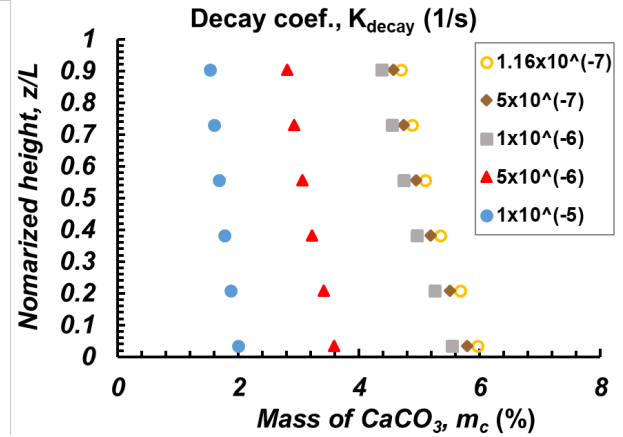
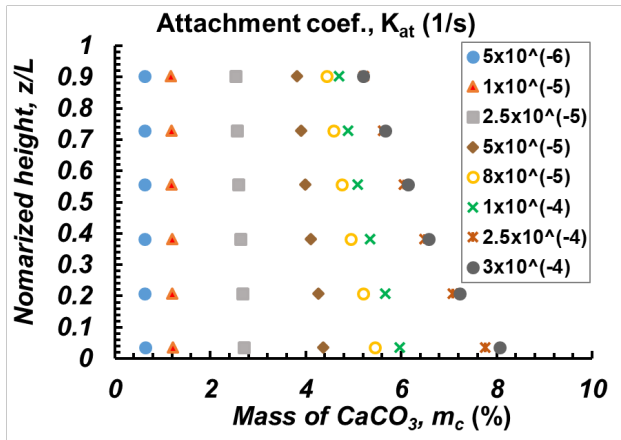
- Silliman, S.E. 1995. "Particle transport through two-dimensional, saturated porous media: Influence of physical structure of the medium." *J. Hydrol.*, 167: 79–98.
- Sleep, B. E., and J. F. Skyes. 1989. "Modeling the transport of volatile organics in variably saturated media." *Water Resources Research*, 25(1), 81-92. <https://doi.org/10.1029/WR025i001p00081>.
- Stone, H. L. 1970. "Probability model for estimating three-phase relative permeability." *Journal of Petroleum Technology*, 22(1), 214-218. <https://doi.org/10.2118/2116-PA>.
- Stocks-Fischer, S., J. K. Galinat, and S. S. Bang. 1999. "Microbiological precipitation of CaCO₃." *Soil Biol. Biochem.* 31 (11): 1563–1571. [https://doi.org/10.1016/S0038-0717\(99\)00082-6](https://doi.org/10.1016/S0038-0717(99)00082-6).
- Swanton, S. W. 1995. "Modelling colloid transport in groundwater; the prediction of colloid stability and retention behavior." *Adv. Colloid Interface Sci.*, 54: 129-208.
- Terracon Consultants Inc. 2018. "Preliminary site assessment of 267 Western Boulevard project, Jacksonville, NC." Parcel 43 - William F and Eva M Rouse, TIP No. U-5736, Project No. 70187063.
- Tobler, D.J., Cuthbert, M.O., Phoenix, V.R. 2014. "Transport of *Sporosarcina pasteurii* in sandstone and its significance for subsurface engineering technologies." *Applied Geochemistry*, 42:38–44, <https://doi.org/10.1016/j.apgeochem.2014.01.004>.
- Tong, M., Li, X., Brow, C. N., and W. P. Johnson .2005. "Detachment influenced transport of an adhesion-deficient bacterial strain within water-reactive porous media." *Environ. Sci. Technol.*, 39: 2500–2508.
- Tufenkji, N., and M. Elimelech. 2005. "Breakdown of colloid filtration theory: Role of the secondary energy minimum and surface charge heterogeneities", *Langmuir*, 21: 841–852.
- Valdés, J.R., and J.C., Santamarina. 2006. "Particle clogging in radial flow: microscale Mechanisms." *SPE Journal*, 11(02): 193-198.
- Van Geel, P. J., and J. F. Sykes. 1994. "Laboratory and model simulation of a LNAPL spill in a variably-saturated sand, 1. Laboratory experiment and image analysis techniques." *Journal of Contaminated Hydrology*, 17 (1), 1-25. [https://doi.org/10.1016/0169-7722\(94\)90075-2](https://doi.org/10.1016/0169-7722(94)90075-2).
- Van Genuchten, M.T. 1980. "A closed-form equation for predicting the hydraulic conductivity of unsaturated soils." *Soil Science Society of America Journal*, 44(5), 892-898.
- van Paassen, L.A. 2009a. "Biogrout: Ground improvement by microbially induced carbonate precipitation." Ph.D. Dissertation, Delft University of Technology.
- van Paassen, L. A., Harkes, M. P., van Zwieten, G. A., van Der Zon, W. H., van Der Star, W. R. L., and M. C. M. van Loosdrecht, 2009b. "Scale up of BioGrout: A biological ground

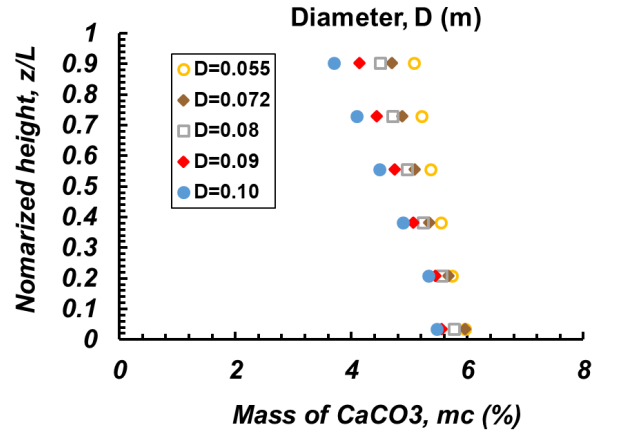
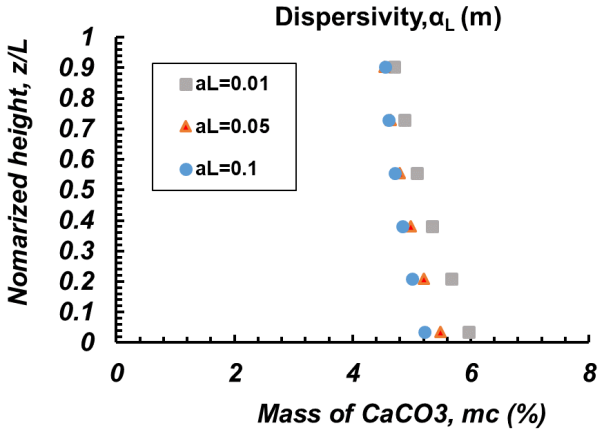
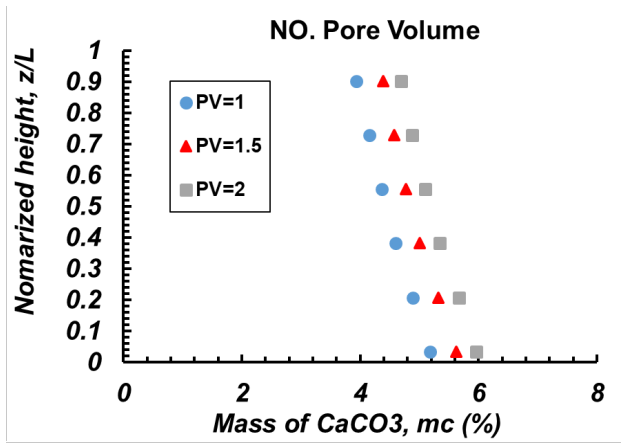
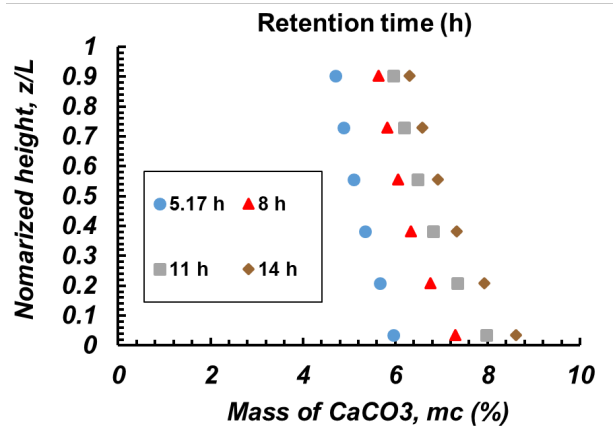
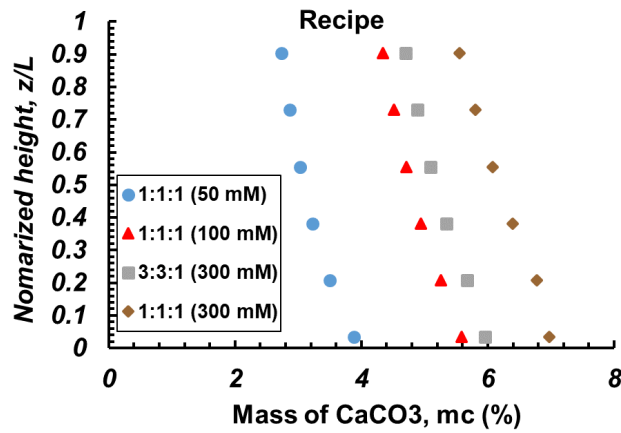
- reinforcement method.” 17th ICSMGE, 2328–2333.
- van Wijngaarden, W.K., Vermolen, F. J. , van Meurs, G. A. M., and C. Vuik. 2011. “Modelling biogrout: A new ground improvement method based on microbial-induced carbonate precipitation.” *Transport in Porous Media*, 87:397–420, <https://doi.org/10.1007/s11242-010-9691-8>.
- van Wijngaarden, W.K., Vermolen, F.J., van Meurs, G.A.M., and C. Vuik. 2012. “A mathematical model and analytical solution for the fixation of bacteria in biogrout.” *Transp. Porous Media*, 92(3), 847–866. <https://doi.org/10.1007/s11242-011-9937-0>.
- van Wijngaarden, W.K., van Paassen, L.A, Vermolen, F. J. , van Meurs, G. A. M., and C. Vuik. 2016. “Simulation of front instabilities in density-driven flow using a reactive transport model for biogrout combined with a randomly distributed permeability field.” *Transport in Porous Media*, 112:333–359, <https://doi.org/10.1007/s11242-016-0649-3>.
- Wang, Y., Soga, K., DeJong, J. T., and A. J. Kabla. 2021. “Effects of bacterial density on growth rate and characteristics of microbial-induced CaCO₃ precipitates: particle-scale experimental study.” *J. Geotech. Geoenviron. Eng.*, 147(6): 04021036, [https://doi.org/10.1061/\(ASCE\)GT.1943-5606.0002509](https://doi.org/10.1061/(ASCE)GT.1943-5606.0002509).
- Whiffin, V.S., van Paassen, L.A., Harkes, M.P. 2007. “Microbial carbonate precipitation as a soil improvement technique.” *Geomicrobiology Journal*, 24:5, 417-423, <https://doi.org/10.1080/01490450701436505>.
- Yang, Q. 2012. “Modelling of benzene distribution in the subsurface of an abandoned gas plant site after a long term of groundwater table fluctuation.” *Hydrological Process*, 27, 3217–3226. <https://doi.org/10.1002/hyp.9442>.
- Zeng, C., Veenis, Y., Hall, C. A., Young, E. S., van der Star, W. R. L., Zheng, J., and L. A. van Paassen. 2021. “Experimental and numerical analysis of a field trial application of microbially induced calcite precipitation for ground stabilization.” *J. Geotech. Geoenviron. Eng.*, 147(7): 05021003. [https://doi.org/10.1061/\(ASCE\)GT.1943-5606.0002545](https://doi.org/10.1061/(ASCE)GT.1943-5606.0002545).
- Zhang, T., and I. Klapper. 2010. “Mathematical model of biofilm induced calcite precipitation.” *Water Sci. Technol.*, 61(11), 2957–29.

APPENDICES

Appendix A

Figure 1A CaCO₃ distribution with variations of 15 parameters.





Appendix B

Table 1B Model parameters.

Model Parameter	Symbol	Unit	Value		
Simulated Experiment			Do (2019)	Montoya (2021)	San Pablo (2020)
Experiment type			Small-scale column	Large-scale box	Large-scale horizontal trough
Domain Dimension		m	0.07x0.07 x 0.14	0.90x0.90x0.9	0.2x0.2x3.7
Soil Type			Silica Sand d ₅₀ =0.49 mm	Silica Sand d ₅₀ =0.49 mm	Concrete/Teichert Sand d ₃₀ =0.54,d ₆₀ =1.54
Initial bulk porosity	θ_0		0.45	0.44	0.34
Initial hydraulic con.	k_s	m/s	3.56×10^{-5}	1.73×10^{-4}	1.00×10^{-3}
Specific ureolysis rate	K_u	mol/l.s.OD ₆₀₀	$(1.06-2.4) \times 10^{-6}$	2.0×10^{-6}	$(1.0-2.0) \times 10^{-6}$
Half-saturation rate const.	K_m	mol/l (M)	$3.5 \times 10^{-3}-1.0 \times 10^{-2}$	1.0×10^{-2}	1.0×10^{-2}
Decay rate coefficient	K_{decay}	1/s	1.15×10^{-7}	1.15×10^{-7}	1.15×10^{-7}
Dispersivity	$\alpha_L = \alpha_t$	m	0.01	0.3	0.1
Diffusion coefficient	D_e	m ² /s	1×10^{-9}	1×10^{-9}	1×10^{-9}
Soil dry density	γ_d	kg/m ³	1489	1489	1600
fluid density	γ_f	kg/m ³	1000	1000	1000
Compressibility of fluid	X_f	1/Pa	4.4×10^{-10}	4.4×10^{-10}	4.4×10^{-10}
Matrix effective compressibility	X_p	1/Pa	1×10^{-8}	1×10^{-8}	1×10^{-8}
Dynamic fluid viscosity	μ	Pa.s	8.9×10^{-4}	8.9×10^{-4}	8.9×10^{-4}
Molar mass of CaCO ₃	m_{CaCO_3}	g/mol	100.087	100.087	100.087
CaCO ₃ bulk density	ρ_{CaCO_3}	kg/m ³	2710	2710	2710
Injection flow rates	$q(t)$	cm ³ /s (ml/min)	0.167 (10)	1.0-10.0 (60-600)	6.67(400)
Bacterial solution	Bacteria-Urea-NH ₄ Cl	OD-M-M	1-0.333-0.374	1-0.333-0.374	(1-0.015)-0-0
Cementation solution	Urea-NH ₄ Cl-CaCl ₂	M-M-M	0.333-0.374-0.25	0.333-0.374-0.05	0.25-0.0125-0.25
Bacterial cell density		cells/ml	$(2-5) \times 10^7$	$(2-5) \times 10^7$	9.4×10^7 (1) 1.4×10^6 (2)
Total treatment duration		d	14	30	13
Injection time		h	0.83	2-3	3.15 (19 h for 2 nd bio)
Retention time		h	5.17-5.17-11.17 (Repeated each 3 intervals)	21	20.8-24.5
No of cementation treatment			42	18	9
No of biological treatment			1 (+biodosing)	6	2
Source location			Bottom	0.2D-4D from top surface	Trough end